Mathematical Problems in Engineering

Computational Methods in Design and Manufacturing Processes

Lead Guest Editor: Sutasn Thipprakmas
Guest Editors: Yingyot Aue-u-lan, Anders E. W. Jarfors, and Suwat Jirathearanat

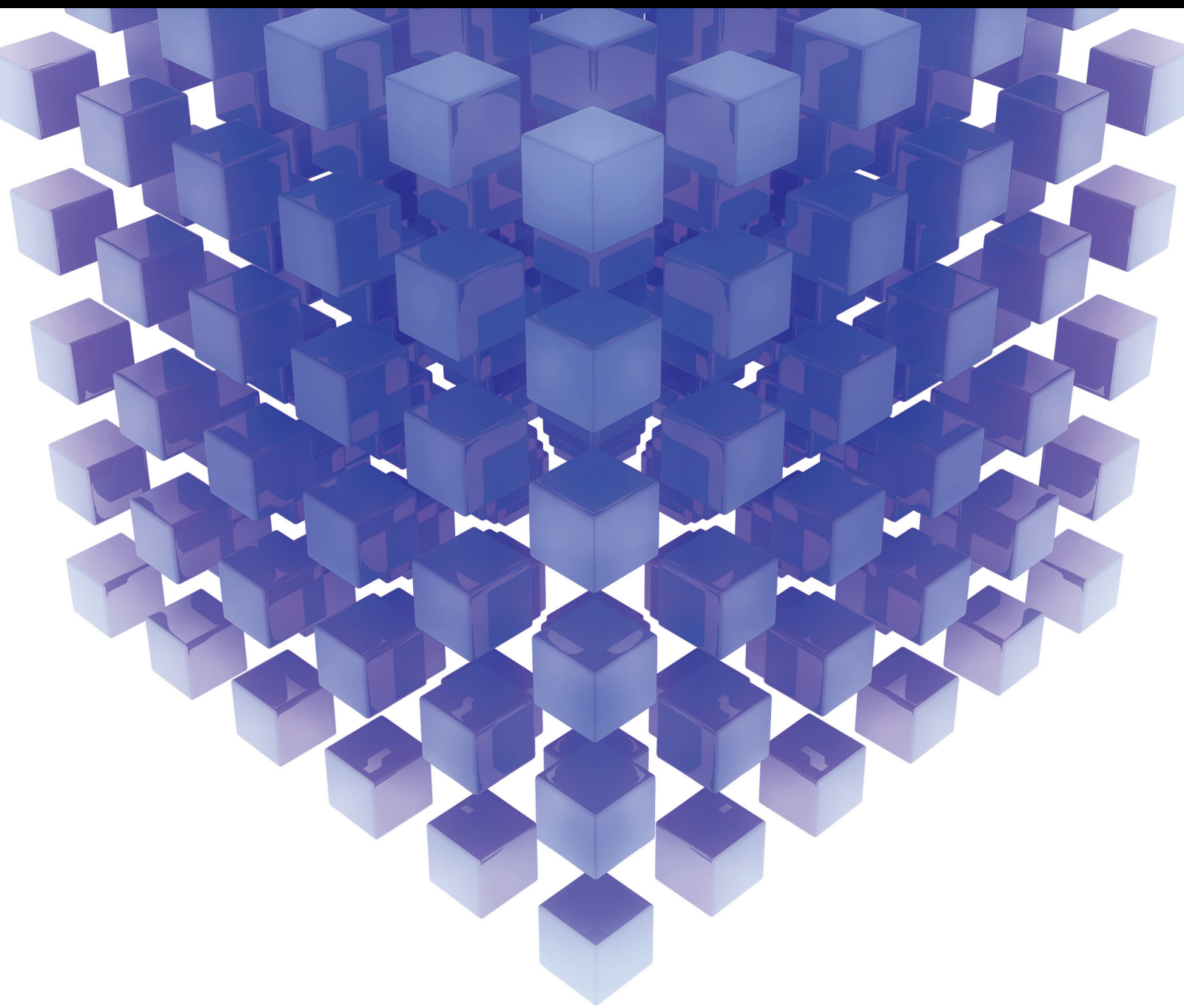

Computational Methods in Design and Manufacturing Processes

Mathematical Problems in Engineering

Computational Methods in Design and Manufacturing Processes

Lead Guest Editor: Sutasn Thipprakmas
Guest Editors: Yingyot Aue-u-lan, Anders E. W. Jarfors, and Suwat Jirathearanat

Editorial Board

Contents

Hindawi
Mathematical Problems in Engineering
Volume 2019, Article ID 1920871, 1 page
https://doi.org/10.1155/2019/1920871

Editorial

Computational Methods in Design and Manufacturing Processes

Sutasn Thipprakmas,[1] **Yingyot Aue-u-lan**,[2] **Anders E. W. Jarfors**,[3] **and Suwat Jirathearanat**[4]

[1] *King Mongkut's University of Technology Thonburi, Bangkok, Thailand*
[2] *King Mongkut's University of Technology North Bangkok, Thailand*
[3] *Jönköping University, Sweden*
[4] *Singapore Institute of Manufacturing Technology (SIMTech), Singapore*

Correspondence should be addressed to Sutasn Thipprakmas; sutasn.thi@kmutt.ac.th

Received 10 April 2019; Accepted 10 April 2019; Published 9 May 2019

During the last decades, across all fields of engineering sciences, the evolution of complex systems in design and manufacturing processes has progressed along with the development of computational methods that can treat more and more complex design and simulation problems. Many design and manufacturing processes are now tackled using computational methods that aim at improvement in manufacturing performance. The development of increasingly sophisticated computational methods and the improvement in computer performance represent an emerging issue from both an industry and an academic viewpoint. Nowadays, a lot of research activities in the field of design and manufacturing processes have been accomplished and there are a wide range of applications where the computational methods are used.

The objective of this special issue is to present a wide spectrum of computational methods used as a valuable tool for solving more and more complex design and manufacturing processes as well as providing readers with a representative outlook of the latest achievements in this field. The focus of this special issue is placed on the understanding of the enabling computational simulation to replace a big data of experiments and computational optimization to handle and implement multidisciplinary design in complex manufacturing processes.

This special issue offers an articulated overview of the examined topics. It contains fourteen original research articles. Eight research articles in this special issue cover a wide range of computational simulation techniques to design and construct mechanical elements applied in several manufacturing processes such as a high-energy mill for handling magnesium powder and to design PID controllers. Four research articles discuss various computational optimization techniques to determine optimal working process parameters applied in several manufacturing processes such as a pick-and-place optimization of the die attaching process in semiconductor industry and an optimization of a robotic arm under fuzziness. Two research articles in this special issue also address computational evolving techniques for casting process modeling and a new mathematical method applied to the singularity problem of 3-RSR multimode mobile parallel mechanism.

The guest editors hope the information provided in this special issue is useful and offers stimulation to the new developments and applications of computational methods in design and manufacturing processes.

Conflicts of Interest

The editors declare that they have no conflicts of interest.

Acknowledgments

We would like to thank the authors for the excellent contribution of their research works. We also would like to thank the reviewers for their time and valuable review results.

Sutasn Thipprakmas
Yingyot Aue-u-lan
Anders E. W. Jarfors
Suwat Jirathearanat

Hindawi
Mathematical Problems in Engineering
Volume 2019, Article ID 6164092, 15 pages
https://doi.org/10.1155/2019/6164092

Research Article

Computational Evolving Technique for Casting Process of Alloys

Amir M. Horr

Leichtmetallkompetenzzentrum Ranshofen GmbH, Austrian Institute of Technology, Vienna, Austria

Correspondence should be addressed to Amir M. Horr; amir.horr@ait.ac.at

Received 15 November 2018; Accepted 23 March 2019; Published 8 May 2019

Guest Editor: Suwat Jirathearanat

The challenging task of bringing together the advanced computational models (with high accuracy) with reasonable computational time for the practical simulation of industrial process applications has promoted the introduction of innovative numerical methods in recent decades. The time and efforts associated with the accurate numerical simulations of manufacturing processes and the sophisticated multiphysical and multiscale nature of these processes have historically been challenging for mainstream industrial numerical tools. In particular, the numerical simulations of industrial continuous and semicontinuous casting processes for light metal alloys have broadly been reinvigorated to investigate the optimization of casting processes. The development of advanced numerical techniques (e.g., multiscale/physical, finite zoning, and evolving domain techniques) for industrial process simulations including the transient melt flow, heat transfer, and evolution of stress/strain and damage during continuous casting processes have endeavored many new opportunities. However, smarter and broader improvements are needed to capture the underlying physical/chemical phenomena including multiscale/physical transient fluid-thermal-mechanical coupling and dynamic heat-transfer changes during these processes. Within this framework, the cooling system including its fluid flow and its characteristic heat transfer has to be modelled. In the research work herein, numerical studies of a novel transient evolving technique including the thermal-mechanical phenomena and Heat Transfer Coefficient (HTC) estimation using empirical and reverse analyses are presented. The phase change modeling during casting process including liquid/solid interface and also the implementation of dynamic HTC curves are also considered. One of the main contributions of this paper is to show the applicability and reliability of the newly developed evolving numerical simulation approach for in-depth investigations of continuous casting processes.

1. Introduction

The speed and the quality of industrial production processes are totally depending on efficient and sound material processes based on rigorous scientific and engineering knowledge, experiences, and numerical simulations. For many light metal alloy industries, it is required to establish a framework for continuous innovation in design and productions and a sound and comprehensive strategy for confronting crucial challenges and competitions. The combination of state-of-art innovative mathematical, physical, and phenomenological models (with accurate predictive powers) and sound parallel experimental and numerical simulation studies to explore what technical solutions are viable for these processes is not yet exploited to the extend it could. Today's integrated computer-based simulation tools which consist of advanced/practical multiphysical/scale models (continuous and discrete), data-driven schemes (Artificial Intelligence, AI, Machine learning, ML), and pioneering integrated process simulation tools would reflect the essence of whole engineering and industrial experiences and knowledge. These new industrial design and production tools can be developed in a systematic way to handle vast related processes/databases, lightweight industrial experiences/knowledge-bases, and information [1]. One of the most important ingredients of these integrated systems is numerical simulation tools where properties and the performance of production chain processes based on conventional and/or advanced techniques are implemented.

The combination of physical, mathematical, and computational topics to approach the fundamental question of optimum process parameters and conditions has been promoted in recent years. Instead of having single numerical domain with its associated grid (mesh), the emerging idea includes a new approach to represent various complexities (e.g., change of phase, micro cracks, etc.) within limited dynamic zones in

the computational domain that works for both implementing advanced mathematical models (e.g., solidification, plasticity, etc.) and also computational time. This provides the basis for multiple numerical domains (zones), running in parallel (with multiple instances of solvers) and their communication using advanced interface routines (using mapping, condensation, etc., techniques). The interaction/communication of these evolving zones within the simulation system can be managed smartly using advanced controllers (AI and ML technologies) and optimum design can be carried out using the combination of analytical and smart data-driven schemes.

One of the main concerns for these new-generation techniques is how to represent changes of the dynamic system (e.g., change of phase, cracking, nonlinearities, etc.) to understand the consequences of solution and optimization techniques on the process. The overarching research work herein is a step towards the founding of the procedure to combine complexity-driven solution techniques (e.g., nonlinearity within dynamic zones) with efficient interfacing and computationally efficient solution schemes. The technique relies on separate and parallel efforts devoted to predicting the response of complex system (e.g., solidification and heat energy evolution during casting process). The research work also combines different aspects of thermal-fluid-mechanical interactions of industrial processes to predict optimum parameters and avoid damage and failure through the implementation of multiscale (e.g., micro-macro) mechanical models at selected dynamic zones.

As part of the integrated simulation approach for multiphysical, multiscale simulation, the development of cooling zones at boundaries, dynamic mesh modules along with parallel processing, and computational efficiency have also been promoted herein. The purpose of the research work is to present steps towards an integrated numerical method, which would help improve the simulation of dynamic material processes and their optimization for the future manufacturing.

2. Conventional Modelling Concepts

The life-long performance of engineering components along with their costs, agility, and versatility requires sound and practical processes within manufacturing chain. To help optimizing these processes for different light metal alloys, various numerical techniques/tools have been developed and employed in the last sixty years. The early numerical approaches developed during second half of the 20th century (e.g., Finite Element, FE, etc.) have employed simple discretization and solver techniques for static and dynamic processes including fixed and adaptive meshing [2, 3]. Additionally, different types of 2D and 3D elements along with variety of shape functions have been developed to discretize numerical domains for simulation of industrial processes including casting, extrusion, rolling, etc. as static, pseudostatic and/or full dynamic processes (e.g., element activation, and deactivation). The discretized domain is then solved at sequential time steps (or frequency steps) using conventional time/frequency integration techniques. The time-history results are then assembled using deterministic and/or statistical schemes to study the dynamic behavior of industrial processes under real-life scenarios [2, 3].

For industrial casting applications, the fixed Lagrangian and/or Eulerian [4] discretized techniques have traditionally been used where the variation of material confined by the numerical grid is solved at different points in time (time steps). In the conventional pure Lagrangian and also updated Lagrangian approaches (with adaptive remeshing), the process of large deformation (or flow) of a body is resembled as a material flow where each material particle (cell) transports its own properties (such as microstructure, temperature, density, etc.). For the simulation of dynamic systems, as the deformation/flow front advances, its properties may change in time. However, their inability of following large distortions of the computational grid without recourse to frequent remeshing (e.g., adaptive remeshing) schemes [4] is its main shortcoming (it is a computationally expensive task). For the Lagrangian approach, let us consider two overlapping domains as a physical material domain, $\boldsymbol{R_X}$, and a spatial domain, $\boldsymbol{R_x}$ (spatiotemporal conditions are only considered at discrete time steps). The mapping function $\boldsymbol{\varphi}$ for these two overlapping domains can be defined as [5]

$$\boldsymbol{\varphi}: \boldsymbol{R_X} \times [t_0, t_T[\longrightarrow \boldsymbol{R_x} \times [t_0, t_T[\tag{1}$$

$$(\boldsymbol{X}, t) \longrightarrow \boldsymbol{\varphi}(\boldsymbol{X}, t) = (\boldsymbol{x}, t) \tag{2}$$

where t_0, t_T are time at original and updated (terminal) configurations and mapping at discrete time points can be allowed as

$$\boldsymbol{x} = \boldsymbol{x}(\boldsymbol{X}, t) \quad t = t \tag{3}$$

which states that the spatial coordinates depend and also strictly track the material particle at discrete time points (no convection). The definitions of time at both domains are real and no hypothetical time definition/interpretations are carried out in a single numerical Lagrangian domain.

Alternatively, in the Eulerian fixed and moving mesh approaches, rather than tracking each material cell (e.g., at deformation front), the evolution of the material flow properties at every point in space (vortices) can be recorded at sequential time steps. This means that the material flow properties at a specified location within the grid depend on its location and time (advection). In this approach, the conservation of material is satisfied at spatial and time points and the computational mesh is mostly fixed where material moves with respect to the grid. The large distortions (and melt flow) of the material motion can be handled with relative ease using convective feature of the method where relative motion of deforming front in respect to the discretized grid is calculated [6–10]. Figure 1 shows the Lagrangian and Eulerian deformation concepts along a with typical temperature field for a 2D Eulerian simulation of material flow in horizontal casting.

Many of the mainstream industrial casting simulation tools have combined the benefits of both techniques in the way that the simulations of melt flow into the mold (filling simulation) are carried out using Eulerian technique, while the thermal-mechanical simulations for the solidified billet

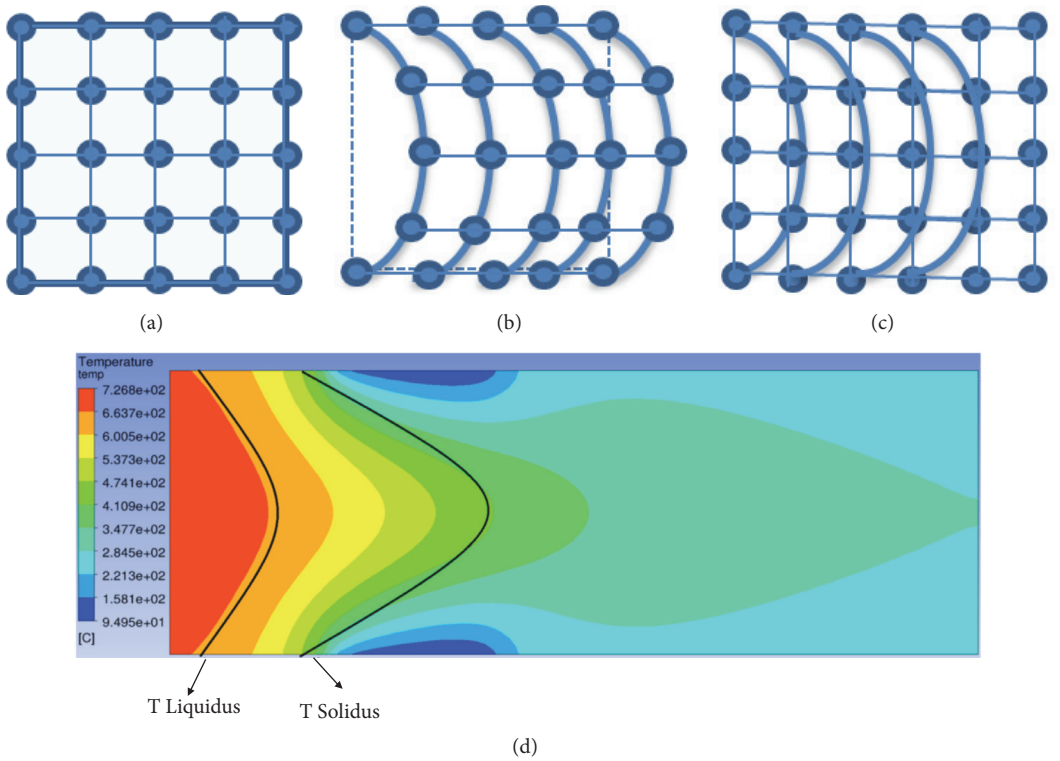

FIGURE 1: (a) Reference grid and deformation in (b) Lagrangian and (c) Eulerian schemes, (d) temperature field for 2D Eulerian material flow in horizontal casting simulation.

are performed using Lagrangian fixed-meshed technique [5]. The Arbitrary Lagrangian Eulerian (ALE), Mixed Lagrangian Eulerian (MiLE), and other similar hybrid methods have been used in these tools where benefits of both numerical schemes are combined [9, 10]. For the ALE approach the material motion/deformation and the spatial configuration are referenced to the third overlapping domain through using mapping functions. The general practice for the discretized grid is to have a mapping function for the material configuration, spatial coordinates, and the third domain defining the grid points. Three different mapping transformations are defined to overlap the numerical domain where the motion of the grid points can be distinguished from the material motion. If the mapping from the third referential domain to the spatial domain is defined by $\boldsymbol{\phi}$, then [5]

$$\boldsymbol{\phi} : \boldsymbol{R}_{\boldsymbol{\chi}} \times [t_0, t_T[\longrightarrow \boldsymbol{R}_{\boldsymbol{x}} \times [t_0, t_T[\tag{4}$$

$$(\boldsymbol{\chi}, t) \longrightarrow \boldsymbol{\phi}(\boldsymbol{\chi}, t) = (\boldsymbol{x}, t) \tag{5}$$

where $\boldsymbol{R}_{\boldsymbol{\chi}}$ is referential domain. The grid motion (e.g., casting speed or billet speed) can then be defined as

$$v_g(\boldsymbol{\chi}, t) = \left.\frac{\partial x}{\partial t}\right|_{\boldsymbol{\chi}} \tag{6}$$

where both material deformation/motion and grid motion are calculated with respect to real time during the simulations. Figure 2 shows the time snap shots of Eulerian mold filling simulation along with subsequent Lagrangian thermal-mechanical simulations for an aluminum semicontinuous industrial casting [11].

The computational concepts for dynamic material processes have been going through fundamental changes since the start of 21st century by introduction of dynamic discretization and multiscaling concepts [12]. The novel ideas of evolution of material properties, updating domain's discretization/boundaries and also computational partitioning during the numerical simulations have been developed [12, 13]. Furthermore, the introduction of material evolutions and their associated physical/mathematical models at different scales (macro, meso, micro, etc.) has helped to overcome numerical problems related to resolution and accuracy of dynamic processes [12]. For the material continuous casting case, the transient nature of the numerical domain and its continuous expansion throughout the process has conventionally been handled using either a birth and death approach or the splitting of element layers at the stationary-moving interface [14]. However, since the change of geometry, mesh, boundary, and energy source within dynamical domain (e.g., continuous casting simulation) can have profound effects on the computational accuracy/time, new schemes had to be developed for higher performance, more generality, and broader versatility.

In the proposed dynamic multiscale and multiresolution approach herein, new subdomains/zones are generated at specific time points to resemble the extension of the cast billet. These newly generated zones are overlapping/attached

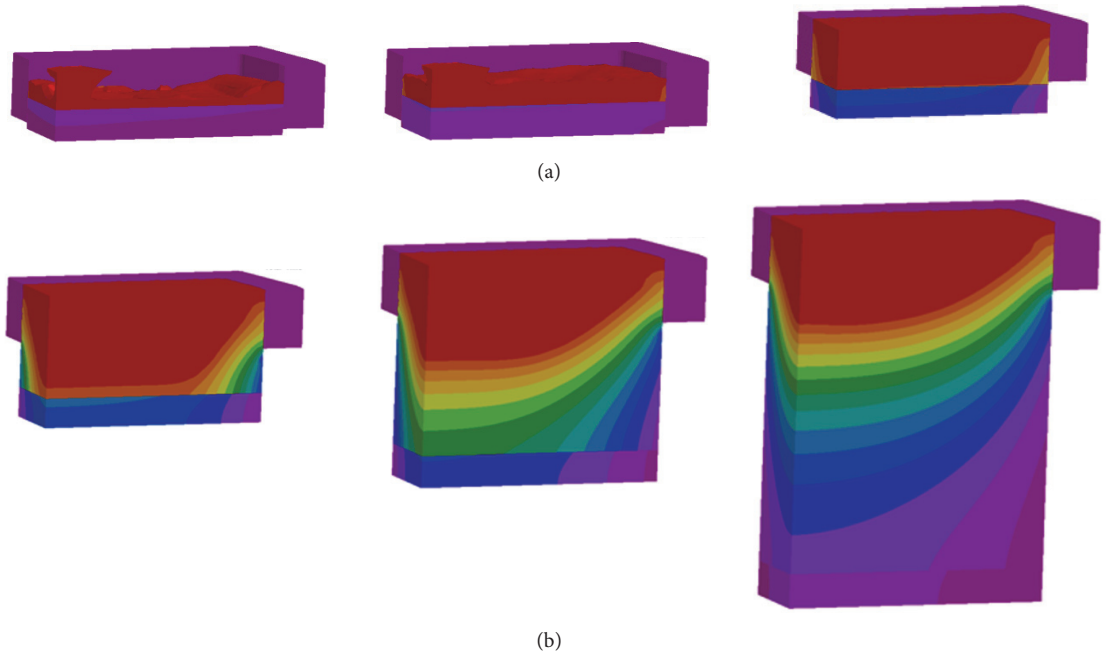

(a)

(b)

Figure 2: (a) Eulerian filling simulation of mold and (b) subsequent Lagrangian extension of the cast billet with their temperature contours for double-symmetric quarter model.

to the main domain at discrete time points where comprehensive mapping procedure (including grid overlapping, nodal condensation, propagation interface, etc.) are applied to reassemble the domain to handle the new material and energy input (new melt and solidified melt material). The added dynamic subdomains/zones can be stationary or moving depending on requirement of the numerical model for the industrial process. As the numerical solution is performed on a full parallel-processing machine, multiple instances of the same solver (or alternatively different solvers) can independently be employed for the base domain and attached/overlapping zones. The generated subdomains (which can be at different length/time scales) would gradually integrate into the main domain (and become a part of main domain) as the evolution phases within the subdomains/zones come to the end (e.g., solidification and nonlinearities).

For the interfacing between the main domain and subdomains (or between subdomains) and to overlap grids with multiresolutions and/or multiscale natures (e.g., overlapping meshes at different length scales) some mathematical representations have already been developed. The Partition of Unity Finite Element Method (PUFEM), Overlapping Sphere Elements (OSE), and few other techniques have already been proposed to handle the grid-inconsistency [15]. For overlapping zones within the numerical domain, let us assume two interfacing grids with overlapping at the boundaries of $\Omega 1$ and $\Omega 2$ numerical domains. For linear finite element grids with base functions $\{v_i\}_{i\in I}$ and $\{w\}_{j\in J}$, the overlapping set can be written as [15]

$$\left\{\emptyset_1 v_i, \emptyset_2 w_j\right\}_{i\in I, j\in J} \tag{7}$$

If the overlapping grid zone is represented with a linear independent relation as

$$\emptyset_1 \sum_i \alpha_i v_i + \emptyset_2 \sum_j \beta_j w_j = 0 \tag{8}$$

and if it is assumed that $\emptyset_2 = 1 - \emptyset_1$ then it can be shown that

$$\begin{gathered} \emptyset_1 \left(\sum_i \alpha_i v_i - \sum_j \beta_j w_j \right) = -\sum_j \beta_j w_j \longrightarrow \\ \sum_i \alpha_i v_i - \sum_j \beta_j w_j = Const. \end{gathered} \tag{9}$$

and the stiffness matrix for the interfacing/overlapping grids can be assembled for firstly nonoverlapping elements (as usual) and, secondly, overlapping elements with multiple entries. Figure 3 shows the typical partial overlapping zonal grids which can represent different part of a numerical domain. More comprehensive discussions about the multiresolution interfacing/overlapping grids can be found in the literature [15–17].

3. Finite Zonal Concept and Interfacing

The investigation of dynamic numerical simulation for industrial continuous casting processes where geometry, mesh, and boundaries of the domain can evolve during the solution has been considered in the last twenty years and different evolution schemes have been proposed [11]. The zonal evolution and smart subdomain technique have been proposed recently and the application of their techniques for the industrial continuous casting process has been investigated [11]. The

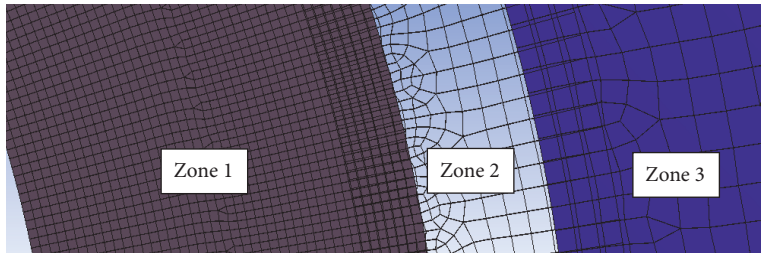

Figure 3: Overlapping zonal representation for nonmatching FE grids.

introduction of dynamic boundaries, evolution zones, and physical/mathematical sink-sourcing energy concepts can facilitate steps towards the formulation of the next generation of numerical techniques for practical and industrial applications.

3.1. Multiresolution Evolution Scheme. The multiscale and multiresolution prerequisites of many industrial process simulation platforms have prompted the use of domain evolution concepts during numerical simulations. The research work herein briefly describes some aspects of basic concepts for innovative evolving domain technique for the full-parallel processing. The newly proposed approach would treat the evolving/progressing cast billet during the continuous casting simulation as a dynamic zone. The zone can move in predefined or calculated manner which would be attached to the main domain through overlapping boundary concept. The generated zones can gradually join the main domain (and become a part of main domain) or stay independent for further processing as flagged evolution phases within the zones (e.g., deformation, solidification, etc.) come to the end.

For the continuous casting simulation (vertical or horizontal), a directional boundary evolution scheme has been implemented using extensive in-house coding. The technique can be summarized in the following steps.

(i) The initial starting conditions are modelled using the results of either Thermal-Computational Fluid Dynamics (CFD) melt delivery simulations or filling-thermal assumptions.

(ii) The initial geometry of the main domain (i.e., mold) and its discretization are defined and initial system matrices are assembled.

(iii) The initial time steps/iterations are solved (using a thermal-mechanical solver) and based on the casting speed the billet domain coordinates are updated.

(iv) The geometry and discretized grids are modified and adapted by adding a single/multiple layer mesh zone based on the evolution of the domain (updated spatial coordinates and shrinkage and thermal deformation changes).

(v) The system matrices are modified/appended and the input energy is distributed amongst the newly generated subdomain.

(vi) Time-history results (from previous time steps) are mapped to the newly generated subdomain.

(vii) The energy balance (thermal energy) is achieved through the energy sink/source concept and the previous converged solution is used as a first step for a newly updated domain.

(viii) The simulation scheme continues with the new geometry/mesh till the next evolution step is triggered.

The lower-scale material evolution phenomena (e.g., microstructure formation during solidification) and its coupling with macro-scale properties can also be considered using numerically efficient overlapped grid technique (not presented in this paper). Figure 4 shows snap shots of a casting numerical simulation of simple double-symmetric rectangular cross-section billet using dynamic evolution technique.

3.2. Simulation of Lower-Scale Phenomena. The solidification of melt during the casting process can be described in different levels of scales/details. Since most of the conventional casting simulations are carried out at macro-scale, many of the conventional numerical solidification modules are based on the macro-kinematics of material behavior. For these macro-scale simulations, there are different approaches for defining the phase transition. Most common is the application of the Scheil-Gulliver equation [18, 19] where a nonequilibrium approach is formulated for solute redistribution during solidification (no solute would diffuse back into the solid). The solid fraction in this method is defined by local current, solidus, and liquidus temperatures as well as the partition coefficient. The Scheil-Gulliver equation in its simple and standard form can be written as [18, 19]

$$C_L = C_0 f_l^{k-1}$$
$$C_S = kC_0 \left(1 - f_S\right)^{k-1} \tag{10}$$

where C_L, C_S, and C_0 are liquid, solid, and initial compositions and f_S, f_S, and k are solid and liquid mass fractions and coefficient $k = C_S/C_L$ (which can be determined from phase diagram), respectively. The formulation is valid for a local equilibrium state between the solid and liquid interface and for moderate-to-low cooling rates. The numerical methodology for the simulation of solidification front during casting process where phase changes and different phases exist (liquid, mushy, and solids) can be

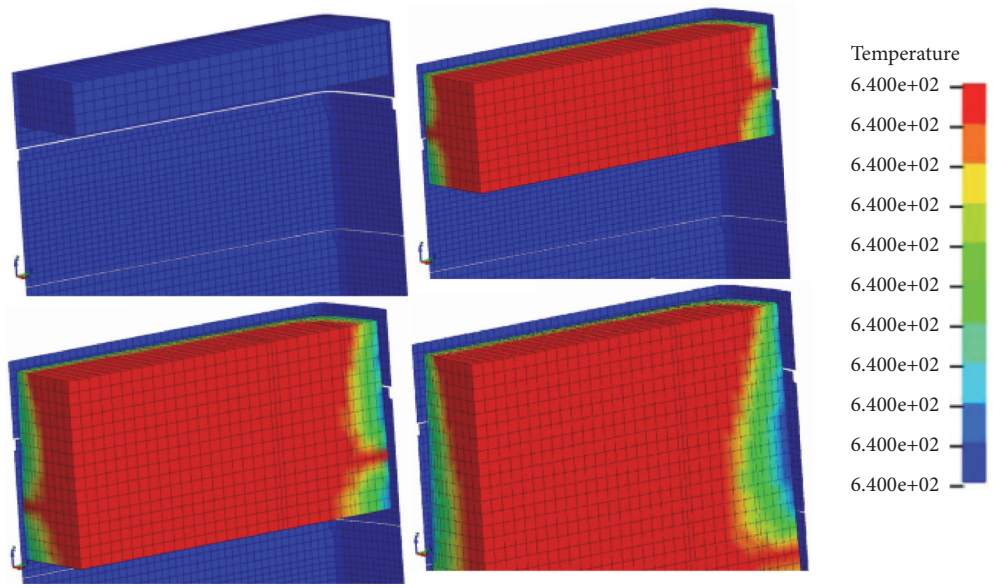

Figure 4: Dynamic evolving technique for double-symmetric rectangular cross-section billet using directional evolving scheme.

challenging. Different numerical methodologies have been developed [11] to handle the phenomena within numerical domains, namely, conduction-based, conduction-convection based, and enthalpy-based methods. In the conduction-based method, the energy transfer during solidification is calculated based on conduction heat transfer and to account for the convection heat transfer effects (melt flow), an artificially high fluid conductivity is defined. While in the conduction-convection method the melt convection is taken into account explicitly with mass transfer and thermal convections are formulated using governing differential equations for the melt flow. The third alternative way is to use the enthalpy concept. Enthalpy is a thermodynamic quantity defining total heat energy of a system which can be combined with other numerical features to account for change of phase during solidification. In the mainstream industrial software tools for casting simulations, the enthalpy method is generally combined with Volume of Fluid (VOF) and domain porosity features (to damp the fluid momentum when it turns into solid). The VOF method can trace the solidification front within the numerical domain while the domain porosity would enable the smooth change of phase from liquid to solid by damping the momentum equation using momentum sink terms. The introduction of momentum sink terms in the energy equation might introduce more numerical challenges since the convergence of the system becomes more difficult. Consider the mass continuity and momentum equation for the melt flow inside the mold as [4]

$$\nabla . U = 0,$$
$$\frac{\partial (\rho U)}{\partial t} + \nabla \cdot (\rho U \otimes U) = -\nabla \mathrm{p} + \nabla \cdot (\mu \nabla \mathrm{U}) \tag{11}$$

where ρ, μ, p, and U are fluid density, viscosity, pressure, and velocity, respectively. Momentum sink term is traditionally inserted into melt momentum equation (for temperatures between liquidus and solidus) to damp the melt velocity due to solidification phenomena. A simple and practical approach for momentum damping can be defined using the Kozeny, Carman approach, and its modification by Blake [20–23]. Let us assume the basic equation for fluid flow in resistive media as

$$\frac{\Delta p}{L} = \alpha \left(\frac{(1-k)^{\beta}}{k^3} \right) \left(\frac{\mu v}{d^2} \right) \tag{12}$$

where $\Delta p/L$, k, μ, d, and v are pressure gradient, domain porosity (liquid volume fraction), melt viscosity, primary channel width, and melt superficial velocity. Variables α, β can be defined for material processes during solidification based on the alloy and process properties. Two different types of momentum sink terms can be defined for the melt solidification, namely, viscous and quadratic terms. The basic viscous sink term for fluid flow in a porous media can be defined as [22]

$$L_V = \frac{\mu}{K} U \tag{13}$$

where K is permeability of the resistive domain. Voller et al. have modified [24–26] the fluid viscous loss model and the permeability of the domain as

$$L_q = -\frac{\mu}{K} \cdot (u - u_s) \tag{14}$$

where u_s is the solidified slab speed (can be assumed as casting speed) and K is permeability which can be calculated based on the resistance against the melt flow inside the dendrite channels during solidification. Ignoring the remelting and the solute concentration effects (temperature exchange

at interface, etc.), Gu et al. [27] have proposed the following equation for the permeability:

$$K = C\frac{f_l^3}{f_s^2}\lambda_1^2 \tag{15}$$

where f_l, f_s, and λ_1 are volume fractions of liquid and solid phases (at the solidification front) and primary dendrite arm spacing. The constant C can be assumed as C=6×10^{-4} [27]. The secondary arm spacing and its resistance effect has not been explicitly defined in (15). The broader equation for estimation of permeability has been derived by author using the combination of physical and analytical approach as [28]

$$C_{LV} = C * \lambda^2 \left(\frac{(1 - f(\mathrm{T}))^{\alpha}}{f(T)^{\beta}}\right)$$
$$f(T) = C_1 * \left(1 - \left(\frac{(\mathrm{T} - \mathrm{T}_s)}{\Delta T}\right)^{\gamma}\right) \quad \Delta T = \mathrm{T}_L - \mathrm{T}_s \tag{16}$$

where C, C_1 are constant coefficients, λ is the primary dendrite arm spacing, and α, β, γ are power coefficient which can be calibrated for the alloy processes (for aluminum alloys α= 3, β=2, and γ =1). Coefficients C and C_1 can be assumed as C= 0.0006 (similar to Gu et. al) and C_1=1 - 1.2 [28]. A more detailed version of the simplified loss term can also be developed [28] using primary and secondary dendrite arm spacing and melt isolation phenomena. Similarly, based on physical concepts of energy damping and a mathematical formulation of melt flow kinetic energy, a quadratic sink term can also be derived as [28]

$$C_{LQ} = \begin{cases} C.\beta.\left(1 - \left(\dfrac{T - T_E}{T_E - T_S}\right)^{\alpha}\right) & T_E < T < T_L \quad \alpha = 1 \\ \beta + C.(1 - \beta).\left(1 - \left(\dfrac{T - T_S}{T_E - T_S}\right)^{\alpha}\right) & T_S < T < T_E \quad \alpha = 2 \end{cases} \tag{17}$$

where T_E is a temperature which denotes the starting point for dendrites bridging phase during solidification. For aluminum alloys, the simple assumption can be that $T_E = (T_L - T_S)/2$ and $\beta = \gamma.((T_E - T_S)/(T_L - T_S))$ where γ is a coefficient which depends on material microstructure development during solidification (when growth and progression of dendrites starts to create significant resistance against the melt flow near the interface). For aluminum alloys where equiaxed grain growth are perceived, it can be assumed as γ = 0.6. The coefficient C can be calculated/measured and calibrated from the total momentum of the melt within the mold prior to the solidification phenomena. More comprehensive discussions about these mathematical derivations of momentum sink terms can be found in [28].

3.3. Simulation of Cooling and Heat Transfer. Using water spray cooling in light metal alloy productions (e.g., continuous and semicontinuous casting processes) is popular and the numerical modelling of these processes is essential in developing a deep understanding of the thermal evolution and temperature fields (including thermal stresses) during industrial processes. For the casting process, the melt material flowing into the mold can be considered as a viscous liquid which confines in a tiny solidified shell formed during initial cooling (during convective air cooling). In many casting processes, the cast billet is then sprayed (or submerged) with a water flow to extract more thermal energy from inside the billet. During this secondary water cooling, the billet undergoes large temperature fluctuations, especially near its surface. Here it is essential to investigate and control the thermal event to minimize the occurrence of defects on the surface or subsurface (hot tearing, cold cracking, etc.). These thermal fluctuations arise due to primary air cooling at the top (thermal convection and radiation), water spray cooling (including shrinkage and thermal conduction throughout the body of the billet), and possible secondary air cooling.

Numerical modelling/estimation of water spray cooling effects is one of the most challenging parts of the cooling system design. It would give rise to the estimation of thermal evolution and thermal fluctuations including its associated stresses. Many thermal evolution studies have been carried out in last two decades to develop an estimation technique for the dynamic HTC on the cast billet surface considering different water boiling regimes (nucleate, unstable, and stable filming regimes) and also Leidenfrost effects. One of the simplest models presented in the literature to start modelling of the water spray systems is to define a spray wet area as [29]

$$A = f(x, y, z)\frac{Q}{V_s} \tag{18}$$

where $f(x, y, z)$, V_s, and Q are coordinate distribution function, surface flow rate, and water flow rate, respectively. Different parameters would affect the thermal energy dissipation during water spray cooling, namely, temperature difference between billet surface and water, water flow rate, angle of impingement, water quality, surface roughness, and some other minor parameters. The boiling regime of the water on the surface of the billet at high temperature has profound effects on the heat dissipation and the complex interface between alloy/steam/water would determine the real cooling HTC. Many researchers have tried to carry out the inverse heat transfer calculation using available experimental data and fitting techniques [30–32]. However, in recent years the combination of empirical and numerical techniques has been used to model the surface boiling regimes and HTC calculations [29]. To start with the physical-mathematical study of HTC calculation, let us start with the simplified governing equations for the water spray cooling system which can be written in a simple form assuming the incompressibility as [31]

$$\nabla.U = 0$$
$$\frac{\partial U}{\partial t} = -\nabla\left(\frac{\mathrm{P}}{\rho}\right) + \frac{1}{Re}\nabla^2 U \tag{19}$$

where U, P, ρ, and Re are velocity vector, pressure, density, and Reynolds number,respectively. After some mathematical manipulation, for the case of continuous liquid phase (water)

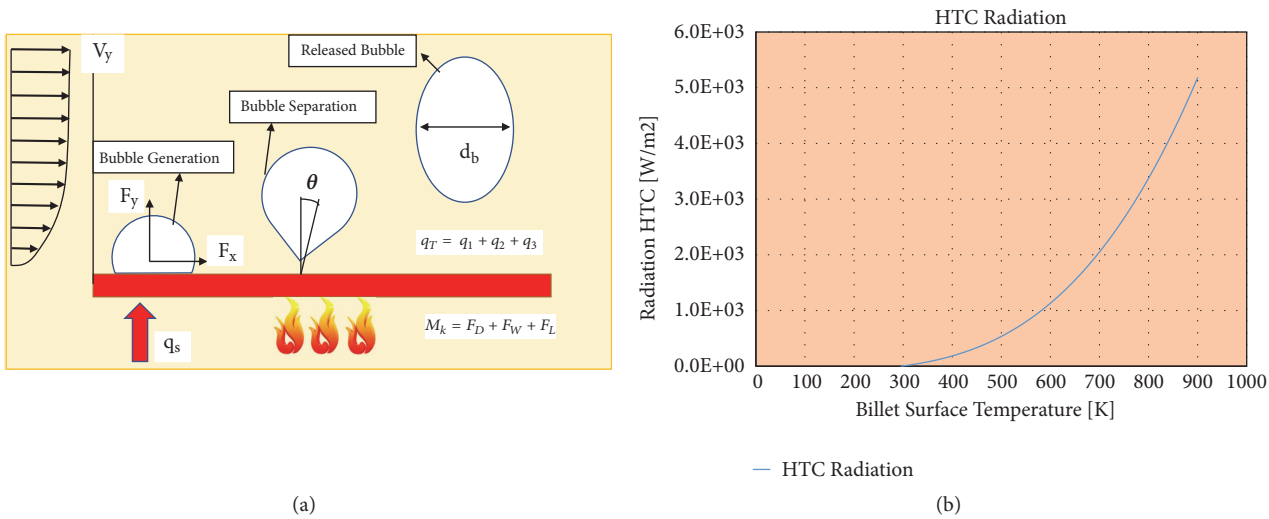

FIGURE 5: (a) Bubble generation and separation mechanisms from hot surface and (b) radiation of heat from aluminum billet at different temperatures.

and dispersive gases (vapor and air) using the three-phase continuity equation, the phase k can be written as [33]

$$\frac{\partial \alpha_k}{\partial t} + \nabla\left(\alpha_k \vec{U}_k\right) = \frac{\Gamma_{ki} - \Gamma_{ik}}{\rho_k} \tag{20}$$

and the total interfacial force in the momentum equation can be elaborated to find the bubble generation and movement relative to the billet surface (see Figure 5). For the water spray cooling system during casting process, the total heat flux can be defined as [33]

$$q_T = q_1 + q_2 + q_3 \tag{21}$$

where q_1, q_2, and q_3 are single-phase convective, evaporation, and quenching heat flux densities, respectively. Different models for the range of bubbling schemes in water flow boiling regimes have been developed in the past decades. In many of these models the condition that a vapor bubble would grow if the surrounding liquid temperature is equal to or more than the saturation temperature of the vapor inside the bubble is satisfied. In the research work herein, attempt has been made to formulate new mathematical models for the HTC at different boiling regimes during water spray (and submerge) cooling. For the initial air cooling during casting, conventional HTC approximation technique which includes convection and radiation terms can be adopted. If the temperature of billet surface is assumed as T_b and air bulk (free-stream) temperature is T_a, the thermal resistance (or inversely conductivity) at the interface A_T can be defined as [34]

$$R = \frac{1}{\left(h_{r+}h_c\right) A_T} \tag{22}$$

where h_r and h_c are, respectively, the radiation and convection HTCs, calculated as follows:

$$h_r = \varepsilon\sigma T^4 \quad \text{per unit area} \tag{23}$$

where σ is a constant (Stefan–Boltzmann constant) which can be assumed as 5.672×10^{-8} (W/m^2 K^4), T is the absolute temperature in Kelvin and ε is the billet surface emissivity. The convective HTC (h_c) for air cooling can also be calculated using [34]

$$h_c = \frac{kN_u}{\lambda} \tag{24}$$

where Nu is Nusselt number, k is the air thermal conductivity, and λ is the characteristic length. The Nusselt number (the ratio of conductive thermal resistance to the convective thermal resistance of the air) can be calculated as

$$\begin{aligned} N_u &= C\left(G_r P_r\right)^n \\ G_r &= \frac{g\beta\left(T_b - T_a\right)}{\nu^2}\lambda^3 \\ P_r &= \frac{\nu}{k}c_p \end{aligned} \tag{25}$$

where C and n are constants and P_r is the Prandtl number (defined as the ratio of momentum diffusivity to thermal diffusivity). G_r is the Grashof number (defined as the ratio of the buoyancy to viscous force acting on air) for vertical flat plates, β is the coefficient of thermal expansion (approximately 1/T$_a$, for air), ν is the kinematic viscosity, and g is gravitational acceleration. Figure 5 shows the schematic bubble generation and separation event during surface cooling and temperature dependent radiation HTC for aluminum alloy.

The water cooling HTC values change rapidly during the casting startup condition where continuous cooling regime adds to the modelling complications. The HTCs generally rise rapidly with the billet surface temperature until a critical temperature is reached above which unstable and film boiling regimes, with their lower associated HTCs' starts. The estimation of critical heat flux (CHF) temperature point and its associated heat flux can help to understand

and optimize the billet surface cooling rates and thermal-mechanical stress/strain conditions. The variation of HTC against the billet surface temperature can be divided into four distinctive zones, namely,

(i) below water saturation temperature,

(ii) between water saturation and CHF temperature (nucleate boiling regime),

(iii) from CHF temperature to Leidenfrost temperature (unstable boiling regime),

(iv) above Leidenfrost temperature (film boiling regime).

Some aspects of these boiling regimes have already been investigated [34] where mathematical formulation and also empirical estimation of heat transfer have been developed. For the work herein, different sets of mathematical works and experimental verification for the heat transfer during cooling process have been carried out to optimize the HTC during casting [35]. For the preboiling regime a simplified approach can be employed (the preboiling has minor thermal energy exchange effect) and HTC can be defined as [35]

$$HTC_{pre} = \alpha \left(\frac{Q}{L_b}\right)^{\beta} (7e2 * T_b - 1.67e3) \tag{26}$$

where Q, L_b, T_b are water flow rate, billet perimeter, and billet surface temperature, respectively. The parameters α, β that can be defined using the impingement conditions are billet surface quality (for aluminum billets α, β can be assumed as α = 1.35 and β = 0.3). For the more challenging nucleate boiling regimes, a more detailed formulation has been sought [35] and HTC can be defined as

$$HTC_{nu} = \left(\frac{\mu H_{fg}}{T_{sat} c_f^{\alpha}}\right)\left(\frac{C_p T_b}{H_{fg}}\right)^{\alpha}\left(\frac{\sigma \mu C_p}{Kg\left(\rho_w - \rho_v\right)}\right)^{\beta} \tag{27}$$

where μ, H_{fg}, c_f, C_p, K, g, ρ_w, ρ_v, and σ are coolant dynamic viscosity, latent heat of evaporation, flow heat parameter, specific heat, conductivity, gravitational acceleration, density, and vapor density, respectively. T_{sat} and T_b are defined as coolant saturation and billet surface temperature values where spatiotemporal distribution of temperatures on billet surface can be calculated using numerical domain. α and β are again cooling system parameters (these parameters can be assumed as α =0.8 and β =-0.515 for aluminum alloys).

The third boiling regime during cooling process is the unstable film boiling where the interphase boundary is unstable and vapor film can be broken periodically for water to make contact with billet surface. The estimation of HTC for unstable boiling zone has been a challenge for both scientist and engineers trying to overcome the full dynamic and oscillatory nature of the boiling event. As the billet surface temperature decreases during cooling process, the duration of vapor near the surface reduces, while the number and duration of liquid-wall contact increase. Such sporadic on/off contacts of liquid water with the billet surface result in an abrupt discharge of vapor from the surface, causing splashing and turbulence (and driving away vapor from the wall). The HTC for this zone can be estimated using the fraction of billet surface wetted by liquid water during the cooling process. The proposed empirical formulation for this zone can be defined as [35]

$$\begin{aligned} q &= q_w A_c + q_v \left(1 - A_c\right) \\ HTC_{tra} &= HTC_{nu}\left(1 - \left(\frac{T_b - T_{CHF}}{T_b}\right)^{\gamma}\right) \end{aligned} \tag{28}$$

where T_{CHF} is water critical heat flux temperature (can be assumed as T_{CHF} = 185°C for aluminum alloys). The final boiling regime during cooling process is the stable film boiling zone where a vapor blanket would be covering the surface of the billet. Generally, the estimated HTC values by the water spray is accredited to the intensified forced convection in the liquid film caused by the large flow momentum in the gravitational direction and consequent improvements in nucleate boiling. It also promotes the transient conduction which occurs on the heated surface due to the quick refresh of the liquid film. The proposed HTC estimation formula for cooling zone IV (film boiling regime) during cooling process can be proposed as [35]

$$HTC_f = HTC_{tra}\left(1 - \left(\frac{T_b - T_{Le}}{T_b}\right)\left(H_1 + H_2\right)^{\mathfrak{k}}\right) \tag{29}$$

$$H_1 = \frac{\gamma}{T_b} \times \left(\frac{k_w^3 g \rho_w H_{fg}\left(\rho_w - \rho_v\right)\left(1 + c_p T_b / 2H_{fg}\right)}{\mu_w T_b \left(\sigma / g\left(\rho_w - \rho_v\right)\right)^{\beta}}\right)^{\alpha} \tag{30}$$

$$H_2 = \frac{5.4 \times 10^4}{T_b}\left(1 + 0.055 T_b\right) v_s^{\kappa} \tag{31}$$

where T_{Le}, T_b, μ_w, H_{fg}, C_p, σ, ρ_w, K_w ρ_v, are water Leidenfrost temperature (≈400°C), billet surface temperatures, dynamic viscosity, latent heat of evaporation, specific heat, surface tension, density, and thermal conductivity, respectively. ρ_v is the vapor density and α, β, γ, κ, and $\mathfrak{k}$ are film cooling system parameters (these parameters can be assumed as α =0.4, β =0.5, γ = 0.5, κ = 0.6, and $\mathfrak{k}$ = 0.15 for aluminum alloys). The film HTC calculation is valid for surface temperature (T_b) between 400°C and 550°C. More detailed discussion about numerical modelling of boiling and bubble generation can be found in [35].

4. Case Studies

The first part of the casting simulation technique is the thermal-fluid mold filling and its material thermal evolution using CFD technique. CFD technique has extensively been used in the last couple of decades for fluid and fluid-structure engineering problems. Understanding the motion of fluids, its thermal conduction, convection/radiation, and also its interactions with solids is crucial for the design of engineering systems in many branches of engineering. To develop a new numerical industrial casting simulation tool, two comprehensive sets of parallel simulation-experimental studies have been planned, namely, thermal-fluid CFD

simulation for mold filling/solidification and evolving thermal-mechanical simulation for stress/strain states and cracking. The most challenging parts of thermal-fluid CFD applications for the industrial process engineering and in particular casting processes are the numerical solidification and cooling simulations.

4.1. Thermal-Fluid Casting Simulation. As described in the previous sections, for the proposed casting simulation tool, it is essential to model the change of phase from fluid to mushy and solid state under the thermal gradient caused by cooling process. In the research work herein, a new solidification module based on momentum sink terms described in the previous section has been implemented and coded in-house. The thermal gradient and cooling effects during solidification phenomena have also been implemented using an in-house code which incorporate the developed HTC functions for different stages of water boiling regimes.

For the experimental studies, two sets of casting trials have been selected, namely, horizontal and vertical direct chill casting procedures. These casting trials are performed on semi-industrial scale where aluminum billets are cast using direct chill method (air and water cooling). Figure 6 shows the vertical direct chill casting trials in which rectangular and round cross-section billets were cast. Two sets of parallel numerical simulations have also been carried out to examine and calibrate the developed mathematical models for solidification and HTC estimations. For the vertical experimental casting trial, two series of Thermo-Couples (TC) are installed across the cross-section at different elevation to measure temperature for both "start of cast" and "during cast" conditions (thermal transient and steady state cases). These two TC series are installed on an especially designed supporting "frame system" (see Figure 6) which is fixed on the bottom tray during casting.

A second experimental-simulation case study has also been carried out using a horizontal continuous casting technology to study the continuous casting process of lightweight alloys (see Figure 7). The fluid-thermal conditions of the process have been simulated with user-defined modules developed for the CFD solver (2D axisymmetric and 3D half models). The casting process cooling rates and change of phase (solidification phenomena) within the mold have also been modelled using developed mathematical functions. Figure 7 shows casting of round billet using the horizontal casting machine for light weight alloys and its numerical 2D axisymmetric and 3D half models.

4.2. Thermal-Mechanical Casting Simulation. The industrial casting process techniques for metals and alloys, including continuous and semicontinuous processes have intrinsically a dynamic nature, where billets are produced by solidification of melt material at "casting-speed" rate. The optimization of these casting technologies and the issues of product final mechanical properties, production speed, and energy/cost saving have been major topics for many years. The process of developing a numerical dynamic and flexible tool to model the thermal-mechanical evolution of the billets during a continuous casting process is among the most important ambitions for researchers and engineers in this field. As presented in the previous sections, following vast expansion of computational resources and also introduction of efficient parallelization schemes, a new concept of evolving domain has been developed herein to address the transient casting conditions. The combination of multidomain concept, energy input/output balancing (for melt thermal energy content), and advanced history mapping (using overlapping scheme) has been implemented [11].

The dynamic mesh procedure with its system-matrix reassembly/appending capability would enable the development of a fully transient scheme to introduce/append new subdomains (melt entry) based on material and energy balance concepts. The thermal-mechanical casting simulation framework herein has integrated the following modules for industrial applications:

(i) evolving domain module which can handle different engineering dynamic processes with internal interfacing/moving parts using developed cooling, solidification, overlapping, and mapping techniques;

(ii) a comprehensive set of experimental mechanical tests at room and elevated temperatures for calibration of numerical damage models (including tension tests, etc.);

(iii) a multiresolution zoning technique [11] for simultaneous modelling of phenomena at different length scale during solidification (macro-meso simulation of grain growth using Lattice-Boltzmann and Cellular Automata which have not been presented in this paper; please refer to [36])

Figure 8 shows the experimental-simulation trials for thermal-mechanical numerical simulation using tension testing machine.

5. Discussion and Concluding Remarks

The speed and the quality of the industrial production process are depending on sound design and optimisation procedures which can be numerically simulated using rigorous scientific/engineering virtual tools. For many industrial material processes and their numerical simulation tools it is required to establish a framework for continuous innovation and sound predictive apparatuses for confronting accumulative challenges and competitive market. The combination of state-of-art innovative numerical approaches (with flexibility, agility, and predictive power) and thorough calibration and verification schemes to develop and explore what technical solutions are viable can be promoted for future of process engineering. The integrated framework for casting simulation developed herein consists of practical evolution scheme, pioneering analytical approaches (for solidification and cooling), and multiresolution grid technology (only briefly discussed in this paper; please refer to [36]) which would reflect the essence of new engineering and industrial virtual tools. The generic simulation framework would help to improve industrial material casting processes and to tailor

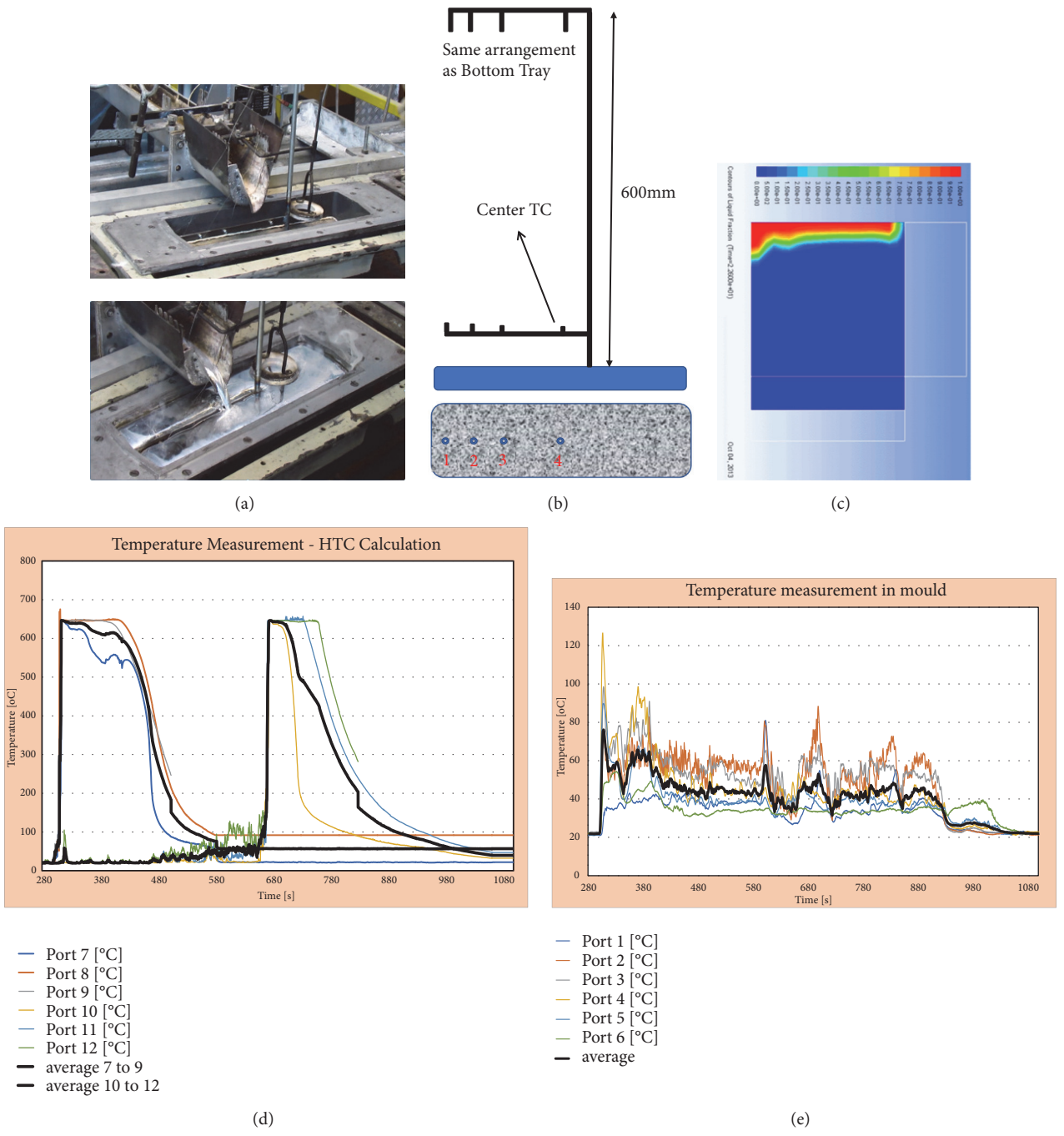

FIGURE 6: (a) Vertical direct chill casting trial; (b) plan and side view of TC arrangement for temperature measurement; (c) thermal-fluid simulation; (d) measured temperature on billet surface; and (e) measured temperature in mold.

future research works on optimized process parameters for various industrial applications using its developed modules. A series of carefully designed experimental trials have also been planned and carried out which helped to verify and calibrate numerical models. The idea herein was to develop a framework for an efficient numerical technique and integrated it into mainstream industrial simulation tools to help

(i) optimise and tailor casting production processes for reduction of costs and increase part quality and properties based on integration of practical numerical predictive modules;

(ii) develop innovative and reduced-risk of design/production strategies based on affordable advanced material process models;

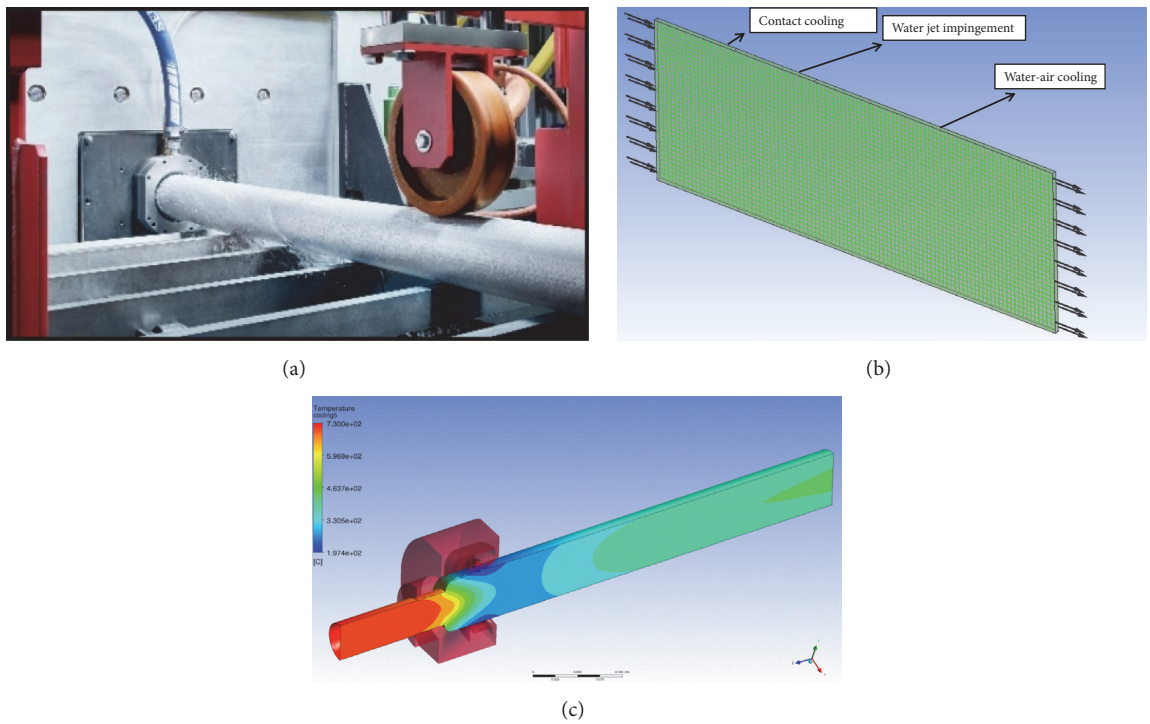

Figure 7: (a) Horizontal direct chill casting trial, (b) 2D axisymmetric CFD model, and (c) temperature results for CFD half model.

(iii) amplify the use of computer-based virtual modelling and simulation systems for material process industries by developing affordable advanced numerical tool;

(iv) improve the confidence and reliance of industrial use of numerical tools and their predictive powers

Although conventional numerical tools and software have been used for the simulation of industrial processes with relative success, their limited applications, large computational CPU timing, accuracy issues, and their lack of modelling for vital lower-scale phenomena are well understood. In addition, the single-domain and single-solver simulation framework of software would limit the application of them for multiphysical and multiscale process simulation.

In the first part of this paper, the analytical and theoretical basis of the evolving domain technique and its overlapping and mapping methods were briefly presented. It was shown that these methods can be combined with new mathematical and analytical models to enable the making of accurate prediction for material evolution during industrial casting processes. The approach is new, as the conventional industrial numerical tools appear to lack accuracy and modelling power for underlying material phenomena. The parallel experimental-simulation trials have also been shown in the second part of the paper where the calibration and benchmarking of the numerical method have been studied. It can be concluded that the numerical simulation framework founded on combination of mathematical-analytical schemes with conventional solver technology can be implemented and employed in an upfront manner. The solidification and cooling models presented herein allow for the continuous transition of phases from melt to solid state.

As far as numerical stability and efficiency are concerned, it can be assessed that the assemblage of global matrices has to be repeated for evolving numerical domain (starting with small matrices and appending at discrete steps) in comparison with the single assemblage procedure for the conventional methods (with large full matrices). However, further numerical benchmarking of these two methods has proved that the proposed method outperforms the conventional method for industrial-scale process simulations (results not reported in this paper; it would a subject of next submission). Furthermore, the proposed method is capable of dealing with material evolution at lower scales (e.g., solidification phenomena) through multiple overlapping and mapping schemes in a straightforward manner without the need for sequential simulation steps.

Data Availability

Requests for data belonging to experimental work for verification studies will be considered by the corresponding author.

Disclosure

Some results of this research work have been also published in "Solidification Processing 2017", "Mat. Sci. Forum 2014", "LS DYNA Forum 2016", and "9th World Congress on Mat. Sci. and Eng.".

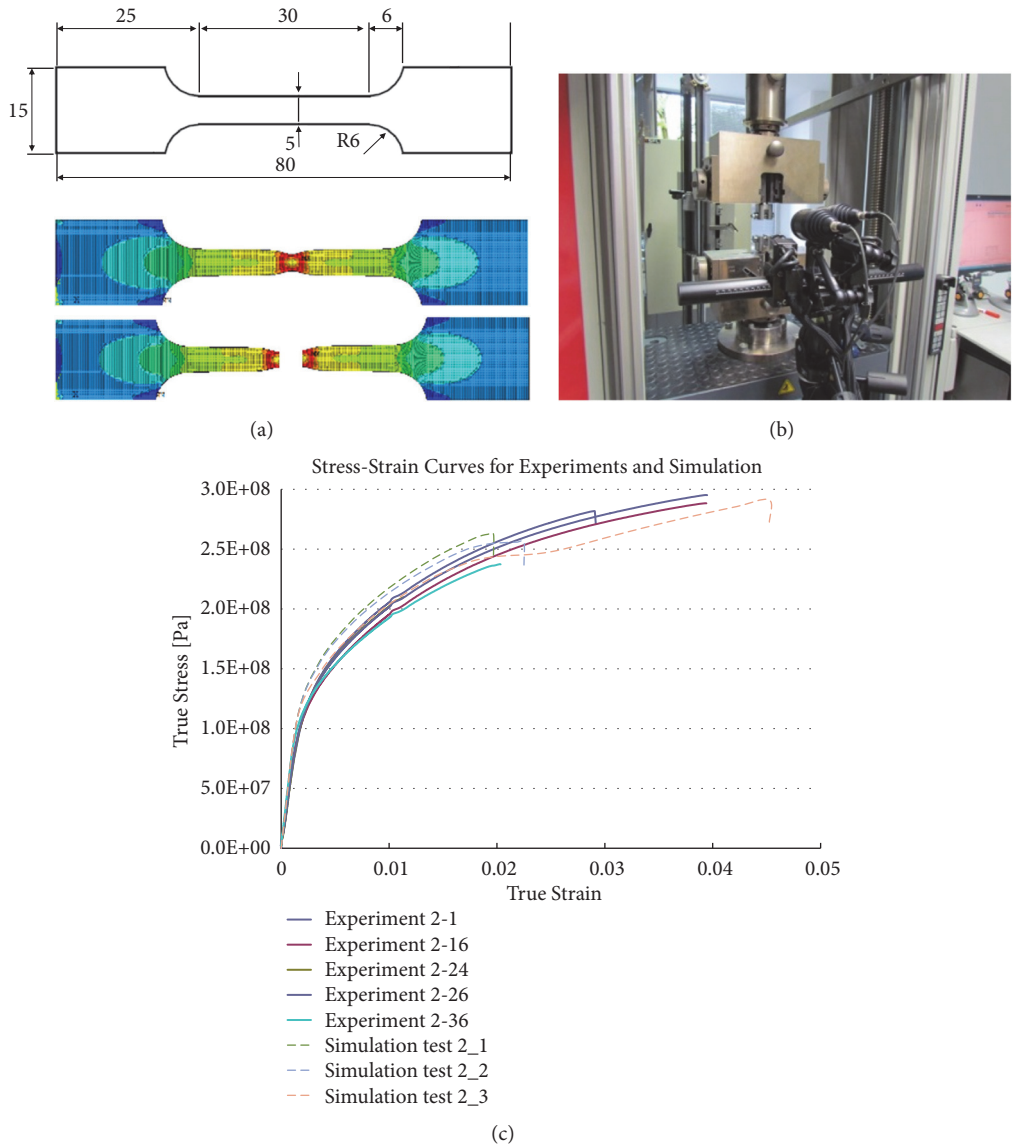

Figure 8: (a) Aluminum sample geometry and its fracture simulations. (b) Tension test machine. (c) Measured and simulated true stress-strain curves for aluminum samples.

Conflicts of Interest

The author declares no conflicts of interest.

Acknowledgments

The author would like to thank the Austrian Federal Ministry for Transport, Innovation and Technology (BMVIT), Land of Federal State of Upper Austria in the FD Framework (within PSHeRo project "OÖ Aktenzahl Wi-2017-289120/16"), and also the Austrian Institute of Technology (AIT) for the technical/financial support in this research work. The author would also like to thank DI Stefan Scheiblhofer, Stephan Jäger, Dr Stefan Ucsnik, DI Johannes Kronsteiner, DI Andreas Kraly of Leichtmetallkompetenzzentrum Ranshofen (LKR) GmbH, and Dr Christian Chimani of AIT, Austria, for their contributions and support.

References

[1] A. M. Horr, "Energy-efficient lightweight material processes for e-mobility applications," in *Proceedings of the European Aluminium Congress*, vol. 2 of *Body Structure & E-Mobility II session*, pp. 1–12, Dusseldorf, Germany, 2017.

[2] K. J. Bathe, *Finite Element Procedure in Engineering Analysis*, Prentice-Hall, Englewood Cliffs, NJ, USA, 1996.

[3] R. W. Clough and J. Penzien, *Dynamics of Structures*, McGraw-Hill, New York, NY, USA, 1996.

[4] J. H. Ferziger and M. Peric, *Computational Methods for Fluid Dynamics*, Springer Verlag, 2nd edition, 1999.

[5] J. Donea, A. Huerta, J. Ponthot, and A. Rodríguez-Ferran, "Chapter 14, Fundamentals," in *Encyclopedia of Computational Mechanics*, E. Stein, R. de Borst, and T. J. R. Hughes, Eds., vol. 1, John Wiley & Sons, 2004.

[6] J. Donea, S. Giuliani, and J. P. Halleux, "An arbitrary lagrangian-eulerian finite element method for transient dynamic fluid-structure interactions," *Computer Methods in Applied Mechanics and Engineering*, vol. 33, no. 1–3, pp. 689–723, 1982.

[7] N. Takashi and T. J. R. Hughes, "An arbitrary lagrangian-eulerian finite element method for interaction of fluid and a rigid body," *Computer Methods in Applied Mechanics and Engineering*, vol. 95, no. 1, pp. 115–138, 1992.

[8] W. K. Liu, T. Belytschko, and H. Chang, "An arbitrary lagrangian-eulerian finite element method for path-dependent materials," *Computer Methods in Applied Mechanics and Engineering*, vol. 58, no. 2, pp. 227–245, 1986.

[9] R. W. Lewis, S. E. Navti, and C. Taylor, "A mixed lagrangian-eulerian approach to modelling fluid flow during mould filling," *International Journal for Numerical Methods in Fluids*, vol. 25, no. 8, pp. 931–952, 1997.

[10] H. Udaykumar, W. Shyy, and M. Rao, "ELAFINT - A mixed Eulerian-Lagrangian method for fluid flows with complex and moving boundaries," in *Proceedings of the AIAA/ASME 6th Joint Thermophysics and Heat Transfer Conference*, Colorado Springs, Colo, USA, 1994.

[11] A. M. Horr, J. Kronsteiner, C. Mühlstätter, and S. Scheiblhofer, "Recent advances in aluminium casting simulation: evolving domains & dynamic meshing," in *Proceedings of the Aluminium Two Thousand World Congress*, Verona, Italy, 2000, http://www.aluminium2000.com/index.php/en/event-profile/previous-congresses/previous-congress-verona-2017.

[12] A. M. Horr, "Integrated material process simulation for light-weight metal products," *Computational Methods and Experimental, WIT Transactions on Modelling and Simulation*, vol. 59, 2015.

[13] A. M. Horr, C. Angermeier, and A. Harrison, "Full through process simulation for low pressure die casting - from casting to design," *Materials Science Forum*, vol. 794-796, pp. 118–123, 2014.

[14] A. M. Horr, *Evolving Domain for Numerical Simulation of EM Semi-Continuous Casting Process, Amoree Core Document*, LKR, AIT, Vienna, Austria, 2015.

[15] F. Liu, Z. Nashed, G. N'Guerekata et al., *Advances in Applied and Computational Mathematics*, Nova Science Publishers, New York, NY, USA, 2006.

[16] X.-C. Cai, M. Dryja, and M. Sarkis, "Overlapping nonmatching grid mortar element methods for elliptic problems," *SIAM Journal on Numerical Analysis*, vol. 36, no. 2, pp. 581–606, 1999.

[17] H. Mingyan, H. Ziping, W. Cheng, S. Pengtao, and Z. Shuang, "An overlapping domain decomposition method for a polymer exchange membrane fuel cell model," *Procedia Computer Science*, vol. 4, pp. 1343–1352, 2011.

[18] E. Scheil, "Bemerkungen zur schichtkristallbildung," *Zeitschrift Für Metallkunde*, vol. 34, pp. 70–72, 1942.

[19] G. H. Gulliver, "The quantitative effect of rapid cooling upon the constitution of binary alloys," *Journal of the Institute of Metals*, vol. 9, pp. 120–157, 1913.

[20] J. Kozeny, "Ueber kapillare leitung des wassers im boden," *Sitzungsberichte Akademie der Wissenschaften in Wien, Mathematisch-naturwissenschaftliche Klasse*, vol. 136, no. 2a, pp. 271–306, 1927, https://scholar.google.com/scholar_lookup?title=%C3%9Cber%20die%20kapillare%20Leitung%20des%20Wassers%20im%20Boden.%20Sitzungsber.%20Abt.%20IIa%20d.%20Math.%20naturwiss&author=J..%20Kozeny&journal=Klasse%20der%20Wiene%20Akad%20Wiss.&volume=136&pages=271%2F306&publication_year=1927.

[21] P. C. Carman, "Fluid flow through granular beds," *Transactions of Institution of Chemical Engineers, London*, vol. 15, pp. 150–166, 1937.

[22] P. C. Carman, *Flow of Gases through Porous Media*, Butterworths Scientific Publications, London, UK, 1956.

[23] F. C. Blake, "The resistance of packing to fluid flow," *Transactions of the Institution of Chemical Engineers*, vol. 14, pp. 415–421, 1922.

[24] V. R. Voller and C. Prakash, "A fixed grid numerical modelling methodology for convection-diffusion mushy region phase-change problems," *International Journal of Heat and Mass Transfer*, vol. 30, no. 8, pp. 1709–1719, 1987.

[25] V. R. Voller, A. D. Brent, and C. Prakash, "The modelling of heat, mass and solute transport in solidification systems," *International Journal of Heat and Mass Transfer*, vol. 32, no. 9, pp. 1719–1731, 1989.

[26] V. R. Voller, A. D. Brent, and C. Prakash, "Modelling the mushy region in a binary alloy," *Applied Mathematical Modelling*, vol. 14, no. 6, pp. 320–326, 1990.

[27] J. P. Gu and C. Beckermann, "Simulation of convection and macrosegregation in a large steel ingot," *Metallurgical and Materials Transactions A: Physical Metallurgy and Materials Science*, vol. 30, no. 5, pp. 1357–1366, 1999.

[28] A. M. Horr, *Analytical and Numerical Analyses of Horizontal Direct Chill Casting, PSHeRo Project Report*, Light Metals Technologies Ranshofen, Austrian Institute of Technology, Vienna, Austria, 2018.

[29] Y. Pan and B. W. Webb, "Heat transfer characteristics of arrays of free-surface liquid jets, general papers in heat and mass transfer, insulation and turbomachinery," *Journal of Heat Transfer*, vol. 271, pp. 23–28, 1994.

[30] M. A. Wells, D. Li, and S. L. Cockcroft, "Influence of surface morphology, water flow rate, and sample thermal history on the boiling-water heat transfer during direct-chill casting of commercial aluminum alloys," *Metallurgical and Materials Transactions B: Process Metallurgy and Materials Processing Science*, vol. 32, no. 5, pp. 929–939, 2001.

[31] D. H. Wolf, F. P. Incropera, and R. Viskanta, "Local jet impingement boiling heat transfer," *International Journal of Heat and Mass Transfer*, vol. 39, no. 7, pp. 1395–1406, 1996.

[32] D. Greif, Z. Kovacic, V. Srinivasan, D. M. Wang, and M. Suffa, "Coupled numerical analysis of quenching process of internal combustion engine cylinder head," *BHM Journal*, vol. 154, pp. 522–530, 2009.

[33] S. J. Slayzak, R. Viskanta, and F. P. Incropera, "Effects of interactions between adjoining rows of circular, free-surface jets on local heat transfer from the impingement surface," *Journal of Heat Transfer*, vol. 116, no. 1, pp. 88–95, 1994.

[34] J. H. Lienhard, "Liquid jet impingement," *Annual Review of Heat Transfer*, vol. 6, no. 6, pp. 199–270, 1995.

[35] A. M. Horr, *Calculation of Thermal Evolution and Heat Transfer Coefficient during EMC Process, Amoree Project Report*, Light Metals Technologies Ranshofen, Austrian Institute of Technology, Vienna, Austria, 2016.

[36] S. Jäger, A. Horr, and S. Scheiblhofer, "Thermal evolution effects on solidification process during continuous casting," in *Proceedings of the 6th Decennial International Conference on Solidification Processing*, pp. 675–678, Old Windsor, England, 2017.

Hindawi
Mathematical Problems in Engineering
Volume 2019, Article ID 1327167, 11 pages
https://doi.org/10.1155/2019/1327167

Research Article

A New Mathematical Method to Study the Singularity of 3-RSR Multimode Mobile Parallel Mechanism

Chunyan Zhang[1,2] **Yu Wan**[2] **Dan Zhang**[1] **and Qihua Ma**[1,3]

[1]*College of Mechanical Engineering, Dong Hua University, Shanghai 201620, China*
[2]*College of Mechanical and Automotive Engineering, Shanghai University of Engineering Science, Shanghai 201620, China*
[3]*The State Key Laboratory for Modification of Chemical Fibers and Polymer Materials, Dong Hua University, Shanghai 201620, China*

Correspondence should be addressed to Dan Zhang; dan_zhang99@hotmail.com

Received 26 October 2018; Revised 18 February 2019; Accepted 25 February 2019; Published 11 April 2019

Guest Editor: Sutasn Thipprakmas

In the process of parallel mechanism design, it is difficult to avoid the singularity, especially in the mobile parallel mechanism. Therefore, a new mathematical method to study the singularity of multimode mobile parallel mechanism is proposed. In this paper, the singularity of 3-RSR parallel mechanism (PM) is analyzed by using reciprocal screw methods and linear geometry theory from two aspects of fixed mode and all-attitude multiple motion modes. Specifically, the complete Jacobian matrix of the PM is obtained by using the screw theory, and the reciprocal screw of each branch is expressed with algebraic method and geometric drawing method. Furthermore, the singularity of the PM can be obtained by analyzing the reciprocal screw correlation and using the spatial linear geometry theory. Finally, we analyze the singular configuration of the PM under various modes, which provide theoretical guidance for the gait planning of the multimode mobile PM and will be useful for the selection of mechanism drive and time-sharing control.

1. Introduction

Parallel mechanisms with high load bearing capacity and precision have been widely used in processing and manufacturing, testing, logistics, and many other applications [1]. Recently, the parallel mechanisms have been used in mobile applications and developed into the 'mobile parallel mechanism', such as the multiple branches of the parallel mechanism which are represented directly as the legs of the mobile mechanism or the mobile robot [2, 3]; for example, these mechanisms are shown in [4–6]. The other is the 'all-attitude mode mobile parallel mechanism' which is represented by Yao [7, 8]. However, it is difficult to avoid singularities due to the structural characteristics of parallel mechanisms. In the process of mechanism design, many scholars have proposed a variety of methods to study singular configurations in [9–17] and tried to avoid singular configurations [18], but most of these methods use the calculation method to determine whether the value of the Jacobian matrix determinant is zero, or whether the Jacobian matrix is downgraded to judge whether the mechanism is singular. For the more complex Jacobian matrix, these methods can be used to study the singularity, but the calculation is cumbersome and the workload is large.

Therefore, we proposed a new mathematical method to study the singularity of parallel mechanism. In the reference of [19], the singularity of a 3-RSR in the fixed mode is only analyzed by screw theory. Different motion modes of 3-RSR mechanism with all-attitude multiple motion modes movement are proposed by Tian [20]. However, the driving control choices and avoidance of singularities in realizing these motion modes are unclear. This paper analyzes the singularity of 3-RSR multimode mobile parallel mechanism by means of the reciprocal screw theory and the spatial geometric theory from two points of view: the fixed mode and the all-attitude multiple motion modes, and the driving selection and control of mechanism in the moving mode are further studied. In the following, Section 3 uses algebraic methods to deduce the complete screw Jacobian matrix of the PM, and Section 4 analyzes the linear correlations of the constrained reciprocal and driving reciprocal screws and discusses the singularities of the PM under five different

configurations. In Section 5, on the basis of the theoretical methods proposed in Sections 3 and 4, the driving selection and the avoidance and utilization of singularities of 3-RSR parallel mechanism in realizing all-attitude multiple motion modes are analyzed. Compared with the previous analytical approaches, this method offers an intuitive and simple way to calculate the singularity. And more important, we established the relationship between the topology of a parallel mechanism and singular configurations. Through proper topology optimization, the singularity can be avoided.

2. Introduction to Reciprocal Screw Theory

A unit screw can be defined as a 6×1 matrix form [21]:

$$\widehat{\$_i} = \begin{pmatrix} s_i \\ r_i \times s_i + \lambda s_i \end{pmatrix} \tag{1}$$

where s_i is the unit vector representing the direction of the screw axis and r_i is the position vector of any points on the screw axis in terms of a reference coordinate system. The pitch of a screw is λ, and $r_i \times s_i$ is defined as the motion along the spiral direction.

For revolute joint, $\lambda = 0$. The screw form can be expressed as

$$\widehat{\$_i} = \begin{pmatrix} s_i & r_i \times s_i \end{pmatrix}^T \tag{2}$$

For prismatic joint, $\lambda = \infty$. The screw form can be expressed as

$$\widehat{\$_i} = \begin{pmatrix} 0 & s_i \end{pmatrix}^T \tag{3}$$

When the two screws are opposite to each other, the reciprocal product of two screws is zero and can be given by

$$\widehat{\$_r} \circ \widehat{\$_i} = 0 \tag{4}$$

The following conditions must be satisfied:

$$\widehat{\$_r^T} \cdot \widehat{\$_i} = 0 \tag{5}$$

The indices range is i=1,2,3,4,5,6-n, r=1,2,....n.

The transposition of a screw can be defined as

$$\widehat{\$_r^T} = \begin{bmatrix} s_{r4} & s_{r5} & s_{r6} & s_{r1} & s_{r2} & s_{r3} \end{bmatrix} \tag{6}$$

Equation (5) can be expressed as

$$\widehat{\$_r^T} \circ \widehat{\$_i} = s_{r4}s_1 + s_{r5}s_2 + s_{r6}s_3 + s_{r1}s_4 + s_{r2}s_5 + s_{r3}s_6 \tag{7}$$

where s_{ri} (i=1~6) is the *ith* component of the *rth* unit screw, s_i is (i=1...6), the reciprocal screw form of s_r.

3. Mechanism Description and Mobility Analysis

3.1. The Configuration of the Mechanism. The parallel mechanism is composed of two scaling platforms and three RSR chains, as shown in Figure 1. In this mechanism, the chains are symmetrical about the central plane, and the upper and the lower platform are composed of three 'V'-shaped rods through the prismatic joints to connect. All the revolute joints in each chain are always parallel with each other. When the mechanism is in the fixed mode, the lower platform becomes the base platform, and the upper platform becomes the moving platform. For the parallel mechanism with multiple motion modes, the upper and lower platforms are in contact with the ground alternately to form an 'all-attitude multiple modes mobile parallel mechanism'.

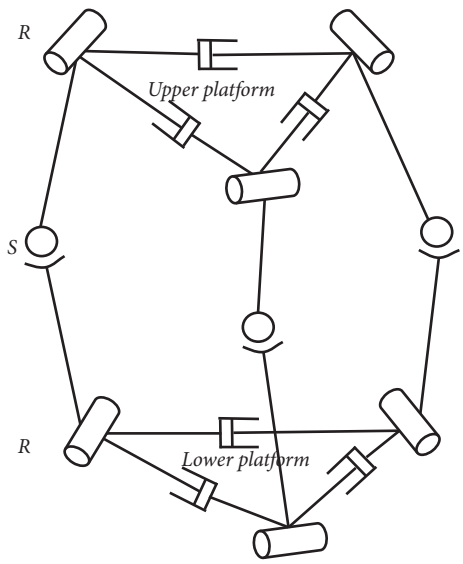

Figure 1: The 3-RSR parallel mechanism diagram.

3.2. Degree of Freedom Analysis in the Fixed Mode. The proposed mechanism is a novel 5-DoF parallel mechanism that is based on 3-RSR architecture. When the mechanism is in the fixed mode, the P of upper and lower platforms is locked, and the 3-RSR parallel mechanism is an underconstrained mechanism [22]. The DOF can be calculated by the following formula:

$$M = d\left(n - g - 1\right) + \sum_{i=1}^{g} f_i + \upsilon - \xi \tag{8}$$

where M is the mobility of the mechanism, d represents the order of the mechanism, n is the number of links, g is the number of kinematic pairs, f_i is the freedom of the *ith* pair, υ represents the parallel redundancy constraint, and ξ is the passive DOF, respectively. By (8), the DOF of the mechanism can be obtained and equal to 3.

The prismatic joints of the upper and lower platforms are synchronously scaled in the moving process, so that the total degree of freedom of the upper and lower platforms is 2. Thus, the DOF of the mechanism is 5.

4. Complete Screw Jacobian Matrix of 3-RSR Parallel Mechanism in the Fixed Mode

The singularity of the parallel mechanism is usually determined by solving the Jacobian matrix of the mechanism, which reflects the mapping relationship between the input and output of the mechanism. The complete Jacobian matrix consists of the constrained submatrix that reflects the force applied on each branch, and the driving submatrix that reflects the mapping between the linear velocity and angular velocity of the moving platform and the velocity of the driving joint. Therefore, the singularity of the mechanism can be determined by judging whether the Jacobian matrix of the mechanism is reduced in order.

In this section, the kinematic screw of the 3-RSR parallel mechanism is established by using screw theory. As shown in Figure 2, the spherical joint G_i can be equivalent to three intersecting noncoplanar revolute joints (axis $S_{2,i}$, $S_{3,i}$, $S_{4,i}$) and the axes of revolute joint at P_i point and Q_i point are represented by $S_{1,i}$ and $S_{5,i}$, respectively. Then each branch chain is composed of five single degrees of freedom revolute joints. The instantaneous kinematic screw of the moving platform $\$_c$ can be represented as a linear combination of five instantaneous kinematic screws.

$$\$_c = \dot{\beta}_{1,i}\,\$_{1,i} + \dot{\beta}_{2,i}\,\$_{2,i} + \dot{\beta}_{3,i}\,\$_{3,i} + \dot{\beta}_{4,i}\,\$_{4,i} + \dot{\beta}_{5,i}\,\$_{5,i} \quad (i = 1 \sim 3) \tag{9}$$

where $\dot{\beta}_{j,i}$ $(j = 1 \sim 5,\ i = 1 \sim 3)$ represents the angular velocity of the *jth* revolute point of the *ith* branch chain, $\$_{j,i}$ $(i = 1 \sim 3,\ j = 1 \sim 5)$ represents a unit screws, $\$_C = [w_c; v_c]$, w_c represents the angular velocity of the moving platform relative to the base coordinate system, and v_c represents the linear velocity of the moving platform relative to the base coordinate system.

The screw of each branch chain can be expressed as

$$\begin{aligned}
\$_{1,i} &= \left[s_{1,i}; \overrightarrow{CP_i} \times s_{1,i}\right] \\
\$_{2,i} &= \left[s_{2,i}; \overrightarrow{CG_i} \times s_{2,i}\right] \\
\$_{3,i} &= \left[s_{3,i}; \overrightarrow{CG_i} \times s_{3,i}\right] \\
\$_{4,i} &= \left[s_{4,i}; \overrightarrow{CG_i} \times s_{4,i}\right] \\
\$_{5,i} &= \left[s_{5,i}; \overrightarrow{CQ_i} \times s_{5,i}\right]
\end{aligned} \tag{10}$$

$\$_{r,1,j}$ $(i = 1 \sim 3)$ is used to represent a reciprocal screw corresponding to the five-screw system $\$_{1,i}$, $\$_{2,i}$, $\$_{3,i}$, $\$_{4,i}$, $\$_{5,i}$ in the *ith* branch, and the dimension of the reciprocal screw is one. The reciprocal screw of each branch is obtained by finding the intersection of the two line vectors. In the following, the reciprocal screw of each branch can be obtained by the method of using the two-line vector intersection.

4.1. Constrained Submatrices. According to the principle that the two coplanar line vectors are reciprocal screw [20], the reciprocal screw can be obtained by finding the intersection point of the two line vectors. Thus, the specific method is to find a line vector passing through the spherical joint G_i and let this line vector intersect with the vector $\$_{1,i}$ of P_i point (the direction is $Unit(\overrightarrow{P_{i+2}P_{i+1}})$) and the vector $\$_{5,i}$ of Q_i point (the direction is $Unit(\overrightarrow{Q_{i+2}Q_{i+1}})$). According to reference [19], it can be seen that the line vector passing through the spherical joint G_i is $\overrightarrow{G_iD_{Di}}$.

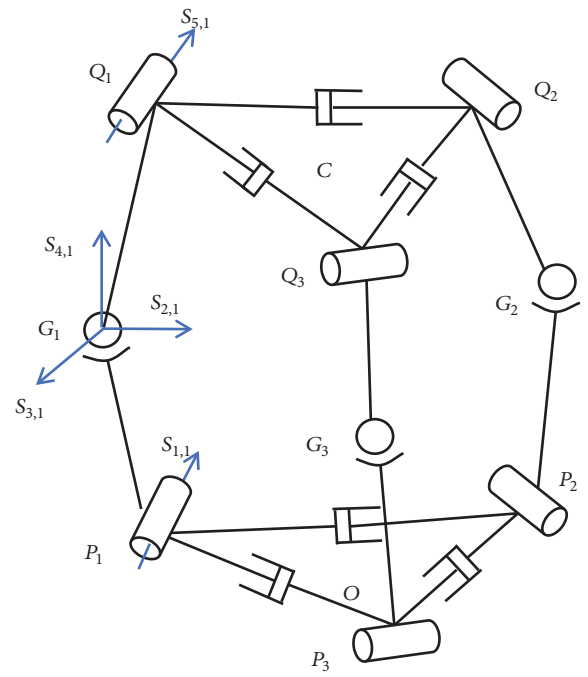

FIGURE 2: Kinematic screw of the 3-RSR parallel mechanism.

Therefore, the reciprocal screw $\$_{r,1,i}$ can be derived as

$$\$_{r,1,i} = \left[Unit\left(\overrightarrow{G_iD_{Di}}\right); \overrightarrow{C_iG_i} \times Unit\left(\overrightarrow{G_iD_{Di}}\right)\right] \tag{11}$$

$\$_{r,1,i}$ is a line vector, the reciprocal product of $\$_{r,1,i}$ and (9) can be calculated and written as the following formula:

$$\$_{r,1,i} \circ \$_c = 0 \quad (i = 1 \sim 3) \tag{12}$$

According to reciprocal screw theory, (12) produces an equation for each branch chain, written as the form of a matrix:

$$J_A \cdot \$_C = 0 \tag{13}$$

where

$$J_A = \begin{bmatrix} \left(\overrightarrow{CG_1} \times Unit\left(\overrightarrow{G_1D_{D1}}\right)\right)^T & Unit\left(\overrightarrow{G_1D_{D1}}\right)^T \\ \left(\overrightarrow{CG_2} \times Unit\left(\overrightarrow{G_2D_{D2}}\right)\right)^T & Unit\left(\overrightarrow{G_2D_{D2}}\right)^T \\ \left(\overrightarrow{CG_3} \times Unit\left(\overrightarrow{G_3D_{D3}}\right)\right)^T & Unit\left(\overrightarrow{G_3D_{D3}}\right)^T \end{bmatrix} \tag{14}$$

The matrix J_A is a 3×6 constrained Jacobian matrices. Each row of J_A represents a unit constrained force screw applied by all joints of a branch chain.

4.2. Driving Submatrix. When the driving joint of each chain is locked, each branch chain contains only four single-degree-of-freedom revolute joint, the dimension of the reciprocal screw system is 2, and the $\$_{r,1,i}$ is a subset of the reciprocal screw system. The next step is to solve another reciprocal screw $\$_{r,2,i}$ ($i = 1 \sim 3$), which is called the driving force screw. The reciprocal product of $\$_{r,2,i}$ and $\$_{2,i}, \$_{3,i}, \$_{4,i}, \$_{5,i}$ is zero. However, the reciprocal product of $\$_{r,2,i}$ and $\$_{1,i}$ cannot be zero. Furthermore, the screw must pass the points G_i and Q_i; it can be derived as

$$\$_{r,2,i} = \left[Unit\left(\overline{G_iQ_i}\right); \overline{CG_i} \times Unit\left(\overline{G_iQ_i}\right)\right] \tag{15}$$

Equation (15) is a line vector, the reciprocal product of $\$_{r,2,i}$ and (9) can be calculated and written as the following formula:

$$\$_{r,2,i} \circ \$_c = \dot{\beta}_{1,i}\ \$_{r,2,i} \circ \$_{1,i} \tag{16}$$

Equation (16) produces an equation for each branch chain, written as the form of a matrix:

$$J_x \$_C = J_q \bullet \dot{q} \tag{17}$$

$$J_x = \begin{bmatrix} \left(\overline{CG_1} \times Unit\left(\overline{G_1Q_1}\right)\right)^T & Unit\left(\overline{G_1Q_1}\right)^T \\ \left(\overline{CG_2} \times Unit\left(\overline{G_2Q_2}\right)\right)^T & Unit\left(\overline{G_2Q_2}\right)^T \\ \left(\overline{CG_3} \times Unit\left(\overline{G_3Q_3}\right)\right)^T & Unit\left(\overline{G_3Q_3}\right)^T \end{bmatrix} \tag{18}$$

$$J_q = \begin{bmatrix} \$_{r,2,1} \circ \$_{1,1} & 0 & 0 \\ 0 & \$_{r,2,2} \circ \$_{1,2} & 0 \\ 0 & 0 & \$_{r,2,3} \circ \$_{1,3} \end{bmatrix} \tag{19}$$

$$\dot{q} = \begin{bmatrix} \dot{\beta}_{1,1} & \dot{\beta}_{1,2} & \dot{\beta}_{1,3} \end{bmatrix}^T \tag{20}$$

J_x is a 3×6 matrix. J_q is a 3 × 3 matrix.

Equation (17) is multiplied by J_q^{-1}; the $\dot{q}$ can be derived as

$$\dot{q} = J_a \$_C \tag{21}$$

where

$$J_a = J_q^{-1} J_x = \begin{bmatrix} \left[\left(\overline{CG_1} \times Unit\left(\overline{G_1Q_1}\right)\right)^T & Unit\left(\overline{G_1Q_1}\right)^T\right] / \$_{r,2,1} \circ \$_{1,1} \\ \left[\left(\overline{CG_2} \times Unit\left(\overline{G_2Q_2}\right)\right)^T & Unit\left(\overline{G_2Q_2}\right)^T\right] / \$_{r,2,2} \circ \$_{1,2} \\ \left[\left(\overline{CG_3} \times Unit\left(\overline{G_3Q_3}\right)\right)^T & Unit\left(\overline{G_3Q_3}\right)^T\right] / \$_{r,2,3} \circ \$_{1,3} \end{bmatrix} \tag{22}$$

For (22), we only need to know the direction of each vector in each row, regardless of the magnitude of each vector, so the above matrix can be simplified as

$$J_b = \begin{bmatrix} \left(\overline{CG_1} \times Unit\left(\overline{G_1Q_1}\right)\right)^T & Unit\left(\overline{G_1Q_1}\right)^T \\ \left(\overline{CG_2} \times Unit\left(\overline{G_2Q_2}\right)\right)^T & Unit\left(\overline{G_2Q_2}\right)^T \\ \left(\overline{CG_3} \times Unit\left(\overline{G_3Q_3}\right)\right)^T & Unit\left(\overline{G_3Q_3}\right)^T \end{bmatrix} \tag{23}$$

J_b is 3×6 driving Jacobian matrices, which is the mapping between the linear velocity and angular velocity of the moving platform and the velocity of the driving joint.

4.3. The Complete Jacobian Matrix. The constrained submatrix and the driving submatrix of the mechanism can be written as a complete 6×6 matrix; that is, the screw expression of the complete Jacobian matrix of the mechanism is as follows:

$$J_W = \begin{bmatrix} \left(\overline{CG_1} \times Unit\left(\overline{G_1D_{D1}}\right)\right)^T & Unit\left(\overline{G_1D_{D1}}\right)^T \\ \left(\overline{CG_2} \times Unit\left(\overline{G_2D_{D2}}\right)\right)^T & Unit\left(\overline{G_2D_{D2}}\right)^T \\ \left(\overline{CG_3} \times Unit\left(\overline{G_3D_{D3}}\right)\right)^T & Unit\left(\overline{G_3D_{D3}}\right)^T \\ \left(\overline{CG_1} \times Unit\left(\overline{G_1Q_1}\right)\right)^T & Unit\left(\overline{G_1Q_1}\right)^T \\ \left(\overline{CG_2} \times Unit\left(\overline{G_2Q_2}\right)\right)^T & Unit\left(\overline{G_2Q_2}\right)^T \\ \left(\overline{CG_3} \times Unit\left(\overline{G_3Q_3}\right)\right)^T & Unit\left(\overline{G_3Q_3}\right)^T \end{bmatrix} \tag{24}$$

The line geometry can be used to determine the linear correlation of the reciprocal screws in the matrix to determine whether the mechanism is full rank or not, so as to judge the singular configuration of the mechanism.

According to linear algebra, the correlation of each line vector is the same as the vector $\overline{G_iD_{Di}}$ and $\overline{G_iQ_i}$. In order to represent the linear correlation of the Jacobian matrix more easily, the constrained reciprocal screw and driving reciprocal screw are expressed by vector $\overline{G_iD_{Di}}$ and $\overline{G_iQ_i}$. Taking the first branch chain as an example, when the revolute axes of the upper and lower platforms are not parallel to each other, the geometric representations of constrained reciprocal screw and driving reciprocal screw of a branch chain are as shown in Figures 3 and 4

5. Study the Singularity of the 3-RSR PM

5.1. Singularity Analysis of 3-RSR PM in the Fixed Mode. The fundamental reason for the singularity of the parallel mechanism is that the force screw vectors of each branch of the mechanism acting at the end of the operation are linearly correlated, so that the required degree of freedom cannot be achieved. The screw expression of a Jacobian matrix is obtained by the analysis in Section 3. The theory of linear geometry which is a systematic theory for the study of linear correlation of space vectors [10], which can judge the correlation of the screw vectors in different positions of the mechanism. Therefore, according to the line geometry theory, the singularity of the mechanism can be analyzed, which makes the singularity of the mechanism more intuitive in space and avoids the cumbersome calculation process. At the same time, this method also provides a new idea for finding the singularity of the parallel mechanism with multiple moving modes during the movement.

From the analysis of (24), the algebraic expressions of the constrained reciprocal screw and the driving reciprocal screw of the mechanism can be obtained. At the same time, the

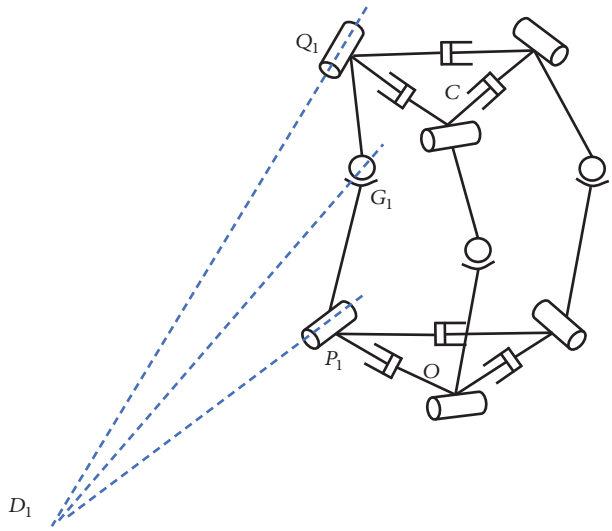

Figure 3: The geometric representation of the constrained reciprocal screw space.

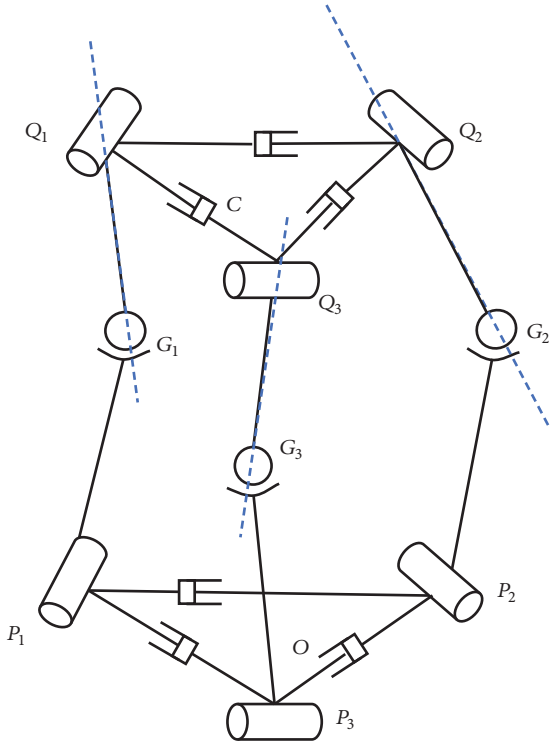

Figure 4: The geometric representation of the driving reciprocal screw space.

corresponding vector representation of the constrained reciprocal screw and the driving reciprocal screw in space can be drawn. The constrained reciprocal screw can be regarded as a line vector with pitch h=0, which represents the constrained force on the mechanism, and the driving reciprocal screw can be regarded as a couple of pitch $h = \infty$, which represents the constrained couple of the mechanism. According to the conclusion of the correlation and reversibility of the screw [21], we can get the general position of the 3-RSR mechanism in the traditional fixed mode, the three spherical joints are completely coincident, the connecting rod and the upper platform are in the same plane, the connecting rods are parallel in space, the connecting rod and the driving rod axis are coincident, etc. In this case, we have the correction between the constrained reciprocal screw and the driving reciprocal screw of the mechanism, that is, the constrained singularity and the driving singularity of the mechanism.

Thus, the correlation and expression of spatial vectors for the mechanism's constrained reciprocal screw and the driving reciprocal screw in various cases are shown in Table 1.

From Table 1, the singular configurations of 3-RSR in fixed mode can be as follows.

Case 1. When the mechanism is in a general position, according to the theory of linear geometry, the maximum linear independent number of the space line vector is 3, and the maximum linear independent number of the couple in any case is 3. It can be seen that in the general mode, the constrained reciprocal screw of the mechanism is linearly independent of the driving reciprocal screw, and there is no constrained singularity or structural singularity of the mechanism.

Case 2. When the three spherical joints of the mechanism are completely coincided, according to the theory of linear geometry, the three line vectors are coplanar and merged at one point. At this time, the maximum linear irrelevant number is two, and the three line vectors are linearly related, so that the mechanism generates constrained singularities. However, the three-driving reciprocal screws are couple, and the maximum linear independent number is three, no structural singularity.

Case 3. When the 3-RSR connecting rod and the upper platform are in the same plane, according to the theory of linear geometry, the maximum linear independent number of the space line vector is 3, and the maximum linear independent number of the couple in the same plane is 2. At this time, it can be seen that the driving reciprocal screws of the three branches are linearly related. Thus, the mechanism has no constrained singularities, but it has structural singularities.

Case 4. When the connecting rods of the mechanism are parallel in space, according to the theory of linear geometry, the three couples in space are parallel to each other and the maximum linear independent number is 1. At this time, it can be seen that the driving reciprocal screws of the three branches are linearly related. Thus, the mechanism has no constrained singularities, but it has structural singularities.

Case 5. When the axes of the driving rods and the connecting rods of the mechanism coincide, according to the theory of linear geometry, the maximum linear independent number of the spatial line vector is 3. At this time, the mechanism has no constrained singularities, the reciprocal screws of the mechanism's branches do not exist, but the mechanism has structural singularities.

Table 1: Study the singularity of the 3-RSR PM in the fixed mode.

Order	Geometric characteristics	Mechanism constrained reciprocal screws sptial representation	Mechanism driven reciprocal screw spatial representation
1	General position	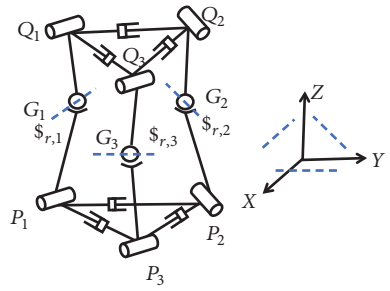	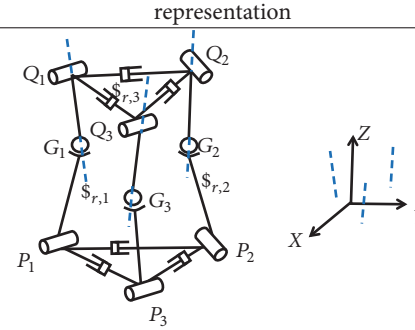
2	Complete coincidence of three spherical joints	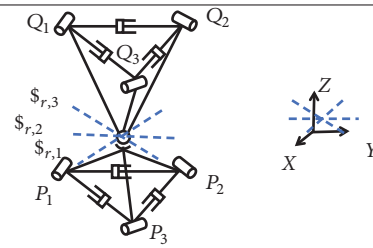	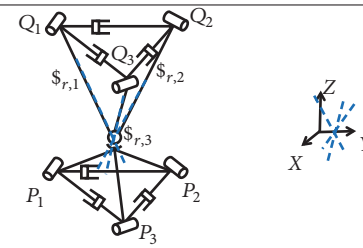
3	The connecting rods and the upper platform are in the same plane	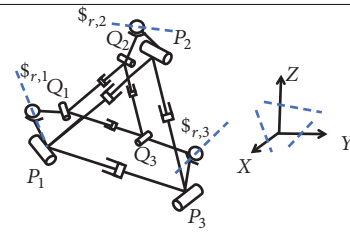	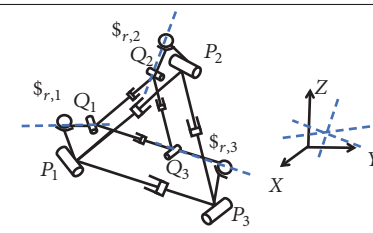
4	The connecting rods are parallel in space	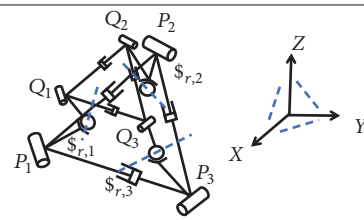	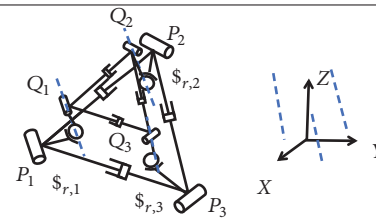
5	The axes of the connecting rods coincide with the axes of the driving rods	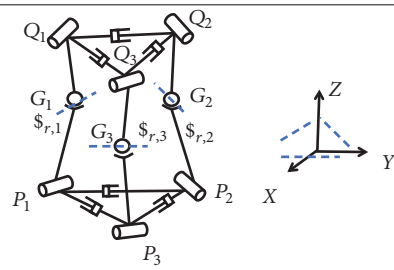	Currently, the mechanism driving reciprocal screws do not exist, and the mechanism has structural singularity.

6. Singularity Analysis of 3-RSR with Full Attitude and Multiple Motion Modes

Parallel mechanisms have unique closed-loop characteristics. In the design of mobile mechanisms and mobile robots, we make full use of kinematic relationship between the parallel mechanism platforms and the branch chains and combine the idea of multiple operating modes of the parallel platform [23, 24] to integrate multiple motion modes [25] on a mobile parallel mechanism and let the branch chains and platforms participate in rolling, walking, self-traversing, and so on. Finally, all-attitude multiple modes mobile parallel mechanism can be formed.

In this paper, the 3-RSR mobile PM can realize multi-direction rolling and self-traversing modes due to its own mechanism characteristics [20]. However, the driving choices and avoidance of singularity in realizing these motion modes are unclear.

In the process of realizing rolling motion and self-traversing movement, when the gait changes, the surface formed by the rods connected with the ground can be regarded as a base platform, and the other rods can be

Table 2: Study the singularity of the 3-RSR PM in the rolling mode.

Order	Gait planning of rolling mode	Study the singularity in each gait
step1 to step2	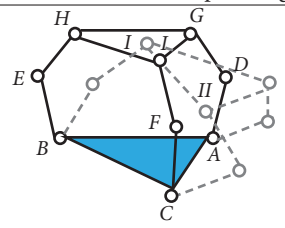 step 1 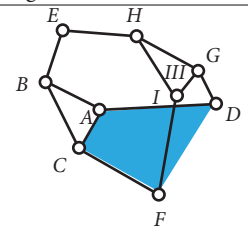 step 2	According to Table 1, from step1 to step2, the singular configurations shown in Table 1 do not appear.
step 2 to step3	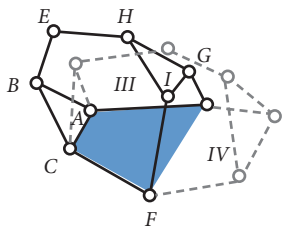 step 2 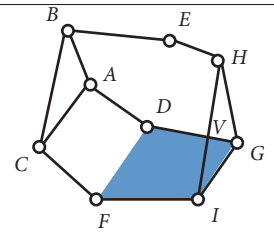 step 3	During this process, the singular configuration that may occur according to Table 1 is the constrained singular configuration 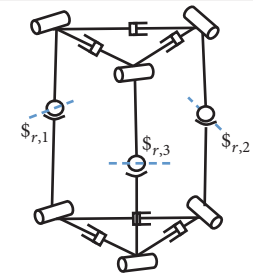
Step3 to step4	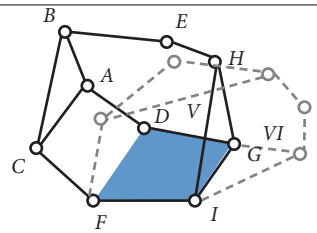 step 3 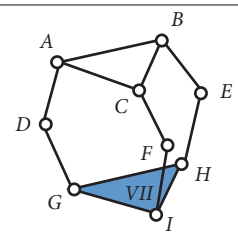 step 4	According to Table 1, from step3 to step4, the singular configurations shown in Table 1 donot appear.

regarded as the moving platform. That is to say, the moving platform and the base platform will change with the change of each gait.

Based on this idea, the singularities of the 3-RSR parallel mechanism listed in Table 1 under the traditional fixed mode can provide a theoretical basis for each gait transformation of the mechanism in the all-attitude movement process, and for choosing the most suitable joint or driving rods when avoiding or utilizing the singularity.

6.1. Study the Singularity in Rolling Mode. A rolling cycle of the 3-RSR mobile PM in the rolling mode is shown in Figure 5. According to the position of the upper and lower platform in the rolling process, a rolling cycle can be divided into seven gaits. As shown in Table 2, the gait of *I*~*II*, *III*~*IV*, *V*~*VI* can be regarded as the movement of mechanism in the fixed mode. During the gait of *II*~*III*, *IV*~*V*, *VI*~*VII*, the mechanical structure remains unchanged; only the center of gravity moves. Therefore, there are no singularities in this process.

(i) Step 1 to Step 2. In this process, at the position *I* in Table 2, the plane formed by three points of A, B, and C can be taken as the fixed platform. By driving the rods AD and CF, the projection of center of gravity on the ground falls outside the area of plane ABC, so the mechanism can roll to position *II*. Then, by locking each rod of the mechanism, the mechanism moves around the AC axis to the position *III* under the action of gravity.

(ii) Step 2 to Step 3. From Step 2 to Step 3 in Table 2, the plane formed by the four points ADCF can be taken as the fixed platform when the mechanism is in position *III*. By driving the rods GD and IF, the projection of the center of gravity on the ground falls outside the area of plane ACFD, then reaching position *IV*. According to Table 1, the rod BE and the rod EH maybe collinear in this process, which makes the mechanism singular. Therefore, the motors of driving rod BE and EH rotate at a certain angle, so that the mechanism moves to the position *IV*. Then, each driving motor is locked; the mechanism rotates along the rod DF under the action of gravity to reach position *V*, and the singular configurations that may occur is the constrained singular configuration.

(iii) Step 3 to Step 4. At position *V* in Table 2, the mechanism is fixed on a plane formed by four-point DFIG. The motors of the driving rods AD and CF make the projection of the center of gravity of the mechanism on the ground outside the DFIG plan area. No single configuration can be found during this process as shown in Table 1. Under the action of gravity, the mechanism reaches position *V*.

From Table 2, it reveals that the rolling motion of full attitude multimode mobile 3-*RSR* parallel mechanism is based on ZMP principle. The implementation of each gait

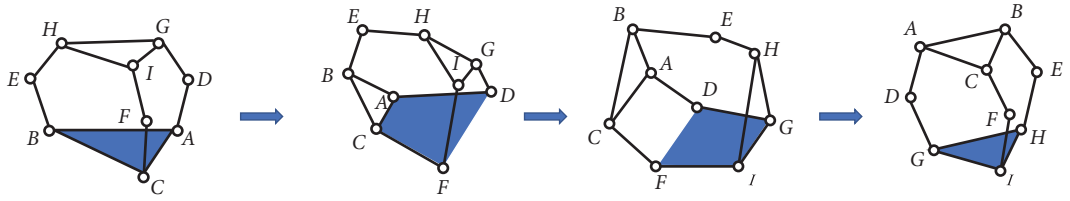

Figure 5: One cycle motion in the rolling mode.

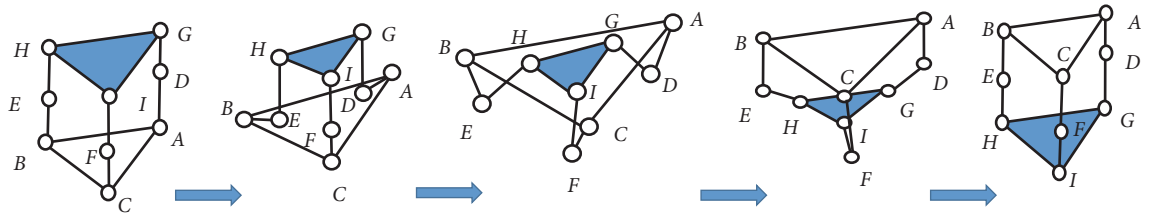

Figure 6: A cycle motion in self-traversing mode.

transition can be divided into two stages: the mechanism configuration change, center of gravity shift, and the roll forward. During the process of shifting the center of gravity, the motion pattern can be regarded as the movement under the fixed platform. The configuration remains variable as it rolls forward, but the center of gravity has not changed relative to the mechanism itself. Therefore, during the rolling process, it is only necessary to analyze the forward movement of the center of gravity.

6.2. Study the Singularity in Self-Traversing Mode. One cycle motion in the self-traversing mode is shown in Figure 6. The self-traversing process can be regarded as the process of alternation between upper and lower platforms. On the basis of the analysis, select the suitable joints to drive in order to avoid the possible singularity of the mechanism. As shown in Table 3, the singularities of the 3-RSR PM in self-traversing mode have been investigated.

(i) Step 1 to Step 2. According to Table 1, the mechanism is in a singular configuration at step 1 in Table 3. In this position, the three motors of the driving rods BE, CF, and AD are working, and the motor of the upper platform is also in use. The driving rods BE, CF, and AD are simultaneously contracting toward the center, and the other driving rods are locked; the mechanism can move from the state shown in step 1 to step 2.

(ii) Step 2 to Step 3. When the mechanism is in step 2, it can be seen from Table 1 that the mechanism is in a structurally singular state. At this time, the driving rods BE, CF, and AD are rotated by three motors, and the other motors are locked. Thus, the mechanism can reach step 3 state from step 2.

(iii) Step 3 to Step 4. In the process of step 3 to step 4, according to Table 1, it is known that the mechanism has no singular configuration, and the three motors that drive rods BE and BC are selected to work, and the motors of the upper and lower platforms and the connecting rod motors do not work.

(iv) Step 4 to Step 5. In the process of step 5 to step 6, when the mechanism moves to the state shown in step 5, the mechanism has no constrained singularity, but the mechanism has a driving singularity. Selecting the connecting rod EH, FI, GD three motors to work, the upper platform contracts to a minimum. The mechanism reaches the state indicated by step 5. When the mechanism is in the position of step 5, according to Table 1, the mechanism is in a singular configuration. All drivers need to be locked to avoid instability in this configuration. At this time, the three motors of the driving rod are locked, and the three motors of the connecting rods EH, FI, and GD are selected to work, and the upper platform is contracted to the minimum state. When the mechanism is in the position of step 5, according to Table 1, the mechanism is in a singular configuration. All drivers need to be locked to avoid instability in this configuration. Therefore, during the self-traversal mode, the possible singular configurations listed in Table 3 need to be considered in each gait. In addition, these singular configurations can be avoided or used by selecting the mechanism to drive and plan the motion gait.

7. Conclusions

In this paper, we offered a new mathematical method to study the singularity of parallel mechanism, the purpose is to select suitable driving motors for parallel mechanism in multiple motion modes to use and avoid singularity. This method is used to study the singularity of 3-RSR parallel mechanism in the fixed platform mode and all-attitude multimotion modes. Furthermore, the singularity diagrams of each movement mode are given respectively. Analysis results show that the method is feasible and practical compared with other research methods. In the near future, we would like to use this mathematical method to analyze the singularity

Table 3: Study the singularity of the 3-RSR PM in self-traversing mode.

Order	Gait planning	Study the singularity in each gait	
Step1	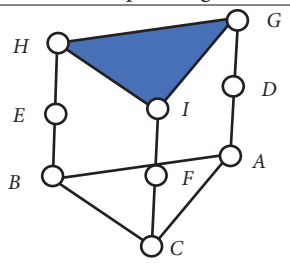	According to Table 1, the mechanism is in the constrained singular configuration at step 1.	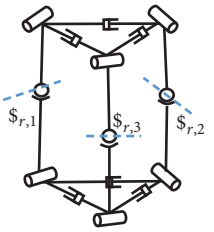
Step2	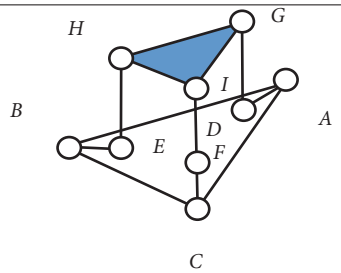	In step 2, Table 1 shows that the mechanism is in a structurally singular state.	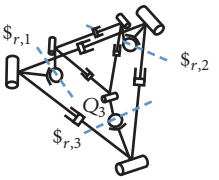
Step3	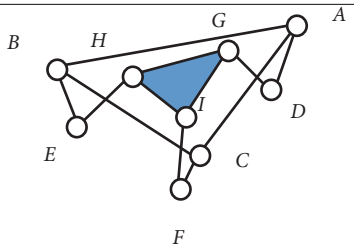	In the process of step 3 to step 4, the singular configurations shown in Table 1 do not appear.	
Step4	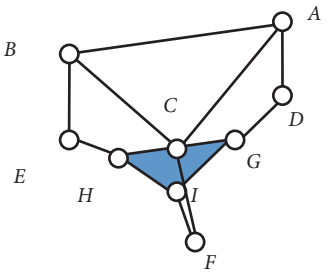	In the process of step 4 to step 5, Table 1 show that the mechanism is in the structure singular configuration and constrained singular configuration.	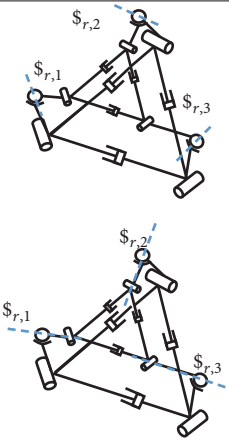
Step5	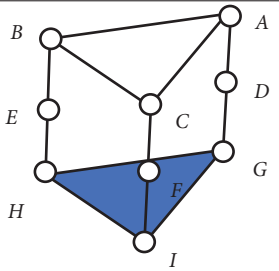	According to Table 1, the mechanism is in the constrained singular configuration in step 5.	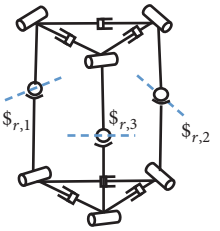

of multimode moving parallel mechanism. Also, multimode mobile parallel mechanism topology is the next plan. It also provides theoretical basis for the topology of multimode mobile parallel mechanism.

Data Availability

We propose a new mathematical method to study the singularity of multimode mobile parallel mechanism. The singularity of 3-RSR parallel mechanism (PM) is analyzed by using reciprocal screw methods and linear geometry theory from two aspects of fixed mode and full attitude multimotion mode. The complete Jacobian matrix of the PM is obtained by using the screw theory and the reciprocal screw of each branch is expressed with algebraic method and geometric drawing method. The singularity of the PM can be obtained by analyzing the reciprocal screw correlation and using the spatial line geometry theory. Finally we analyze the singular configuration of the PM under various modes, which provide theoretical guidance for the gait planning of the multimode mobile PM, and it is a theoretical derivation calculation. The formulas and graphs in the manuscript can completely derive the following conclusions, so no additional data can be uploaded.

Conflicts of Interest

The authors declare that there are no conflicts of interest regarding the publication of this paper.

Acknowledgments

Chunyan Zhang, the main author of this paper, would like to thank the Ph.D. degree supervisor, Professor Dan Zhang, for his excellent guidance. One of the authors would also like to express appreciation to the author's research partners Mr. Yu Wan and Mr. Qihua Ma who always help in solving some technical and fund problems. This research was partly supported by the National Natural Science Foundation of China (Grant No. 11604205), the State Key Laboratory for Modification of Chemical Fibers and Polymer Materials, Donghua University of China (Grant No. KF1826), and the Fundamental Research Funds for the Central Universities of China (Grant No. 2232018A3-02).

References

[1] J. P. Merle, *Parallel Robots*, Springer, Dordrecht, The Netherlands, 2nd edition, 2006.

[2] L. Patnaik and L. Umanand, "Kinematics and dynamics of Jansen leg mechanism: a bond graph approach," *Simulation Modelling Practice and Theory*, vol. 60, pp. 160–169, 2016.

[3] M. Russo, S. Herrero, O. Altuzarra et al., "Kinematic analysis and multi-objective optimization of a 3-UPR parallel mechanism for a robotic leg," *Mechanism and Machine Theory*, vol. 120, pp. 192–202, 2018.

[4] H. Wang, L. Sang, and X. Zhang, "Redundant actuation research of the quadruped walking chair with parallel leg mechanism," in *Proceedings of the 2012 IEEE International Conference on Robotics and Biomimetics (ROBIO)*, pp. 11–14, IEEE, Guangzhou, China, December 2012.

[5] Y. Pan and F. Gao, "A new six-parallel-legged walking robot for drilling holes on the fuselage," *Proceedings of the Institution of Mechanical Engineers, Part C: Journal of Mechanical Engineering Science*, vol. 228, no. 4, pp. 753–764, 2014.

[6] M. Wang and M. Ceccarelli, "Design and simulation of walking operation of a Cassino biped locomotor," *New Trends in Mechanism and Machine Science*, pp. 613–621, 2015.

[7] W. Ding, T. Detert, B. Corves et al., "Reconbot: a reconfigurable rescue robot composed of serial-parallel hybrid upper humanoid body and track mobile platform," *Mechanisms and Machine Science*, vol. 46, pp. 241–249, 2017.

[8] Z. Gao and F. Gao, "Singular configuration analysis of a novel parallel robot," *Journal of Mechanical Engineering*, vol. 44, no. 1, pp. 133–138, 2008.

[9] D. J. Sanger, *Kinematic Geometry of Mechanisms*, K. H. Hunt, Ed., vol. 9, 1991.

[10] J. P. Merlet, "Singular configurations of parallel manipulators and glassman geometry," *The International Journal of Robotics Research*, vol. 8, no. 5, pp. 194–212, 1989.

[11] C. Collins and G. Long, "The singularity analysis of an in-parallel hand controller for force-reflected teleoperation," *IEEE Transactions on Robotics and Automation*, vol. 11, no. 5, pp. 661–669, 1995.

[12] C. Gosselin and J. Angeles, "Singularity analysis of closed-loop kinematic chains," *IEEE Transactions on Robotics and Automation*, vol. 6, no. 3, pp. 281–290, 2002.

[13] V. Kumar, "Instantaneous kinematics of parallel-chain robotic mechanisms," *Journal of Mechanical Design*, vol. 114, no. 3, pp. 349–358, 1992.

[14] A. Mo and J. Angeles, "Architecture singularities of platform manipulators," in *Proceedings of the IEEE International Conference on Robotics and Automation*, pp. 11–15, IEEE, Sacramento, CA, USA, 2012.

[15] C. L. Collins and J. M. McCarthy, "The quartic singularity surfaces of planar platforms in the Clifford algebra of the projective plane," *Mechanism and Machine Theory*, vol. 33, no. 7, pp. 931–944, 1998.

[16] F. C. Park and J. W. Kim, "Singularity analysis of closed kinematic chains," *Journal of Mechanical Design*, vol. 121, no. 1, pp. 32–38, 1999.

[17] H. Pendar, M. Mahnama, and H. Zohoor, "Singularity analysis of parallel manipulators using constraint plane method," *Mechanism and Machine Theory*, vol. 46, no. 1, pp. 33–43, 2011.

[18] J.-P. Merlet, "Singular configurations of parallel manipulators and grassmann geometry," *International Journal of Robotics Research*, vol. 8, no. 5, pp. 45–56, 1989.

[19] W. K. Chen, *Kinematics and Dynamics Modelling and Simulation of 3-RSR parallel Robot [M.S. thesis]*, 2017.

[20] Y. B. Tian, "Theoretical study on Multi-mode moving Linkage Mechanism," *Mechanical Transmissions and Robotics*, pp. 241–249, 2017.

[21] Z. Huang, Y. S. Zhao, and T. S. Zhao, *Advanced Space Mechanism*, Higher Education Press, Beijing, China, 2014.

[22] F. Bichard, "Reconbot: a reconfigurable rescue robot composed of serial-parallel hybrid upper humanoid body and track mobile platform," *Mechanical Transmissions and Robotics*, pp. 241–249, 2017.

[23] S. Refaat, J. M. Hervé, S. Nahavandi et al., "Two-mode over-constrained three-DOFs rotational-translational linear-motor-based parallel-kinematics mechanism for machine tool applications," *Robotica*, vol. 25, no. 4, pp. 461–466, 2007.

[24] X. Kong, C. M. Gosselin, and P. L. Richard, "Type synthesis of parallel mechanisms with multiple operation modes , mechanical transmissions and robotics," *Mechanical Transmissions and Robotics*, pp. 241–249, 2017.

[25] Z. H. Miao, J. Wang, and B. Li, "Mobile robot with multiple modes based on 4-URU parallel mechanism," *New Trends in Mechanism and Machine Science*, vol. 43, pp. 399–407, 2017.

Hindawi
Mathematical Problems in Engineering
Volume 2019, Article ID 4847072, 12 pages
https://doi.org/10.1155/2019/4847072

Research Article

One Novel and Optimal Deadlock Recovery Policy for Flexible Manufacturing Systems Using Iterative Control Transitions Strategy

Ter-Chan Row,[1] Wei-Ming Syu,[2] Yen-Liang Pan ,[3,4,5] and Ching-Cheng Wang[2]

[1]*Department of Electronic Engineering, Army Academy, Taoyuan, Taiwan*
[2]*Institute of Manufacturing Information and System, National Cheng Kung University, Tainan, Taiwan*
[3]*Mathematics and Physics Division, General Education Center, Air Force Academy, Kaohsiung, Taiwan*
[4]*Artificial Intelligence and Robotics Design Lab, Air Force Academy, Kaohsiung, Taiwan*
[5]*Department of Electronic Engineering, National Kaohsiung University of Science and Technology, Kaohsiung, Taiwan*

Correspondence should be addressed to Yen-Liang Pan; peterpan960326@gmail.com

Received 13 November 2018; Revised 30 January 2019; Accepted 17 February 2019; Published 27 March 2019

Guest Editor: Sutasn Thipprakmas

This paper focuses on solving deadlock problems of flexible manufacturing systems (FMS) based on Petri nets theory. Precisely, one novel control transition technology is developed to solve FMS deadlock problem. This new proposed technology can not only identify the maximal saturated tokens of idle places in Petri net model (PNM) but also further reserve all original reachable markings whatever they are legal or illegal ones. In other words, once the saturated number of tokens in idle places is identified, the maximal markings of system reachability graph can then be checked. Two classical S^3PR (the Systems of Simple Sequential Processes with Resources) examples are used to illustrate the proposed technology. Experimental results indicate that the proposed algorithm of control transition technology seems to be the best one among all existing algorithms.

1. Introduction

Nowadays, in a rapidly changing society, every factory tries to use robots to possess complicated manufacturing workings. Flexible manufacturing systems (FMS) [1] are therefore designed to process these workings. However, for FMS there could exist an undesired phenomenon while robots are scramble for the shared resources of one FMS. The kind of competition is called the deadlock state. Besides, in order to solve above deadlock problem, three technologies are proposed [2]. The first one is deadlock avoidance. It can immediately avoid a deadlock and do the next step. The next one is called deadlock detection. It can find all deadlocks and recover the blocks. Please note that the above two technologies are adopted in dynamic method. They could have the time-consuming problem. The last one belongs to static. It considers the whole deadlocks in a model and solves them in advance. This technology is called deadlock prevention. Papers [3–11] presented a deadlock prevention to maintain the optimal permissiveness.

In deadlock prevention domain, Barkaoui and Abdallah firstly propose a deadlock prevention concept and method for a class of FMS called System of Simple Sequential Processes with Resources (S^3PR) [12]. In the following, Ezpeleta *et al.* [1] also presented a particular Petri net model for this kind of FMS. They used siphons concept and tried to add control places and related arcs to ensure the liveness of the FMS model. However, permissive is not large enough in deadlock free situation.

In the following, Huang *et al.* [3] presented a method called maximal siphons control technology to solve the deadlock problem. The proposed algorithm can extract the strict minimal siphon from maximal siphons such that all siphons are successfully avoided. The method seems to be better than [1] since its permissive markings are more than [1]. Besides, Huang *et al.* [4] proposed another algorithm named iterative approach with mixed integer programming

(MIP) method to improve conventional maximal siphons so as to enhance the computational efficiency. However, the two kinds of siphon based methods are still not maximally permissive.

On the other hand, Li and Zhou [5] proposed the elementary siphon concept to minimize the redundant siphons. The dependent siphons can then be controlled simultaneously once elementary siphons are controlled. Besides, Li and Zhou [6] clarified the elementary siphons and then simplified the number of control places. The permissiveness is also ameliorative. Liu *et al*. [7] introduced and proved a live Petri net controller can be established by adding a control place and related arcs to each strict minimal siphon in a controllable siphon basis. They presented a new novel deadlock prevention policy based on the concept of a controllable siphon basis. It is pity; the above deadlock prevention policies are still not maximally permissive. For all siphon control methods, refer to [14, 15].

Besides, Uzam [8] and Uzam and Zhou [9] follow the theory of region to obtain the optimal permissiveness. They classified all reachable states into two zones, deadlock-zone and deadlock-free-zone. The deadlock-zone was composed of dead markings and crucial dead markings. Finally, using the algorithm was successful to avoid the crucial dead markings and to make the net live. However, redundant the event-state-separation-problems (ESSPs) cannot be entirely avoided for large FMS cases. Huang and Pan [16, 17] and Huang *et al*. [18] further develop a computationally more efficient optimal deadlock control policy to improve the computational efficiency of the conventional theory of region.

Piroddi *et al*. [10] also proposed selective siphon control method for solving deadlock problems in deadlock prevention domain. The policy merged selective siphons and crucial markings. By every iteration, the redundant siphons will be controlled simultaneously once selective siphons are controlled. Its most advantage is maximally permissive markings which can still be held. However, its drawback is that reachability graph is needed to run in every iteration. Therefore, Pan *et al*. [19] develop one computationally improved methodology to enhance its computational efficiency. For improving above shortcoming, Pan *et al*. [11] further try to merge theory of regions and the selective siphons control method to achieve optimal control goal. This proposed method can identify all crucial markings in first reachability graph and use the theory of regions to check these crucial markings. Finally, selective siphons method is used to control all minimal siphons. Maximally permissive markings are surely still held. Preciously, reachability graph is just one time needed to run. At the same time, Pan *et al*. [20] also use the selective siphons technology with the method in [18] to further enhance the computational time of traditional theory of regions.

In siphon control domain, Chao and Pan [21] also proposed the uniform formulas for compound siphons, complementary siphons, and characteristic vectors to solve the deadlock problems of flexible manufacturing systems easily. This can simplify the computational efficiency.

On the other hand, Huang *et al*. [13] firstly presented transition-based deadlock prevention policy to solve the deadlocks problem of FMS. However, there are three main drawbacks in [13]. Firstly, they cannot identify the exact number of tokens in idle places in advance. Besides, they need to check all reachable markings of FMS reachability graph to avoid getting live lock. Finally, their some controllers seem to be redundant. Therefore, in our previous work [22], we first propose all reachability graph and First Dead Marking (FDM) viewpoints based on control transition to improve the computational efficiency of [13]. The improved work [22] does overcome the disadvantage of [13]. It is a pity; its example is a small PNM.

Zhang and Uzam [23] also adopted control transition method to solve the deadlocks of flexible manufacturing systems. They improved the computational efficiency of [13] since the redundant controller's problem was overcome. However, they still cannot identify the correct saturated number of tokens of idle places in the process of seeking the maximal number of reachable markings.

Recently, Chen *et al*. [24] also propose one deadlock policy to solve FMS deadlock problem using control transition concept. They define a minimal recovery transitions using iterative approach by an integer linear programming problem (ILPP) and objective functions. However, it is not an efficient method since ILPP is used to obtain proper supervisors.

Based on above survey, one can know that how to solve deadlock problems of flexible manufacturing systems is a very difficult issue. Many experts make their most effort in the issue [1, 3, 5, 9, 10, 25–34]. Most important, how to keep systems maximally permissive is needed to concern.

To focus the maximally live performance, this paper proposes one new, different, and simple control method based on control transition technology. It presents a very different and novel concept in solving deadlock problems. First of all, the number of saturated tokens in idle (source or sink) places must be identified. Then, the maximal markings of its reachability graph can then be checked. Further, control transitions can be obtained. Finally, the maximally permissive live markings can be present once the controllers are added it into PNM.

The rest of this paper is as follows. Section 2 presents the preliminaries about the Petri nets. Section 3 proposes a new deadlock prevention approach and proves it can be executed. Section 4 presents two examples to verify by our prevention policy. The last, Section 5 is the conclusion.

2. Preliminaries

A Petri net model (PNM) is formed by five elements. The model will become actively according to the tokens firing. A PNM will be defined as follows.

Definition 1 (see [1, 2, 35]). $N = (P, T, F, W, M_0)$, where

P is a finite, nonempty, and disjoint set of places which shows $P = \{p_1, p_2, p_3, \ldots, p_m\}$.$T$ is also a finite, nonempty, and disjoint set of transitions which shows $T = \{t_1, t_2, t_3, \ldots, t_m\}$. The third element F is called the flow relation or the set of directed arcs with the arrows from places to transitions or from transitions to places. The characteristic of F is $F \subseteq (P \times T) \cup (T \times P)$. $W(\cdot)$ is assigned the weight to

an arc. Furthermore, the set of arcs in PNM are nonnegative integer. The net is called ordinary when the weight of arcs in PNM is all one. M_0 is named the initial marking combined with net system (N, M_0).

In a net system (N, M_0) and a node $x \in P \cup T$, then the preset of node x is defined as $\bullet x = \{y \in P \cup T \mid (y, x) \in F\}$. The postset of node x is defined as $x\bullet = \{y \in P \cup T \mid (x, y) \in F\}$.

A transition $t \in T$ is enabled at marking M by iff $\forall p \in \bullet t$ and $M(p) \geq W(p,t)$ that will be denoted as $M[t\rangle$. Afterward enabled and firing a transition, M will get a new marking M'. It indicates $M[t\rangle M'$. A marking M reaches to M' shown by $M[\sigma\rangle M'$ if there exists a firing sequence $\sigma = t_1 t_2 t_3 \ldots t_n$. The set of marking reachable from M in N is called a reachability set as $R(N, M)$ in net system (N, M_0). The net system (N, M_0) is live iff $\forall t \in T$ is enabled and dead iff $\exists t \in T$ is disabled.

Definition 2 (see [35, 36]). Given ${}^\bullet S \subset P$, (resp., $S^\bullet$) denotes the set of transitions with at least one output (resp., input) place belonging to S. Formally, ${}^\bullet S = \bigcup_{p \in s} {}^\bullet p$ and $S^\bullet = \bigcup_{p \in s} p^\bullet$. S is called a *siphon* if ${}^\bullet S \subseteq S^\bullet$; i.e., any input transition of S is also an output transition of S. It is called a *trap* if $S^\bullet \subseteq {}^\bullet S$. A siphon (resp. trap) is said to be *minimal* if it does not contain other siphons (resp., traps).

Definition 3 (see [1, 37–39]). A S^3PR is the union of a set from the two combined simple sequential processes with resources (S^2PR) nets $N_i = (P_i \cup \{p_i^0\} \cup P_{Ri}, T_i, F_i)$ by sharing common places, and the following statements are true.

(1) P_i and P_{Ri} are called operation and resource places of N_i, respectively. $\boldsymbol{p_i^0}$ is called the process idle places.

(2) $P_i \neq \phi$; $P_{Ri} \neq \phi$; $p_i^0 \notin P_i$; $(P_i \cup \{p_i^0\}) \cap P_{Ri} = \phi$; $\forall p \in P_i$, $\forall t \in {}^\bullet p$, $\forall t' \in p^\bullet$, $\exists r_p \in P_{Ri}$, ${}^\bullet t \cap P_{Ri} = t'^\bullet \cap P_{Ri} = \{r_p\}$; $\forall r \in P_{Ri}$, ${}^{\bullet\bullet} r \cap P_i = r^{\bullet\bullet} \cap P_i \neq \phi$; $\forall r \in P_{Ri}$, ${}^\bullet r \cap r^\bullet = \phi$; ${}^{\bullet\bullet}(p_i^0) \cap P_{Ri} = (p_i^0)^{\bullet\bullet} \cap P_{Ri} = \phi$.

(3) ${N_i}'$ is a strongly connected state machine, where $N_i' = (P_i \cup \{p_i^0\}, T_i, F_i)$ is the resulting net after the places in P_{Ri} and related arcs are removed from N_i.

(4) Every circuit of ${N_i}'$ contains place p_i^0.

(5) Any two N_i and N_j are composable if they share a set of common resource places. Every shared place must be a resource.

(6) The transitions of $(p_i^0)^\bullet$ and ${}^\bullet(p_i^0)$ are called source and sink transitions of S^3PR, respectively.

(7) For $r \in P_R$, $H(r) = ({}^{\bullet\bullet} r) \cap P_A$ is the set of operation places that use r and are called holders of r.

(8) For $p \in P_A$, $({}^{\bullet\bullet} p) \cap P_R = \{r_p\}$ where resource place r_p is called the resource used by p.

3. One Novel Deadlock Prevention Policy

Since this paper tries to propose one novel deadlock recovery policy by adopting control transition method, in this section, the authors will present the important concept of the proposed policy and how it works. First of all, the number of saturated tokens in idle (e.g., source or sink) places should be identified. Secondly, the maximal number of markings in its reachability graph can then be checked and calculated.

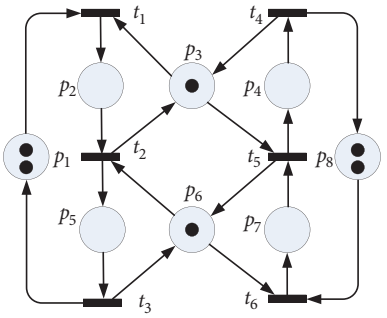

Figure 1: Petri net model of two idle places.

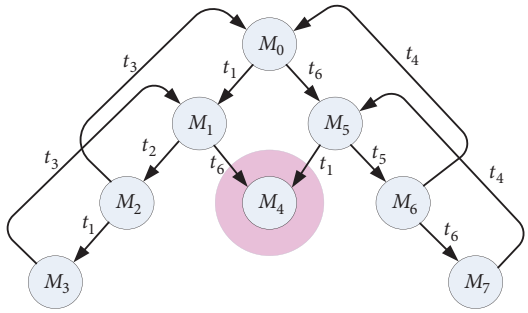

Figure 2: The reachability states of above simple PNM.

Further, control transitions can hence be obtained. Finally, the maximally permissive live markings can be present once the transition-based controllers are added to the deadlock prone PNM. In the following, the authors will show the detailed information as follows.

3.1. Saturated Number of Tokens in Idle Places. In this subsection, we will show how to identify the saturated number of tokens in PNM's idle places. The first step is that one needs to pick all idle places and try to change the number of their tokens. Please note that the number is from small to large. Then, all reachable states will hence change due to the different number of tokens in idle places. Finally, the number of reachable states will reach one maximal number whatever the number of tokens increased in idle places. Under the situation, we call it the optimal number or saturated number of token in idle places. For example (please refer to Figure 1), Table 1 shows the different number of tokens in two the idle places (i.e., p_1 and p_8). From the Table 1 we can see that the PNM reaches the maximal reachable states when (p_1, p_8) is $(2, 2)$. The experimental groups 15~16, 18~20, and 22~24 are just used to present that the maximal reachable states of the PNM are equal to 8. Further, the maximal reachable states are 8 whatever how large number of tokens is added or increased into the idle place. The set of $(2, 2)$ is what we want, it is the saturated number (or called optimal) of tokens in idle places of this PNM.

In the following, we demonstrate our algorithm by using above example. Please review the first example again; from Figure 2, we can easily see that there exists one deadlock in its reachability graph. All information of reachable markings (states) is shown in Table 2 so that all readers can easily check them.

Table 1: The variety of reachability states by different tokens in idle places of Figure 1.

Experimental Group	(p_1, p_8)	Reachable States	Experimental Group	(p_1, p_8)	Reachable States
1	(1, 0)	3	13	(2, 1)	7
2	(2, 0)	4	**14**	**(2, 2)**	**8**
3	(3, 0)	4	15	(2, 3)	8
4	(4, 0)	4	16	(2, 4)	8
5	(0, 1)	3	17	(3, 1)	7
6	(0, 2)	4	18	(3, 2)	8
7	(0, 3)	4	19	(3, 3)	8
8	(0, 4)	4	20	(3, 4)	8
9	**(1, 1)**	**6**	21	(4, 1)	7
10	(1, 2)	7	22	(4, 2)	8
11	(1, 3)	7	23	(4, 3)	8
12	(1, 4)	7	24	(4, 4)	8

Table 2: The detailed information of all reachable markings in Figure 2.

Marking No.	Classification	Information of Markings $[p_1, p_2, p_3, p_4, p_5, p_6, p_7, p_8]^T$
M_0	*Initial Marking*	$[2, 0, 1, 0, 0, 1, 0, 2]^T$
M_1	*Live marking*	$[1, 1, 0, 0, 0, 1, 0, 2]^T$
M_2	*Live Marking*	$[1, 0, 1, 0, 1, 0, 0, 2]^T$
M_3	*Live Marking*	$[0, 1, 0, 0, 1, 0, 0, 2]^T$
M_4	*Dead Marking*	$[1, 1, 0, 0, 0, 0, 1, 1]^T$
M_5	*Live Marking*	$[2, 0, 1, 0, 0, 0, 1, 1]^T$
M_6	*Live Marking*	$[2, 0, 0, 1, 0, 1, 0, 1]^T$
M_7	*Live Marking*	$[2, 0, 0, 1, 0, 0, 1, 0]^T$

3.2. Identify the Control Transition. According to the definitions as follows, control transitions can be calculated and obtained in one PNM.

Definition 4. A Petri net N is with an initial marked M_0; the set of all reachable markings for the Petri net N is denoted by $R(N, M_0)$.

Definition 5 (see [40]: reversibility). (1) A Petri net N has a home state M_h for an initial state M_0 if for every reachable state $M \in R(N, M_0)$, a firing sequence σ_i exists such that $M[\sigma_i\rangle M_h$.

(2) A Petri net N is reversible for an initial state M_0 if M_0 is a home state.

Definition 6 (dead marking). M_d is a dead marking and is defined as follows:

$$M_d = \{M \mid \forall M \in R(N, M_0), \nexists t \in T, \ni M[t\rangle\} \quad (1)$$

Definition 7 (reachability tree). Reachability tree is called reachability graph (RG) or reachability states (RS). A Petri net N with an initial marking M_0 is called a Petri net system (N, M_0). The reachability graph of (N, M_0) is defined as follows:

$$\forall t \in T, \exists t, \text{s.t. } M_i[t\rangle M_j \Longrightarrow \cup\left(M_i[t\rangle M_j\right) \quad \text{where } M_i, M_j, \text{and } t \in R(N, M_0) \quad (2)$$

The reachability graph is represented as $R(N, M_0)$.

Definition 8 (a transition t is enabled and firing). A transition t is enabled $\forall p \in P \wedge p \in {}^\bullet t \wedge M(p) \geq W(p, t)$. One can show that, as $M[t\rangle$, the next step is firing. A transition t is firing if a new marking M' yields. One can denote $M[t\rangle M'$.

Definition 9 (control transition). A Petri net with a dead marking M_d, $\forall M_d \in R(N, M_0)$, $M \in R(N, M_0)$, $M_d \subset M$, $\exists t_c \notin T$, s.t. $M_d[t_c\rangle M$. t_c is called a control transition.

Definition 10 (saturated number of tokens in idle places (SNTIP)). $\exists \min(n)$ in a P_{id} such that the RG is maximal.

$\sum P_{id}(\min(n))$ are obtained the maximal RG. Then, $\sum P_{id}(\min(n))$ are called SNTIP.

n is a token number in an idle place. $n = 0, 1, 2, 3, \ldots$.

P_{id} is an idle place.

Theorem 11. *A deadlocked Petri net (S^3PR), $\forall M_d \in R(N, M_0)$, $\exists t_c \notin T$, such that M_d can reach to M_0 and M_d, becomes live.*

Proof. It is well known that the state equation is $M_k = M_{k-1} + A^T u_k$, $k = 1, 2, 3, \ldots$ [41]. Here, we change the state equation to $M_{k-1} = M_k - A^T u_k$ then $M_{k-1} = M_k + A^T(-u_k)$. Let $-u_k = y_k$. Obtaining the new state equation is $M_{k-1} = M_k + A^T y_k$ $k = 1, 2, 3, \ldots$. One expands and pluses by every series. The result is $M_0 = M_k + A^T \Sigma y_k$. Assume $M_k = M_d$ and $x = \Sigma y_k$, then $M_0 - M_d = A^T x$, which can be written $M_0 - M_d = \Delta M$. This means $A^T x = \Delta M$. When $\Delta M = 0$, then $A^T x = 0$ is a homogenous equation. $\exists x$ such that $M_0 =$

Table 3: The flow step of our novel deadlock recovery policy.

Maximally Permissive Deadlock Recovery Policy
(i) Input: one deadlock S^3PR PNM.
(1) Identify the saturated number of tokens in idle places.
(2) Identify the crucial dead markings from reachability graph.
(3) Calculate all control transitions.
(4) Add all control transitions into original PNM.
(ii) Output: one live S^3PR PNM.

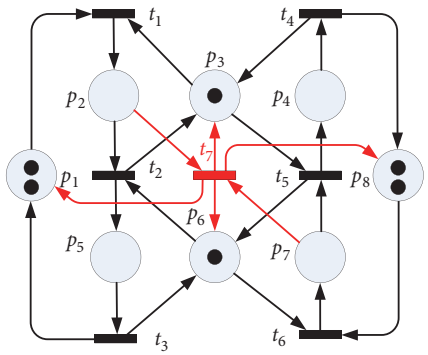

Figure 3: The Petri net model with control transition.

$M_d + A^T x$. Based on [42], ones know $A^T x = O(t, p) - I(t, p)$. It means $\exists t_c$ ($t_c = O(t, p) - I(t, p)$) such that M_d can reach M_0. We can infer that M_0 is reachable from M_d.

To obtain the equation of $M_0 = M_k + A^T \Sigma y_k$, one has the following:

$$M_0 = M_1 + A^T y_1 \quad (3)$$

$$M_1 = M_2 + A^T y_2 \quad (4)$$

$$M_2 = M_3 + A^T y_3 \quad (5)$$

$$\vdots \quad (6)$$

$$M_{k-2} = M_{k-1} + A^T y_{k-1} \quad (k\text{-}2)$$

$$M_{k-1} = M_k + A^T y_k \quad (k\text{-}1)$$

Equations (3) + (4) + (5)...(k-2) + (k-1) are equal to $M_0 = M_k + A^T \Sigma y_{k\diamondsuit}$. □

The example of Figure 1 is present to obey Theorem 11 and obtain a control transition in the next section.

3.3. The Flow Steps of Our Deadlock Prevention Policy. The deadlock recovery policy and its steps are shown in Table 3.

In the following, we want to calculate the optimal control transitions so that they can be added to one deadlock PNM and live it. Please notice that the controller is calculated by initial marking ($M_0 = [2, 0, 1, 0, 0, 1, 0, 2]^T$) and the dead marking ($M_4 = [1, 1, 0, 0, 0, 0, 1, 1]^T$) based on Theorem 11. The firing count vector $x = [-2, -1, -1, 0, 0, -1]^T$ and the transpose of incidence matrix A^T are as follows:

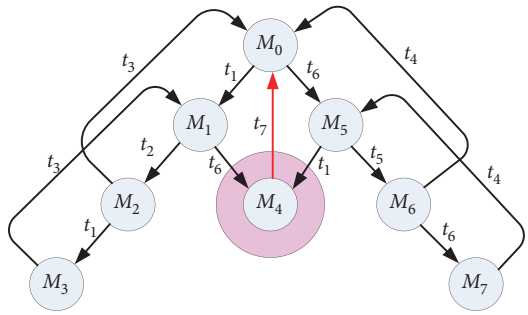

Figure 4: The reachability states of Figure 3.

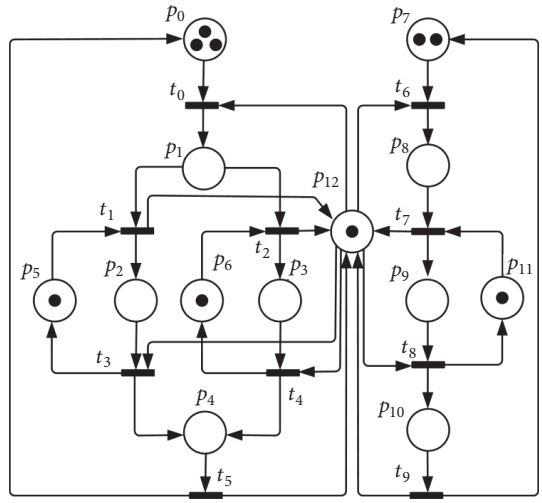

Figure 5: One simple Petri net model [13].

$$A^T = \begin{bmatrix} -1 & 0 & 1 & 0 & 0 & 0 \\ 1 & -1 & 0 & 0 & 0 & 0 \\ -1 & 1 & 0 & 1 & -1 & 0 \\ 0 & 0 & 0 & -1 & 1 & 0 \\ 0 & 1 & -1 & 0 & 0 & 0 \\ 0 & -1 & 1 & 0 & 1 & -1 \\ 0 & 0 & 0 & 0 & -1 & 1 \\ 0 & 0 & 0 & 1 & 0 & -1 \end{bmatrix} \quad (7)$$

The equation of $M_0 = M_d + A^T x$ is shown as follows:

$$\begin{bmatrix} 2 \\ 0 \\ 1 \\ 0 \\ 0 \\ 1 \\ 0 \\ 2 \end{bmatrix} = \begin{bmatrix} 1 \\ 1 \\ 0 \\ 0 \\ 0 \\ 0 \\ 1 \\ 1 \end{bmatrix} + \begin{bmatrix} -1 & 0 & 1 & 0 & 0 & 0 \\ 1 & -1 & 0 & 0 & 0 & 0 \\ -1 & 1 & 0 & 1 & -1 & 0 \\ 0 & 0 & 0 & -1 & 1 & 0 \\ 0 & 1 & -1 & 0 & 0 & 0 \\ 0 & -1 & 1 & 0 & 1 & -1 \\ 0 & 0 & 0 & 0 & -1 & 1 \\ 0 & 0 & 0 & 1 & 0 & -1 \end{bmatrix} \begin{bmatrix} -2 \\ -1 \\ -1 \\ 0 \\ 0 \\ -1 \end{bmatrix} \quad (8)$$

Therefore, according to our proposed algorithm, the all output places of the control transition are $O(t_7) = p_1 + p_3 + p_6 + p_8$, and the all input places of the control transition are $I(t_7) = p_2 + p_7$. The detailed information of the controller is shown in Figure 3. The PNM is deadlock free when we added the controller to initial deadlock PNM. The detailed information is shown in Figure 4.

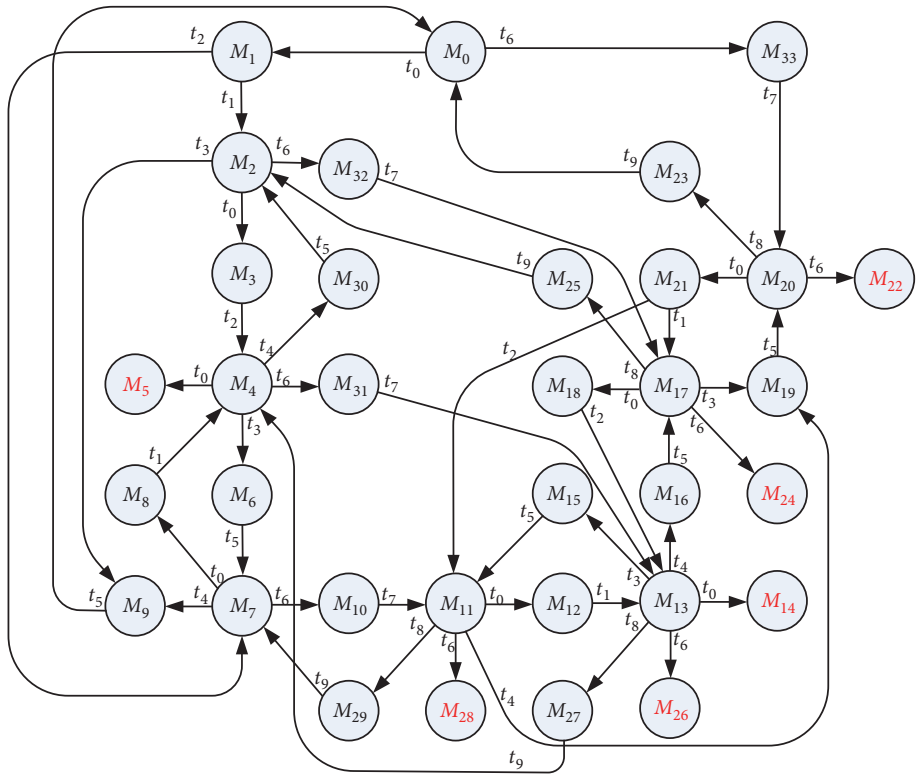

Figure 6: The reachability graph of Figure 5.

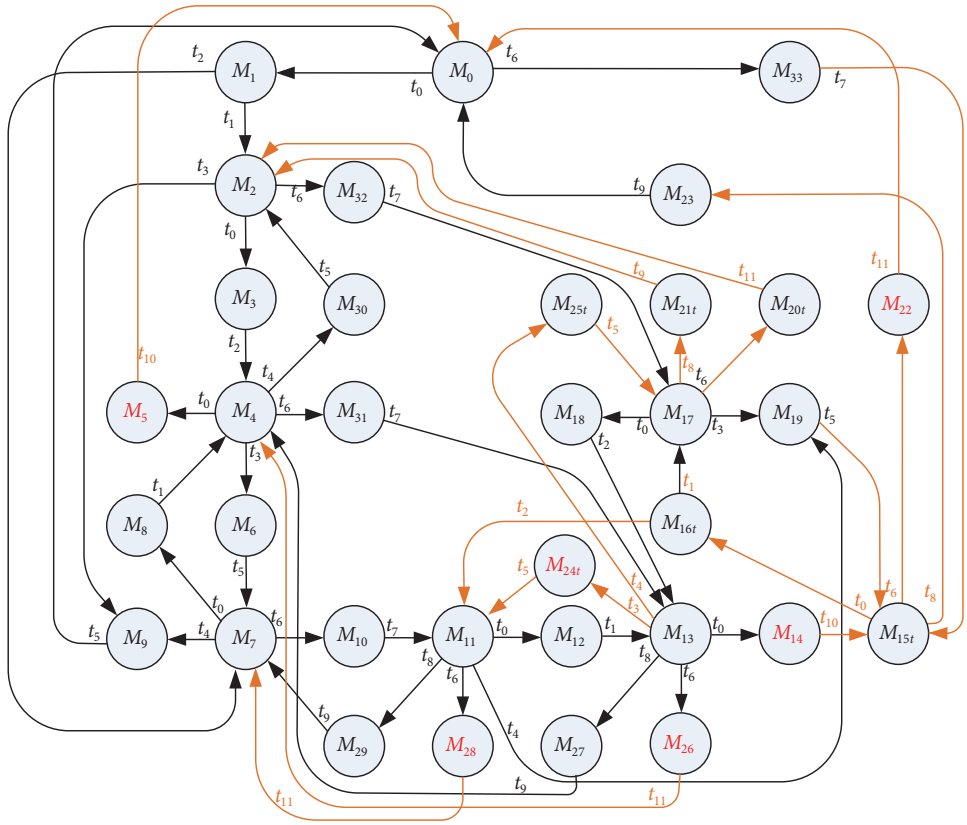

Figure 7: Its deadlock free reachability graph of Figure 5.

Table 4: The variety of reachability states by different tokens in idle places of Figure 5.

Set No.	(p_0, p_7)	Reachable States	Set No.	(p_0, p_7)	Reachable States
1	(1, 0)	5	10	(1, 2)	19
2	(2, 0)	10	11	(1, 3)	19
3	**(3, 0)**	**11**	12	(2, 1)	28
4	(4, 0)	11	13	(2, 2)	32
5	(0, 1)	4	14	(2, 3)	32
6	**(0, 2)**	**5**	15	(3, 1)	30
7	(0, 3)	5	**16**	**(3, 2)**	**34**
8	(0, 4)	5	17	(3, 3)	34
9	(1, 1)	16	18	(4, 3)	34

Table 5: Two crucial control transitions.

No.	Property of Crucial Dead Markings	$I(t_{ci})$	$O(t_{ci})$	Identified in Which Idle Places
1	$p_1 + p_2 + p_3 + p_{11}$	$I(t_{c1}) = p_1 + p_2 + p_3$	$O(t_{c1}) = 3p_0 + p_5 + p_6 + p_{12}$	(3, 0)
2	$p_5 + p_6 + p_8 + p_9$	$I(t_{c2}) = p_8 + p_9$	$O(t_{c2}) = 2p_7 + p_{11} + p_{12}$	(0, 2)

4. Examples and Comparisons

In this section, we want to evaluate our proposed deadlock prevention and make some comparisons with existing literature. Two classical examples are used to illustrate the proposed algorithm. The first example is one simple PNM. For easy tracing, we present the detailed information step by step. Please note that there are at least two dead markings in the two PNMs. In other words, some deadlock markings are redundant. Therefore, we not only want to identify the optimal number of tokens in its idle places, but also identify its crucial dead markings so that we can use them to calculate final controllers. For easy checking, the two PNM used TINA to run their reachability graph.

4.1. The Simple Petri Net Model [13]

Step 1 (identify the optimal number of tokens in idle places). In this step, we firstly used one famous software TINA [43] to check the optimal number of tokens in idle places. Table 4 shows the variety of reachable states by changing different number of tokens in idle places of Figure 5. Please notice that the maximal number of tokens in p_0 is equal to 3 when the number of tokens in p_7 is set to zero. Similarly, the maximal number of tokens in p_7 is 2 when the number of tokens in p_0 is set to zero. The third group and the sixth group in Table 4 show the optimal number of tokens in its idle places, respectively. It is obvious that in sixteenth group when (p_0, p_7) is equal to $(3, 2)$ the idle places have the optimal number of tokens. $(p_0, p_7) = (3, 2)$ is the saturated number of tokens because the reachable states of this PNM are in its maximal value even one gives more tokens in (p_0, p_7). The maximal number of reachable markings is checked once the optimal number of tokens in one's idle places is identified. The seventeenth and the eighteenth groups in Table 4 show the above description.

Step 2 (identify the crucial dead markings from reachability graph). In this PNM, there are 34 reachable markings in total including 6 dead markings when the idle places are in saturation (please refer to Figure 6). Based on TINA, the detailed information of the 6 dead markings is $M_5 = (p_1, p_2, p_3, 2p_7, p_{11})$, $M_{14} = (p_1, p_2, p_3, p_7, p_9)$, $M_{22} = (3p_0, p_5, p_6, p_8, p_9)$, $M_{24} = (2p_0, p_2, p_6, p_8, p_9)$, $M_{26} = (p_0, p_2, p_3, p_8, p_9)$, and $M_{28} = (2p_0, p_3, p_5, p_8, p_9)$, respectively. However, the 6 dead markings could be dependent. In other words, controllers could be redundant although the PNM also can be deadlock free when all controllers are added to above PNM. Therefore, one needs to identify crucial dead markings so as to obtain all independent controllers. By using the proposed algorithm, we can obtain 2 crucial dead markings, $(p_1+p_2+p_3+p_{11})$ and $(p_5+p_6+p_8+p_9)$, respectively. The detailed information is shown in Table 5.

Step 3 (calculate all control transitions). According to the state equation (i.e., $M_0 - M_d = O(t, p)–I(t, p)$), two sets of control transitions can then be obtained. The detailed information of them is (1) $I(t_{c1}) = p_1 + p_2 + p_3$, $O(t_{c1}) = 3p_0 + p_5 + p_6 + p_{12}$ and (2) $I(t_{c2}) = p_8 + p_9$, $O(t_{c2}) = 2p_7 + p_{11} + p_{12}$ also shown in Table 5.

Step 4 (add all control transitions into original PNM). The PNM is deadlock free when the two sets of control transitions are put into the original PNM. Besides, the number of its final reachable live markings is still 34. The proposed deadlock prevention policy not only solves the deadlock problem of the PNM of Figure 5 but also holds all reachable markings even they are dead markings in the beginning. Its deadlock free reachability graph is shown in Figure 7. Please notice that the contents of six markings M_{15t}, M_{16t}, M_{20t}, M_{21t}, M_{24t}, and M_{25t} are different from the initial markings.

4.2. Another Classical Complex PNM. In the following, we want to show that the proposed deadlock prevention policy can be used to solve a complex PNM shown in Figure 8 [1]. In this PNM, it is composed of three robots named R_1, R_2, and R_3, denoted by p_{20}, p_{21}, and p_{22}, four machines named M_1, M_2, M_3, and M_4 denoted by p_{23}, p_{24}, p_{25} and p_{26}, respectively. Finally, three idle places (I_1/O_1, I_2/O_2, and I_3/O_3) are given named p_1, p_{14}, and p_5, respectively. The others in this model are operation places. Further, there are

Table 6: The 20 sets of crucial dead markings of Figure 8.

No.	Idle Places (p_1, p_5, p_{14})	Crucial Dead Markings
1	(3, 0, 0)	$p_2 + 2p_3 + p_{20} + p_{22} + 2p_{23} + 2p_{25} + 2p_{26}$
2	(1, 1, 2)	$p_1 + p_{12} + 2p_{18} + p_{20} + p_{22} + 2p_{23} + 2p_{24} + 2p_{25}$
3	(1, 2, 1)	$p_1 + 2p_{11} + p_{17} + p_{20} + p_{22} + 2p_{23} + 2p_{24} + 2p_{26}$
4	(1, 2, 2)	$p_1 + p_{12} + p_{13} + p_{18} + p_{19} + p_{20} + 2p_{23} + 2p_{24} + 2p_{25}$
5	(1, 2, 3)	$p_2 + 2p_9 + 2p_{18} + p_{19} + p_{20} + 2p_{23} + 2p_{25}$
6	(1, 2, 3)	$p_3 + p_8 + p_9 + 2p_{18} + p_{19} + p_{20} + 2p_{23} + 2p_{25}$
7	(1, 3, 1)	$p_1 + p_{12} + 2p_{13} + p_{19} + p_{20} + 2p_{23} + 2p_{24} + 2p_{25}$
8	(1, 3, 2)	$p_2 + 2p_9 + p_{13} + p_{18} + p_{19} + p_{20} + 2p_{23} + 2p_{25}$
9	(1, 3, 2)	$p_3 + p_8 + p_9 + p_{13} + p_{18} + p_{19} + p_{20} + 2p_{23} + 2p_{25}$
10	(1, 3, 3)	$p_1 + p_6 + 2p_7 + 2p_{16} + p_{17} + p_{22} + 2p_{24} + 2p_{26}$
11	(1, 3, 3)	$p_1 + p_8 + 2p_9 + 2p_{18} + p_{19} + p_{20} + 2p_{23} + 2p_{25}$
12	(1, 4, 1)	$p_3 + p_8 + p_9 + 2p_{13} + p_{19} + p_{20} + 2p_{23} + 2p_{25}$
13	(1, 4, 1)	$p_2 + 2p_9 + 2p_{13} + p_{19} + p_{20} + 2p_{23} + 2p_{25}$
14	(1, 4, 2)	$p_1 + p_6 + 2p_7 + p_{11} + p_{16} + p_{17} + p_{22} + 2p_{24} + 2p_{26}$
15	(1, 4, 2)	$p_1 + p_8 + 2p_9 + p_{13} + p_{18} + p_{19} + p_{20} + 2p_{23} + 2p_{25}$
16	(1, 5, 1)	$p_1 + p_8 + 2p_9 + 2p_{13} + p_{19} + p_{20} + 2p_{23} + 2p_{25}$
17	(2, 1, 0)	$2p_3 + p_8 + p_{20} + p_{22} + 2p_{23} + 2p_{25} + 2p_{26}$
18	(2, 1, 3)	$p_2 + p_3 + p_9 + 2p_{18} + p_{19} + p_{20} + 2p_{23} + 2p_{25}$
19	(2, 2, 2)	$p_2 + p_3 + p_9 + p_{13} + p_{18} + p_{19} + p_{20} + 2p_{23} + 2p_{25}$
20	(2, 3, 1)	$p_2 + p_3 + p_9 + 2p_{13} + p_{19} + p_{20} + 2p_{23} + 2p_{25}$

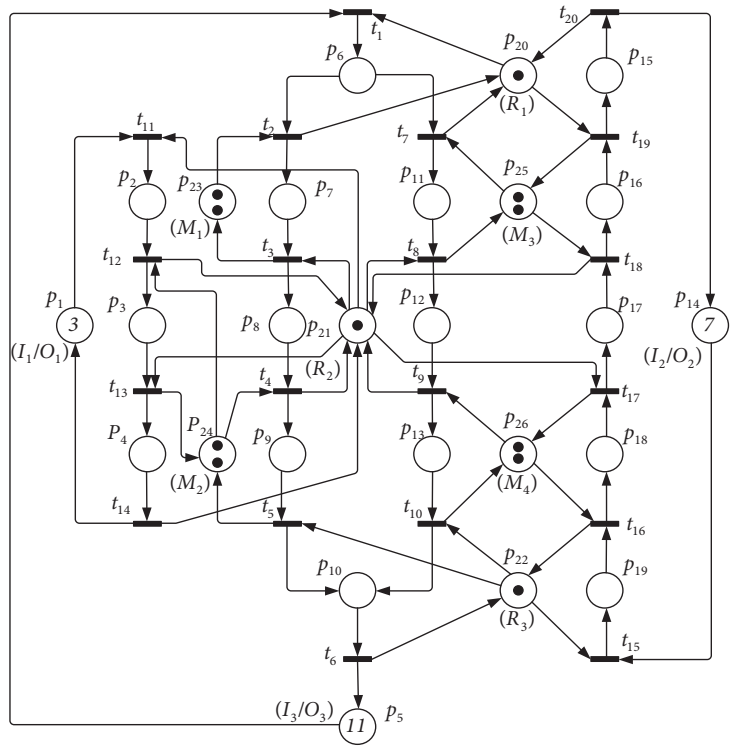

Figure 8: One classical complex S^3PR system [1].

26750 reachable markings and 120 dead markings when its idle places are in saturation. Therefore, we want to show that our control policy can not only recover all 120 dead markings of the complex PNM but reserve all original 26750 reachable markings.

According to our deadlock prevention policy, the optimal number of tokens in each idle place are $M_0(p_1) = 3$, $M_0(p_5) = 11$ and $M_0(p_{14}) = 7$ in this PNM. And 20 crucial dead markings in total are identified and are shown in Table 6. Please notice that the original dead markings are

Table 7: The 20 crucial control transitions of Figure 8.

No.	In formation of Crucial control Transitions
1	$O(t_{c21}) = (3p_1 + p_{21} + 2p_{24})$ $I(t_{c21}) = (p_2 + 2p_3)$
2	$O(t_{c22}) = (p_5 + 2p_{14} + p_{21} + 2p_{26})$ $I(t_{c22}) = (p_{12} + 2p_{18})$
3	$O(t_{c23}) = (2p_5 + p_{14} + p_{21} + 2p_{25})$ $I(t_{c23}) = (2p_{11} + p_{17})$
4	$O(t_{c24}) = (2p_5 + 2p_{14} + p_{21} + p_{22} + 2p_{26})$ $I(t_{c24}) = (p_{12} + p_{13} + p_{18} + p_{19})$
5	$O(t_{c25}) = (p_1 + 2p_5 + 3p_{14} + p_{21} + p_{22} + 2p_{24} + 2p_{26})$ $I(t_{c25}) = (p_2 + 2p_9 + 2p_{18} + p_{19})$
6	$O(t_{c26}) = (p_1 + 2p_5 + 3p_{14} + p_{21} + p_{22} + 2p_{24} + 2p_{26})$ $I(t_{c26}) = (p_3 + p_8 + p_9 + 2p_{18} + p_{19})$
7	$O(t_{c27}) = (3p_5 + p_{14} + p_{21} + p_{22} + 2p_{26})$ $I(t_{c27}) = (p_{12} + 2p_{13} + p_{19})$
8	$O(t_{c28}) = (p_1 + 3p_5 + 2p_{14} + p_{21} + p_{22} + 2p_{24} + 2p_{26})$ $I(t_{c28}) = (p_2 + 2p_9 + p_{13} + p_{18} + p_{19})$
9	$O(t_{c29}) = (p_1 + 3p_5 + 2p_{14} + p_{21} + p_{22} + 2p_{24} + 2p_{26})$ $I(t_{c29}) = (p_3 + p_8 + p_9 + p_{13} + p_{18} + p_{19})$
10	$O(t_{c30}) = (3p_5 + 3p_{14} + p_{20} + p_{21} + 2p_{23} + 2p_{25})$ $I(t_{c30}) = (p_6 + 2p_7 + 2p_{16} + p_{17})$
11	$O(t_{c31}) = (3p_5 + 3p_{14} + p_{21} + p_{22} + 2p_{24} + 2p_{26})$ $I(t_{c31}) = (p_8 + 2p_9 + 2p_{18} + p_{19})$
12	$O(t_{c32}) = (p_1 + 4p_5 + p_{14} + p_{21} + p_{22} + 2p_{24} + 2p_{26})$ $I(t_{c32}) = (p_3 + p_8 + p_9 + 2p_{13} + p_{19})$
13	$O(t_{c33}) = (p_1 + 4p_5 + p_{14} + p_{21} + p_{22} + 2p_{24} + 2p_{26})$ $I(t_{c33}) = (p_2 + 2p_9 + 2p_{13} + p_{19})$
14	$O(t_{c34}) = (4p_5 + 2p_{14} + p_{20} + p_{21} + 2p_{23} + 2p_{25})$ $I(t_{c34}) = (p_6 + 2p_7 + p_{11} + p_{16} + p_{17})$
15	$O(t_{c35}) = (4p_5 + 2p_{14} + p_{21} + p_{22} + 2p_{24} + 2p_{26})$ $I(t_{c35}) = (p_8 + 2p_9 + p_{13} + p_{18} + p_{19})$
16	$O(t_{c36}) = (5p_5 + p_{14} + p_{21} + p_{22} + 2p_{24} + 2p_{26})$ $I(t_{c36}) = (p_8 + 2p_9 + 2p_{13} + p_{19})$
17	$O(t_{c37}) = (2p_1 + p_5 + p_{21} + 2p_{24})$ $I(t_{c37}) = (2p_3 + p_8)$
18	$O(t_{c38}) = (2p_1 + p_5 + 3p_{14} + p_{21} + p_{22} + 2p_{24} + 2p_{26})$ $I(t_{c38}) = (p_2 + p_3 + p_9 + 2p_{18} + p_{19})$
19	$O(t_{c39}) = (2p_1 + 2p_5 + 2p_{14} + p_{21} + p_{22} + 2p_{24} + 2p_{26})$ $I(t_{c39}) = (p_2 + p_3 + p_9 + p_{13} + p_{18} + p_{19})$
20	$O(t_{c40}) = (2p_1 + 3p_5 + p_{14} + p_{21} + p_{22} + 2p_{24} + 2p_{26})$ $I(t_{c40}) = (p_2 + p_3 + p_9 + 2p_{13} + p_{19})$

120. In our deadlock prevention policy, we can identify the 20 deadlock markings and use them to calculate and obtain 20 controllers.

First of all, please refer to Table 6; the first crucial dead marking (i.e., $p_2 + 2p_3 + p_{20} + p_{22} + 2p_{23} + 2p_{25} + 2p_{26}$) is identified when the three idle places are in $M_0(p_1) = 3$, $M_0(p_5) = 0$, and $M_0(p_{14}) = 0$, respectively. And then, its relative controller ($I(t_{c21}) = p_2 + 2p_3$ and $O(t_{c21}) = 3p_1 + p_{21} + 2p_{24}$) can be calculated and obtained (i.e., the first set in Table 7). Eight dependent dead markings (M_1, M_2, M_{45}, M_{55}, M_{66}, M_{80}, M_{93}, and M_{105} are checked in saturated situation based on TINA) also become live simultaneously (please refer to No. 1 in Table 8). Please notice that all markings presented in Table 9 are identified initially by the famous software TINA. Due to the space limitation of this paper, we just show the marking number in Table 8. For further detailed information, please refer to all data by using TINA. Anyway, 120 dead markings will reduce to 112. Surely, the total number of all reachable markings still is 26750. Keep doing the same process and step by step, 112 dead markings eventually become live. In sum, our deadlock prevention policy based on control transition live all reachable markings.

4.3. Comparison with Existing Researches. In this subsection, we make some comparisons with existing literature based on the classical complex PNM. Please note that the "No. C_P" represents the number of control places, "No. C_T" represents the number of control transitions, "No. R_L" represents the number of live reachable markings, and "% R" represents the recover percent relative to original 26750 markings. From Table 9, it is obvious that our algorithm is the only algorithm which can achieve 100 % maximally permissive markings among all published researches.

5. Conclusions

In this paper, we successfully propose one novel iterative method to obtain maximally permissive states based on control transitions. Generally, "maximal permissive" means the number of legal markings in an original deadlock PNM. Further, it does not include the initial illegal markings. For example, they just can obtain 21581 maximally permissive markings in the second example of Section 4. However, our proposed algorithm does obtain the real 26750 maximally permissive markings. In other words, our deadlock prevention recovers one deadlock PNM. In our approach, we do not consider any controllability of siphons. We just focus on crucial dead markings. All markings are live and reachable once these crucial markings are controlled. Our approach is now suitable to all S^3PR model. The future work is to reduce the computing time (i.e., reduce running the number of reachability graph or reduce the number of controllers) and extends the method applying for more general models in Petri net.

Data Availability

The data used to support the findings of this study are included within the supplementary information file(s).

Conflicts of Interest

The authors declare that they have no conflicts of interest.

Table 8: The 20 dependent dead markings checked in saturated situation based on TINA of Table 6.

No.	Dependent Deadlock Markings	The Number of Deadlock Markings After Relative controllers are added into PNM
1	$M_1, M_2, M_{45}, M_{55}, M_{66}, M_{80}, M_{93}, M_{105}$	112
2	$M_6, M_7, M_{14}, M_{15}, M_{21}, M_{22}, M_{31}, M_{32}, M_{33}, M_{34}, M_{78}, M_{79}$	100
3	$M_{24}, M_{26}, M_{27}, M_{28}, M_{29}, M_{30}, M_{47}, M_{48}, M_{51}, M_{52}, M_{53}, M_{58}$	88
4	$M_{42}, M_{43}, M_{50}, M_{54}, M_{56}, M_{57}, M_{60}, M_{92}, M_{117}, M_{118}, M_{119}, M_{120}$	76
5	M_{17}, M_{23}, M_{73}	73
6	M_{12}, M_{13}, M_{71}	70
7	$M_{96}, M_{99}, M_{100}, M_{101}, M_{102}, M_{104}, M_{108}, M_{111}, M_{112}, M_{113}, M_{114}, M_{116}$	58
8	M_{38}, M_{44}, M_{87}	55
9	M_{49}, M_{65}, M_{85}	52
10	$M_{67}, M_{69}, M_{70}, M_{72}, M_{74}, M_{76}, M_{81}, M_{83}, M_{84}, M_{86}, M_{88}, M_{90}$	40
11	M_{19}, M_{20}, M_{75}	37
12	M_{95}, M_{107}	35
13	M_{97}, M_{109}	33
14	$M_3, M_8, M_{10}, M_{11}, M_{16}, M_{18}, M_{36}, M_{37}, M_{39}, M_{61}, M_{63}, M_{64}$	21
15	M_{40}, M_{41}, M_{89}	18
16	M_{98}, M_{110}	16
17	$M_4, M_5, M_{59}, M_{62}, M_{77}, M_{91}, M_{103}, M_{115}$	8
18	M_9, M_{25}, M_{68}	5
19	M_{35}, M_{46}, M_{82}	2
20	M_{94}, M_{106}	0

Table 9: Comparison with existing literature.

	Ezpeleta et al. (1995) [1]	Huang et al (2001) [3]	Li & Zhou (2004) [5]	Uzam & Zhou (2006) [34]	Chao (2009b) [26]	Piroddi et al. (2008) [10]	Chen et al (2011) [27]	Chen et al (2012) [28]	Hong et al. (2015) [29]	Row et al. [This paper]
No. C_P	18	16	5	19	7	13	17	6	9	0
No. C_T	0	0	0	0	0	0	0	0	0	20
No.R_L	6287	12656	15999	21562	21585	21581	21581	21581	20444	26750
% R	23.5%	47.3%	59.8%	80.6%	80.7%	80.7%	80.7%	80.7%	94.7%	100%

Supplementary Materials

The detailed information of all 120 deadlocks of Figure 8 based on the famous software TINA [31]. *(Supplementary Materials)*

References

[1] J. Ezpeleta, J. M. Colom, and J. Martinez, "A petri net based deadlock prevention policy for flexible manufacturing systems," *IEEE Transactions on Robotics and Automation*, vol. 11, no. 2, pp. 173–184, 1995.

[2] G. Liu, Z. Li, and C. Zhong, "New controllability condition for siphons in a class of generalised Petri nets," *IET Control Theory & Applications*, vol. 4, no. 5, pp. 854–864, 2010.

[3] Y. Huang, M. Jeng, X. Xie, and S. Chung, "Deadlock prevention policy based on Petri nets and siphons," *International Journal of Production Research*, vol. 39, no. 2, pp. 283–305, 2001.

[4] Y. S. Huang, M. D. Jeng, X. L. Xie, and T. H. Chung, "Siphon-based deadlock prevention policy for flexible manufacturing systems," *IEEE Transactions on Systems, Man and Cybernetics, Part A, Systems and Humans*, vol. 36, no. 6, pp. 2152–2160, 2006.

[5] Z. W. Li and M. C. Zhou, "Elementary siphons of Petri nets and their application to deadlock prevention in flexible manufacturing systems," *IEEE Transactions on Systems, Man, Cybernetics A, Humans*, vol. 34, no. 1, pp. 38–51, 2004.

[6] Z. Li and M. Zhou, "Clarifications on the definitions of elementary siphons in Petri nets," *IEEE Transactions on Systems, Man, and Cybernetics: Systems and Humans*, vol. 36, no. 6, pp. 1227–1229, 2006.

[7] H. Liu, K. Xing, W. Wu, M. C. Zhou, and H. Zou, "Deadlock Prevention for Flexible Manufacturing Systems via Controllable Siphon Basis of Petri Nets," *IEEE Transactions on Systems, Man and Cybernetics*, vol. 45, no. 3, pp. 519–529, 2015.

[8] M. Uzam, "An optimal deadlock prevention policy for flexible manufacturing systems using petri net models with resources and the theory of region," *International Journal of Advanced Manufacturing Technology*, vol. 19, no. 3, pp. 192–208, 2002.

[9] M. Uzam and M. Zhou, "An iterative synthesis approach to Petri net-based deadlock prevention policy for flexible manufacturing systems," *IEEE Transactions on Systems, Man, and Cybernetics: Systems*, vol. 37, no. 3, pp. 362–371, 2007.

[10] L. Piroddi, R. Cordone, and I. Fumagalli, "Selective siphon control for deadlock prevention in Petri nets," *IEEE Transactions on Systems, Man, and Cybernetics: Systems*, vol. 38, no. 6, pp. 1337–1348, 2008.

[11] Y.-L. Pan, Y.-S. Huang, M. Jeng, and S.-L. Chung, "Enhancement of an efficient control policy for FMSs using the theory of regions and selective siphon method," *The International Journal of Advanced Manufacturing Technology*, vol. 66, no. 9-12, pp. 1805–1815, 2013.

[12] K. Barkaoui and I. B. Abdallah, "Deadlock prevention method for a class of FMS," in *Proceedings of the International Conference on Systems, Man and Cybernetics. Intelligent Systems for the 21st Century*, vol. 5, pp. 4119–4124, IEEE, October 1995.

[13] Y. Huang, Y. Pan, and P. Su, "Transition-based deadlock detection and recovery policy for FMSs using graph technique," *ACM Transactions on Embedded Computing Systems*, vol. 12, no. 1, pp. 1–13, 2013.

[14] Y. Hou and K. Barkaoui, "Deadlock analysis and control based on petri nets: a siphon approach review," *Advances in Mechanical Engineering*, vol. 9, no. 5, pp. 1–30, 2017.

[15] G. Liu and K. Barkaoui, "A survey of siphons in Petri nets," *Information Sciences*, vol. 363, pp. 198–220, 2016.

[16] H. Yi-Sheng and P. Yen-Liang, "Enhancement of an efficient liveness-enforcing supervisor for flexible manufacture systems," *The International Journal of Advanced Manufacturing Technology*, vol. 48, pp. 725–737, 2010.

[17] Y.-S. Huang and Y.-L. Pan, "An improved maximally permissive deadlock prevention policy based on the theory of regions and reduction approach," *IET Control Theory & Applications*, vol. 5, no. 9, pp. 1069–1078, 2011.

[18] Y.-S. Huang, Y.-L. Pan, and M. Zhou, "Computationally improved optimal deadlock control policy for flexible manufacturing systems," *IEEE Transactions on Systems, Man, and Cybernetics: Systems*, vol. 42, no. 2, pp. 404–415, 2012.

[19] Y.-L. Pan, C.-F. Yang, and M.-D. Jeng, "Enhancement of selective siphon control method for deadlock prevention in FMSs," *Mathematical Problems in Engineering*, vol. 2015, Article ID 196514, 6 pages, 2015.

[20] Y.-L. Pan, Y.-S. Huang, Y.-S. Weng, W. Wu, and M. Jeng, "Computationally improved optimal control methodology for linear programming problems of flexible manufacturing systems," *Journal of Applied Mathematics*, vol. 2013, Article ID 294835, 11 pages, 2013.

[21] D. Y. Chao and Y. Pan, "Uniform formulas for compound siphons, complementary siphons and characteristic vectors in deadlock prevention of flexible manufacturing systems," *Journal of Intelligent Manufacturing*, vol. 26, no. 1, pp. 13–23, 2015.

[22] T.-C. Row and Y.-L. Pan, "Maximally permissive deadlock prevention policies for flexible manufacturing systems using control transition," *Advances in Mechanical Engineering*, vol. 10, no. 7, pp. 1–10, 2018.

[23] X. Zhang and M. Uzam, "Transition-based deadlock control policy using reachability graph for flexible manufacturing systems," *Advances in Mechanical Engineering*, vol. 8, no. 2, pp. 1–9, 2016.

[24] Y. Chen, Z. Li, A. Al-Ahmari, N. Wu, and T. Qu, "Deadlock recovery for flexible manufacturing systems modeled with Petri nets," *Information Sciences*, vol. 381, pp. 290–303, 2017.

[25] Y. Pan, C. Tseng, and T. Row, "Design of improved optimal and suboptimal deadlock prevention for flexible manufacturing systems based on place invariant and reachability graph analysis methods," *Journal of Algorithms & Computational Technology*, vol. 11, no. 3, pp. 261–270, 2017.

[26] D. Y. Chao, "Reaching more states for control of FMS," *International Journal of Production Research*, vol. 48, no. 4, pp. 1217–1220, 2009.

[27] Y. F. Chen and Z. W. Li, "Design of a maximally permissive liveness-enforcing supervisor with compressed supervisory structure for flexible manufacturing systems," *Automatica*, vol. 47, no. 5, pp. 1028–1034, 2011.

[28] Y. F. Chen, Z. W. Li, and M. C. Zhou, "Behaviorally optimal and structurally simple liveness-enforcing supervisors of flexible manufacturing systems," *IEEE Trans. System, Man, Cybernetics A*, vol. 42, no. 3, pp. 615–629, 2012.

[29] L. Hong, Y. Hou, J. F. Jing et al., "Deadlock prevention policy with behavioral optimality or suboptimality achieved by the redundancy identification of constraints and the rearrangement of monitors," *Discrete Dynamics in Nature and Society*, vol. 2015, Article ID 579623, 15 pages, 2015.

[30] S. Wang, W. Wu, and J. Yang, "Deadlock prevention policy for a class of petri nets based on complementary places and elementary siphons," *Journal of Intelligent Manufacturing*, vol. 26, no. 2, pp. 321–330, 2015.

[31] F. Wang, K. Xing, X. Xu, and L. Han, "Research on finding elementary siphon in a class of petri nets," *Springer, Communications and Information Processing*, vol. 289, no. 2, pp. 435–442, 2012 (Arabic).

[32] M. H. Abdul-Hussin, "Elementary siphons of petri nets and deadlock control in FMS," *Journal of Computer and Communications*, vol. 3, no. 7, pp. 1–12, 2015.

[33] Y. F. Chen, Z. W. Li, K. Barkaoui, and M. Uzam, "New petri net structure and its application to optimal supervisory control: interval inhibitor arcs," *IEEE Transactions on Systems, Man, and Cybernetics: Systems*, vol. 44, no. 10, pp. 1384–1400, 2014.

[34] M. Uzam and M. C. Zhou, "An improved iterative synthesis method for liveness enforcing supervisors of flexible manufacturing systems," *International Journal of Production Research*, vol. 44, no. 10, pp. 1987–2030, 2006.

[35] T. Murata, "Petri nets: properties, analysis and application," *Pro. IEEE*, vol. 77, no. 4, pp. 541–580, 1989.

[36] Z. W. Li, H. M. Hanish, and M. C. Zhou, "Deadlock prevention based on structure reuse of petri net supervisors for flexible manufacturing systems," *Systems, Man and Cybernetics, part A: System and Humans, IEEE Transactions*, vol. 42, no. 1, 2012.

[37] S. Wang, C. Wang, M. Zhou, M. Zhou, Z. Li, and Z. Li, "A method to compute strict minimal siphons in a class of petri nets based on loop resource subsets," *IEEE Transactions on Systems, Man, and Cybernetics: Systems and Humans*, vol. 42, no. 1, pp. 226–237, 2012.

[38] H. Liu, K. Xing, W. M. Wu, M. C. Zhou, and H. L. Zou, "Deadlock prevention for flexible manufacturing systems via controllable siphon basis of petri nets," *IEEE Transactions on Systems, Man, and Cybernetics: Systems*, vol. 45, no. 3, pp. 519–529, 2015.

[39] Z. Li and M. Zhou, "On siphon computation for deadlock control in a class of Petri nets," *IEEE Transactions on Systems, Man, and Cybernetics: Systems*, vol. 38, no. 3, pp. 667–679, 2008.

[40] R. David and H. Alla, *Discrete, Continuous and Hybrid PetriNets*, Springer-Verlag, Berlin, Germany, 2nd edition, 2005.

[41] T. Murata, "State equation, controllability, and maximal matchings of petri net," *IEEE Transactions on Automatic Control*, vol. 22, no. 3, pp. 412–416, 1977.

[42] M. A. Marsan, G. Balbo, G. Conte, S. Donatelli, and G. Franceschinis, *Modeling with Generalized Stochastic Petri Nets*, John Wiley and Sons Press, 1st edition, 1995.

[43] "TINA (Time petri Net Analyzer) has been developed in the OLC then VerTICS, research groups of LAAS/CNRS," http://projects.laas.fr/tina//download.php.

Hindawi
Mathematical Problems in Engineering
Volume 2019, Article ID 6476037, 11 pages
https://doi.org/10.1155/2019/6476037

Research Article

Anti-Defect Design for Mechanical Elements under Severe Condition Based on a Half-Real Defect Model

Xinyue Zhao, Hongyuan Wang, Jiaomei Yin, and Zaixing He

State Key Lab of Fluid Power and Mechatronic Systems, School of Mechanical Engineering, Zhejiang University, China

Correspondence should be addressed to Zaixing He; zaixinghe@zju.edu.cn

Received 6 November 2018; Revised 16 February 2019; Accepted 6 March 2019; Published 20 March 2019

Guest Editor: Sutasn Thipprakmas

For mechanical elements running under severe working condition, there inevitably exist some small defects caused during working. The weak area, which is sensitive to defects, of the structure is more vulnerable, resulting in early damage during service. This paper describes a novel anti-defect design method for optimizing structure to enhance the reliability of vulnerable areas. First, a half-real defect model derived from the real defect is developed to model the geometrical characteristics of defects. Then, the damage degrees of model parameters are identified by Sobol's sensitivity method and the vulnerable area can be labeled according to the damage degree. Finally, we take the vulnerable area as the object of anti-defect optimization for structure and the optimization variables are selected tendentiously based on parameters with larger damage degrees. The multiobjective particle swarm algorithm is then employed to find the optimal distribution of the variables in order to improve the safety of the sensitive area of structure. We take the impeller blade as the research subject to verify the validity of the proposed method. Analysis results showed that the proposed method can increase the structure strength and delay the damage of the mechanical elements.

1. Introduction

Structure optimization plays an important role in ensuring the reliability of mechanical equipment. Nowadays, more and more researchers have been devoted to this field. Generally, the improvement of structure involves size optimization, shape optimization, and performance optimization. Ananthasuresh [1] first extended the techniques of topological optimization for structure to the design of compliant mechanism. He proposed three models to describe the design problem of compliant mechanism. Zhu et al. [2] used a level set method with distance-suppression scheme for structural topology and shape optimization. Xia et al. [3] used a level set based method to optimize the configuration of piezoresistive sensors. Han et al. [4] investigated the flutter of a compressor blade. They analyzed the influence of clearance parameter, bending stiffness, and torsion on the flutter characteristics of the blade. Fei et al. [5] studied the radial deformation of the turbine blade. Based on ERSM and IDM methods, they proposed an approach and a model for the dynamic reliability optimal design of complex motorial structure and dynamic systems. Staino and Basu [6] proposed a multimodal mathematical model with variable rotor speed for wind turbine blades and studied the impact of blade rotor speed variation on the edgewise vibration. Li et al. [7] studied the flapwise dynamic response of a rotating wind turbine blade subjected to unsteady aerodynamic loads in superharmonic resonance. They used a multiple-scale method to get analytical solutions for positive aerodynamic dampings having the same order with dynamic displacements. Hong et al. [8] studied the optimal design of engine cylinder head by the topology optimization, which would be helpful to structure design.

In recent years, the intelligent optimization algorithm has become a new hot subject for the improvement of structure. Islam et al. [9] presented a numerical optimization framework based on coupled Genetic Algorithm and Finite Element Analysis for optimizing the arc welding process. Liu et al. [10] used a microgenetic algorithm to calculate the optimal solution of variables for improving the efficiency of the mixed-flow pump. Song et al. [11] used intelligent CAD and Finite Element Analysis to design turbine blade fir-tree root. They examined the effects of critical geometric features on stress distribution at the interface between the blade and

disk. Chen et al. [12] developed a procedure combining Finite Element Analysis and particle swarm algorithm to optimize composite structures of the wind turbine blades.

Most of the above optimization methods are built on nondamage mechanical elements. For mechanical elements running under the circumstance of heavy loads, corrosion, and other bad factors, there inevitably exist small defects due to the severe working condition. Different structures have their own weak areas. Once the defects grow in these areas, damage will be caused immediately, which may result in serious accidents [13, 14] . Without considering defects, these methods could not improve structure through targeted optimization.

To overcome this problem, in this paper, a novel anti-defect optimization method based on a half-real defect model and Sobol's sensitivity is proposed to enhance structure for defect resisting. First a parameterized model for defects based on the image is introduced to identify the essential features of the real defects. With this model, the damage state of the structure is simulated by changing the model parameters. Then based on Sobol's sensitivity, the weak area which is sensitive to defects is found according to the influence levels of model parameters. Finally the structure can be improved by optimizing the defect-sensitive area with the SVM (Support Vector Machine) [15] and the PSO (particle swarm optimization) methods [16]. SVM is a kind of supervised learning model used for classification and regression analysis. In our approach, the final prediction model of optimization variables and optimization goal are formed based on SVM. PSO is a computational method that optimizes a problem by iteratively trying to improve a candidate solution with regard to a given measure of quality. The PSO method is adopted finally to determine the optimal solution set.

The contributions of the paper are summarized as follows.

(1) A Half-Real Defect Model Is Built to Improve the Strength of Mechanical Elements. So far, most of the studies focus on the nondamage structure optimization. They ignore the influence of defects. Even if a few of them consider defects, they only simplify the defect to an ellipse or a line, which may lose some effective information and could not describe the real situation [17, 18]. On the other hand, it is not feasible to express all properties of the real defect. From this point, in this paper, we proposed a half-real defect model based on the real defect shape information to simulate the injured components.

(2) Sobol's Sensitive Method Is Adopted to Avoid the Blindness of Choosing Optimization Variables. The traditional optimization variables are usually defined according to all the related structural parameters. In this paper, based on Sobol's sensitive method, the vulnerable area of the structure is determined based on the damage degree of the model parameters. The defect-sensitive parameters are chosen as optimization variables selectively. This process can simplify the optimization parameters, making it more specific and more targeted.

This paper is organized as follows. In Section 2, a half-real defect model is developed. In Section 3, Sobol's sensitivity method is adopted based on the model and the PSO optimization method is introduced. In Section 4, an example with the impeller blade is discussed in detail. Finally, conclusions are summarized in Section 5.

2. The Half-Real Defect Model

Most of the defect models simplify the crack to the ellipse or the line shapes, which may lose some effective information and could not describe the real situation. But on the other hand, the geometric characteristics of the real defects in the components are really complicated. Most cracks have highly irregular shapes and very small sizes. Thus, it is not feasible to express all properties of the real defect. Since it is difficult to build the real defect model, a half-real defect model based on the shape information of the crack is proposed in this paper.

2.1. Real Defect Extraction. The real geometric shape of the defect can be obtained completely using the image processing methods [19–21] . It is proved that the image processing methods have the advantage of convenience and accuracy in the research of obtaining geometric features of defects.

The crack is the most common defect of the mechanical components. A typical crack usually involves the crack length, the crack width, the crack depth, and the crack propagation. Therefore, the selected crack image which is used for building the defect model should have these typical representative characteristics.

In this paper, the typical crack image which is shown in Figure 1(a) is used. There are three segments of the crack, and we picked the rightmost one which has the obvious shape characteristic and its curve is relatively clear. Since a parameterized step will be adopted later, the differences of crack images do not influence the final modeling greatly.

To extract the real defect, the original image is first converted to the binary one by suitable threshold (Figure 1(b)). Since the binary operation can produce cavities and noises, morphological processing methods are processed to make the defect more compact and reduce small noises in the background (Figure 1(c)). Then, the cleaning processing is applied to remove the regions of no-interests (Figure 1(d)). Finally, the crack boundary (Figure 1(e)) and the crack skeleton (Figure 1(f)) are acquired.

2.2. Parameterization of the Defect Model. The extracted real defects are parameterized which can express the geometrical characteristic of the defects well and are more universal in some respects. This process contains two aspects: the model simplification and the model parameterization.

2.2.1. Model Simplification. To parameterize the model, we have to simplify the extracted defects at first. Crack edges are not straight and are usually shown as irregular lines. For this reason, a geometrical approximation is required to find the bending shape of the crack. This is done by subdividing the crack edge into a number of straight segments defined by the gradient of the crack skeleton points. The detailed steps are as follows.

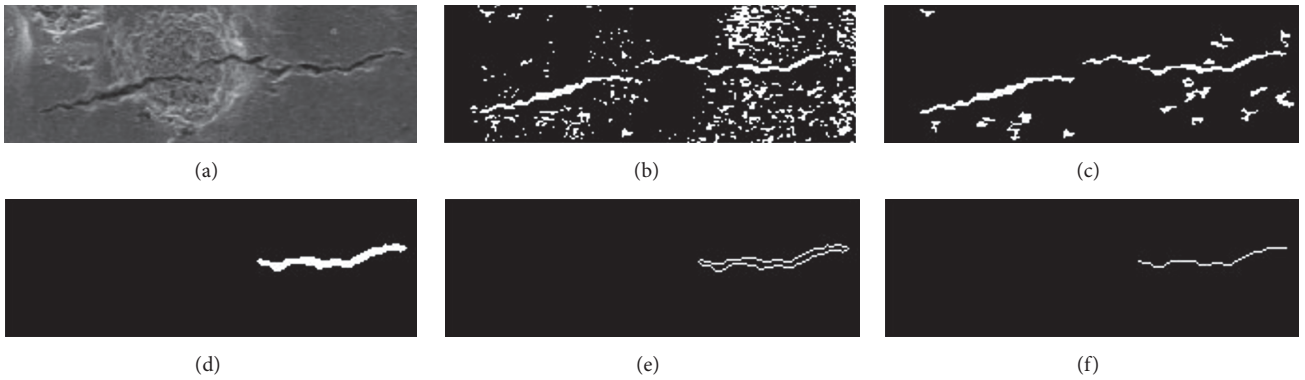

Figure 1: Real defect extraction. (a) Original image, (b) binary-conversion, (c) morphological processing, (d) cleaning processing, (e) edge obtaining, and (f) skeleton obtaining.

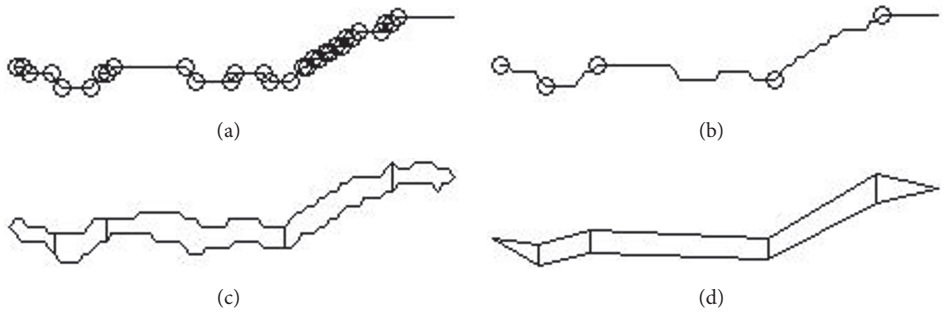

Figure 2: Defect model simplification. (a) Skeleton turning points, (b) subdivision points, (c) crack subdivision, and (d) crack linearization.

(a) It is assumed that i refers to the x coordinate of crack skeleton and $f(i)$ represents the y coordinate of it. Additionally, $f'(i) = \nabla f(i)$ presents the gradient of skeleton line and the large gradient stands for the segmentation of cracks. A threshold α is then defined. If the condition $f'(i) \geq \alpha$ is satisfied, the pixel i is counted as the turning point. Compute the gradient of each pixel in the skeleton line and store them in the set of $\psi(i)$. The skeleton turning points $\psi(i)$ are picked in terms of the slope changes of adjacent points. The results of the skeleton turning points are shown in Figure 2(a).

(b) Remove close skeleton turning points which satisfy the condition $\rho(\psi(i), \psi(j)) = \sqrt{(\psi_x(i) - \psi_x(j))^2 + (\psi_y(i) - \psi_y(j))^2} < \beta$ (ψ_x and ψ_y define coordinates of the pixels) to avoid unnecessary segmentations and screen out the proper ones (shown in Figure 2(b)).

(c) Take the screened skeleton turning points to divide the crack edge into several segments. It can be seen that the crack edge is divided into several connected crack segments in Figure 2(c). Each endpoint of segment is stored in the set of $\chi(i)$ and is called the boundary turning point.

(d) Since the boundaries of crack segments are irregular, it is necessary to build a simplified crack pattern approximating the original crack segment by straight lines. For each segment of the crack, connect boundary turning points $\chi(i)$ into straight lines and the edge of the original image can be changed into a series of line segment lists (shown in Figure 2(d)).

The overall simplified crack is presented as segments created by a set of straight lines forming a trapezoid space. It is easy to be parameterized to quantize the overall crack.

2.2.2. Model Parameterization. The damages of components are usually determined by the setting of defect positions and shapes. The changes of defect sizes, shapes, and positions can result in different weakening effects. Moreover, the damage degrees are different with different geometrical parameters. Thus, parameterization is applied for the future sensitive analysis.

For the tortuous crack, each crack segment is labeled by defined parameters, such as width, length, and orientation. Assume there are k ($k = 1, 2, \ldots, K$) boundary turning points stored in the vector of $\zeta(k) = (\zeta_x, \zeta_y)$ from small to large order of $\chi(k)$.

The parameters of the defect model include geometric parameters and position parameters, which are defined as follows.

(X, Y): the position (X, Y) is defined as the initial position of the crack tip, which is denoted as

$$X = \zeta_x(1) \tag{1}$$

$$Y = \zeta_y(1) \tag{2}$$

L: the length L is the average length of each crack segment n in the middle line, which is denoted as

$$L = \frac{2\sum_{n=1}^{K/2} L_n}{K} \tag{3}$$

where

$$L_n = \begin{cases} \dfrac{\sqrt{4\left(\zeta_x(2)-\zeta_x(1)\right)^2+\left(\zeta_y(3)+\zeta_y(2)-2\zeta_y(1)\right)^2}}{2} & n=1 \\ \dfrac{\sqrt{4\left(\zeta_x(K)-\zeta_x(K-1)\right)^2+\left(2\zeta_y(K)-\zeta_y(K-1)-\zeta_y(K-2)\right)^2}}{2} & n=\dfrac{K}{2} \\ \dfrac{\sqrt{4\left(\zeta_x(2n)-\zeta_x(2n-2)\right)^2+\left(\zeta_y(2n)+\zeta_y(2n+1)-\zeta_y(2n-1)-\zeta_y(2n-2)\right)^2}}{2} & others \end{cases} \tag{4}$$

W: the width W is the average width of each crack segment n in the vertical projection. Although the width of the actual crack groove may be more accurate, for the easy calculation, we choose the vertical coordinate difference, which does not have significant effect on the final result. W is denoted as

$$W = \frac{2\sum_{n=1}^{K/2-1}\left(\zeta_y(2n+1)-\zeta_y(2n)\right)}{K-2} \tag{5}$$

A: the angle A is defined as the average angle of connecting adjacent segments

$$A = \frac{2\sum_{n=1}^{K/2-1} A_n}{K-2} \tag{6}$$

where

$$\cos A_n = \begin{cases} \dfrac{4L_2^2+4L_1^2-4\left(\zeta_x(4)-\zeta_x(1)\right)^2-\left(\zeta_y(5)+\zeta_y(4)-2\zeta_y(1)\right)^2}{8L_2L_1} & n=1 \\ \dfrac{4L_{K/2}^2+4L_{K/2-1}^2-4\left(\zeta_x(K)-\zeta_x(K-3)\right)^2-\left(2\zeta_y(K)-\zeta_y(K-3)-\zeta_y(K-4)\right)^2}{8L_{K/2}L_{K/2-1}} & n=\dfrac{K}{2} \\ \dfrac{4L_n^2+4L_{n-1}^2-4\left(\zeta_x(2n+2)-\zeta_x(2n-2)\right)^2-\left(\zeta_y(2n+3)+\zeta_y(2n+2)-\zeta_y(2n-1)-\zeta_y(2n-2)\right)^2}{8L_nL_{n-1}} & others \end{cases} \tag{7}$$

D: the depth D of the crack is simplified to constant in order to exclude its impact on the structure based on the shape assumption [17, 22]. It is defined as

$$D = C \quad (C > 0) \tag{8}$$

in which C is a constant greater than 0 and smaller than the thickness of the blade.

3. Defect Model Sensitivity Analysis Optimization

The appearances of defects are random, and the lifecycles of different areas of the structure with defects are different. By discussing the parameters of the defect model, we can use the Sobol-based sensitivity analysis method to find the easily damaged area. Then in the next step, an optimization method can be adopted to strengthen this area to reduce the damage probability.

3.1. Sensitivity Selection Based on Sobol's Method. Parameters of the defect model have close relationship with structure damages. Since the crack may cause uneven stress distribution and concentrated stress, resulting in fracturing, we take the max equivalent stress as the evaluating indicator for sensitivity analysis. According to the geometric relations between crack and structure, the vulnerable area can be selected.

Figure 3 shows distributions of the equivalent stress in different conditions of the impeller blade. The impeller is constrained by the cylindrical coordinate in the axle hole with the inertial load of rotational angular velocity. It is shown in Figure 3 that the stress change is related to the crack location. Figure 3(a) indicates the stress distribution without crack, in which the value of maximum equivalent stress is 253.18MPa, and Figure 3(b) shows the stress distribution with crack in the nonfragile location, which shows that the maximum equivalent stress may not change a lot when the crack is not at the sensitive place. Figure 3(c) indicates that the maximum equivalent stress increases sharply to 414.15MPa when the crack is in the fragile location. It is shown that distributions of the equivalent stress change when the crack

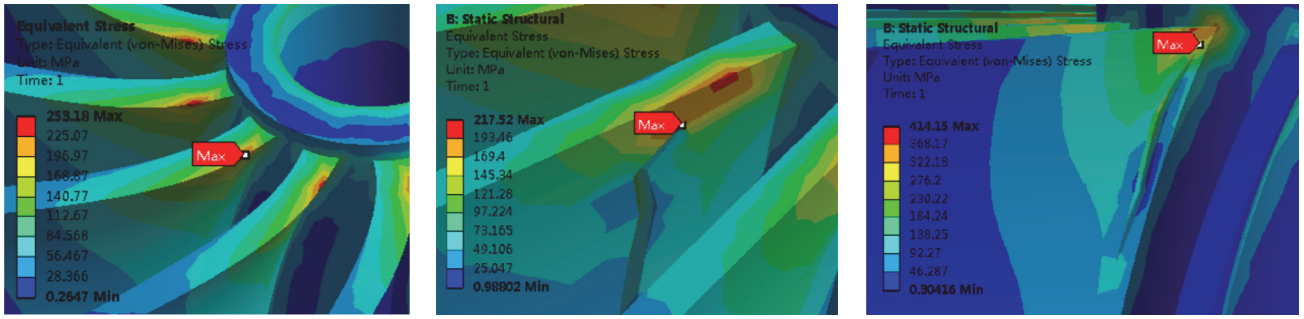

(a) (b) (c)

FIGURE 3: Stress distributions of the impeller blade. (a) Stress distribution without crack, (b) stress distribution with crack in the nonfragile location, and (c) stress distribution with crack in the fragile location (near the root of the impeller).

locations change. Thus, some areas may be vulnerable to the crack and the optimization of these areas is important for ensuring the safety of the component structure.

Sobol's method is a variance-based global sensitivity analysis technique that has been applied to computational models to assess the relative importance of input parameters on the output [23]. The usual Sobol sensitivity indices include the main and total effects for each input, but the method can also provide specific interaction terms, if desired. Based on Sobol's method, steps to obtain the parameter sensitivities of the half-real defect model are in the following.

(1) Sample defect model parameters twice independently with the sampling number n and make strength analysis. Denote output stress values as $f(x_1,x_2,x_3,x_4,x_5,x_6)$, $f(x_1, x_2', x_3', x_4', x_5', x_6')$, $f(x_1', x_2, x_3, x_4, x_5, x_6)$, $f(x_1', x_2, x_3', x_4', x_5, x_6')$, $f(x_1, x_2', x_3, x_4, x_5, x_6)$, $f(x_1', x_2', x_3, x_4', x_5', x_6')$, $f(x_1, x_2, x_3', x_4, x_5, x_6)$, $f(x_1', x_2', x_3', x_4, x_5', x_6')$, $f(x_1, x_2, x_3, x_4', x_5, x_6)$, $f(x_1', x_2', x_3', x_4', x_5, x_6')$, $f(x_1', x_2', x_3', x_4', x_5', x_6)$, $f(x_1, x_2, x_3, x_4, x_5', x_6)$, $f(x_1', x_2', x_3', x_4', x_5', x_6)$, and $f(x_1, x_2, x_3, x_4, x_5, x_6')$.

x is the position parameter for the first sampling, and x' is the parameter for the second sampling. x_1, x_2, x_3, and x_4 indicate parameters L, W, D, and A for the i^{th} segment, and x_5 and x_6 indicate parameters X and Y, respectively.

(2) Put equivalent stress values of the n groups in Sobol's function so that we can get the sensitivity value for each model parameter.

$$S_i = \frac{D_i}{D} \tag{9}$$

in which

$$D \approx \frac{1}{n}\sum_{m=1}^{n} f^2(x_m) - f_0^2 \tag{10}$$

$$D_i \approx \frac{1}{n}\sum_{m=1}^{n} f\left(x_{(\sim i)m}^{(1)}, x_{im}^{(1)}\right) f\left(x_{(\sim i)m}^{(2)}, x_{im}^{(1)}\right) - f_0^2 \tag{11}$$

$$D_{\sim i} \approx \frac{1}{n}\sum_{m=1}^{n} f\left(x_{(\sim i)m}^{(1)}, x_{im}^{(1)}\right) f\left(x_{(\sim i)m}^{(1)}, x_{im}^{(2)}\right) - f_0^2 \tag{12}$$

where x_{m} indicates the sampling points in the $\mathbf{I}^6$ space, and the superscripts (1) and (2) denote the $n \times 6$ sampling array of x.

Then the first-order sensitivity of the model parameter can be determined by $S_i = D_i/D$; the total sensitivity is determined by $S_{Ti} = 1 - D_{\sim i}/D$. The S_i shows the damage degree with the influence of the single parameter i, while S_{Ti} shows the damage degree with the influence of other parameters and i.

(3) Based on the value of S_{i}, sort model parameters and pick the larger one, which will cause a larger impact on the structure damage.

According to the sensitivity results, the most sensitive area and design parameters of the structure can be chosen as the optimized object. It provides selection basis for the next step.

3.2. Local Area Optimization. Generally, the structure design requires uniform stress distribution and less structure weight. For the structure with crack, the crack area usually has concentrated stress. Therefore, the objective function is formed as

$$\min F = [f_1, f_2] \tag{13}$$

where f_1 is the max equivalent stress, and f_2 is the structure weight. These two functions are affected by many parameters, and these parameters are different for different mechanical elements. Given a specific element, according to the results of sensitivity analysis, we can select the corresponding structural parameters for optimization, and we will take the impeller blade for example in the experimental section and introduce it in detail later.

Thus, steps for local area optimization are as follows.

(1) The defect model parameters with high sensitivity are determined according to Sobol's sensitivity results.

(2) Sampling is carried out according to the variation range of the determined parameters, and the output value of each sampling point is analyzed.

(3) Based on the SVM method, the prediction model of optimization variables and optimization goal can be formed (Mech, 2015). The SVM algorithm consists of the

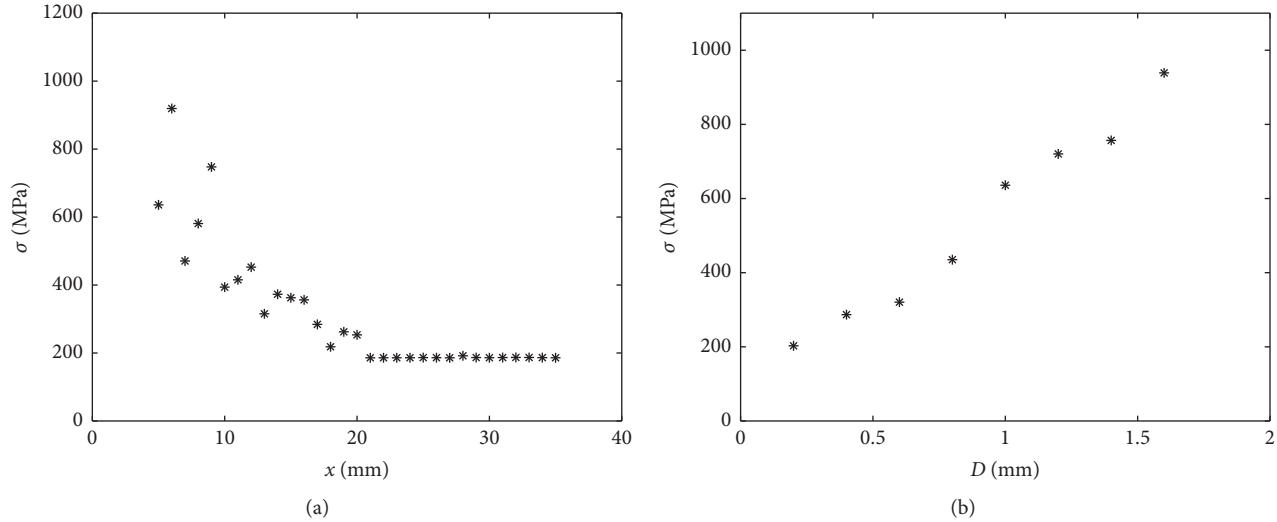

Figure 4: The relationship between parameters with large sensitivity and the maximum equivalent stress σ. (a) In the situation of X. (b) In the situation of D.

following steps. (1) The input space is transformed into a high-dimensional space by nonlinear transformation, which is realized by defining an appropriate inner product kernel function. (2) Solve convex quadratic programming problem under the condition of maximizing interval. (3) Find the optimal classification surface in the new space, which is the maximum interval classification surface.

(4) The PSO method is adopted finally to determine the optimal solution set [24] . The PSO algorithm consists of three steps: (1) Evaluate fitness of each particle and each evaluation solution is represented by a particle in the fitness landscape (search space). (2) Update individual and global best values. (3) Update velocity and position of each particle, which are based on some parameters: inertial coefficient and acceleration coefficients and individual best solution of both particle and swarm. These steps are repeated until the results of two adjacent iterations are similar.

4. Example with the Impeller Blade

4.1. Model Validation. Impeller is the main bearing part of the compressor. It stands various alternating stress and has a very bad working condition. Therefore, cracks often appear which will result in fatigue fracture of impeller and can cause damage to the people and equipment around.

Thus, in this paper, we take the impeller blade as the research subject to verify the validity of the proposed method. Since blade is thin and the probability of occurrence of deep cracks is low, we only discuss the influence of the surface crack. We choose the root of the impeller entry end as the reference point of the crack mode. By sampling the model parameters twice with the sampling number 100, we can obtain sensitivity analysis results for the maximum equivalent stress in Table 1.

The absolute value in the sensitivity result indicates the sensitivity of the input parameters to the output. The vulnerable area can be picked according to the parameters

Table 1: The sensitivity analysis results for the maximum equivalent stress.

Sensitivity	S	S_T
L	9.1	2.6
W	10.7	-3.6
D	58.8	2.2
A	5.6	1.2
X	44.3	-9.9
Y	5.2	-9.8

which have larger sensitivity values. In Table 1, S is the first-order sensitivity which indicates the effect of this single parameter on the results, and S_T is the total sensitivity which shows the effect of this parameter and other ones. It can be seen that model parameters D and X have larger values of S, and none of parameters has large value of S_T. The results showed that the depth and the horizontal position have larger influence on the blade damage. For these two parameters, we discuss their relationships with the maximum equivalent stress in Figure 4.

Figure 4(a) indicates the relationship between X and σ, and Figure 4(b) indicates the relationship between D and σ. From Figure 4(a), it is shown that the stress is enhanced with the crack location being closer to the blade root. Meanwhile, when the parameter X is larger than 20, the stress value remains stable. According to this result, the area near the blade root is easy to be damaged by cracks. This easily damaged area is needed to be strengthened to resist fatigue fracture; so we take the blade root as the optimization area. From Figure 4(b), stress increases with the increase of crack depth. According to the corresponding relationship between the crack depth and the blade thickness, we choose the blade thickness of the blade root as the optimization object to thicken the blade root area.

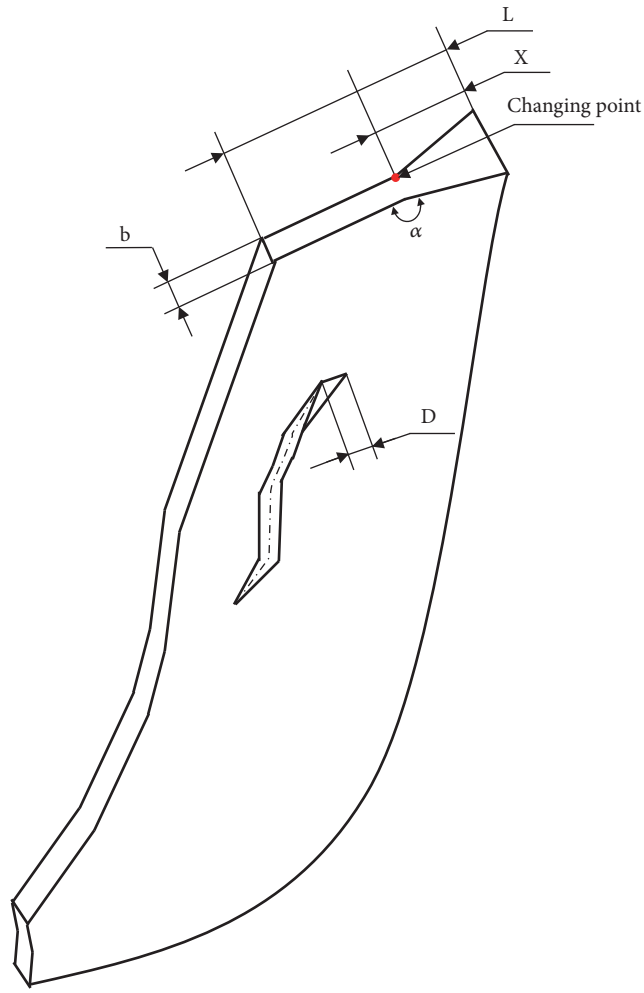

Figure 5: Relationship between crack parameters and optimization variables.

Figure 5 shows the relationship between crack parameters and optimization variables in the impeller blade. The changing point is determined by X and α (angle of thickening area) and b represents blade thickness away from root. It is known that the parameters X and D of impeller have a great influence on the blade. In order to improve the reliability of impeller, it is necessary to optimize the blade structure to enhance the resistance of the blade to these two parameters. The resistance of blade to cracks increases when the ratio D/b gets smaller. In the same way, the blade's resistance to cracks can also be enhanced when root thickness is designed larger as the root is more sensitive to cracks. Obviously, the values of X and α determine the thickness of the root. When the other optimization parameter remains unchanged, the large value of X and the small value of α both cause the increase of root thickness.

4.2. Optimization Process. The changing position and the angle of the thickening area are chosen as optimization variables, and maximum equivalent stress and structure weight are simultaneously set as the optimization goal. Thus, the objective function is formed as

$$\begin{aligned} \min \quad & \underset{b,\alpha,X}{F} = [f_1, f_2] \\ s.t. \quad & b > 0 \\ & 90^\circ < \alpha < 180^\circ \\ & 0 < X < L \end{aligned} \tag{14}$$

where f_1 is the max equivalent stress, and f_2 is the structure weight. b is the blade thickness, α is the angle of thickening area, X is the changing position of thickening area from the root, and L is the length of the blade.

We sampled the optimization variables to obtain 300 sets of sample points. The 230 groups of sample points are selected for training, and 70 groups are used for testing. We used the RBF (Basis Function Radial) kernel function in the SVM prediction model. By using the cross validation method, the best parameter can be searched. The prediction results are shown in Figure 6.

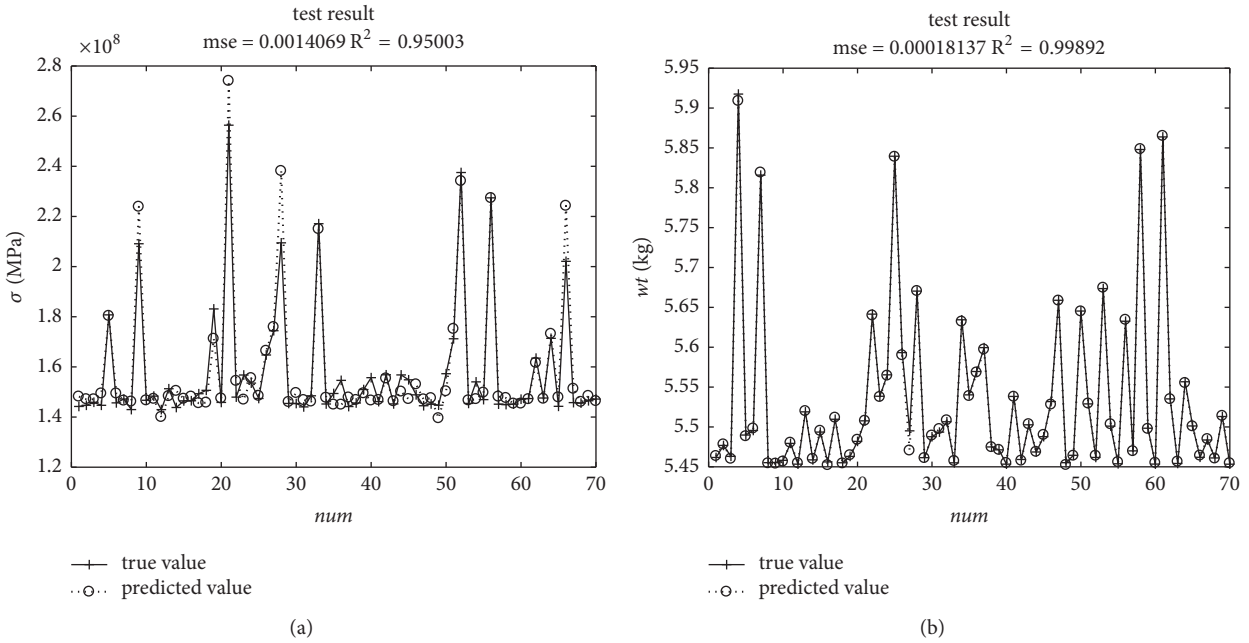

Figure 6: The prediction results based on SVM. (a) The result of the maximum equivalent stress σ. (b) The result of the structure weight wt.

It can be seen that the mean square error MSE and the decision coefficient R2 in the testing results all meet the requirements, which means the prediction effect is good. We also compared this result with the response surface method and the BP neural network method based on the same sample groups. The response surface method uses quadratic polynomial to establish the forecasting model. The comparison results are shown in Table 2.

It is shown that the SVM prediction model has higher precision value and can better establish the mapping relationship between the optimization variables and the optimization goal. Thus, SVM is chosen as the prediction model for the subsequent structural optimization.

Based on the SVM, we optimize the sensitive area for the impeller blade according to the selected optimization variables and optimization goal.

In the particle swarm optimization algorithm, we set c_1=1.2 and c_2=1.2. The population size is 200, the number of iteration is 500, and the weight coefficient is set as $\omega_{\min} = 0.1$ and $\omega_{\max} = 1.2$. The distribution of the Pareto solution set is obtained as shown in Figure 7 and Table 3. The final plan can be selected according to the preference of the optimization object.

By considering both of the safety and the cost, the maximum equivalent stress and the weight have equal weighting factor. Thus, the optimal solution is plan 7. The optimal variation angle is 173.26° and the optimal variation position is 27.37 mm. Before optimization, the thickness of blade was 20.00mm. Thus, the change of thickness is 7.37mm and the change of angle is 6.74°.

Using the optimization result discussed above, the blade structure can be strengthened. To verify the effectiveness of the proposed optimization method, we placed a crack on the vulnerable root area of the blade and analyzed the strength of the structure. The crack depth is set as D=1mm and its position parameters are set as X=5mm and Y=1mm. We also compared the proposed method with other two methods in Shi et al. [26] and Wang [25]. Wang [25] used the equal thickness to avoid structure fatigue. The thickness has a gradual change from the root to the tip in Shi et al. [26]. The comparison analysis results are shown Figure 8.

Table 2: The comparison results by using different prediction models.

Method	MSE	R2
SVM	0.0014069	0.95003
BP neural network	0.0022762	0.93924
Response surface	26.9243	0.5442

Figure 8(a) is the analysis result before optimization. Figure 8(b) is the result after optimization by using the proposed method. Figures 8(c) and 8(d) are results by using the optimization methods mentioned in Wang [25] and Shi et al. [26]. It is shown that the three optimization methods can reduce the maximum equivalent stress more or less. However, the two compared methods ignore the defect factors during the optimization process. They only improve the distribution of stress based on the analysis of the defect-free structure. Although the stress value can be reduced accordingly, the maximum equivalent stress is still concentrated in the area of crack, which means that the crack will grow rapidly and cause the early scrap of the impeller easily. The proposed

Table 3: Pareto solution set.

Plan	Variation angle/(°)	Variation position/mm	Maximum equivalent stress /MPa	Weight/kg
1	172.30	26.22	145.7021	5.4756
2	172.56	29.27	145.1803	5.4927
3	172.43	32.32	145.9901	5.5177
4	172.86	31.94	145.1191	5.5113
5	173.11	25.23	156.7075	5.4692
6	173.00	24.01	156.8309	5.4649
7	173.26	27.37	146.2355	5.4786
8	171.90	30.79	147.4149	5.5079
9	171.72	24.24	157.3187	5.4676
10	173.18	31.02	145.1802	5.5018
11	172.64	32.93	145.5296	5.5216
12	171.82	30.34	145.6820	5.5045
13	171.78	23.02	158.8557	5.4631

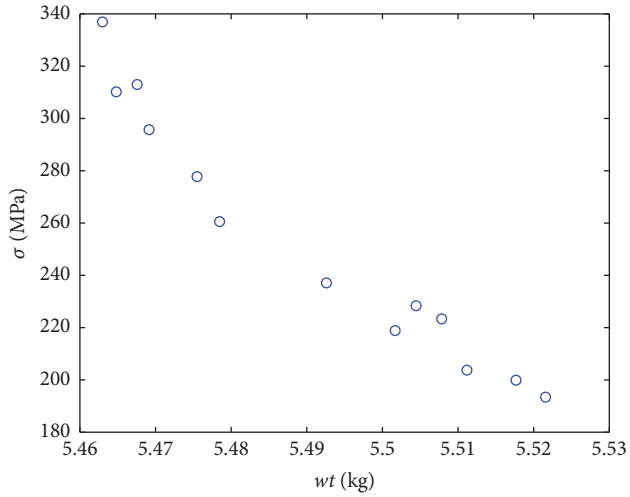

Figure 7: Distributions of the Pareto solution set.

method optimizes structure directly from the view of anti-defect method. It can both increase impeller strength and avoid the stress concentration.

We also record the weight and the max equivalent stress value of the comparison methods in Table 4. After the optimization, the weight of the impeller is 5.4832 kg and the max equivalent stress of the proposed method is 146.86 MPa. It can be seen that the increase of weight is the smallest and the decrease of stress is the largest. Compared to the other two methods, the proposed method has the best optimization results. Furthermore, the structure strength is enhanced well and the max equivalent stress is not concentrated in the crack region. Thus, based on the proposed method, the impeller can have a certain resistance to defect so that the weakening effect of the defect can be delayed.

Besides the max stress and weight, the flow field is another main factor that may be influenced after the optimization. However, due to the uniform thickness of the optimized impeller blades in the axial direction, the cross-section of the flow path formed by the impeller blades has the same trend and thus does not affect the impeller performance.

5. Conclusion

For mechanical elements running under severe working condition, there inevitably exist small defects. The weak areas are more affected, resulting in early damage during service. Thus, a novel anti-defect optimization method based on half-real defect model and Sobol's sensitivity is proposed to decrease the weakening effect of defects. Finally, we take the impeller blade, for example, to test the effectiveness of the proposed method. From the results we can conclude the following.

(1) A half-real defect model was built on the basis of the plane characteristics of the defect image. Influences of geometrical and location parameters of the defect model are analyzed for the defect-resisting performance. The model

Table 4: The comparison results of the three methods.

	Before optimization	After optimization using Wang [25]	After optimization using Shi [26]	After optimization using the proposed
Weight /kg	5.4543	6.07	5.7536	5.4842
Max stress /MPa	217.52	187.99	192.16	146.86
Max stress region	crack region	crack region	crack region	other region

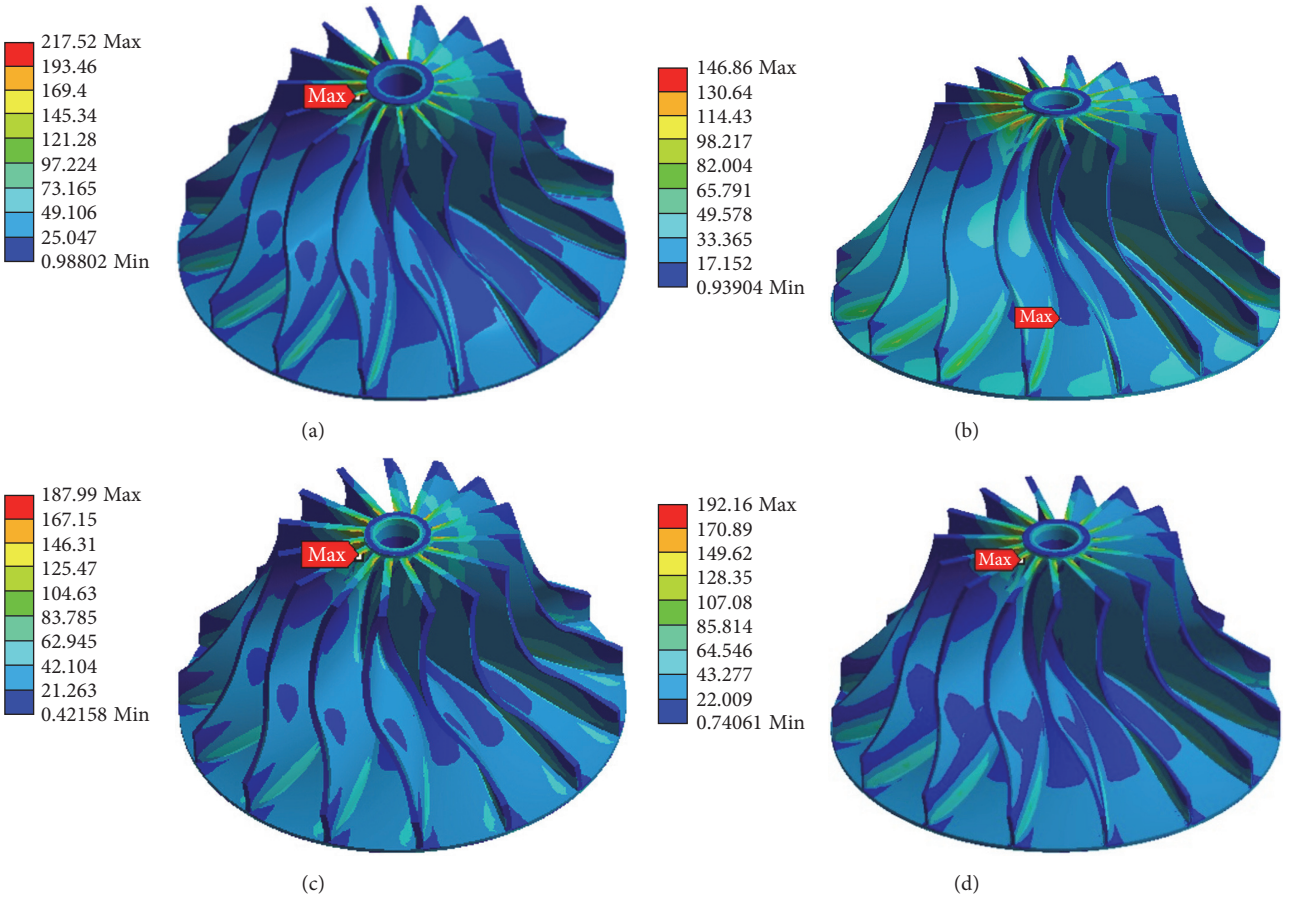

Figure 8: Stress comparison results. (a) The analysis result before optimization. (b) The result after optimization using the proposed method. (c) The result after optimization using Wang [25]. (d) The result after optimization using Shi et al. [26].

parameters can possibly play an effective role in the simulation of the weakening effect on structure.

(2) The weakness of the structure was analyzed combining Sobol's sensitivity method. The optimization area and optimization variables are selected pertinently according to the parameters with high sensitivity. Based on the PSO algorithm, the weakening effect of defects on the structure can be decreased effectively.

Data Availability

All data included in this study are available upon request from the corresponding author.

Conflicts of Interest

The authors declare that there are no conflicts of interest.

Acknowledgments

This research was supported by National Key R&D Program of China (2018YFB1700504), NSFC (51775498, 51775497), and ZPNSFC (LY17F030011).

References

[1] G. Ananthasuresh K, *A nEw Design Paradigm for Micro-Electro-Mechanical Systems and Investigations on the Compliant*

Mechanism Synthesis [Ph.D. thesis], University of Michigan, Ann Arbor, Mich, USA, 1994.

[2] B. Zhu, X. Zhang, and S. Fatikow, "Structural topology and shape optimization using a level set method with distance-suppression scheme," *Computer Methods in Applied Mechanics & Engineering*, vol. 283, pp. 1214–1239, 2015.

[3] Q. Xia, T. Shi, S. Liu, and M. Y. Wang, "Shape and topology optimization for tailoring stress in a local region to enhance performance of piezoresistive sensors," *Computers & Structures*, vol. 114-115, no. 1, pp. 98–105, 2013.

[4] G. Han, Y. Chen, and X. Wang, "Flutter analysis of bending–torsion coupling of aero-engine compressor blade with assembled clearance," *Applied Mathematical Modelling*, vol. 39, no. 9, pp. 2539–2553, 2015.

[5] C. W. Fei, W. Z. Tang, and G. C. Bai, "Novel method and model for dynamic reliability optimal design of turbine blade deformation," *Aerospace Science & Technology*, vol. 39, pp. 588–595, 2014.

[6] A. Staino and B. Basu, "Dynamics and control of vibrations in wind turbines with variable rotor speed," *Engineering Structures*, vol. 56, no. 6, pp. 58–67, 2013.

[7] L. Li, Y. H. Li, Q. K. Liu, and H. W. Lv, "A mathematical model for horizontal axis wind turbine blades," *Applied Mathematical Modelling*, vol. 38, no. 11-12, pp. 2695–2715, 2014.

[8] J. Hong, B. Li, Y. Chen, and H. Peng, "Study on the optimal design of engine cylinder head by parametric structure characterization with weight distribution criterion," *Journal of Mechanical Science & Technology*, vol. 25, no. 10, p. 2607, 2011.

[9] M. Islam, A. Buijk, M. Rais-Rohani, and K. Motoyama, "Simulation-based numerical optimization of arc welding process for reduced distortion in welded structures," *Finite Elements in Analysis & Design*, vol. 84, no. 1, pp. 54–64, 2014.

[10] Y. Liu, L. Tan, and S. L. Cao, "The micro genetic algorithm and its usage in the optimization design of mixed-flow pump," *Machinery Design & Manufacture*, vol. 9, pp. 1–3, 2012 (Chinese).

[11] W. Song, A. Keane, J. Rees, A. Bhaskar, and S. Bagnall, "Turbine blade fir-tree root design optimisation using intelligent CAD and finite element analysis," *Computers & Structures*, vol. 80, no. 24, pp. 1853–1867, 2002.

[12] J. Chen, Q. Wang, W. Z. Shen, X. Pang, S. Li, and X. Guo, "Structural optimization study of composite wind turbine blade," *Materials & Design*, vol. 46, no. 4, pp. 247–255, 2013.

[13] V. N. Shlyannikov, R. R. Yarullin, and A. P. Zakharov, "Fatigue of steam turbine blades with damage on the leading edge," in *Proceedings of the European Conference on Fracture*, vol. 3, pp. 1792–1797, 2014.

[14] N. Ejaz and A. Tauqir, "Failure due to structural degradation in turbine blades," *Engineering Failure Analysis*, vol. 13, no. 3, pp. 452–463, 2006.

[15] S. M. Clarke, J. H. Griebsch, and T. W. Simpson, "Analysis of support vector regression for approximation of complex engineering analyses," in *Proceedings of the ASME 2003 International Design Engineering Technical Conferences and Computers and Information in Engineering Conference*, vol. 127, pp. 1077–1087, American Society of Mechanical Engineers, 2005.

[16] Y. Shi, "Particle swarm optimization: developments, applications and resources," in *Proceedings of the 2001 Congress on Evolutionary Computation*, vol. 1, pp. 81–86, IEEE, 2001.

[17] J. G. Wu, *Theoretical and Applied Research on Crack Growth and Damage Evolution [Ph.D. thesis]*, Beijing University of Aeronautics and Astronautics, 2009.

[18] J. M. Yin, X. Y. Zhao, and S. Y. Zhang, "Method for designing parts structure to resist harsh environments considering sobol defects sensitivity," *Journal of Zhejiang University (Engineering Science)*, vol. 49, no. 8, pp. 1487–1494, 2015 (Chinese).

[19] W. Withayachumnankul, P. Kunakornvong, C. Asavathongkul, and P. Sooraksa, "Rapid detection of hairline cracks on the surface of piezoelectric ceramics," *The International Journal of Advanced Manufacturing Technology*, vol. 64, no. 9-12, pp. 1275–1283, 2013.

[20] B. Y. Lee, Y. Y. Kim, S.-T. Yi, and J.-K. Kim, "Automated image processing technique for detecting and analysing concrete surface cracks," *Structure and Infrastructure Engineering*, vol. 9, no. 6, pp. 567–577, 2013.

[21] R. S. Adhikari, O. Moselhi, and A. Bagchi, "Image-based retrieval of concrete crack properties for bridge inspection," *Automation in Construction*, vol. 39, pp. 180–194, 2014.

[22] A. Saito, M. P. Castanier, and C. Pierre, "Estimation and veering analysis of nonlinear resonant frequencies of cracked plates," *Journal of Sound & Vibration*, vol. 326, no. 3, pp. 725–739, 2009.

[23] I. M. Sobol, "Sensitivity estimates for nonlinear mathematical models," *Mathematical Modelling and Computational Experiment*, vol. 1, no. 1, pp. 112–118, 1993.

[24] E. Zahara and Y.-T. Kao, "Hybrid Nelder-Mead simplex search and particle swarm optimization for constrained engineering design problems," *Expert Systems with Applications*, vol. 36, no. 2, pp. 3880–3886, 2009.

[25] S. X. Wang, *Semi-Closed Pump Impeller*, China, 2014.

[26] Y. Q. Shi, W. M. Wang, and X. Ning, *Development of Parameterized Design Programme for Centrifugal Compressor T Type Impeller*, Compressor Blower & Fan Technology, 2012.

Hindawi
Mathematical Problems in Engineering
Volume 2019, Article ID 4602052, 8 pages
https://doi.org/10.1155/2019/4602052

Research Article

Interactive Q-Learning Approach for Pick-and-Place Optimization of the Die Attach Process in the Semiconductor Industry

Gilseung Ahn,[1] Myunghwan Park,[1] You-Jin Park,[2] and Sun Hur [1]

[1]*Department of Industrial and Management Engineering, Hanyang University, Ansan 15588, Republic of Korea*
[2]*Department of Industrial Engineering and Management, National Taipei University of Technology, Taipei, Taiwan*

Correspondence should be addressed to Sun Hur; hursun@hanyang.ac.kr

Received 13 November 2018; Revised 11 January 2019; Accepted 6 February 2019; Published 18 February 2019

Guest Editor: Anders E. W. Jarfors

In semiconductor back-end production, the die attach process is one of the most critical steps affecting overall productivity. Optimization of this process can be modeled as a pick-and-place problem known to be NP-hard. Typical approaches are rule-based and metaheuristic methods. The two have high or low generalization ability, low or high performance, and short or long search time, respectively. The motivation of this paper is to develop a novel method involving only the strengths of these methods, i.e., high generalization ability and performance and short search time. We develop an interactive Q-learning in which two agents, a pick agent and a place agent, are trained and find a pick-and-place (PAP) path interactively. From experiments, we verified that the proposed approach finds a shorter path than the genetic algorithm given in previous research.

1. Introduction

The entire semiconductor manufacturing process can largely be divided into two sequential subprocesses of front-end production and back-end production. Both production processes involve many complicated steps for wafer fabrication, probe testing and sorting, assembly, final testing, etc. [1]. The front-end process refers to wafer fabrication (fab) and a wafer probe test called electrical die sorting (EDS), whereas the back-end process refers to preassembly, packaging (assembly), and burn-in and functional tests of individual semiconductor chips. Once the front-end processes are completed, the wafers are transferred to back-end production to facilitate their integration into electronic devices and to undergo a final performance test. Particularly, in back-end production, based on quality and location information of individual chips (die) derived from the EDS test, only good semiconductor chips are individually picked and attached to the support structure (e.g., the lead frame) on a strip by an automatic robot arm. This process is called the die attach process [2]. In semiconductor back-end production, this process is regarded as one of the most critical steps since it is the first packaging layer in contact with the die, which demands a high level of operational precision. Thus, optimization of the die attach process is important to maximize the overall productivity in semiconductor back-end production.

Optimization of the die attach process can be formulated as a typical pick-and-place (PAP) problem. The PAP problem is to find the shortest path to pick every component (good dies) and place it on the plate (strip). Because it is a well-known NP-hard problem [3], heuristic approaches such as the rule-based and metaheuristic methods are usually adopted. The rule-based approach is to define a proper dispatching rule and find the shortest path using the predefined rule. Park et al. [1] introduced 11 rules for PAP of the die attach process, which are categorized according to direction and starting point (e.g., the counterclockwise path starting from the center). Huang et al. [4] applied a greedy rule, which is to pick the nearest component and place it on the nearest plate, to solve a PAP problem of multirobot coordination. The metaheuristic approach is to design a metaheuristic algorithm, such as genetic algorithm (GA), particle swarm optimization (PSO), and Tabu search, and apply it to solve PAP problems. Park et al. [1] developed GA, which uses

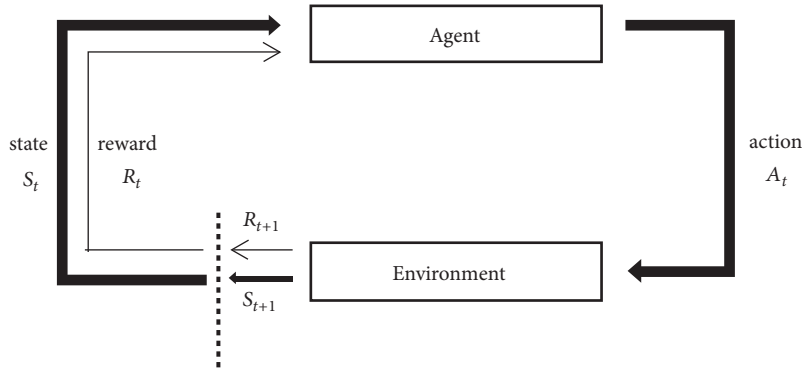

Figure 1: Process of reinforcement learning.

a binary matrix as an encoding scheme and batch and row-string crossover operations. Torabi et al. [5] solved a nozzle selection (pick) and component allocation (place) problem to minimize the workload of the bottleneck while maximizing all corresponding appropriateness factors by a multiobjective particle swarm optimization. Liu and Kozan [6] proposed a blocking job shop scheduling problem with robotic transportation and developed a hybrid algorithm based on a Tabu search.

Each approach can be evaluated by generalization ability, performance, and search time. The generalization ability reveals how easily the approach can be applied to solve various PAP problems once the model including rules and algorithms is defined or developed. The distance of a path determines the performance of the approach. Finally, the search time is the time to find a path. Rule-based approach is better than metaheuristic approach in terms of generalization ability and search time. That is, predefined rules can be applied to solve any PAP problems in a short time, but the metaheuristic approach designed for a problem cannot be applied to different ones and requires relatively long time to solve a problem. However, the performance of metaheuristic approach is better than that of rule-based approach because the path yielded from metaheuristic is usually shorter than that from rule-based approach.

Reinforcement learning explores the space of feasible solutions efficiently and effectively [7] and therefore has been actively applied to solve various optimization problems as alternatives of metaheuristic and rule-based approaches [8–14]. For example, Dou et al. [8] proposed a path planning method for mobile robots in intelligent warehouses based on Q-learning. In this method, the reward is designed to encourage fewer steps of the robots. As another example, Shiue et al. [9] applied a reinforcement learning approach to solve real-time scheduling problems in a smart factory, where Q-learning is used to determine the dispatching rule given remaining jobs.

The objective of this paper is to develop an approach that overcomes the weak points of the typical approach but incorporates the strengths. That is, this approach can show high performance and generalization capability and a shorter search time. With this motivation, we develop an interactive Q-learning method including two interactive agents. That is, a pick agent and a place agent transfer information, restrict or encourage certain actions, and have an impact on the training process of the other. This approach shows higher performance than the metaheuristic approach, relatively shorter training time, and a similar search time to the rule-based approach.

The rest of this paper is organized as follows. Section 2 briefly explains reinforcement learning and Q-learning, which is the basis of our approach. Section 3 states the PAP problem in a die attach process and develops a mathematical model. Section 4 develops the interactive Q model, and Section 5 compares the developed model and metaheuristic approach. Finally, Section 6 concludes the paper and suggests a future research direction.

2. Reinforcement Learning

Reinforcement learning is to train an agent to discover a sequence of actions that yields the highest reward by searching for many pairs of states and actions [15], as presented in Figure 1.

To be more specific, when the system stays at state S_t and an agent performs action A_t, the environment returns reward R_{t+1}, and the system transfers to the new state S_{t+1}. An episode is the sequence of an agent's actions starting from initial state S_0 to terminal state S_T. The purpose of the reinforcement learning is to find the action sequence $A_1^* - A_2^* - \cdots - A_T^*$ (or state sequence $S_1^* - S_2^* - \cdots - S_T^*$) with the trained agent experiencing many episodes.

Among the reinforcement learning methods, Q-learning selects an action on a state in a greedy manner with regard to Q-function. That is, the action achieving the maximum Q-function on a state is selected. Q-function for a pair of state and action (S, A) is defined as the expected sum of discounted rewards when performing A on state S [16]. Q-table is a matrix whose (i, j)th component is the Q-function value of the i^{th} state and the j^{th} action, (S_i, A_j).

The Q-table is updated through episodes from the (old) Q-table by the Bellman equation [17]:

$$\widetilde{Q}(S_t, A_t) = (1-\alpha)\cdot Q(S_t, A_t) + \alpha \cdot \left(r_t + \gamma \cdot \max_A \widetilde{Q}(S_{t+1}, A)\right), \quad (1)$$

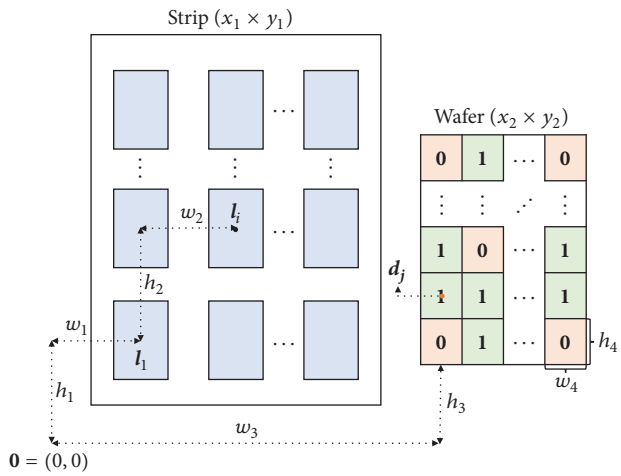

Figure 2: Coordinate information of the strip and wafer.

where t is time period of an episode; $\widetilde{Q}(S_t, A_t)$ and $Q(S_t, A_t)$ are the updated Q-function and old Q-function for S_t and A_t, respectively; $0 < \alpha \leq 1$ is the learning rate; $0 \leq \gamma \leq 1$ is the discount rate; and r_t is the reward when performing A_t on S_t. In this equation, $\widetilde{Q}(S_t, A_t)$ is a weighted sum of the old value and the learned value, where the weights are obtained from the learning rate. The discount rate γ reflects the importance of the expected value of the next action $\max_A \widetilde{Q}(S_{t+1}, A)$.

3. Problem Statement and Mathematical Model

3.1. Problem Statement. In postfabrication process of the semiconductor manufacturing, the probe test is performed on individual die (chip) of wafers to identify defect of dies and classify dies by the level of its quality. Then, the only "good" dies (i.e., conforming chips) are assembled and packaged in the assembly step in back-end production [18, 19]. After the test, a robot arm repeatedly picks up a good die in a wafer and places it on a lead frame in a strip until every good die is transferred in the die attach process. The robot arm starts and ends the process at the origin. That is, the start point and end point are the same and fixed. The total moving distance highly depends on the order of pick and place (i.e., path). Therefore, the considered problem is to find the shortest path to transfer every good die to a lead frame with the robot arm. Note that the Manhattan distance metric is employed to calculate distance, because the robot arm moves only vertically or horizontally due to several technical issues.

We assume that the strip and wafer are located at the left and right sides on the coordinate, respectively, and are rectangular, as presented in Figure 2. Even though these assumptions may be unrealistic (e.g., the wafer is round), they do not affect the modeling and development of the interactive Q-learning approach.

3.2. Notations. Notations used in this paper are as follows.

Indices

i: Lead frame index, ($i = 1, 2, \ldots, n$)

j: Good die index, ($j = 1, 2, \ldots, m$)

z: Agent index, ($z = 1$: pick agent, $z = 2$: place agent)

Problem Parameters

(x_1, y_1): Strip shape

(x_2, y_2): Wafer shape

$\boldsymbol{l}_i$: Coordinate of lead frame i

$\boldsymbol{d}_j$: Coordinate of good die j

w_1: Horizontal distance between the origin and $\boldsymbol{l}_1$

h_1: Vertical distance between the origin and $\boldsymbol{l}_1$

w_2: Horizontal distance between the two consecutive lead frames

h_2: Vertical distance between the two consecutive lead frames

w_3: Horizontal distance between the origin and the first die

h_3: Vertical distance between the origin and the first die

w_4: Horizontal distance between two consecutive dies

h_4: Vertical distance between two consecutive dies

Model Parameters

T: Maximum number of iterations

Ω^z: State space of agent z

S^z: Current state of agent z

A^z: Action space of agent z

$\mathscr{F}^z$: Feasible action space of agent z

Q^z: Q-table of agent z

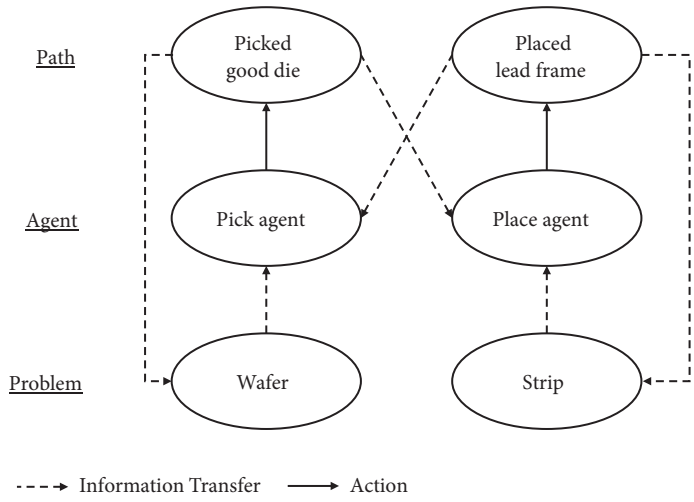

Figure 3: Interactive Q Model configuration.

P: Path, $P = P^0 - P^1 - P^2 - \cdots - P^{|P|} - P^{-1}$, where P^0 and P^{-1} are the starting and ending points of the path, respectively. P^n is the n^{th} point (good die if n is odd and lead frame otherwise) and $|P|$ is the length of the path

$dist(P)$: Total distance of path P

3.3. Mathematical Model. The mathematical model is presented as follows:

$$\text{Minimize} \quad dist\,(P)\,, \tag{2}$$

$$\text{Subject to} \quad \bigcup_{k=1}^{|P|/2} P^{2k-1} = \{\boldsymbol{d}_1, \boldsymbol{d}_2, \ldots, \boldsymbol{d}_m\}\,, \tag{3}$$

$$P^{2k} \in \{\boldsymbol{l}_1, \boldsymbol{l}_2, \ldots, \boldsymbol{l}_n\}\,, \quad \text{for } k = 1, 2, \ldots, \frac{|P|}{2}, \tag{4}$$

$$\bigcup_{k=n\times t+1}^{n\times(t+1)} P^{2k} = \{\boldsymbol{l}_1, \boldsymbol{l}_2, \ldots, \boldsymbol{l}_n\}\,, \quad \text{for } t = 0, 1, \ldots, \left\lceil \frac{m}{n} \right\rceil \tag{5}$$

$$\bigcup_{k=n\times([m/n]+1)}^{|P|/2} P^{2k} \in \{\boldsymbol{l}_1, \boldsymbol{l}_2, \ldots, \boldsymbol{l}_n\}\,. \tag{6}$$

The objective function in (2) is to minimize the total distance, where

$$\begin{aligned} dist\,(P) = {} & \left(P_x^1 + P_y^1\right) \\ & + \sum_{k=1}^{|P|/2} \left(\left|P_x^{2k-1} - P_x^{2k}\right| + \left|P_y^{2k-1} - P_y^{2k}\right|\right) \\ & + \left(P_x^{|P|} + P_y^{|P|}\right), \end{aligned} \tag{7}$$

where (P_x^{2k-1}, P_y^{2k-1}) and (P_x^{2k}, P_y^{2k}) are the coordinates of the k^{th} selected good die and lead frame, respectively. $(P_x^1 + P_y^1) = |P_x^1 - 0| + |P_y^1 - 0|$ denotes the distance from the origin to the first selected good die, and $(P_x^{|P|} + P_y^{|P|}) = |0 - P_x^{|P|}| + |0 - P_y^{|P|}|$ denotes the distance from the last selected lead frame to the origin.

Constraints (3) and (4) indicate that the robot arm picks a good die and places it on the empty lead frame. Constraints (5) and (6) show that the good dies are transferred until an empty strip is full; once the strip is full, it is replaced with a new one until every good die is transferred. Two typical example paths satisfying these constraints when $m = 5$ and $n = 2$ are $\mathbf{0} - \boldsymbol{d}_1 - \boldsymbol{l}_1 - \boldsymbol{d}_2 - \boldsymbol{l}_2 - \boldsymbol{d}_3 - \boldsymbol{l}_1 - \boldsymbol{d}_4 - \boldsymbol{l}_2 - \boldsymbol{d}_5 - \boldsymbol{l}_2 - \mathbf{0}$ and $\mathbf{0} - \boldsymbol{d}_3 - \boldsymbol{l}_2 - \boldsymbol{d}_2 - \boldsymbol{l}_1 - \boldsymbol{d}_3 - \boldsymbol{l}_1 - \boldsymbol{d}_1 - \boldsymbol{l}_2 - \boldsymbol{d}_5 - \boldsymbol{l}_1 - \mathbf{0}$. As one can see, the path starts and ends at the origin, there is no duplicate of good dies in a path, and a new strip is installed only when the previous strip is full.

4. Interactive Q Model

4.1. Configuration and Deployment. The proposed interactive Q model is configured as shown in Figure 3.

As seen in Figure 3, the model consists of three layers: problem, agent, and path. The problem layer transfers the information of the problem (i.e., number and location of the remaining good dies in the wafer and empty lead frames in the strip) to the agent layers. The pick and place agents in the agent layer select a good die to be picked and a lead frame to which the good die is placed considering the information, respectively. The selected good die and lead frame are appended to the path. Finally, the information that the selected good die and lead frame are no longer feasible is transferred to the problem layer.

Agent $z \in \{1, 2\}$ consists of state space Ω^z, action space A^z, feasible action space $\mathscr{F}^z$, and Q-table Q^z. $\Omega^1 = \{\boldsymbol{l}_1, \boldsymbol{l}_2, \ldots, \boldsymbol{l}_n\}$ and $\Omega^2 = \{\boldsymbol{d}_1, \boldsymbol{d}_2, \ldots, \boldsymbol{d}_m\}$ are sets of locations of the robot arm before picking and placing, respectively. $A^1 = \{a_1^1, a_2^1, \ldots, a_m^1\}$ and $A^2 = \{a_0^2, a_1^2, a_2^2, \ldots, a_n^2\}$ are action

Input: Ω^1, Ω^2, A^1, A^2, Q^1, Q^2
Procedure: Initialize $\mathscr{F}^1 = A^1$ and $\mathscr{F}^2 = A^2$
Initialize $P^0 = \mathbf{0}$ and $P^{2m+2} = \mathbf{0}$
Initialize $S^1 = \mathbf{0}$ # S^1: current state of the pick agent
Initialize $p = 0$
Until $\mathscr{F}^1 = \emptyset$ **do** {
Increase p by 1
If $\mathscr{F}^2 = \emptyset$ **do** {# If a strip is full, the strip is replaced with a new one
$\mathscr{F}^2 = A^2$}
Pick agent procedure
$a^1_{j^*} = \text{argmax}_{a^1_j \in \mathscr{F}^1}(Q^1_{S^1,j})$ # Select an action of the pick agent
$P^p = \boldsymbol{d}_{j^*}$
$S^2 = \boldsymbol{d}_{j^*}$ # Update the current state of the place agent
$\mathscr{F}^1 = \mathscr{F}^1 - \boldsymbol{d}_{j^*}$ # Update the feasible action space of the pick agent
Place agent procedure
Increase p by 1
$a^2_{i^*} = \text{argmax}_{a^2_i \in \mathscr{F}^2}(Q^2_{S^2,i})$ # Select an action of the place agent
$P^p = \boldsymbol{l}_{i^*}$
$S^1 = \boldsymbol{l}_{i^*}$
$\mathscr{F}^2 = \mathscr{F}^2 - \boldsymbol{l}_{i^*}$ # Update the feasible action space of the place agent
}
Output: $P = P^0 - P^1 - P^2 - \cdots - P^{|P|} - P^0$

Algorithm 1: Routing algorithm of the interactive Q model.

spaces of the pick agent and place agent, respectively, where a^1_j is to pick a good die j, and a^2_i is to place the selected good die on lead frame i. Here, a^2_0 indicates that the robot arm returns to the origin. Feasible actions of the pick agent $\mathscr{F}^1 \subset A^1$ and place agent $\mathscr{F}^2 \subset A^2$ include good dies in a wafer and empty lead frames, respectively. That is, good dies in a wafer and empty lead frames are feasible. $Q^1_{i,j}$ indicates a Q-function of a^1_j when the current state is $\boldsymbol{l}_i$ for $i = 0, 1, \ldots, n$ and $j = 1, \ldots, m$, where $\boldsymbol{l}_0$ is the origin. Likewise, $Q^2_{j,i}$ indicates a Q-function of a^2_i when the current state is $\boldsymbol{d}_j$ for $i = 1, \ldots, n$ and $j = 0, 1, \ldots, m$, where $\boldsymbol{d}_0$ is the origin.

Pick and place agents act in a greedy manner with respect to Q-table, whose training method is explained in Section 4.2. The pick agent picks a good die with the maximum Q-value in a wafer (i.e., it selects the action with the maximum Q-value among feasible actions) when the current state is $\boldsymbol{l}_i$, as follows:

$$a^1_{j^*} = \underset{a^1_j \in \mathscr{F}^1}{\text{argmax}} \left(Q^1_{i,j}\right), \tag{8}$$

where $a^1_{j^*}$ is the selected action of the pick agent. The place agent places the selected good die j on an empty lead frame with the maximum Q-value, as follows:

$$a^2_{i^*} = \underset{a^2_i \in \mathscr{F}^2}{\arg\max} \left(Q^2_{j,i}\right), \tag{9}$$

where $a^2_{i^*}$ is the selected action of the place agent. After the actions are determined, the feasible action space is updated.

Algorithm 1 shows the routing process of the interactive Q model.

4.2. Training Algorithm. Q^1 and Q^2 are updated using the Bellman equation presented in (1). When updating the Q-tables, they impact one other because the estimated optimal future values (i.e., $\max_{a^2_k \in \mathscr{F}^2}(\widetilde{Q}^2_{j,k})$ and $\max_{a^1_k \in \mathscr{F}^1}(\widetilde{Q}^1_{i,k})$) of the pick and place agents are the Q-function values of the place and pick agents, as given in (10) – (11).

$$\widetilde{Q}^1_{i,j} = (1-\alpha) \times Q^1_{i,j} + \alpha \times \left(r^1_{i,j} + \gamma \times \max_{a^2_k \in \mathscr{F}^2} \left(\widetilde{Q}^2_{j,k}\right)\right), \tag{10}$$

$$\widetilde{Q}^2_{j,i} = (1-\alpha) \times Q^2_{j,i} + \alpha \times \left(r^2_{j,i} + \gamma \times \max_{a^1_k \in \mathscr{F}^1} \left(\widetilde{Q}^1_{i,k}\right)\right), \tag{11}$$

where $\widetilde{Q}^1_{i,j}$ and $\widetilde{Q}^2_{j,i}$ are updated (new) Q-functions, while $Q^1_{i,j}$ and $Q^2_{j,i}$ are old Q-functions. $r^1_{i,j}$ is the reward of the pick agent for selecting a^1_j from $\boldsymbol{l}_i$, which is computed as the reciprocals of distances $\boldsymbol{l}_i$ and $\boldsymbol{d}_j$. $r^2_{j,i}$ is also similarly defined and computed. Note that $Q^1_{i,j}$ and $Q^2_{j,i}$ are updated only when a^1_j and a^2_i are selected when the current states are $\boldsymbol{l}_i$ and $\boldsymbol{d}_j$, respectively.

Algorithm 2 shows the training algorithm for Q^1 and Q^2 based on general Q-learning's exploration strategy, considering both current and future reward. To be more concrete, Q-value of agent z ($z = 1, 2$) is updated by taking the weighted average of the current reward $Q^z_{S^z,j^*}$ and future reward $r^z_{S^1,j^*} + \gamma \times \max_{a^{3-z}_k \in \mathscr{F}^{3-z}}(\widetilde{Q}^2_{j^*,k})$, which means that each agent whose current state is S_t at time t considers distance between S_t and S_{t+1} as well as between S_{t+1} and S_{t+2}. It trains Q-tables using the wafer including no bad dies, but the trained Q-tables can be used to solve every problem if the wafer and strip

Input: Ω^1, Ω^2, A^1, A^2, T
Procedure: Initialize every element in $\widetilde{Q}^1$, Q^1, $\widetilde{Q}^2$, Q^2 with arbitrary numbers
Initialize $t = 1$
Until ($\widetilde{Q}^1 = Q^1$ and $\widetilde{Q}^2 = Q^2$) **or** $t = T$ **do** {
$\widetilde{Q}^1 = Q^1$
$\widetilde{Q}^2 = Q^2$
Initialize $\mathscr{F}^1 = A^1$ and $\mathscr{F}^2 = A^2$
Initialize $S^1 = \mathbf{0}$ # S^1: current state of the pick agent
Until $\mathscr{F}^1 = \emptyset$ **do** {
If $\mathscr{F}^2 = \emptyset$ **do** {# If a strip is full, it is replaced with a new one
$\mathscr{F}^2 = A^2$}
Pick agent update
$a^1_{j^*} = \text{argmax}_{a^1_j \in \mathscr{F}^1}(Q^1_{S^1,j})$
$\widetilde{Q}^1_{S^1,j^*} = (1-\alpha) \times Q^1_{S^1,j^*} + \alpha \times (r^1_{S^1,j^*} + \gamma \times \max_{a^2_k \in \mathscr{F}^2}(\widetilde{Q}^2_{j^*,k}))$
$S^2 = \boldsymbol{d}_{j^*}$ # Update the current state of the place agent
$\mathscr{F}^1 = \mathscr{F}^1 - \boldsymbol{d}_{j^*}$ # Update the feasible action space of the pick agent
Place agent update
$a^2_{i^*} = \text{argmax}_{a^2_i \in \mathscr{F}^2}(Q^2_{S^2,i})$ # Select the action of the place agent
$\widetilde{Q}^2_{S^2,i^*} = (1-\alpha) \times Q^2_{S^2,i^*} + \alpha \times (r^2_{S^2,i^*} + \gamma \times \max_{a^1_k \in \mathscr{F}^1}(\widetilde{Q}^1_{i^*,k}))$
$S^1 = \boldsymbol{l}_{i^*}$
$\mathscr{F}^2 = \mathscr{F}^2 - \boldsymbol{l}_{i^*}$ # Update the feasible action space of the place agent
Increase t by 1
}
Output: $\widetilde{Q}^1$, $\widetilde{Q}^2$

Algorithm 2: Q-tables update algorithm.

shapes are the same. Thus, the interactive Q-model has higher generalization capability than metaheuristic algorithms.

5. Experiment

In this section, we compare the performance of our interactive Q-learning model with those of the GA model and rule-based models presented in the literature [1].

5.1. Parameters. The problem parameters are obtained from Park et al. [1] as follows: $(x_1, y_1) = (10, 4)$, $(x_2, y_2) = (9, 9)$, $w_1 = 14$, $w_2 = 12$, $w_3 = 66$, $w_4 = 8$, $h_1 = 22$, $h_2 = 20$, $h_3 = 18$, $h_4 = 4$.

Four wafers are considered according to the yield rates of dies (80% and 90%) and the bad die distribution (bivariate normal and uniform distribution). The wafers are depicted in Figure 4, where colored cells denote bad dies.

Four rules are adopted from Park et al. [1], where they are defined as follows.

Rule 1. The robot arm moves good dies from the upper-left side of a wafer to empty lead frames in the upper-left side of a strip.

Rule 2. The robot arm starts moving the good dies from the upper-left side of a wafer to empty lead frames in the upper-right side of a strip.

Rule 3. The robot arm moves good dies from the upper-right side of a wafer to empty lead frames in the upper-right side of a strip.

Rule 4. The robot arm starts moving the good dies from the upper-right side of a wafer to empty lead frames in the upper-left side of a strip.

The parameters of GA were set as follows: (1) the number of initial solutions: 200, (2) the number of iterations: 100, and (3) crossover operation: batch and row-string crossover operation. The interactive Q-learning model's parameters are set as $\alpha = 0.01$, $\gamma = 0.99$, and $T = 1000$, and the model is trained using the same sized wafer and strip. Note that the wafer for training is assumed to have no bad die, and the trained model can be applied to every problem if the shapes of the wafer and strip remain fixed.

5.2. Results. Figure 5 shows the performance comparison results.

Figure 5 shows that the proposed model outperforms the GA and rule-based models in every problem, implying that the model has sufficient generalization ability, as well as excellent performance. Specifically, 13.14%, 13.23%, 7.05%, and 8.09% of the total distance are decreased from GA for wafers A, B, C, and D, respectively. All rule-based models have produced longer total distances than GA for all wafers. From the experiment result, we can conclude that (1) the interactive Q model outperforms GA, (2) it is more effective when the yield rate is low or when the defective rate is high, and (3) it is robust to the bad die distribution.

As for the running time, the proposed model and rule-based models take less than a second, but GA takes more than an hour to yield a path and is highly dependent on the number

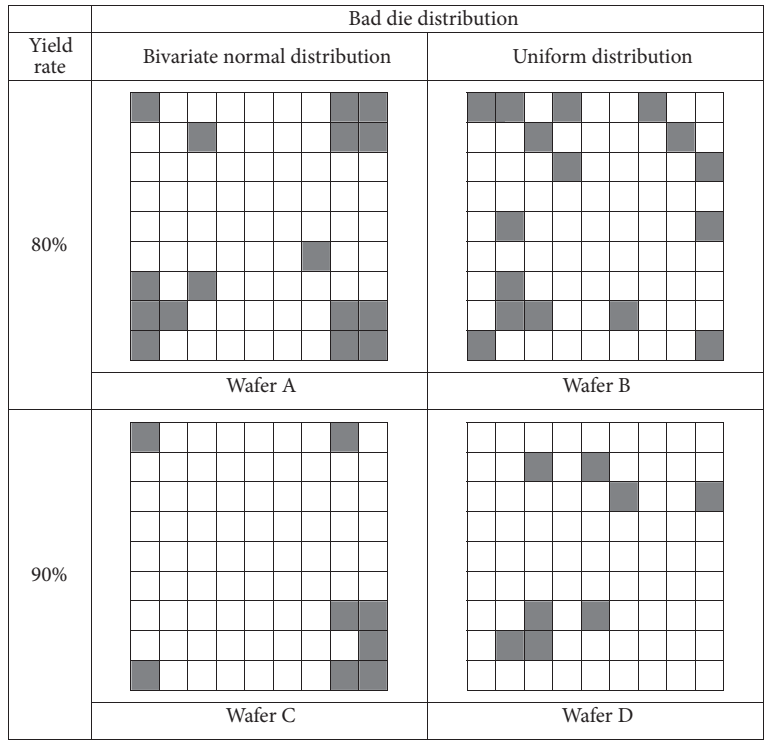

Figure 4: Wafers for the experiments.

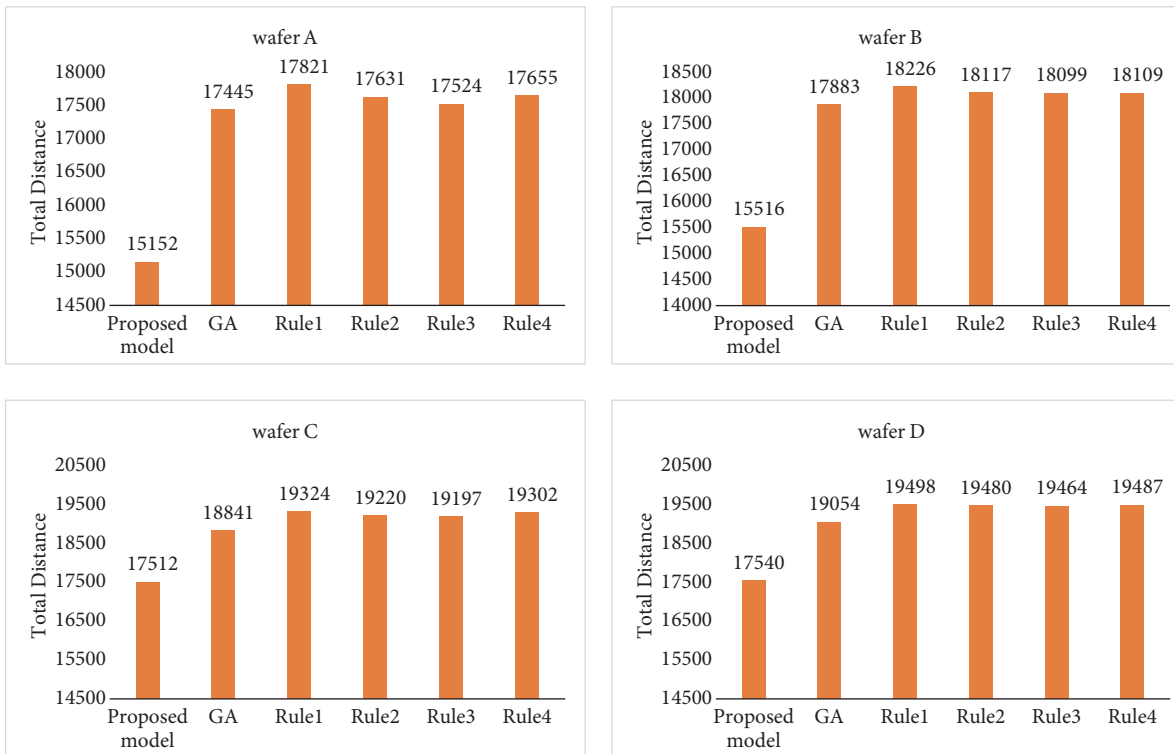

Figure 5: Comparison results of the interactive Q model, GA, and rules.

of iterations and initial solutions. In addition, the interactive Q model requires short training time. In our experiment, the training time when $(x_1, y_1) = (10, 4)$ and $(x_2, y_2) = (9, 9)$ is 254 seconds. That is, one episode requires only 0.254 seconds. In addition, yielding a path by means of the model takes less than 1 second. This may imply that the model can be trained and applied to solve the problem in real time.

6. Conclusion

In this paper, we addressed the PAP problem of the die attach process to maximize the overall productivity in semiconductor back-end production. Due to the NP-hardness of this problem, rule-based and metaheuristic approaches have been applied. These approaches, however, should be improved because the metaheuristic approach has low generalization ability. With this motivation, we developed an interactive Q-learning approach equipped with two interactive agents to find a path. The experiment revealed that the proposed model shows higher performance than GA and has almost the same search time as the rule-based approach.

In future work, one can modify our interactive Q-learning to solve various optimization problems in the semiconductor industry and PAP problems in other industries. In addition, a hybrid approach of Q-learning and other approaches such as rule-based and metaheuristic approaches can be developed to solve more complicated problems efficiently. That is, incorporating the proposed interactive Q-learning with rule-based approach can increase the generalization ability, which will solve PAP problems with different wafers.

Data Availability

The data used to support the findings of this study are available from the corresponding author upon request.

Conflicts of Interest

The authors declare that they have no conflicts of interest.

Acknowledgments

This work has supported by the National Research Foundation of Korea (NRF) grant funded by the Korea government (MSIT) (2017R1A2B4006643).

References

[1] Y.-J. Park, G. Ahn, and S. Hur, "Optimization of pick-and-place in die attach process using a genetic algorithm," *Applied Soft Computing*, vol. 68, pp. 856–865, 2018.

[2] G. Weigert, A. Klemmt, and S. Horn, "Design and validation of heuristic algorithms for simulation-based scheduling of a semiconductor backend facility," *International Journal of Production Research*, vol. 47, no. 8, pp. 2165–2184, 2009.

[3] A. Srivastav, H. Schroeter, and C. Michel, "Approximation algorithms for pick-and-place robots," *Annals of Operations Research*, vol. 107, no. 1-4, pp. 321–338, 2001.

[4] Y. Huang, R. Chiba, T. Arai, T. Ueyama, and J. Ota, "Robust multi-robot coordination in pick-and-place tasks based on part-dispatching rules," *Robotics and Autonomous Systems*, vol. 64, pp. 70–83, 2015.

[5] S. A. Torabi, M. Hamedi, and J. Ashayeri, "A new optimization approach for nozzle selection and component allocation in multi-head beam-type SMD placement machines," *Journal of Manufacturing Systems*, vol. 32, no. 4, pp. 700–714, 2013.

[6] S. Q. Liu and E. Kozan, "A hybrid metaheuristic algorithm to optimise a real-world robotic cell," *Computers & Operations Research*, vol. 84, pp. 188–194, 2017.

[7] J. Kober, J. A. Bagnell, and J. Peters, "Reinforcement learning in robotics: A survey," *International Journal of Robotics Research*, vol. 32, no. 11, pp. 1238–1274, 2013.

[8] J. Dou, C. Chen, and P. Yang, "Genetic scheduling and reinforcement learning in multirobot systems for intelligent warehouses," *Mathematical Problems in Engineering*, vol. 2015, Article ID 597956, 10 pages, 2015.

[9] S. Yeou-Ren, K. C. Lee, and C. T. Su, "Real-time scheduling for a smart factory using a reinforcement learning," *Computers & Industrial Engineering*, vol. 125, pp. 604–614, 2018.

[10] S. Li, L. Ding, H. Gao, C. Chen, Z. Liu, and Z. Deng, "Adaptive neural network tracking control-based reinforcement learning for wheeled mobile robots with skidding and slipping," *Neurocomputing*, vol. 283, pp. 20–30, 2018.

[11] A. S. Xanthopoulos, A. Kiatipis, D. E. Koulouriotis, and S. Stieger, "Reinforcement learning-based and parametric production-maintenance control policies for a deteriorating manufacturing system," *IEEE Access*, vol. 6, pp. 576–588, 2017.

[12] J. Shahrabi, M. A. Adibi, and M. Mahootchi, "A reinforcement learning approach to parameter estimation in dynamic job shop scheduling," *Computers & Industrial Engineering*, vol. 110, pp. 75–82, 2017.

[13] A. Kara and I. Dogan, "Reinforcement learning approaches for specifying ordering policies of perishable inventory systems," *Expert Systems with Applications*, vol. 91, pp. 150–158, 2018.

[14] R. F. Atallah, C. M. Assi, and J. Y. Yu, "A reinforcement learning technique for optimizing downlink scheduling in an energy-limited vehicular network," *IEEE Transactions on Vehicular Technology*, vol. 66, no. 6, pp. 4592–4601, 2017.

[15] R. S. Sutton and A. G. Barto, *Introduction to Reinforcement Learning*, MIT Press, 2018.

[16] M. K. Mainali, K. Shimada, S. Mabu, and K. Hirasawa, "Optimal route based on dynamic programming for road networks," *Journal of Advanced Computational Intelligence and Intelligent Informatics*, vol. 12, no. 6, pp. 546–553, 2008.

[17] L. Buşoniu, R. Babuška, and B. De Schutter, "A comprehensive survey of multiagent reinforcement learning," *IEEE Transactions on Systems, Man, and Cybernetics, Part C: Applications and Reviews*, vol. 38, no. 2, pp. 156–172, 2008.

[18] K. Nakamae, A. Itoh, and H. Fujioka, "Fail pattern classification and analysis system of memory fail bit maps," in *Proceedings of the 2001 International Conference on Modeling and Simulation of Microsystems - MSM 2001*, pp. 598–601, March 2001.

[19] C.-H. Wang, "Recognition of semiconductor defect patterns using spatial filtering and spectral clustering," *Expert Systems with Applications*, vol. 34, no. 3, pp. 1914–1923, 2008.

Hindawi
Mathematical Problems in Engineering
Volume 2019, Article ID 6278365, 10 pages
https://doi.org/10.1155/2019/6278365

Research Article

Design, Construction, and Operation of a High-Energy Mill for Handling Magnesium Powder

J. C. Paredes Rojas,[1] **L. E. Álvarez Ramírez**,[2] **G. Urriolagoitia Sosa**,[2] **C. R. Torres San Miguel**,[2] **B. Romero Ángeles**,[2] **J. A. Leal Naranjo**,[3] **and G. M. Urriolagoitia Calderón**[2]

[1]*Instituto Politécnico Nacional, Laboratorio Nacional de Desarrollo y Aseguramiento de la Calidad en Biocombustibles (LANDACBIO), Centro Mexicano para la Producción más Limpia, Acueducto de Guadalupe s/n, La Laguna Tecomán, 07340, Ciudad de México, Mexico*
[2]*Instituto Politécnico Nacional, Sección de Estudios de Posgrado e Investigación de la Escuela Superior de Ingeniería Mecánica y Eléctrica, Unidad Profesional "Adolfo López Mateos" de México, Edificio 5 Tercer Piso, Del. Gustavo A. Madero, Col. Lindavista, 07738, Mexico*
[3]*Departamento de Electrónica, DICIS, Universidad de Guanajuato, Carr. Salamanca-Valle de Santiago Km 3.5+1.8, Comunidad de Palo Blanco, 36885 Salamanca, GTO, Mexico*

Correspondence should be addressed to J. C. Paredes Rojas; paredesrojasjc@gmail.com

Received 30 October 2018; Revised 23 December 2018; Accepted 22 January 2019; Published 7 February 2019

Guest Editor: Sutasn Thipprakmas

A high-energy mill was designed and built with the purpose of processing magnesium (Mg) powders. The main characteristics of the mill are grinding capacity of 1 kg and demolition elements of 10 kg; it has a distributed form to the interior ten blades of similar geometry, six of which are of the same size and four of them were increased in length in order to avoid the accumulation of the ground material. It has a jacket with a diameter of 240 mm as a cooling system to prevent high temperatures during grinding and possible chemical reactions; likewise, type 304 stainless steel was used for its construction. 10 mills were made during a period of 4, 6, and 8 hours, in order to obtain microparticles; with these particles, an analysis of X-ray spectroscopy was made to verify their physical and chemical characteristics. The outcome shows powder particles with dimensions of 0.1-4 mm, which will be used to the storage and handling hydrogen in the solid state (MgH_2).

1. Introduction

Renewable energy sources are the third largest contributor to global electricity production in 2015 [1]. Renewable energy sources, like solar, wind, biofuels, etc., are needed to mitigate current environmental problems.

Hydrogen is proposed as alternative energy carrier [2]. Hydrogen is the most abundant element in the universe [3]. However, a major problem is the storage of hydrogen, which has to be done safely and with high density. Hydrogen storage in metals has the potential to satisfy these conditions; many metals absorb it [4, 5]. Therefore, world is moving toward the use of metal hydrides, which can "store" per unit cell to two or three times as much hydrogen atoms than the metal itself [6–9]. Metal hydrides are formed by reaction of hydrogen with metals. Deposit metal hydrides and metal compounds containing essentially transition metals and rare earths, with lattices forming interstices which under certain conditions can absorb hydrogen atoms [10]. MgH_2 is studied as a potential hydrogen storage material.

Metal hydrides such as MgH_2 or some complexes as $NaAlH_4$ and $LiAlH_4$ are attractive for this use, store 7.6, 7.3, and 10.1% by weight and hydrogen, respectively, have a low overall weight [11, 12]. Hydrides of pure metals and alloys are an efficient and safe with good hydrogen storage capacity per unit mass storage medium, but generally have slow desorption kinetics and rupture temperatures near 300°C

equilibrium with little stability before repeated cycles of absorption and desorption [13, 14].

In recent studies, the importance of particle size effects on the hydrogen sorption kinetics in Mg and MgH_2 is shown. In that research, the preparation of MgH_2 nanoparticles supported on high surface area carbon aerogels with pore sizes varying from 6 to 20 nm is reported [5]. The metal storage capacity is determined by curves PCT (Pressure, Concentration, and Temperature) [6, 12, 15].

High-energy ball mills equipment is becoming a standard for particle size reduction. This is due to the increasing demand for fine (<1 μm) product particle size and shorter processing cycles [16]. Ball mill is one of the most predominantly used methods for the purpose of mixing and grinding of raw materials [17, 18].

The ball mill process is very complicated process governed by many parameters, such as ball size, ball shape, ball filing, slurry loading (with respect to ball amount), powder loading with respect to the amount of total slurry (slurry viscosity), and rotation speed. A high industrial interest in optimizing such ball mill parameters from the viewpoint of the comminution of ores exists [17].

A recent study reports an optimal ball size for efficient milling with a rotation speed, based on a laboratory-scale wet ball mill. In addition, the effect of powder loading on the particle size reduction has been investigated at given conditions of ball size rotation speed [19]. In ceramic laboratories, ball mill is often carried out to mainly achieve a mixed state powders with initial average particle (d_{50}) of 1-20 μm. In other laboratories, zirconia balls with nominal diameter of approximately 1-10 mm are frequently employed [19]. There have been different studies on the influences of parameters associated with grinding balls such as ball size distribution and ball shape on the particle comminution [20–22].

There are different types of ball mills for obtaining powder, stand out horizontal ball mill (low-energy) and the high efficiency (high-energy) ball mill. The horizontal ball mill was the first equipment used to obtain metastable systems and in the dissolution of metals that exhibit immiscibility. This mill is mounted on rotating rollers by means of which the speed of rotation is controlled, using steel balls, which during the rotation drag the powder cause shock between the particles, deforming and fracturing them, being the basic principle of the alloy mechanics. The equipment is considered low energy and requires extensive grinding times to optimize the same; this type of mill is commonly used in the industry to obtain particles of different materials; these are used in different industries such as cosmetics, mining, metal mechanics, molding of pieces, among others. The mills of high efficiency of grinding work under the principle of the decrease of dead zones; all the materials and the walls of the chamber of the mill are under collision with the balls. This high-energy mill is capable of operation under atmosphere controlled conditions, vacuum, or inert gas, including loading and unloading of powders. High-energy mills are designed primarily for crushing and for laboratory-scale operations [23].

The main difference between mills is the field of application, since the high-energy mill has a scientific application, because advanced materials and small particle sizes (nanometers) are used.

In this study we present the design of a new high-energy mill for the processing of magnesium powders with research objectives; the powder will be used to obtain magnesium hydride (MgH2) and store hydrogen in solid state, with the following objectives:

(i) Obtain magnesium powder, for storage of hydrogen in solid state (hydride), increasing the efficiency of the process through optimum temperature.

(ii) Control the temperature of the mill chamber through a cooling jacket, considering that what is planned obtained primarily pure nanoparticles of magnesium, which will facilitate the storage of hydrogen in the gas phase.

This paper is organized as follows: Section 2 defines the design process of the high-energy mill, as well as the modelling. The manufacturing process is developed in this section. Section 3 defines the process of experimental testing; milling of magnesium is described in detail in this section. In Section 4 the results of the X-ray spectroscopy analysis are shown, where the physical and chemical characteristics of the magnesium particles are verified. Finally, Section 5 presents conclusions and possible future work.

2. Methodology

2.1. Analytical Design and Modelling. For the design of the mill, it was necessary to take certain considerations, which were established based on literature of powder processing, such as the mill capacity (1 kg) and working time (12 hours) in order to have a production of 0.0833 kg/h.

For processing powders with high-energy milling, the use of balls for grinding is indispensable; in the literature it was found that there is a ratio of 10:1; therefore, if the milling capacity is 1 kg, 10 kg balls are needed based on the most conservative parameter. Commonly it used from 30% to 40% of the total mill volume for containing the product to be ground and the grinding elements (steel balls).

The selection of the apparent volume (VA) occupied by the grinding elements arises two litters for optimum performance.

$$V_A = \frac{M_B}{0.7 * \rho_{Steel}} \tag{1}$$

According to the results of previous investigations the total volume (VT) required to contain the grinding elements and the material for grinding is raised in a ratio of 3 to 1 or 3.5 to 1; to accomplish with this requirement the total volume (VT) will be of 6462.25 cm^3.

It is necessary to consider that the machine will be used to grind a mineral, so it is necessary to determine the material of grind (17.287 kW/hr); in this case, the material is magnesium (Mg) and mill production to determine engine power.

$$\begin{aligned} \text{Pe} &= \text{Wi} * \text{Mill production} = \text{Engine power} \\ \text{Pe} &= 17.287\,\text{kW/h} * 0.0833\,\text{kg/h} = 1.44\,\text{kW} \end{aligned} \tag{2}$$

Considering a safety factor of 1.5, the engine power is 2.88 hp.

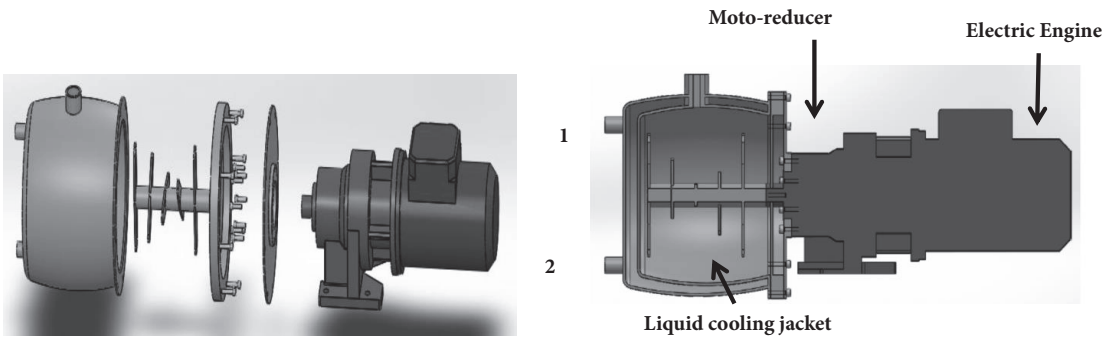

Figure 1: (a) The main components of the high-energy mill where one indicates the output of the coolant and two input. (b) High-energy mill exploded.

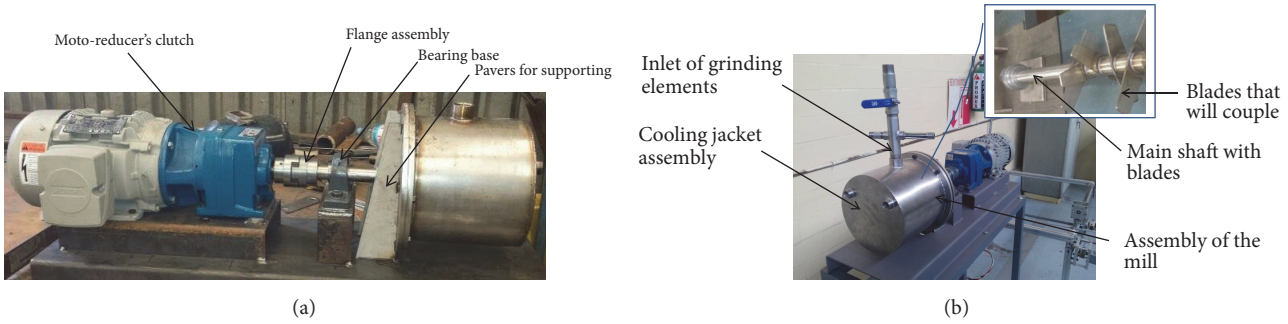

Figure 2: (a) High-energy mill assembly. (b) Final assembly.

The grinding blades are the transmitter of engine power to the grinding elements. It consisted of a total of ten blades similar geometry, six of the same size and the remaining extend below to avoid agglomeration of the mill base.

The shaft diameter required to transmit the engine power was calculated taking into consideration that the work done is twisted. It should take into account the fact that the engine power is 2.23 kW and the angular speed (ω) at the output of the motor-reducer is 73.32 rad/second. In addition, a yield strength type 304 of stainless steel is 310 MPa with a safety factor of 4. Using the following equation shaft diameter was determined:

$$\tau = \frac{16T}{\pi d^3} < \tau_{adm} \tag{3}$$

To support the impeller efforts, it must be at least 15.88 mm. To design and ensure an ideal coupling with the output of the engine, a shaft of 30 mm was the best for the purpose. Once the analytical development was completed, the development was continued to design through Solidworks® software.

In Figure 1, this modelling describes the components of the mill. (a) The main components of the high-energy mill where one indicates the output of the coolant and two inputs and (b) high-energy mill exploded. This describes the entry and exit of coolant 1 and coolant 2, respectively.

2.2. Construction. The first component built was the tank where magnesium will be ground, having an inlet and an outlet for the coolant; the cooling system will aim to fracture the material and to avoid damage due to the high temperature of the mill. Another important point is to keep the temperature constant during the grinding process, in order to avoid any possible chemical reaction.

Figure 2 shows the assembly of the cooling jacket; it is the most delicate part, because there are two cylinders of different diameters, which are welded in high temperature for the 304 stainless steel for a properly welding; it is important to be sure that it has no leakage and mention that the process of milling particles of magnesium requires a vacuum environment and/or inert, to prevent chemical reaction with oxygen.

The cutting process was performed with laser; likewise, the flange assembly is coupled to the tank; the windmill and the base bearing flange were welded at a high temperature. Coupling the moto-reducer with the axis of the mill shown in Figure 2 must be perfectly leveled to avoid problems of fatigue and premature wear on the main shaft.

The magnesium that was used in the grinding tests has the following thermophysical properties (see Table 1). It was also necessary to carry out a certificate of analysis of the chemical composition of magnesium (see Table 2). The experimental methodology of milling is described below.

The magnesium ingots used in this study are not 100% pure, due to the following considerations:

Table 1: Thermophysical properties of magnesium.

Property	Value
Atomic number	12
Valence	2
Oxidation state	+2
Electronegativity	1.2
Covalent radius (Å)	1.30
Ionic radius (Å)	0.65
Atomic radius (Å)	1.60
Electron configuration	[Ne]3s2
First ionization potential (eV)	7.65
Atomic weight (g/mol)	24.305
Density (g/ml)	1.74
Boiling point (°C)	1107
Melting point (°C)	650

Table 2: Certificate of chemical analysis.

Element	Contend
Mg	99.95 %
Ca	0.0020%
Na	-----
Si	0.0090%
Fe	0.0020%
Mn	0.0170%
Ni	0.00030%
Zn	--------
Cu	0.00170%
Al	0.0180%

(i) The technique used in this work is not entirely clean because the plastic deformation between iron balls and magnesium generates impurities, so for this work, the use of magnesium at 99.99 was not considered.

(ii) The importance of this work lies in demonstrating a method that allows grinding magnesium with certain dimensions shown in the images in X-ray spectrum.

(iii) It is considered that the cost of pure magnesium is excessive for this study since the main objective of the work is to grind magnesium with certain dimensions; in addition, it is judged that the difference in the modulus of elasticity between pure magnesium and magnesium allied exceeds 5% for this case study.

(iv) Another justification for the use of magnesium alloy in the amounts to be mill, since the main use of this equipment is to grind large quantities to transport hydrogen.

3. Experimental Test

The system for obtaining magnesium powders is described in Figure 3; it operates with a three-phase electric motor (A) that is coupled to a geared motor (B), which reduces rotation speed from 3600 RPM to 435 RPM in order to increase the torque. The moto-reducer shaft is coupled via a clutch to the shaft of the mill; the speed of the steel balls increases due to the thrust receiving the blades (C), which causes the magnesium have been ground by the shock effect mechanic.

Due to heat generated from collisions between crushing elements and magnesium, a cooling system is implemented; the ball mill has a cooling jacket (C) where it circulates the coolant (glycol) through a hydraulic pump (D); the liquid refrigerant passes through a heat exchanger (F); in order to lower the temperature, the coolant is in a (E) container. The system also has a vacuum pump (G), in order to remove all the air inside the mill. Once reached the maximum vacuum pressure valves V-3 and V-3 are closed. Valves V-2, V-4, and V-5 open and allow the inlet of inert gas "Argon". Argon is used to maintain stable grinding.

Experimental tests were performed to magnesium milling; the main objective is to obtain nanoparticles of pure Mg. The experimental tests were made under the next conditions: magnesium 1 kg, stainless steel balls 10 kg, temperature 28°C, and vacuum grinding.

Magnesium ingots of 300 grams each were used; these were cut into pieces of 100 grams; it is essential not to saturate large bullion to avoid problems in grinding. Magnesium samples do not need any previous preparation, are at room temperature and for the milling test 10 pieces of 100 grams that is 1 kg, and were used. The size of the demolition elements (balls) was 5 mm. 10 kg of grinding balls was used. The experimental tests were made in a period of time of 4, 6, and 8 hours of milling. The grinding time was established based on the working time established in the design.

The samples obtained were analyzed by scanning electron microscopy in order to determine shape of grain, grain size, uniformity of grain and contamination in the samples. Test scanning electron microscopy was performed in "Centro de Nanociencias y Micro y Nanotecnologías del IPN".

Scanning electron microscopy (SEM) is the most suitable method used to the study the surface morphology, since the image provided by the SEM is generated by the interaction of an electron beam that sweeps an area on the sample surface, while in light microscopy it is used photons in the visible spectrum. The equipment has a device that generates an electron beam to illuminate the sample and with different detectors is then collected to create an image of the surface that provides information related to forms, textures, and chemical composition. The maximum voltage to excite the electrons is 30 KV. The microscope used in this study is a Quanta 3D FEG (FEI brand). This device includes three secondary electron detectors (SE) optimized for use in high vacuum (HV), low vacuum (LV), and environmental mode (ESEM), as well as a backscattered electron detector (BSE) of solid state.

4. Results

The high-energy mill was designed with a cooling system based on a heat exchanger of cross-flow, to keep it at a constant operating temperature and thereby avoid fatigue of materials due to a high temperature; this design has a system

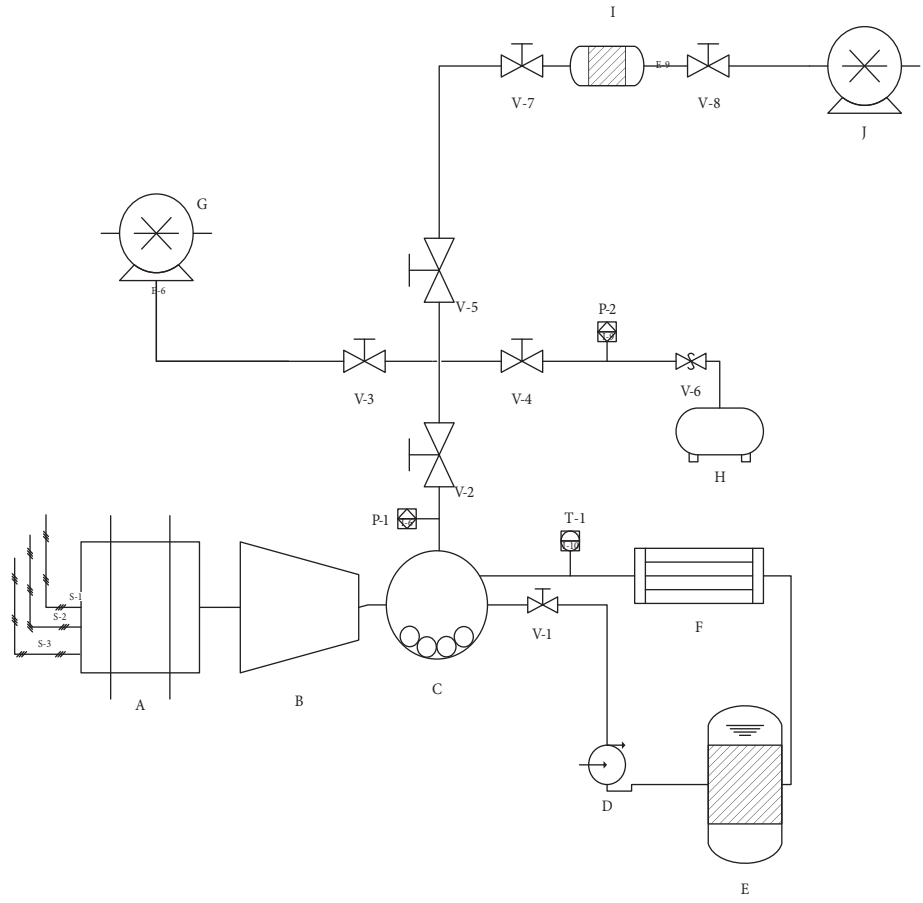

Figure 3: Pneumatic circuit of the high-energy mill.

covering the chamber mill and a compound in which coolant is introduced mainly glycol. To ensure the flow of liquid, the inlet is disposed at one end of the cooling jacket, forcing the fluid to travel the cooling jacket; the outlet is on the opposite side thereof and thus the liquid and it gets stuck and does not allow the system to cool the inside of the mill.

In the camera, the magnesium and the grinding elements were at a constant temperature to avoid fatigue and they were not conducive to a chemical reaction. Because the temperature was kept under control using a cooling jacket, which cover the chamber where the grinding elements work, this cooling jacket works under the principle of operation of a heat exchanger of cross-flow.

The grinding chamber reaches a certain temperature due to the clash between the crushing elements and pieces of magnesium, to have a thermal equilibrium in the grinding and not to promote a chemical reaction; this is wrapped in a cooling jacket, achieving thermal equilibrium.

Another important consideration was that processing magnesium powder must be performed in an inert atmosphere. This atmosphere is created through a pneumatic system, which is connected to the main entrance of the grinding chamber, the same magnesium inlet; once the magnesium is introduced into the mill chamber, vacuum is created through a vacuum pump; once there is no air in the chamber, a controlled amount of Argon is injected to have a completely inert atmosphere to avoid any possible chemical reaction of magnesium. The pneumatic system is also used for the extraction and storage of the product once sprayed.

Figure 4(a) shows that the particles are not uniform with a grinding time of 4 hours; they are of different sizes (particle sizes between 0.1 and 5 mm); the image was taken with an excitation magnetic field of 5.0 KV; the shape of the particles are elongated; the cut is seen very noticeable; this is due to the clash between the ingots; detachment is abundant in burr grinding.

Figure 4(b) shows where a specific image analysis was performed (in the marked box) to determine the percentages of elements in that area

The graphs of X-ray spectrum show that the most abundant element is magnesium with 86.6% by weight. Carbon also has a 10.85% weight but with a 12.94% error in addition to other elements such as oxygen, copper, and zinc with high error rates, which include magnesium ingots used in the milling which are not 100% pure.

Figure 5 shows that the particles are of different sizes (particle sizes between 0.1 and 4 mm), this with a grinding time of 6 hours; the shapes of the magnesium particles are of amorphous type because there is no uniformity of appearance. In Figures 5(b) and 5(d), a slightly more detailed

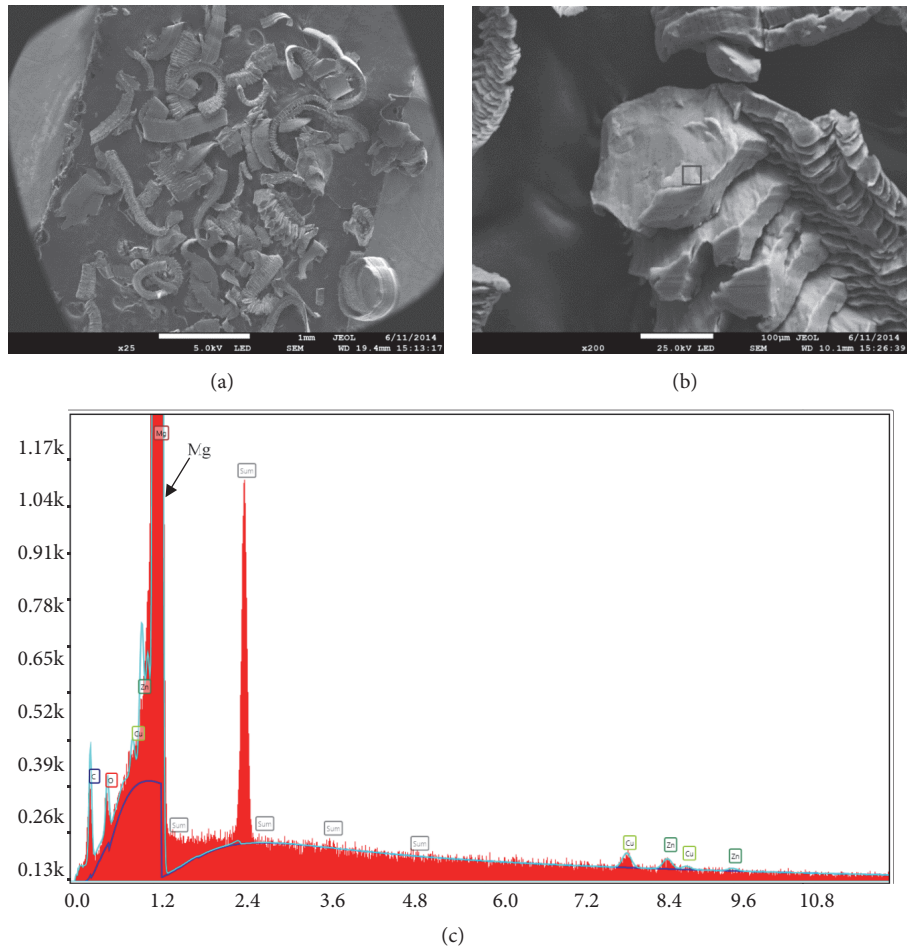

Figure 4: (a) SEM 1A (x 25, 5.0 KV), (b) SEM 1A specific image 1(x200 and 25.0 KV), and (c) results of X-ray spectra.

study shows different features of LED and BED, respectively; in them a trace of elongated shape is observed; this is a contamination of the sample made due to factors such as ingots pollution, pollution of the windmill blades, and release of material from the walls of the mill.

The analysis in Figure 5 shows a substantial percentage of magnesium but there is still contamination by carbon and oxygen. Analysis of X-ray spectrum of Figures 5(b) and 5(d) shows that it is contaminated with other elements such as iron and aluminum. In Figures 6(a), 6(b), and 6(c) with a grinding time of 8 hours, the amount of magnesium is plentiful; even the grain size is not right (particle sizes between 0.1 and 4 mm), but with increasing milling time the uniformity of the particles is noted.

5. Discussion

Breaking metallic materials takes a risk due to the nature of them; they react exothermically if they are suddenly oxidized. Therefore, in this work, the manipulation of them during the high-energy milling process was considered very careful for the own ball mill. The challenge in the development of hydrides is that highly reactive materials are used, as well as pressures and elevated working temperatures; because of that, it was necessary increasing the design requirements of the mill. Performing the milling of magnesium, by means of mechanical manufacture using a high-energy ball mill of its own design, allowed the elaboration of metal particles.

There are different scientific studies that verify the veracity of the high-energy mill.

Osorio et al. found that the statistical models for determining the mechanical efficiency of the mill-cyclone and mill-mill circuits show correlations of 85% and 83%, respectively, and also established that the rotation speed of the mill has no statistical significance and that the most influential parameter for mechanical efficiency is the loading of grinding bodies, which leads to think of a reduction of operational costs to be able to work with low speed values [24]. Graves mentions that an optimum combination of media material properties is very important for efficient operation of the high-energy mill and that some additional media parameters, such as media sphericity and size distribution, will have significant impact on the mill performance [16]. In ceramic laboratories, ball mill is often carried out to mainly achieve a thoroughly mixed state of starting powders with initial average particle (d_{50}) of 1-20 μm. In other laboratories,

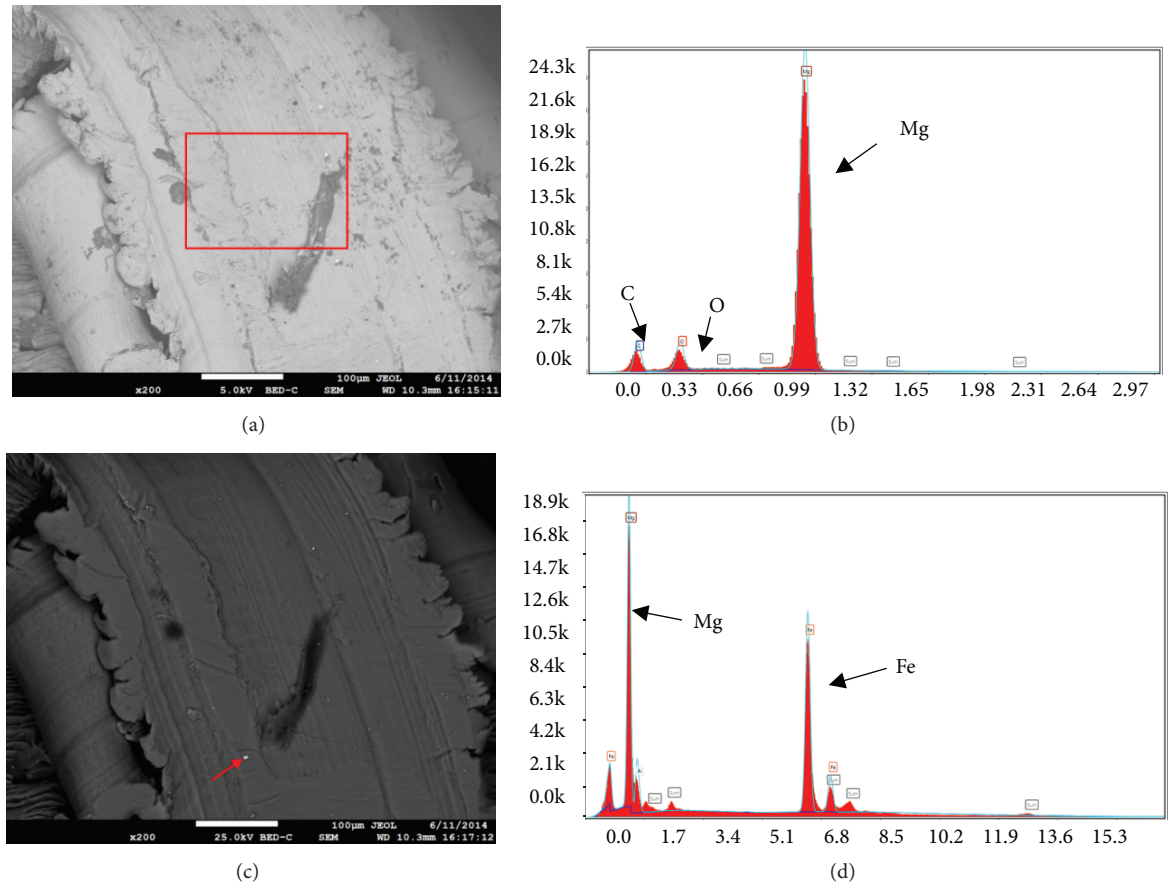

Figure 5: (a) SEM 2A specific image 1, x 200 and 5.0 KV. (b) X-ray spectra. (c) SEM 2A specific image 2, x200, and 5.0 KV. (d) X-ray spectra.

zirconia balls with nominal diameter of approximately 1-10 mm are frequently employed [19].

It is clear that the particle size depends on a large extent on the size of the grinding balls, as mentioned in the related articles. The main difference between this study and the others is the influence of the grinding temperature because a cooling jacket was designed, which aims to control the grinding process under a constant temperature.

The mill reaches a level of grinding between fine and ultra-fine as in commercial equipment (particle sizes between 0.1 and 4 mm), without the restrictions of operation or design presented by them. In addition, the parameters of load of the mill are those that contribute to an effective fragmentation of the equipment of milling (grinding balls 5 mm of diameter), without compromising the quality of the material concluded working time.

The results in this study of the design of the mill for processing magnesium were satisfactory to obtain good functionality, optimal work in grinding, stable temperatures, minimum mechanical vibration, and a correct general operation of the mill, however; the objective of obtaining nanoparticles was not reached; we consider that we do not use the appropriate grinding balls; other similar studies frequently use zirconia balls between 1 and 10 mm of nominal diameter, to obtain particles of 1-20 μm. [19]. As for the cooling system that was designed, no temperatures higher than 100°C were recorded (in the cooling system); it would be convenient in future works to incorporate temperature sensors in different points of the cooling system even inside the chamber of grinding.

According to the experience of the authors during the experimental tests of milling of magnesium, it is established that the optimization required to the mill can be carried out under three areas:

(i) Mechanical, where they try to make numerical models through MEF that allow knowing the fatigue of materials that comprise the milling system.

(ii) Automation of the mill: it is necessary to implement a heuristics method that allows the modulation of the temperature and monitor the amount of explosive gases in the grinding chamber, in order to control the hydration process with high safety standards.

(iii) Inspection of the sample: it is necessary to apply a visual system to monitor the size of the particle in order to control the grinding times.

To store hydrogen in the solid state, particle sizes of (6-20 nm) are reported [5]. In a future work, experimental tests with grinding ball diameters of less than 5 mm will be carried out, dry reactive grinding tests (MRS) will be carried out, and the

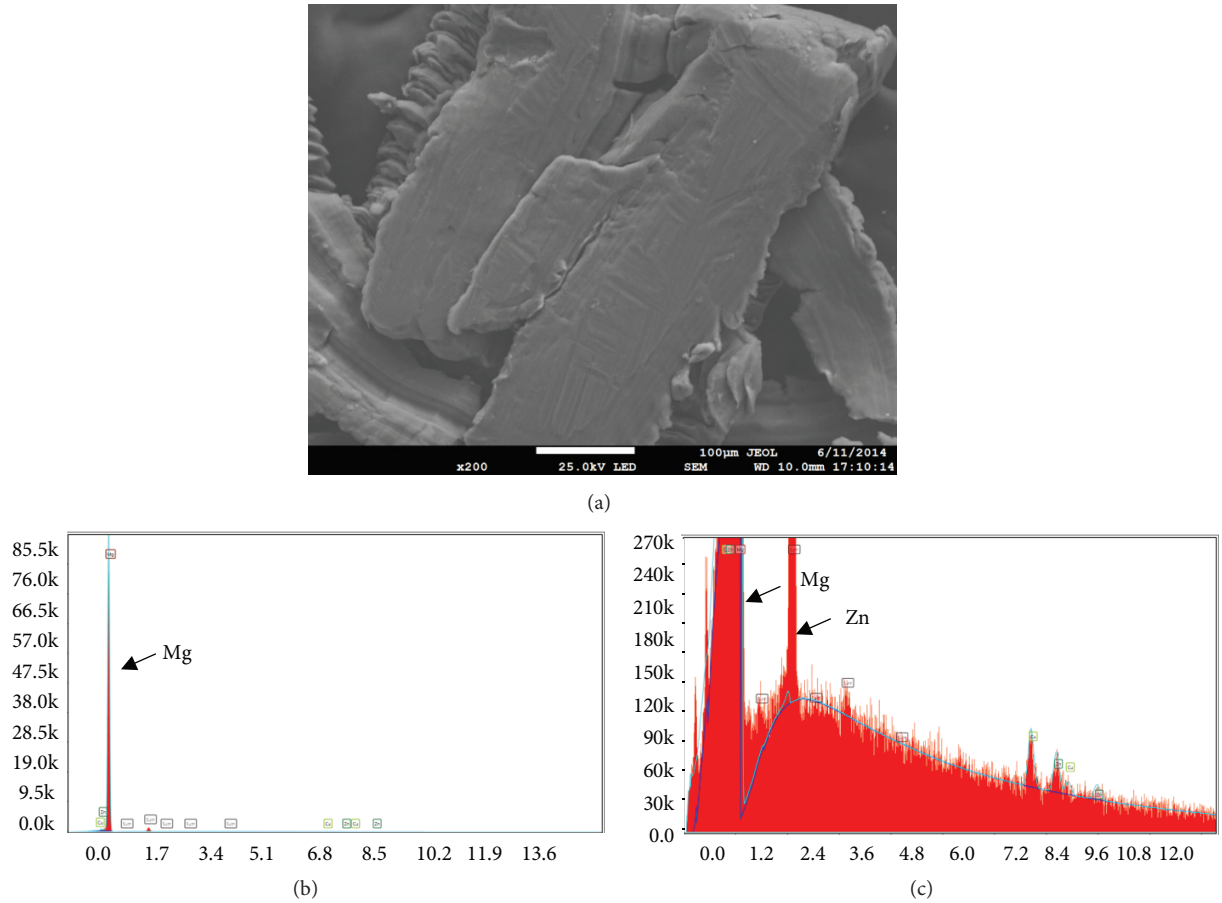

Figure 6: (a) SEM 3A, x200, and 25.0 KV, LED. (b) X-ray spectra. (c) X-ray spectra.

formation of magnesium hydrides by diffraction (DXR) will be demonstrated, as well as the possible pollutants produced by mechanical energy.

6. Conclusion

A high-energy mill was designed, built, and operated to process magnesium powder. The mill has a milling capacity of 1 kg and 10 kg crushing elements (diameter 5 mm); it consists of a total of ten blades similar geometry, six of which are the same size and four extend below to avoid agglomeration of the mill base. It has a cooling jacket to avoid high temperatures and thus grinding favors the milling process. A tire air extraction system and injection of argon are also designed and implemented because the magnesium powder processing must be vacuum or in an inert atmosphere.

A tire air extraction system and injection of argon are also designed and implemented because the magnesium powder processing must be vacuum or in an inert atmosphere.

The samples obtained were analyzed by scanning electron microscopy in order to determine

(i) the grain shape;

(ii) the grain size;

(iii) uniformity of grain in the sample;

(iv) sample contamination.

In sample 1A (4 hours of grinding), it is possible to note that the particles are not uniform and is of different sizes; the image was taken with an excitation magnetic field of 5.0 KV; the shape of the particles is elongated and is seen very well known; this is due the clash between the ingots; detachment is abundant in burr grinding. The particle sizes are between 0.1 and 5 mm.

In sample 2A (6 hours of grinding), the particles are of different sizes (particle sizes between 0.1 and 4 mm); the shape of the magnesium particles is amorphous because there is no uniformity of appearance. Sample contamination is observed due to factors such as pollution ingots, pollution of the windmill blades, and detachment of material from the walls of the mill. The analysis of X-ray spectrum shows that it is contaminated with iron and other elements such as aluminum.

Sample 3A (8 hours of grinding) shows that magnesium is abundant (particle sizes between 0.1 and 4 mm); even the grain size is not right, but with increasing milling time the uniformity of the particles is observed; it is important to mention that, in order to store hydrogen, is necessary that the magnesium particles have a particle size of nanometers.

The efficiency of the high-energy mill is a multifactorial process that depends on different factors. It is commonly accepted that high-energy mill processes are based on the assumption that high the mill is operated under conditions of full media fluidization; i.e., fluidization conditions are determined by a combination of media properties (density, size, and mill volume), product properties (density, size, and mill volume), product properties (density, % solids, and viscosity at processing conditions), and mill operating conditions (product feed rates and shaker speed) [17].

Particle size depends on the size of the demolition elements. If increase in the balls grinding the result will increase dead zones, which would imply a deficiency in the grinding process, the same happens with a high number of blades.

With the results obtained in this study it is possible to obtain a mathematical model of the grinding process; the most important variables to consider in this model would be size of demolition elements, speed of the engine rotation, temperature of the grinding process, and time of the process.

Researchers community requires high-precision machines and processes; as a future objective, it will be considered the methodology reported by [25] for the conceptual redesign and FEM validation, for this customized experimental equipment used in magnesium grinding; it will be possible to estimate the total machine flexibility for other process conditions in a convenient and easy manner. Also, the application of these methodologies will allow finding the tolerances and the accuracy of all components that have the milling system (chamber, blades, and balls) with the purpose to establish the durability of the high-energy ball mill.

Data Availability

The design, modelling, mathematical calculations, manufacturing process, scanning electron microscopy studies, and X-ray spectrum data used to support the findings of this study are included within the article.

Conflicts of Interest

The authors J.C. Paredes Rojas, L.E. Álvarez Ramírez, G. Urriolagoitia Sosa, C.R. Torres San Miguel, B. Romero Ángeles, J. A. Leal Naranjo, and G. M. Urriolagoitia Calderón declare that there are no conflicts of interest regarding the publication of this paper.

Authors' Contributions

All authors have approved the manuscript and agree with its submission to the Journal "Mathematical Problems in Engineering".

Acknowledgments

Thanks are due to the CONACYT-Mexico Scholarship granted to Juan Carlos Paredes, to the research team of the Automotive Systems Engineering Laboratory of the ESIME UC-IPN-Mexico, and to Sección de Estudios de Posgrado e Investigación of ESIME ZAC. The authors gratefully acknowledge the financial support from the Mexican Government by Consejo Nacional de Ciencia y Tecnología, to the Instituto Politécnico Nacional. The authors also acknowledge partial support by Projects 20181141 and 1931, as well as EDI grant, all provided by SIP/IPN.

References

[1] IEA, "International energy agency, statistics renewables information," 2017, http://www.iea.org/topics/renewables/.

[2] G. W. Crabtree, M. S. Dresselhaus, and M. V. Buchanan, "The hydrogen economy," *Physics Today*, vol. 57, no. 12, pp. 39–44, 2004.

[3] D. A. J. Rand and R. M. Dell, *Hydrogen Energy: Changes and Prospects*, RSC Energy Series, RSC Publishing, 2008.

[4] M. Hirscher, *Handbook of Hydrogen Storage: New Materials for futurEnergy Storage*, Wiley-VCH, Weinheim, Germany, 2010.

[5] Y. S. Au, M. K. Obbink, S. Srinivasan, P. C. M. M. Magusin, K. P. De Jong, and P. E. De Jongh, "The size dependence of hydrogen mobility and sorption kinetics for carbon-supported MgH2 particles," *Advanced Functional Materials*, vol. 24, no. 23, pp. 3604–3611, 2014.

[6] I. A. Vertiz, *Análisis experimental de almacenamiento de hidrógeno en estructuras sólidas, Tesis de Doctorado en Diseño*, Instituto Politécnico Nacional, México, 2012.

[7] J. R. Mihelcic and J. B. Zimmerman, *Ingeniería Ambiental*, Editorial Alfaomega, México, 2011.

[8] J. P. Blackledge, *Metal Hydrides*, Academic Press, New York, NY, USA, 1968.

[9] F. A. Cotton and G. Wilkinson, *Advanced Inorganic Chemistry: a comprehensive text*, John Wiley & Sons, EE.UU, 1980.

[10] E. I. Zoulias and N. Lymberopoulos, *Hydrogen-based Autonomous Power Systems*, Springer -Verlag 1, London, UK, 2008.

[11] L. Schlapbach and A. Züttel, "Hydrogen-storage materials for mobile applications," *Nature*, vol. 414, no. 6861, pp. 353–358, 2001.

[12] F. C. Gennari and F. J. Castro, "Formation, composition and stability of Mg-Co compounds," *Journal of Alloys and Compounds*, vol. 396, no. 1-2, pp. 182–192, 2005.

[13] B. Molinas, A. A. Ghilarducci, M. Melnichuk et al., "Scaled-up production of a promising Mg-based hydride for hydrogen storage," *International Journal of Hydrogen Energy*, vol. 34, no. 10, pp. 4597–4601, 2009.

[14] M. Verga, F. Armanasco, C. Guardamagna et al., "Scaling up effects of Mg hydride in a temperature and pressure-controlled hydrogen storage device," *International Journal of Hydrogen Energy*, vol. 34, no. 10, pp. 4602–4610, 2009.

[15] B. Vigeholm, J. Kjoller, B. Larsen, and A. S. Pedersen, "Formation and decomposition of magnesium hydride," *Journal of the Less-Common Metals*, vol. 89, no. 1, pp. 135–144, 1982.

[16] G. A. Graves and T. Boehm, "Mill media considerations for high energy mills," *Minerals Engineering*, vol. 20, no. 4, pp. 342–347, 2007.

[17] L. G. Austin, R. R. Klimpel, and P. T. Luckie, *The Process Engineering of Size Reduction: Ball Milling*, Society for Mining Metallurgy & Exploration, Englewood, 1984.

[18] T. Tokmakci, A. Ozturk, and J. Park, "Boron and zirconium co-doped TiO_2 powders prepared through mechanical ball milling," *Ceramics International*, vol. 39, no. 5, pp. 5893–5899, 2013.

[19] H. Shin, S. Lee, H. Suk Jung, and J.-B. Kim, "Effect of ball size and powder loading on the milling efficiency of a laboratory-scale wet ball mill," *Ceramics International*, vol. 39, no. 8, pp. 8963–8968, 2013.

[20] T. M. Cook and T. H. Courtney, "The effects of ball size distribution on attritor efficiency," *Metallurgical and Materials Transactions A: Physical Metallurgy and Materials Science*, vol. 26, no. 9, pp. 2389–2397, 1995.

[21] F. M. Katubilwa and M. H. Moys, "Effect of ball size distribution on milling rate," *Minerals Engineering*, vol. 22, no. 15, pp. 1283–1288, 2009.

[22] N. S. Lameck, K. K. Kiangi, and M. H. Moys, "Effects of grinding media shapes on load behaviour and mill power in a dry ball mill," *Minerals Engineering*, vol. 19, no. 13, pp. 1357–1361, 2006.

[23] D. Basset, P. Matteazzi, and F. Miani, "Designing a high energy ball-mill for synthesis of nanophase materials in large quantities," *Materials Science and Engineering: A Structural Materials: Properties, Microstructure and Processing*, vol. 168, no. 2, pp. 149–152, 1993.

[24] A. M. Osorio, J. M. Marín, and G. Restrepo, "Diseño y evaluación energética de dos circuitos de molienda y clasificación para un clinker de cemento a escala piloto," *Información tecnológica*, vol. 24, no. 2, pp. 99–108, 2013.

[25] D. Del Pozo, L. N. López de Lacalle, J. M. López, and A. Hernández, "Prediction of press/die deformation for an accurate manufacturing of drawing dies," *The International Journal of Advanced Manufacturing Technology*, vol. 37, no. 7-8, pp. 649–656, 2008.

Hindawi
Mathematical Problems in Engineering
Volume 2019, Article ID 5182629, 14 pages
https://doi.org/10.1155/2019/5182629

Research Article

Numerical Modeling and Experimental Characterization of Elastomeric Pads Bonded in a Conical Spring under Multiaxial Loads and Pre-Compression

Debora Francisco Lalo,[1] Marcelo Greco ,[1] and Matias Meroniuc[2]

[1]*Department of Structural Engineering, Federal University of Minas Gerais, Av. Antônio Carlos 6627, Belo Horizonte 31270-901, MG, Brazil*
[2]*Fluid Mechanics Laboratory, Railway Engineering, National Technological University, París 532, Haedo, Buenos Aires, Argentina*

Correspondence should be addressed to Marcelo Greco; mgreco@dees.ufmg.br

Received 16 November 2018; Revised 22 December 2018; Accepted 27 December 2018; Published 4 February 2019

Guest Editor: Sutasn Thipprakmas

Elastomeric components are widely used in the engineering field since their mechanical properties can vary according to a specific condition, enabling their applications under large deformations and multiaxial loading. In this context, the present study seeks to investigate the main challenges involved in the finite element hyperelasticity simulation of rubber-like material components under different cases of multiaxial loading and precompression. The complex geometry of a conical rubber spring was chosen to deal with several deformation modes; this component is in the suspension system placed between the frame and the axle for railway vehicles. The framework of this study provides the correlation between axial and radial stiffness under precompression obtained by experimental tests in prototypes and virtual modeling obtained through a curve fitting procedure. Since the material approaches incompressibility, different shape functions were adopted to describe the fields of pressure and displacements according to the finite element hybrid formulation. The material parameters were accurately adjusted through an optimization algorithm implemented in Python program language which calibrates the finite element model according to the prototype test data. However, as an initial guess, the proper constitutive model and its parameters were first defined based only on the uniaxial tensile test data, since this test is easy to perform and well understood. The validation of the simulation results in comparison with the experimental data demonstrated that care should be given when the same component is subjected to different multiaxial loading cases.

1. Introduction

Since new products development has always been increasing, several efforts have been focused on reducing time and costs. As the usual prototype construction is generally very expensive and time consuming, numerical simulation tools like the finite element method should become more reliable.

Even though a number of materials are available, elastomers play an important role in the product properties definition since it fulfills a wide range of functional tasks. Their typical applications are related to vibration damping, acoustic insulation, sealing, coupling, tires, consumer goods, and so on. The high elasticity and the ability to support large deformations under external forces are their basic characteristics [1, 2].

In railway industry the rubber springs are very useful, since they accommodate oscillatory motions and allow axes misalignments. They are located in the primary suspension, between the bogie frame and the axle box. Although a wide range of geometries can be found in order to fulfill user requirements, the conical rubber spring is one of the most used designs, since it acts as a universal damping and guiding element [3, 4]. It consists of rubber pads bonded on its inner and outer metal surfaces layers conically arranged. Thus, it is worth mentioning that this component needs to combine high stiffness for axle-guiding and an optimally vertical rigidity due to damping purposes.

Besides the conical rubber spring, the most common rubber components are subjected to different multiaxial loading cases in the real working conditions. For this reason,

choosing a proper material model to be implemented in the numerical simulations is necessary to better describe the component behavior under each loading case [5].

Since rubbers are materials that exhibit nearly incompressible behavior and often experience high strains in service, their strain states are usually very complex. Thus, their mechanical behavior should be defined based on strain energy potentials formulated according to the hyperelasticity theory. They are a mixture of tension, compression, and shear with a very small amount of volume change.

The strain energy density function (W) defines the strain energy stored in the material per unit of reference volume. This function depends on the principal stretches or invariants of the strain tensor and it is directly linked to the material's stress-strain relationship which depends on a series of parameters (material constants) [6]. Therefore, in order to assess the rubber-like material constitutive law, some experiments should be performed for input data in curve fitting procedures for the Finite Element Analysis (FEA).

Several published works related to rubber bushing have been extensively researched since last decades. The first studies have been performed by Adkins and Gent [7], where the authors found a formulation to predict the stiffness variation according to the bushing length for four principal modes of deflection termed: torsional, axial, radial, and tilting. Hill [8–10] performed studies related to the radial deformations of bonded cylindrical rubber bush mountings and its precompression effect. Petek and Kicher [11] experimentally investigated the nonlinear behavior of a shear bushing with conical ends focusing on the axial quasi-static load/deflection properties.

In addition to the empirical bushing models, constitutive modeling through FEA has also been studied. Despite the main challenges about computational efforts and time-consuming process, Morman and Pan [12] performed studies comparing the closed-form analytical equations developed for the application in the design of elastomeric components and simulation response through FEA. They argued that the closed-form equations should not provide accurate results in case of more complicated geometries and complex boundary conditions.

Besides the studies presented above, Horton et al. [13–15] derived more accurate expressions for annular rubber bush mountings subjected to radial loading and tilting deflection based on the classical theory of elasticity. In the meantime, Luo et al. [3] obtained the stress state of a simplified conical rubber spring by FEA according to the von Mises criterion. They compared the prototype experimental data with simulations, but only focusing on strength and durability of metal parts of the system. Kadlowec et al. [16] performed studies in which annular bushings were subjected to radial, torsional, and coupled radial-torsional modes of deformation. They compared the elastic bushing response obtained experimentally with finite element results. As far as the torsional mode is concerned, Horton and Tupholme [17] derived new closed-form expressions for the torsional stiffness of spherical rubber bush mountings in the two principal modes of angular deformation. Despite the reasonably agreement of some analytical relationships, there have been some limitations in the use of closed-form equations, being not possible to cover all the real situations.

Thus, for the last ten years the modeling of rubber components through the finite element method has been increasingly used. Gil-Negrete et al. [18] predicted the dynamic stiffness of filled rubber isolators using a finite element (FE) code. Olsson [19] presented a method to analyze the dynamic behavior of rubber components under radial loading by considering an overlay of viscoelastic and elastoplastic finite element models. Gracia et al. [20] studied two types of filled rubber industrial components subjected to several loads using FE analysis with the overlay model. Finally, Lee et al. [21] proposed a hybrid method based on FEA and empirical modeling to obtain the hysteresis of suspension rubber bushings and predict the dynamic stiffness without performing iterative experiments and avoiding high computational costs.

Since the rubber properties for FEA should be defined from experimental data, Seibert and his coworkers [22] studied an optimized specimen's shape through biaxial extension to calibrate the hyperelastic material parameters for the simulation of an engine mount placed in a car under multiaxial loading. Furthermore, Kaya et al. [23] simulated the behavior of a vehicular rubber bushing using FEA and performed the shape optimization to redesign its geometry and to meet the target static stiffness curve. Lalo and Greco [6] compared the rubber bushing behavior extracted experimentally with hyperelastic models based on shore hardness and uniaxial extension.

Based on the apparent extent of earlier works in modeling bushing response through FEA, it is possible to state that the hyperelastic constitutive models predefined in finite element codes are able to simulate geometry-independent bushings. However, some challenges need to be overcome when dealing with different multiaxial loading cases. In this situation, the present paper seeks to implement an optimization algorithm to characterize the hyperelastic constitutive model according to the applied multiaxial loading. Although the loading directions are axial and radial, the complex geometry of the component results in multiaxial modes of deformation on the rubber pads. It will be shown that care should be taken when the load direction is changed and the previous characterization cannot be valid anymore.

2. Hyperelasticity Theory

Hyperelastic material models are very usual to define the mechanical behavior of elastomers, foams, and many biological tissues. Since elastomers are materials that exhibit nearly incompressible behavior and often experience high strains in service, its states of strain are usually very complex [6].

The constitutive laws for hyperelastic materials are basically defined in two main theories: phenomenological or micromechanical. The phenomenological models capture the overall behavior of some polymers and fit their experimental data with reasonable accuracy aiming to minimize computational effort. The first representative formulations were developed in the works of Mooney [24] and Rivlin [25]. After that, Rivlin and Saunders [26] have proposed a new

constitutive model, currently known as Mooney-Rivlin. In the 90s, Yeoh [27, 28] proposed a model by truncating the polynomial series to the first invariant and added more terms in order to increase accuracy. The simplest form of Rivlin's strain energy function is the neo-Hookean, based only on the first term [28]. The phenomenological models can also be formulated in terms of principal stretches as in Valanis and Landel [29] and Ogden [30].

On the other hand, the micromechanical models are based on statistical mechanics to capture the network evolution of cross-linked polymer chains and to predict the three-dimensional material response. This model can be applied to unusual polymers types, being first studied in the works of Flory and Rehner [31], James and Guth [32], Treloar [33–35], and Wang and Guth [36]. Later, the classical models such as van der Waals proposed by Kilian et al. [37], Arruda-Boyce [38], and Gent [39] were developed and nowadays are implemented in several FEA commercial software. In 2002, Pucci and Saccomandi [40] proposed some modifications in the Gent model seeking to obtain a very good fit to uniaxial data over the full range of deformations. Apart from these models many others have been developed over the years.

The strain energy functions (called "W") used in hyperelastic models are derived according to the invariants of Green strain tensor which are expressed in terms of principal stretch ratios:

$$W = W\left(I_1, I_2, I_3\right) = W\left(\lambda_1, \lambda_2, \lambda_3\right) \tag{1}$$

where the three invariants (I_1, I_2, I_3) are given in terms of the principle stretch ratios λ_1, λ_2, and λ_3 by

$$I_1 = {\lambda_1}^2 + {\lambda_2}^2 + {\lambda_3}^2 \tag{2}$$

$$I_2 = {\lambda_1}^2 \cdot {\lambda_2}^2 + {\lambda_2}^2 \cdot {\lambda_3}^2 + {\lambda_3}^2 \cdot {\lambda_1}^2 \tag{3}$$

$$I_3 = {\lambda_1}^2 \cdot {\lambda_2}^2 \cdot {\lambda_3}^2 \tag{4}$$

Aiming to minimize the numerical instabilities, when the material compressibility is a concern, it is necessary to split out the deviatoric (represented by "superscript bar") and volumetric terms of the strain energy function, represented by W_d and W_b, respectively. As a result, the volumetric term is a function of the volume ratio J only and the deviatoric part depends on the modified stretches $(\overline{\lambda_p})$:

$$W = W_d\left(\overline{\lambda_1}, \overline{\lambda_2}, \overline{\lambda_3}\right) + W_b\left(J\right) \tag{5}$$

$$\overline{\lambda_p} = J^{-1/3} \cdot \lambda_p; \quad p = 1, 2, 3 \tag{6}$$

For large deformations, it is usual to work with the Cauchy stress tensor σ [41], where its representation can be given through the principal stretches $(\lambda_1, \lambda_2, \lambda_3)$ as in

$$\sigma_i = \lambda_i \cdot \frac{\partial W}{\partial \lambda_i} - p; \quad i = 1, 2, 3 \tag{7}$$

where the first term is relative to the deviatoric (the deviatoric stress is related to shape change and it is what is left after subtracting out the hydrostatic stress) part of stress, while p refers to the hydrostatic (the hydrostatic stress is related to volume change) part of stress which is associated with the incompressibility condition.

2.1. Constitutive Models. The strain energy function particular models are defined according to a number of material parameters. Thus, the nominal stress versus nominal strain data obtained from experimental tests is required to fit these parameters in most models' theoretical behavior available. Although several constitutive models have been developed over the years, each one has its peculiarities of application [42, 43]. For this reason, the present paper will be focused on some classical constitutive models which are already implemented in the commercial software of FEA Abaqus®.

2.1.1. Neo-Hooke. The neo-Hookean material model was formulated by truncating the power series of a polynomial form [44]. This is the simplest phenomenological model since it is derived only in terms of the first invariant $(\overline{I_1})$.

$$W = C_{10} \cdot \left(\overline{I_1} - 3\right) + \frac{1}{D_1}\left(J - 1\right)^2 \tag{8}$$

where C_{10} is a material parameter for data fitting and D_1 relates to the compressibility ratio.

Treloar [45] also formulated the neo-Hookean model according to the statistical theory of rubber elasticity. Even though the phenomenological and statistical theories were formulated from quite different premises, they are considered equivalent.

This model can be a good starting point. However, the strains should be limited up to 30-40% in uniaxial extension and up to 80-90% in shear deformation [46].

2.1.2. Mooney-Rivlin. The Mooney-Rivlin model is very usual for representing the large strain nonlinear behavior of elastomers. It is also a phenomenological model and gives a good response for moderately strains in uniaxial extension and shear deformation [47]. The first order Mooney-Rivlin model can be defined by

$$W = C_{10} \cdot \left(\overline{I_1} - 3\right) + C_{01} \cdot \left(\overline{I_2} - 3\right) + \frac{1}{D_1}\left(J - 1\right)^2 \tag{9}$$

This model is based on a polynomial expansion. Thus, to obtain a N^{th} order, more terms can be added to (9). However, according to Sasso et al. [48] the results do not show major improvements.

2.1.3. Ogden. Proposed by Ogden [30], this is a phenomenological model based on the principal stretches rather than strain invariants. This model has been effective for very large strains and it is written as

$$W = \sum_{i=1}^{N} \frac{\mu_i}{\alpha_i} \cdot \left(\overline{\lambda_1}^{\alpha_i} + \overline{\lambda_2}^{\alpha_i} + \overline{\lambda_3}^{\alpha_i} - 3\right) + \sum_{k=1}^{N} \frac{1}{D_k}\left(J - 1\right)^{2k} \tag{10}$$

where μ_i and α_i are real material parameters, being positive or negative.

If a two-term expansion ($N = 2$) is applied with $\alpha_1 = 2$ and $\alpha_2 = -2$, it coincides with the 2 parameter Mooney-Rivlin form for typical values of $\mu_1 = 2 \cdot C_{10}$ and $\mu_2 = -2 \cdot C_{01}$. If N is set to 1 with $\alpha_1 = 2$ and $\mu_1 = \mu_0 = 2 \cdot C_{10}$, it degenerates to the neo-Hookean form [41]. The Ogden model is very useful for simple extension up to 700% [46].

2.1.4. Yeoh. Yeoh [27, 28] introduced a phenomenological model only based on the $\overline{I_1}$. Since a polynomial form of W is used but the other deviatoric strain invariants are not, the Yeoh model can be also called reduced polynomial model and it has the general form:

$$W = \sum_{i=1}^{N} C_{i0} \cdot \left(\overline{I_1} - 3\right)^i + \sum_{k=1}^{N} \frac{1}{D_k} (J-1)^{2k} \tag{11}$$

According to Yeoh [28], the terms containing $\overline{I_2}$ were eliminated from the equation since its variation in the sensitivity of W function is negligible if compared to $\overline{I_1}$. Thus, it is possible to improve the model's ability when predicting the behavior of deformation states over a large strain range even when limited test data is available.

The Yeoh model is commonly considered with $N = 3$, and the upturn of the stress-strain curve can be captured. This model is generally applied in the characterization of carbon-black filled rubbers [27] but is not useful when low strains are involved.

2.1.5. Arruda-Boyce. Proposed by Arruda and Boyce [38], this model was developed based on a statistical treatment of the non-Gaussian chains, and for this reason it is also known as the eight-chain model. As this model represents the physics of network deformation, they are micromechanical models and can be described as follows:

$$W = \mu \sum_{i=1}^{5} \frac{C_i}{\lambda_L^{2i-2}} \cdot \left(\overline{I}_1^i - 3^i\right) + \frac{1}{D}\left(\frac{J^2-1}{2} - \ln J\right) \tag{12}$$

where the material constants are predefined functions of the limiting network stretch "λ_L" as follows:

$$\begin{aligned} C_1 &= \frac{1}{2}; \\ C_2 &= \frac{1}{20}; \\ C_3 &= \frac{11}{1050}; \\ C_4 &= \frac{19}{7000}; \\ C_5 &= \frac{519}{673750} \end{aligned} \tag{13}$$

From (12), it is possible to note that the Arruda-Boyce model is similar to the Yeoh form, but with $N = 5$.

According to Arruda and Boyce [38], this model is unique since it is able to provide great accuracy for multiple modes of deformation based only on the standard uniaxial tensile test.

2.2. Finite Element Hybrid Formulation. In this approach, pressure is treated as an uncoupled variable and it must receive a suitable formulation through the weak form of the Finite Element Method (FEM). Since in almost incompressible problems the bulk modulus K is relatively high, its relation to the pressure is given through the Cauchy stress tensor:

$$\boldsymbol{\sigma} = K(J-1) \cdot \boldsymbol{I} = -p \cdot \boldsymbol{I} \tag{14}$$

$$p = -K(J-1) \tag{15}$$

Linearizing (15) in relation to the displacement field [41], there is

$$p = -K\left(\frac{\partial u}{\partial x} + \frac{\partial v}{\partial y} + \frac{\partial w}{\partial z}\right) \tag{16}$$

Therefore, it is worth mentioning that pressure p has less variation than the displacements field and, for this reason, it must be treated as an uncoupled term. That is, it must be treated separately as an independent variable in the FEM formulation [49]. If the problem is effectively incompressible, a relatively high value of the variable K is assigned, forcing it to an incompressibility condition solved by a penalty procedure, in which the pressure variables act as Lagrange multipliers to force the condition of incompressibility.

In view of the above, the hybrid formulation can be used by FEM, where different shape functions are adopted to describe the fields of pressure and displacement. In the case of pressure, a lower order variation must be attributed:

$$\begin{aligned} p &= \Sigma N_{pi} \cdot p_i; \\ u &= \Sigma N_i \cdot u_i; \\ v &= \Sigma N_i \cdot v_i; \\ w &= \Sigma N_i \cdot w_i \end{aligned} \tag{17}$$

where p_i refers to the nodal pressure variables constituting the vector $\boldsymbol{p}$ and u_i, v_i, w_i the nodal displacements that constitute the vector $\boldsymbol{d}$.

Thus, (17) can be rewritten as

$$\begin{aligned} p &= \boldsymbol{N}_p{}^T \cdot \boldsymbol{p}; \\ \delta p &= \boldsymbol{N}_p{}^T \cdot \delta \boldsymbol{p}; \\ d &= \boldsymbol{N}^T \cdot \boldsymbol{d} \end{aligned} \tag{18}$$

All in all, the boundary value problem can be expressed in the weighted form, integrating the solid domain through a weight function. Therefore, through the Principle of Virtual Work (PVW) the equilibrium condition of the internal forces $\boldsymbol{q}_i$ and external $\boldsymbol{q}_e$ in the volume can be obtained [41].

$$\delta \boldsymbol{q}_e = \delta \boldsymbol{q}_i = \int \boldsymbol{B}_{nl}^T \delta \boldsymbol{S} dV_o + \int \delta \boldsymbol{B}_{nl}^T \boldsymbol{S} dV_o \tag{19}$$

The forces and pressures variables coupling vector is called $\boldsymbol{a}$ and can be derived as

$$\boldsymbol{a} = \int \boldsymbol{B}_{nl}^T \boldsymbol{g}_{tK2} \delta p dV_o = \boldsymbol{P} \delta \boldsymbol{p} \tag{20}$$

where δp is the pressure variation in terms of nodal variables $\delta \boldsymbol{p}$ and $\boldsymbol{g} = \boldsymbol{q}_i - \boldsymbol{q}_e$. The subscript $\boldsymbol{K}2$ shows that the

tensor refers to the 2nd Piola-Kirchoff stress tensor. Thus, the differentiation of the matrix $\boldsymbol{P}$ is given by

$$\boldsymbol{P} = \frac{\partial \boldsymbol{q}_i}{\partial \boldsymbol{p}} = \frac{\partial \boldsymbol{g}}{\partial \boldsymbol{p}} = \int \boldsymbol{B}_{nl}^T \boldsymbol{g}_{tK2} \boldsymbol{N}_p^T dV_o \tag{21}$$

In addition, the pressure-displacement relationship of (15) should still be considered. In this case, the Galerkin Method must be applied to obtain the weak form of (15) by multiplying it by δp and integrating it over the element.

$$\begin{aligned} &\int \left((J-1) + \frac{p}{K} \right) \delta p dV_o \\ &= \delta \boldsymbol{p}^T \int \boldsymbol{N}_p \left((J-1) + \frac{p}{K} \right) dV_o = \delta \boldsymbol{p}^T \boldsymbol{f} = \boldsymbol{0} \end{aligned} \tag{22}$$

This relationship should hold for any $\delta \boldsymbol{p}$, where $\boldsymbol{f}$ represents the lack of pressure compatibility:

$$\boldsymbol{f} = -\int \boldsymbol{N}_p \left((J-1) + \frac{p}{K} \right) dV_o = 0 \tag{23}$$

The equations above represent the governing relationships between the displacement and nodal pressure variables. For a purely incompressible problem, the term p/k from (23) would disappear and this equation could be used in the weak form of the incompressibility constraint.

It is worth mentioning that the governing equation (23) involves the pressure and not its derivative, so the pressure to be continuous between the elements is not necessary. Hence, they can be treated as internal variables of the system. As a way to reduce the number of additional unknowns, in general one of these conditions (force or displacement) is admitted in the strong form, while the second is the weak form obtained by weighting. Since the formulations were adopted in the almost incompressible materials, the weak form has been attributed to the pressure.

3. Data Fitting Optimization Algorithm

Based on optimization techniques the simulation models can be calibrated by minimizing different error measures related to force-displacement experimental response.

The problem arises from a set of arguments that give a minimal function value under a set of constraints. The general mathematical description of an optimization problem can be expressed as indicated in (24), where by convention the problem is often represented as the minimization of an objective function.

$$\begin{aligned} \vec{x}^* = \text{argmin} \quad & f\left(\vec{x}\right) \\ \text{subject to:} \quad & g_i\left(\vec{x}\right) = a_i, \quad i = 1, \ldots, p \\ & h_j\left(\vec{x}\right) \leq b_j, \quad j = 1, \ldots, q \end{aligned} \tag{24}$$

where the vector $\vec{x}$ refers to the material parameters assigned as design variables and $f(\vec{x})$ is the objective function which represents the error function between experimental data and simulation model. The constraints mean the set of requirements the project must meet to be admissible as a solution, being in this case, represented by $g_i(\vec{x})$ and $h_j(\vec{x})$, respectively. The parameters a_i and b_j are vectors that respectively correspond to the values of the equality and inequality constraints for each position i and j.

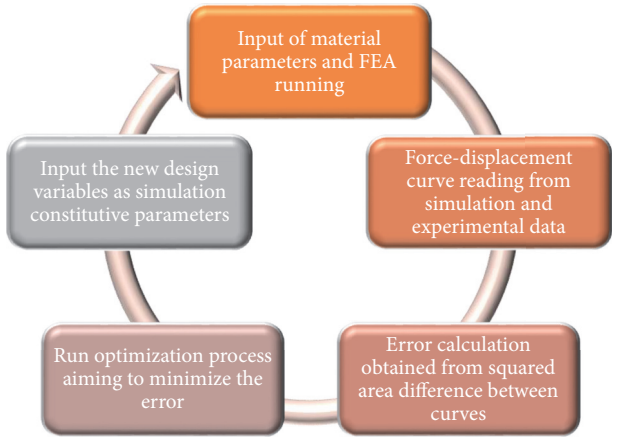

Figure 1: Automation of the process implemented for data fitting optimization.

The implemented pattern search optimization method was proposed by Hooke and Jeeves [50] and does not require a gradient calculation. This algorithm examines points near the current point by perturbing design variables until an improved point is found. It then follows the favorable direction until no more design improvement is possible. The convergence is detected according to a Step Size Reduction Factor until the step-length is sufficiently small or when a maximum number of runs are reached. The implemented algorithm can be found in [51].

Since the nature of the objective function is unknown a priori, this is a well-suited method for the curve fittings obtained by finite element simulation. Performing some adjustments of the tuning parameters like step sizes and number of iterations, it finds the optimal solution even if multiple local minima are present. However, if a quadratic function is used, it is obviously less efficient than gradient methods. The optimization process coupled with finite element simulation is depicted in Figure 1. The design variables change automatically throughout the process and the force-displacement curve depends on the material parameters for accounting the error.

This process was implemented through Python and Abaqus® scripting interface. The files containing the Python commands run with the extension ".py". This option became interesting for the proposed problem since it can be used to perform the following tasks:

(i) Automation of repetitive tasks, such as the sequence of structural analyses via FEM;

(ii) Parametric studies which modify the model, such as the attribution of different physical properties;

(iii) Access to an output database, such as reading the postprocessing results.

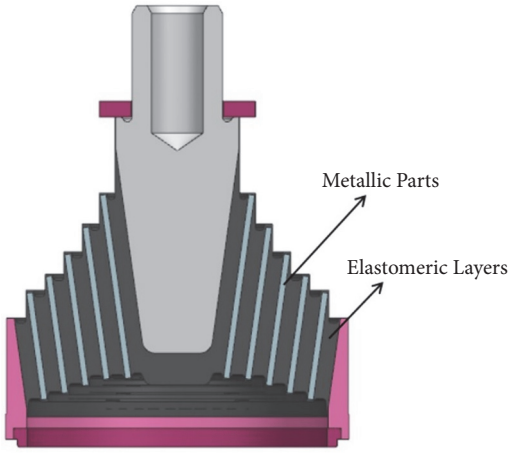

Figure 2: Conical rubber spring design.

Figure 3: Assembly for the axial stiffness test.

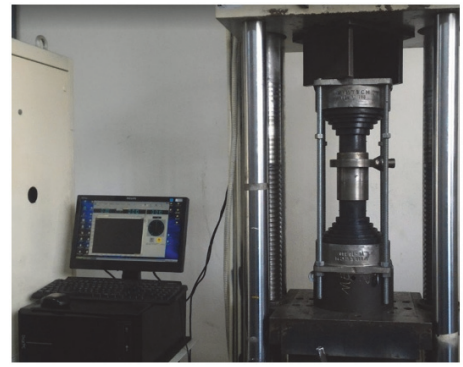

Figure 4: Assembly for a preload equivalent to 20kN, performed before radial stiffness test.

4. Prototype Experimental Tests

Conical rubber springs are used as vibration isolators combining the function of primary damping and axle linkage in a single component. Its design is compact and light, making it easy for retrofitting. It consists of one or several conically arranged elastomeric layers bordered by adequately molded metallic components, the conical metallic molded parts should provide a separation between the various elastomeric layers as shown in Figure 2.

The conical spring application and its performance depend on the number of elastomeric layers, the cone tilt angle, and the selection of an optimum elastomeric compound. As the rubber is in both compression and shear when loaded, the conical springs allow for considerable excursion and have a progressive characteristic curve. It allows the transmission of longitudinal traction/braking loads and transverse guidance loads, as well as the vertical flexibility. It must fulfill with the requirements of the standard NF EN 13913 [52] for rubber-based parts.

The vulcanization characteristic curve should be in accordance with standard NFT 43-015 [53] or ISO 6502 [54] and the mechanical characteristics on test pieces in conformity with standard NFT 46-002 [55] or ISO 37 [56].

The maximum load of 40kN must be supported by the spring without any damage.

4.1. Static Axial Stiffness. The static axial stiffness is measured in the vertical position. First two preload cycles are applied from 0 to 40kN to stabilize the rubber properties due to stress softening. Then, the load/deflection curve is recorded during the third cycle.

The testing machine is illustrated according to Figure 3, where two power screws are responsible for the translational motion to compress the spring through a metal block controlled by a load cell.

4.2. Static Radial Stiffness. To account for static radial stiffness, an axial preload equivalent to the tare load of 20kN is first applied (Figure 4). Following, two preload cycles ranging from equivalent to -6 to 6mm are applied in the radial direction (Figure 5). Then, the load/deflection curve is recorded during the third cycle.

5. Finite Element Method for Analysis Correlation

The finite element method is a popular tool for designing elastomeric components. This numerical method is able to approximate the stress-strain behavior of rubber components based on a theoretical material model.

The least squares method is used to determine the best curve fitting for each constitutive model since the number of stress equations will be greater than the number of unknown constants. Thus, for each "n" stress-strain pair which makes up the test data, the following error measure "Er" is minimized [57]:

$$Er = \sum_{i=1}^{n} \left(1 - \frac{T_i^{th}}{T_i^{test}}\right)^2 \tag{25}$$

where T_i^{test} is the stress value from the test data and T_i^{th} is the theoretical stress from the fitted curve.

Figure 5: Assembly for the radial stiffness test.

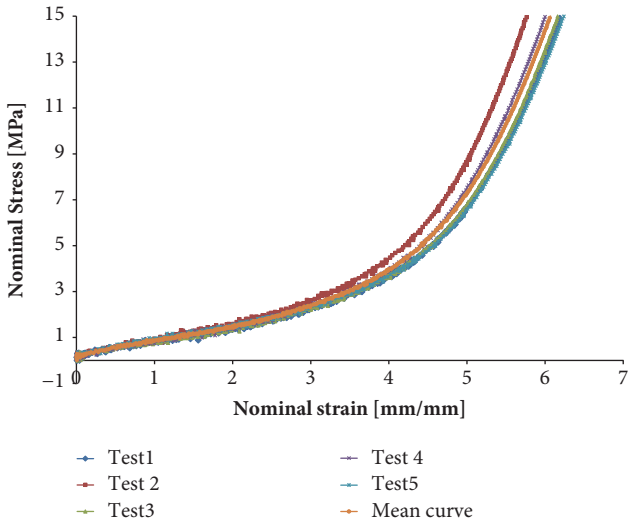

Figure 6: Uniaxial mean curve obtained from experimental tests.

In many cases, the material curve is only fitted according to the uniaxial test data. This happens due to test limitations for the other states of pure deformation. Therefore, the present study carried out uniaxial tensile tests for 5 samples from the same batch according to ASTM D412 [58], in order to obtain the mean uniaxial curve as shown in Figure 6.

The correlation between uniaxial test data and theoretical curves fitted according to the classical constitutive models in study is shown in Figure 7. The biaxial and planar shear behaviors could also be estimated by each constitutive model strain energy, and they are described according to Figures 8 and 9, respectively. The material was assumed to be almost incompressible with a Poisson's ratio equal to 0.4995 (K_0/μ_0 = 1000). The relative errors should also be accounted in order to infer the constitutive models performance as in [59, 60], and they are depicted according to Figure 10 with respect to the uniaxial experimental data over the entire strain range.

It is possible to note that the uniaxial data could be well fitted by higher order phenomenological constitutive models and micromechanics. The lower order models (Mooney-Rivlin, Neo-Hooke, and Ogden-N1) tried to fit the data linearly and for this reason the relative error had only two minimum points over the strain. The accumulated relative error for each model is presented according to Table 1.

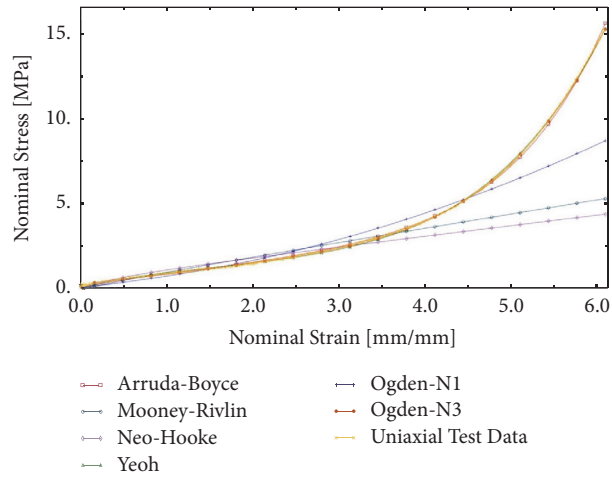

Figure 7: Material curve fitting based on uniaxial experimental data.

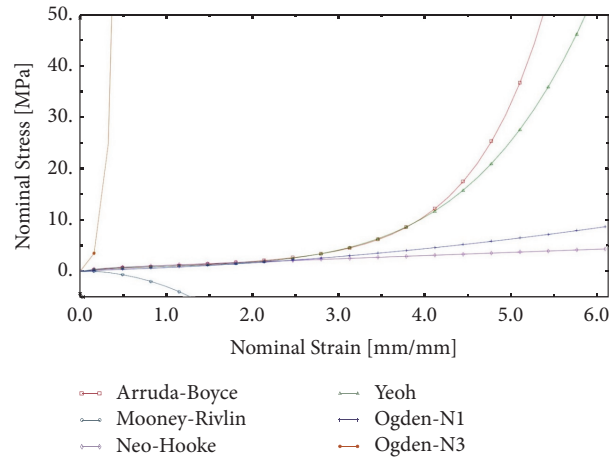

Figure 8: Estimated curve behavior for biaxial deformation mode.

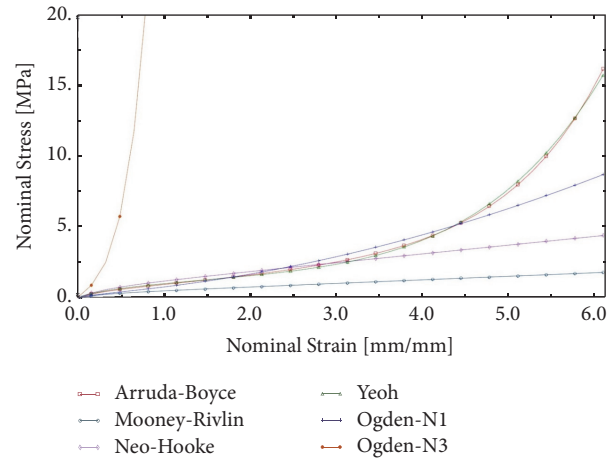

Figure 9: Estimated curve behavior for planar shear deformation mode.

Table 1: Accumulated relative errors for uniaxial data fitting.

Yeoh	Arruda-Boyce	Mooney-Rivlin	Neo-Hooke	Ogden-N3	Ogden-N1
18.7	20.8	107.6	118.5	11.1	77.9

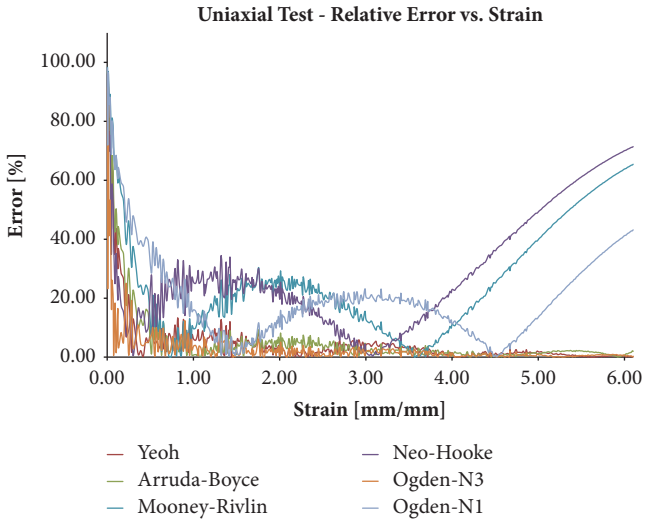

Figure 10: Relative errors (%) against strain range for each constitutive model in study.

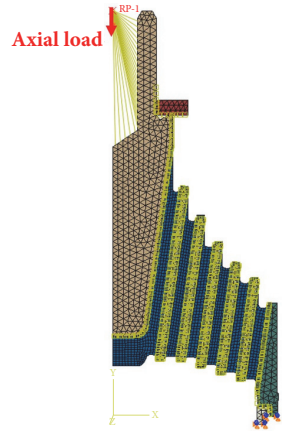

Figure 11: Conical rubber spring finite element model for axial stiffness (axisymmetric section).

5.1. Axial Stiffness FEA Modeling. For the case of axial stiffness simulation, the conical rubber spring under investigation has been treated as an axisymmetric model due to its rotational symmetry and axial load applied in the center point.

The FEA was performed using the commercial software Abaqus®. To represent the rubber material, a 4-node bilinear quadrilateral axisymmetric element with hybrid formulation, constant pressure, and reduced integration with hourglass control (CAX4RH) has been used, and the metal parts were modeled by using a 3-node linear triangle axisymmetric element (CAX3). The hybrid formulation is suitable for strictly incompressible materials, such as rubber, and it is represented by the letter "H" at the end of element name. The capabilities of this implementation with its boundary conditions can be shown in Figure 11, where a simplified 3D model is discretized into 2978 2D axisymmetric elements.

5.2. Radial Stiffness FEA Modeling. For the case of radial stiffness simulation, the conical rubber spring has been treated as a 3D solid model. Here, it is not possible to use the axisymmetric approach since the load is not applied in the axial direction.

In the same way, as in axial stiffness, FEA was performed using the commercial software Abaqus®. The rubber was modeled by an 8-node linear hex element with hybrid formulation and constant pressure (C3D8RH); the reduced integration and hourglass control was also inputted to reduce the volumetric constraints, avoiding the overly stiff behavior due to volumetric locking. The metal parts were modeled by using a 10-node tetrahedron with an improved surface stress formulation (C3D10I).

The implementation must be performed in two analysis steps. The first step refers to the vertical preload to put the component in a prestressed condition. Afterward, in the second step the radial force is applied through an imposed displacement of 6mm.

The 3D model was discretized into 213814 solid elements. The implementation with its boundary conditions for each step is shown in Figure 12.

6. Finite Element Analysis Validation according to Prototype Experimental Data

The performance of some classical constitutive models implemented in the commercial software Abaqus (Yeoh, Mooney-Rivlin, Ogden, Neo-Hooke, and Arruda-Boyce) had been first investigated through uniaxial test data only. Next, the constitutive models with their respective material parameters were implemented in the conical rubber spring model to evaluate its behavior in the axial deflection mode. The comparison between FEA and prototype test data is shown in Figure 13. The relative errors were also accounted over the displacement according to Figure 14 in order to analyze the performance of each constitutive model, but considering now that the same rubber is subjected to multiaxial loading. Table 2 shows the accumulated relative error for each model.

During the simulations, Mooney-Rivlin and Ogden-N1 models were not able to achieve the high axial deflection performed by the prototype test. The Mooney-Rivlin model became unstable under deflections higher than approximately 37mm; on the other hand, Ogden-N1 could overcome 37mm but was only stable for deflections up to 55mm. In both cases, the analyses were aborted due to an artificial

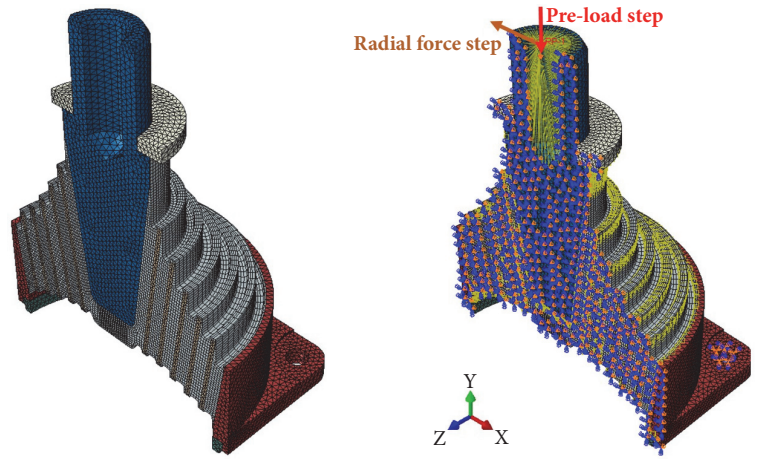

Figure 12: Conical rubber spring finite element model for radial stiffness. (a) Mesh and (b) entire model with its boundary conditions.

Table 2: Accumulated relative errors for conical rubber spring (rubber characterization according to uniaxial tensile test curve fitting).

Yeoh	Arruda-Boyce	Mooney-Rivlin	Neo-Hooke	Ogden-N3	Ogden-N1
114.1	76.8	97.2	195.0	4559.6	61.6

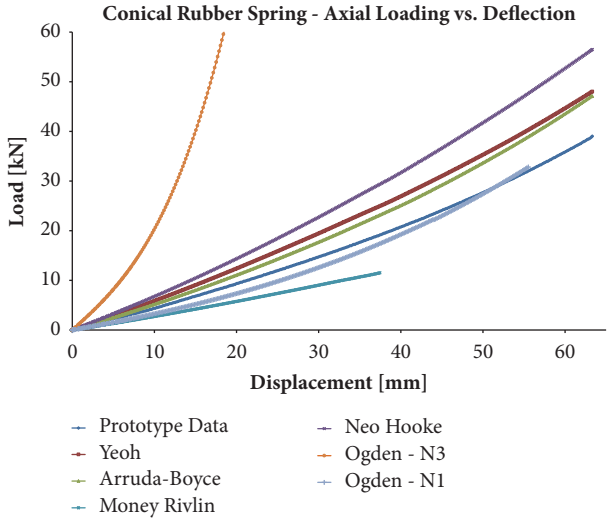

Figure 13: Conical rubber spring behavior comparison with prototype experimental data and classical constitutive models in the axial load direction.

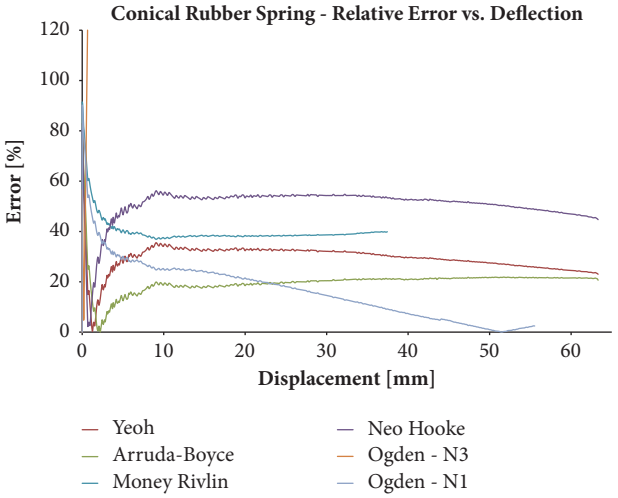

Figure 14: Relative errors (%) against axial deflection for each constitutive model in the conical rubber spring study.

increasing in load-deflection curve at a structural level and an overprediction of the collapse load tending to volumetric locking, despite the hybrid formulation and the reduced integration adopted in the modeling process.

In spite of the good fitting of experimental simple tension data, Ogden-N3 provided very high relative errors. The load-deflection curve presented in Figure 13 showed a much higher stiffness than the experimental response. This may happen, since the planar shear and biaxial curves had been defined with a much higher stiffness for this model. Thus, if test data for some of the other deformation modes is missing, care should be taken with this model when trying to predict the rubber component behavior under multiaxial loading.

According to Figure 15 it is possible to compare the undeformed (a) and deformed (b) shapes. Maximum displacement value occurs around the metal axle, more exactly at the point where the concentrated load was applied. Although the rubber section undergoes large strains, it still keeps a reasonable shape, without excessive distortion.

Thus, by evaluating the relative error curves obtained in Figure 14, it can be observed that the Arruda-Boyce model is the one which best correlated the prototype load-deflection experimental curve. From this model, an optimization study

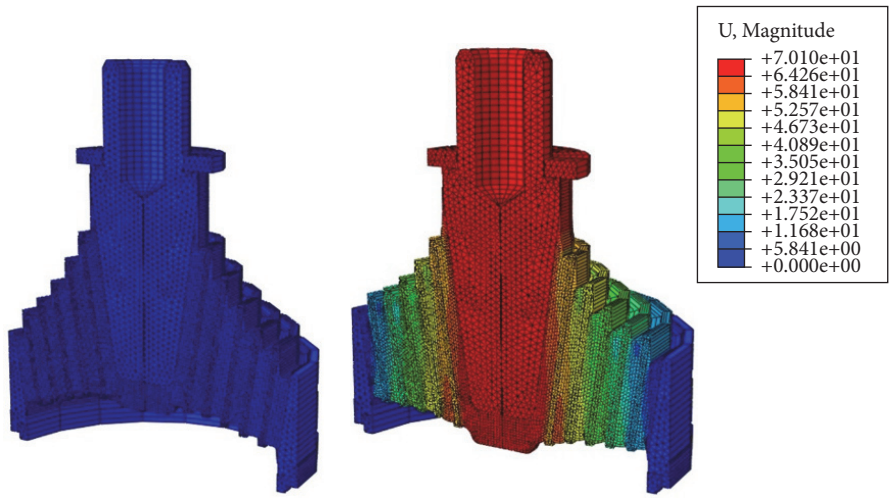

Figure 15: Conical rubber spring deformation under axial load (a) undeformed shape and (b) deformed shape.

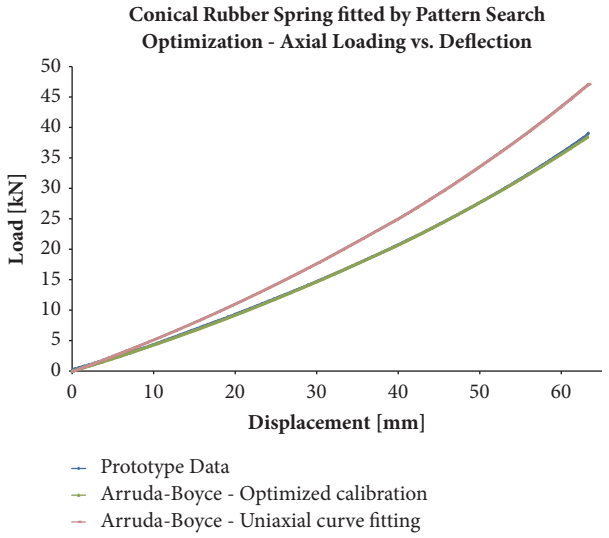

Figure 16: Conical rubber spring axial loading-deflection curve based on pattern search optimization algorithm.

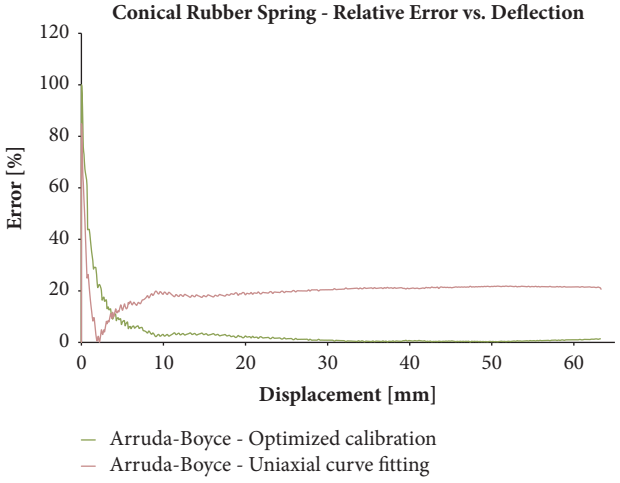

Figure 17: Relative errors (%) against axial deflection for Arruda-Boyce model based on pattern search optimization algorithm.

was performed based directly on the prototype test data in order to recalibrate the material parameters, aiming to increase the accuracy degree in the component behavior that depends on the multiaxial deformation mode in which the rubber is submitted.

Table 3 shows the constants of the Arruda-Boyce model obtained by uniaxial stretching test and which was assigned as initial guesses of the design variables in the pattern search optimization process, as well as their final values after the simulation process is completed.

From the results in Figure 16, we note that the implemented optimization algorithm allows a much more accurate adjustment. However, the prototype test data will always be necessary for the material characterization, aiming as an objective function minimizing the error between the curves computed by the area difference. Figure 17 shows the relative errors over the displacement to prove the optimization algorithm efficiency in the adopted model. The accumulated relative error dropped from 76.8 to 18.1.

Through the material model obtained by the implemented optimization algorithm for axial deflection, the component mechanical behavior under precompression is verified by applying the loading in the radial deflection direction.

Figure 18 shows the force-displacement curve for the second analysis step, taking into account the precompression condition when applying the radial imposed displacement. It can be seen that the material model used in this second study is no longer capable of reproducing the results with the same accuracy as the previous loading mode. This is because the rubber has different properties and consequently different behaviors for each mode of deformation.

Table 3: Arruda-Boyce model material parameters comparison.

Material Parameter	μ	λ_L	μ_0	D	ν
Obtained by uniaxial stretching test	0.452	3.747	0.473	4.229E-3	0.4995
Obtained by optimization process	0.380	4.271	0.393	4.948E-3	0.4995

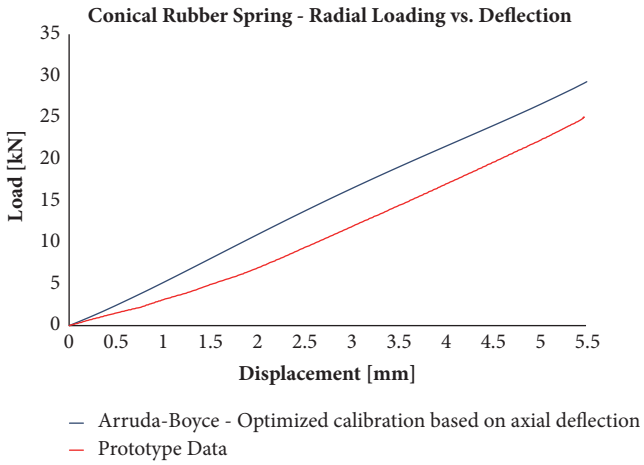

Figure 18: Conical rubber spring behavior comparison with prototype experimental data and Arruda-Boyce model in the radial load direction.

Figure 19 shows the component in the undeformed condition (a), in the deformed condition after precompression (b), and under the action of the radial loading (c). It is worth noting that according to Figure 16, the axial displacement should be approximately 40mm for an axial load of 20kN. Therefore, the precompression behavior was obtained with accuracy, but the radial deflection in the second step lost this accuracy, evidencing the change of rubber properties for a different multiaxial loading mode.

7. Conclusions

In order to illustrate the load-deflection relations for a rubber spring component, the influence of multiaxial loading conditions of a typical railway industry component: the conical rubber spring was inquired.

Although several techniques and assumptions have been developed to simplify the rubber spring behavior, the formulated equations became inapplicable as the geometry becomes more complex. For this reason, the using of FEA was considered the most accurate, versatile, and comprehensive method for solving the presented complex design problem.

The finite element simulations introduced in this work dealt with nearly incompressible hyperelastic material under quasistatic condition. Since Poisson's ratio for elastomers is between 0.49 and 0.5, the elements used in FEA need to be reformulated to accommodate this high value of Poisson's ratio. For this kind of situation, the bulk modulus presents a relatively high value, much larger than the shear modulus (μ); consequently, a small change in displacement produces high changes in pressure, so the solution based purely on the displacement field becomes very numerically sensitive. Due to this instability, the present work applied the hybrid element formulation aiming to avoid the called volumetric locking. This problem may occur when the mesh can no longer represent the strain field due to an excessively stiff behavior.

Concerning the constitutive parameters obtained by the optimization process, it is possible to understand why curve fittings on elastomers are based on the main pure deformation modes (uniaxial, biaxial, and planar shear). Each deformation mode can influence the calibration constants and modify the model fitted curve. This behavior also accounts the compressibility degree since it is related to the hydrostatic part of the strain energy potential.

When the output of the simulation is compared to the experimentally obtained load-deflection curves, the huge influence of the constitutive constants under different multiaxial loading cases can be observed. That is the reason why very complex rubber component geometries show a great challenge for numerical simulations. Even with experimental test data for the main pure deformation modes, it is not always possible to obtain the component response with a high accuracy degree.

In the future, the investigations regarding cyclic multiaxial deformations taking into account the Mullins effect and viscoelastic behavior will be executed. Other deformation modes and constitutive models including the GG-model [40], which states to be very effective during the entire range of uniaxial tension data [60] and simpler than Arruda-Boyce [40], will also be evaluated in order to compare the simulation response with prototypes test and better clarify the rubber complex behavior.

Data Availability

The data used to support the findings of this study are included within the article.

Conflicts of Interest

The authors declare that they have no conflicts of interest.

Acknowledgments

The authors are grateful for the financial support granted by Fundação de Amparo à Pesquisa do Estado de Minas Gerais (FAPEMIG), Conselho Nacional de Desenvolvimento Científico e Tecnológico (CNPq), Programa de Pós-Graduação em Engenharia de Estruturas (PROPEEs-UFMG), and Coordenação de Aperfeiçoamento de Pessoal de Nível Superior (CAPES), under grant numbers TEC-PPM-00409-16, TEC-PPM-00444-18, and 3023762/2016-0. We also

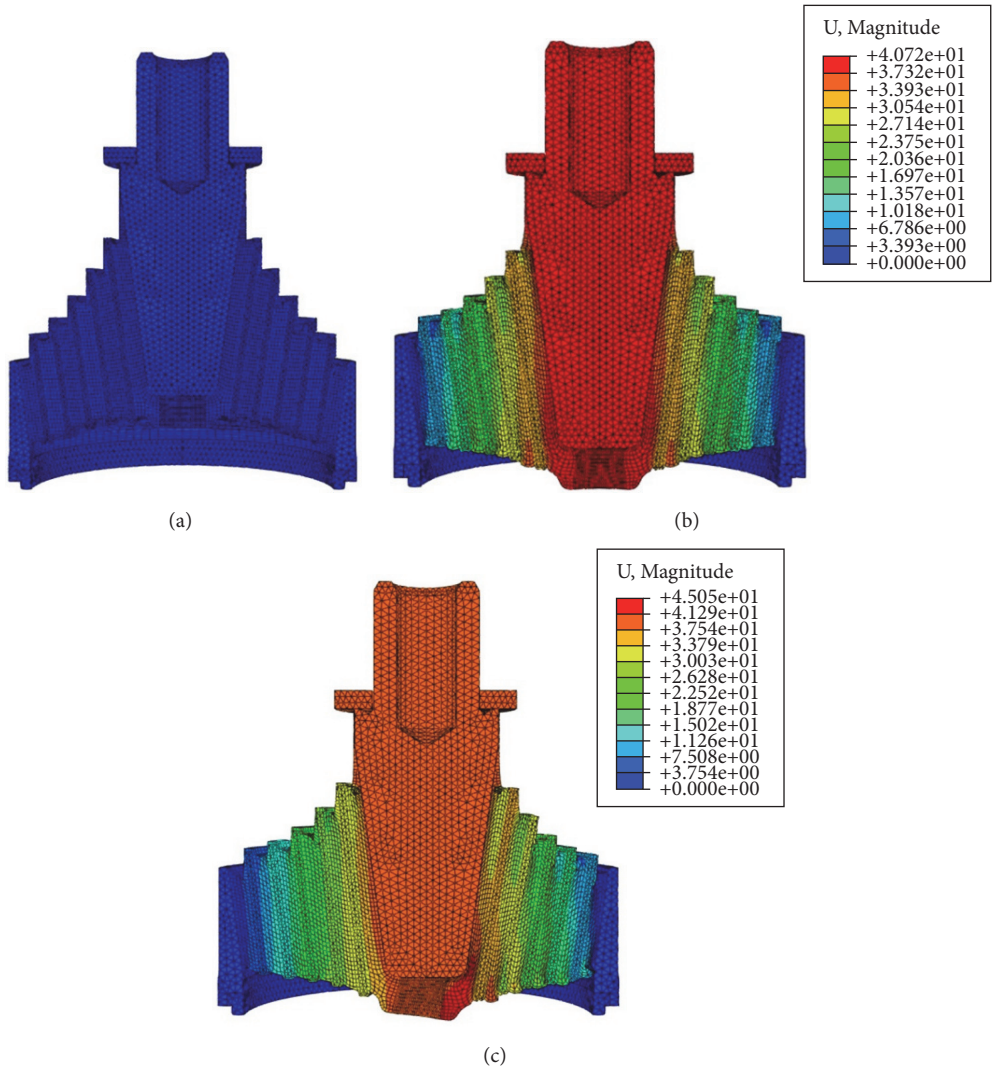

FIGURE 19: Conical rubber spring deformation under radial load (a) undeformed shape, (b) deformed shape under precompression only, and (c) deformed shape under the action of the radial loading.

acknowledge Vibtech Industrial Ltda. for the gently provided materials.

References

[1] A. Gent, "Engineering with rubber: How to design rubber components," *Rubber Chemistry and Technology*, vol. 59, no. 3, 2012.

[2] P. Eyerer, P. Hirth, and T. Elsner, *Polymer Engineering: Technologien und Praxis*, Springer, 2008.

[3] R. K. Luo, B. Randell, W. X. Wu, and W. J. Mortel, "Stress evaluation of conical rubber spring system," *TransModeler Traffic Simulation*, vol. 30, pp. 271–279, 2001.

[4] I. Sebesan, N. L. Zaharia, M. A. Spiroiu, and L. Fainus, "Rubber suspension, a solution of the future for railway vehicles," *Materiale Plastice*, vol. 52, no. 1, pp. 93–97, 2015.

[5] L. Chevalier, S. Calloch, F. Hild, and Y. Marco, "Digital image correlation used to analyze the multiaxial behavior of rubber-like materials," *European Journal of Mechanics - A/Solids*, vol. 20, no. 2, pp. 169–187, 2001.

[6] D. Lalo and M. Greco, "Rubber bushing hyperelastic behavior based on shore hardness and uniaxial extension," in *Proceedings of the 24th ABCM International Congress of Mechanical Engineering*, 2017.

[7] J. E. Adkins and A. N. Gent, "Load-deflexion relations of rubber bush mountings," *British Journal of Applied Physics*, vol. 5, no. 10, pp. 354–358, 1954.

[8] J. M. Hill, "Radical deflections of rubber bush mountings of finite lengths," *International Journal of Engineering Science*, vol. 13, no. 4, pp. 407–422, 1975.

[9] J. M. Hill, "The effect of precompression on the load-deflection relations of long rubber bush mountings," *Journal of Applied Polymer Science*, vol. 19, no. 3, pp. 747–755.

[10] J. M. Hill, "Radial deflections of thin precompressed cylindrical rubber bush mountings," *International Journal of Solids and Structures*, vol. 13, no. 2, pp. 93–104, 1977.

[11] N. K. Petek and T. P. Kicher, "Empirical model for the design of rubber shear bushings," *Rubber Chemistry and Technology*, vol. 60, no. 2, pp. 298–309, 1987.

[12] K. N. Morman and T. Y. Pan, "Application of finite-element analysis in the design of automotive elastomeric components," *Rubber Chemistry and Technology*, vol. 61, no. 3, pp. 503–533, 1988.

[13] J. M. Horton, M. J. Gover, and G. E. Tupholme, "Stiffness of rubber bush mountings subjected to radial loading," *Rubber Chemistry and Technology*, vol. 73, pp. 619–633, 2000.

[14] J. M. Horton, M. J. Gover, and G. E. Tupholme, "Stiffness of rubber bush mountings subjected to tilting deflection," *Rubber Chemistry and Technology*, vol. 73, no. 4, pp. 619–633, 2000.

[15] J. M. Horton and G. E. Tupholme, "Approximate radial stiffness of rubber bush mountings," *Materials and Corrosion*, vol. 27, no. 3, pp. 226–229, 2006.

[16] J. Kadlowec, A. Wineman, and G. Hulbert, "Elastomer bushing response: experiments and finite element modeling," *Acta Mechanica*, vol. 163, pp. 25–38, 2003.

[17] J. Horton and G. Tupholme, "Stiffness of spherical bonded rubber bush mountings," *International Journal of Solids and Structures*, vol. 42, no. 11-12, pp. 3289–3297, 2005.

[18] N. Gil-Negrete, J. Viñolas, and L. Kari, "A simplified methodology to predict the dynamic stiffness of carbon-black filled rubber isolators using a finite element code," *Journal of Sound and Vibration*, vol. 296, no. 4-5, pp. 757–776, 2006.

[19] A. K. Olsson, *Finite Element Procedures in Modelling the Dynamic Properties of Rubber*, Lund University, 2007.

[20] L. Gracia, E. Liarte, J. Pelegay, and B. Calvo, "Finite element simulation of the hysteretic behaviour of an industrial rubber. Application to design of rubber components," *Finite Elements in Analysis and Design*, vol. 46, no. 4, pp. 357–368, 2010.

[21] H. S. Lee, J. K. Shin, S. Msolli, and H. S. Kim, "Prediction of the dynamic equivalent stiffness for a rubber bushing using the finite element method and empirical modeling," *International Journal of Mechanics and Materials in Design*, pp. 1–15, 2017.

[22] H. Seibert, T. Scheffer, and S. Diebels, "Biaxial testing of elastomers—experimental setup, measurement and experimental optimisation of specimen's shape," *Technische Mechanik*, vol. 34, no. 2, pp. 72–89, 2014.

[23] N. Kaya, M. Y. Erkek, and C. Güven, "Hyperelastic modelling and shape optimisation of vehicle rubber bushings," *International Journal of Vehicle Design*, vol. 71, no. 1/2/3/4, pp. 212–225, 2016.

[24] M. Mooney, "A theory of large elastic deformation," *Journal of Applied Physics*, vol. 11, no. 9, pp. 582–592, 1940.

[25] R. S. Rivlin, "Large elastic deformations of isotropic materials. IV. Further developments of the general theory," *Philosophical Transactions of the Royal Society A: Mathematical, Physical & Engineering Sciences*, vol. 241, no. 835, pp. 379–397, 1948.

[26] R. S. Rivlin and D. W. Saunders, "Large elastic deformations of isotropic materials. VII. Experiments on the deformation of rubber," *Philosophical Transactions of the Royal Society A: Mathematical, Physical & Engineering Sciences*, vol. 243, no. 865, pp. 251–288, 1951.

[27] O. H. Yeoh, "Characterization of elastic properties of carbon-black-filled rubber vulcanizates," *Rubber Chemistry and Technology*, vol. 63, no. 5, pp. 792–805, 1990.

[28] O. H. Yeoh, "Some forms of the strain energy function for rubber," *Rubber Chemistry and Technology*, vol. 66, no. 5, pp. 754–771, 1993.

[29] K. C. Valanis and R. F. Landel, "The strain-energy function of a hyperelastic material in terms of the extension ratios," *Journal of Applied Physics*, vol. 38, no. 7, pp. 2997–3002, 1967.

[30] R. W. Ogden, "Large deformation isotropic elasticity. On the correlation of theory and experiment for incompressible rubber-like solids," *Philosophical Transactions of the Royal Society London Series A*, vol. 46, no. 2, pp. 565–584, 1973.

[31] P. J. Flory and J. Rehner, "Statistical mechanics of cross-linked polymer networks," *The Journal of Chemical Physics*, vol. 326, pp. 565–584, 1943.

[32] H. M. James and E. Guth, "Theory of the elastic properties of rubber," *The Journal of Chemical Physics*, vol. 11, no. 10, pp. 455–481, 1943.

[33] L. R. G. Treloar, "The elasticity of a network of long-chain molecules. I," *Transactions of the Faraday Society*, vol. 39, pp. 36–41, 1943.

[34] L. R. G. Treloar, "The elasticity of a network of long-chain molecules - II," *Transactions of the Faraday Society*, vol. 39, pp. 241–246, 1943.

[35] L. R. Treloar, "The elasticity of a network of long-chain molecules III," *Transactions of the Faraday Society*, vol. 42, pp. 83–94, 1946.

[36] M. C. Wang and E. Guth, "Statistical theory of networks of non-gaussian flexible chains," *The Journal of Chemical Physics*, vol. 20, no. 7, pp. 1144–1157, 1952.

[37] H. G. Kilian, H. F. Enderle, and K. Unseld, "The use of the van der Waals model to elucidate universal aspects of structure-property relationships in simply extended dry and swollen rubbers," *Colloid and Polymer Science*, vol. 264, no. 10, pp. 866–876, 1986.

[38] E. M. Arruda and M. C. Boyce, "A three-dimensional constitutive model for the large stretch behavior of rubber elastic materials," *Journal of the Mechanics and Physics of Solids*, vol. 41, no. 2, pp. 389–412, 1993.

[39] A. N. Gent, "A new constitutive relation for rubber," *Rubber Chemistry and Technology*, vol. 69, no. 1, pp. 59–61, 1996.

[40] E. Pucci and G. Saccomandi, "A note on the gent model for rubber-like materials," *Rubber Chemistry and Technology*, vol. 75, no. 5, pp. 839–852, 2002.

[41] M. A. Crisfield, "Nonlinear finite element analysis of solids and structures," *Advanced Topics*, vol. 2, 2000.

[42] G. Marckmann and E. Verron, "Comparison of hyperelastic models for rubber-like materials," *Rubber Chemistry and Technology*, vol. 79, no. 5, pp. 835–858, 2006.

[43] T. Beda, "An approach for hyperelastic model-building and parameters estimation a review of constitutive models," *European Polymer Journal*, vol. 50, no. 1, pp. 97–108, 2014.

[44] R. S. Rivlin, "Large elastic deformations of isotropic materials. II. Some uniqueness theorems for pure, homogeneous deformation," *Philosophical Transactions of the Royal Society A: Mathematical, Physical & Engineering Sciences*, vol. 240, no. 822, pp. 491–508, 1948.

[45] L. R. G. Treloar, *The Physics of Rubber Elasticity*, Oxford University Press, London, UK, 1975.

[46] K. M. Hsiao and F. Y. Hou, "Nonlinear finite element analysis of elastic frames," *Computers & Structures*, vol. 26, no. 4, pp. 693–701, 1987.

[47] M. Shahzad, A. Kamran, M. Z. Siddiqui, and M. Farhan, "Mechanical Characterization and FE Modelling of a Hyperelastic Material," *Materials Research*, vol. 18, no. 5, pp. 918–924, 2015.

[48] M. Sasso, G. Palmieri, G. Chiappini, and D. Amodio, "Characterization of hyperelastic rubber-like materials by biaxial and uniaxial stretching tests based on optical methods," *Polymer Testing*, vol. 27, no. 8, pp. 995–1004, 2008.

[49] D. Al Akhrass, J. Bruchon, S. Drapier, and S. Fayolle, "Integrating a logarithmic-strain based hyperelastic formulation into a three-field mixed finite element formulation to deal with incompressibility in finite-strain elastoplasticity," *Finite Elements in Analysis and Design*, vol. 86, pp. 61–70, 2014.

[50] R. Hooke and R. Jeeves, "Direct search solution of numerical and statistical problems," *Journal of the ACM*, vol. 8, pp. 212–229, 1961.

[51] K. Madsen and H. Nielsen, *Introduction to Optimization and Data Fitting*, Technical University of Denmark, 2010.

[52] "NF EN 13913, Railway Applications - Rubber Suspension Components - Elastomer-Based Mechanical Parts," 2004.

[53] "NFT 43-015, Rubber - Measurement of vulcanization characteristics with the oscillating cure meter," 1996.

[54] "ISO 6502, Rubber - Guide to the use of curemeters," 2016.

[55] "NFT 46-002, Vulcanized or Thermoplastic Rubber - Tensile Test," 1988.

[56] "ISO 37, Rubber, vulcanized or thermoplastic – Determination of tensile stress-strain properties," 2011.

[57] Simulia, *Abaqus Analysis User'S Manual*, Version 6.13 edition, 2016.

[58] "ASTM D412-16, Standard Test Methods for Vulcanized Rubber and Thermoplastic Elastomers—Tension," 2016.

[59] R. W. Ogden, G. Saccomandi, and I. Sgura, "Fitting hyperelastic models to experimental data," *Computational Mechanics*, vol. 34, no. 6, pp. 484–502, 2004.

[60] M. Destrade, G. Saccomandi, and I. Sgura, "Methodical fitting for mathematical models of rubber-like materials," *Proceedings of the Royal Society A: Mathematical, Physical and Engineering Science*, vol. 473, no. 2198, p. 20160811, 2017.

Hindawi
Mathematical Problems in Engineering
Volume 2019, Article ID 8424283, 19 pages
https://doi.org/10.1155/2019/8424283

Research Article

Stiffness Calculation Model of Thread Connection Considering Friction Factors

Shi-kun Lu,[1,2] **Deng-xin Hua**,[1] **Yan Li**,[1] **Fang-yuan Cui**,[1] **and Peng-yang Li**[1]

[1]*Xi'an University of Technology, Xi'an 710048, China*
[2]*Laiwu Vocational and Technical College, Laiwu 271100, China*

Correspondence should be addressed to Deng-xin Hua; dengxinhua@xaut.edu.cn and Yan Li; jyxy-ly@xaut.edu.cn

Received 9 September 2018; Revised 12 December 2018; Accepted 1 January 2019; Published 23 January 2019

Guest Editor: Yingyot Aue-u-lan

In order to design a reasonable thread connection structure, it is necessary to understand the axial force distribution of threaded connections. For the application of bolted connection in mechanical design, it is necessary to estimate the stiffness of threaded connections. A calculation model for the distribution of axial force and stiffness considering the friction factor of the threaded connection is established in this paper. The method regards the thread as a tapered cantilever beam. Under the action of the thread axial force, in the consideration of friction, the two cantilever beams interact and the beam will be deformed, these deformations include bending deformation, shear deformation, inclination deformation of cantilever beam root, shear deformation of cantilever beam root, radial expansion deformation and radial shrinkage deformation, etc.; calculate each deformation of the thread, respectively, and sum them, that is, the total deformation of the thread. In this paper, on the one hand, the threaded connection stiffness was measured by experiments; on the other hand, the finite element models were established to calculate the thread stiffness; the calculation results of the method of this paper, the test results, and the finite element analysis (FEA) results were compared, respectively; the results were found to be in a reasonable range; therefore, the validity of the calculation of the method of this paper is verified.

1. Introduction

The bolts connect the equipment parts into a whole, which is used to transmit force, moment, torque, or movement. The bolt connection is widely used in various engineering fields, such as aviation machine tools, precision instruments, etc. The precision of the threaded connection affects the quality of the equipment. Especially for high-end CNC machine tools, the precision of the thread connection is very high. Therefore, it is important to study the stiffness of the threaded connection to improve the precision of the device. Many researchers have conducted research in this area.

Dongmei Zhang et al. [1], propose a method which can compute the engaged screw stiffness, and the validity of the method was verified by FEA and experiments. Maruyama et al. [2] used the point matching method and the FEM, based on the experimental results of Boenick and the assumptions made by Fernlund [3] in calculating the pressure distribution between joint plates. Motash [4] assumed that the pressure distribution on any plane perpendicular to the bolt axis had zero gradient at $r = d_h/2$ and $r = r_o$, where it also vanishes. They mainly use numerical methods to calculate the influence of different parameters on the stiffness of bolted connections. Kenny B, Patterson E A. [5] introduced a method for measuring thread strains and stresses. Kenny B [6] et al. reviewed the distribution of loads and stresses in fastening threads. Miller D L et al. [7] established the spring model of thread force analysis and, combined with the mathematical theory, analyzed the stress of the thread and compared with the FEA results and experimental results to verify the correctness of the spring mathematical model. Wang W and Marshek K M. et al. [8] proposed an improved spring model to analyze the thread load distribution, compared the load distributions of elastic threads and yielding thread joints, and discussed the effect of the yield line on the load distribution. Wileman et al. [9] performed a two-dimensional (2D) FEA for members stiffness of joint connection. De Agostinis M et al. [10] studied the effect of lubrication on

thread friction characteristics or torque. Dario Croccolo et al. [11–13] studied the effect of Engagement Ratio (ER, namely, the thread length over the thread diameter) on the tightening and untightening torque and friction coefficient of threaded joints using medium strength threaded locking devices. Zou Q. et al. [14, 15] studied the use of contact mechanics to determine the effective radius of the bolted joint and also studied the effect of lubrication on friction and torque-tension relationship in threaded fasteners. Nassar S. A. et al. [16, 17] studied the thread friction and thread friction torque in thread connection. Nassar S. A. et al. [18, 19] also investigated the effects of tightening speed and coating on the torque-tension relationship and wear pattern in threaded fastener applications in order to improve the reliability of the clamping load estimation in bolted joints. Kopfer et al. [20] believe that suitable formulations should consider contact pressure and sliding speed; based on this, the contribution shows experimental examples for main uncertainties of frictional behavior during tightening with different material combinations (results from assembly test stand). Kenny B et al. [21] reviewed the distribution of load and stress in the threads of fasteners. Shigley et al. [22] presented an analytical solution for member stiffness, based on the work of Lehnhoff and Wistehuff [23]. Nasser [24], Musto and Konkle [25], Nawras [26], and Nassar and Abbound [27] also proposed mathematical model for the bolted-joint stiffness. Qin et al. [28] established an analytical model of bolted disk-drum joints and introduced its application to dynamic analysis of joint rotor. Liu et al. [29] conducted experimental and numerical studies on axially excited bolt connections.

There are also several authors that, starting from the nature of thread stiffness, from the perspective of thread deformation, established a mathematical model of the calculation of the distribution of thread axial force. The Sopwith method [30] and the Yamamoto method [31] received extensive recognition. The Sopwith method gave a method for calculating the axial force distribution of threaded connections. Yamamoto method can not only calculate the axial force distribution of threads but also calculate the stiffness of threaded connections. The assumption for Yamamoto method is that the load per unit width along the helix direction is uniformly distributed. In fact, for the three-dimensional (3D) helix thread, the load distribution is not uniform. Therefore, based on the Yamamoto method, Dongmei Zhang et al. [1] propose a method which can compute the engaged screw stiffness by considering the load distribution, and the validity of the method was verified by FEA and experiments. The method of Zhang Dongmei does not consider the influence of the friction coefficient of the thread contact surface. In fact, the friction coefficient of the contact surface of the thread connection has an influence on the distribution of the axial force of the thread and the stiffness of the thread. Therefore, we propose a new method which can compute the engaged screw stiffness more accurately by considering the effects of friction and the load distribution. The accuracy of the method was verified by the FEA and bolt tensile test. The flow chart of the article is shown in Figure 2.

2. Mathematical Model

2.1. Axial Load Distribution. According to Yamamoto [31], the thread is regarded as a cantilever beam, and the thread is deformed under axial force and preload. These deformations include the following (shown in Figure 3): thread bending deformation, thread shear deformation, thread root inclination deformation, thread root shear deformation, radial direction extended deformation, or radial shrinkage deformation.

For the *ISO* thread, the axial deformation of the thread at x at the axial unit width force w_z is thread bending deformation δ_1, thread shear deformation δ_2, thread root inclination deformation δ_3, thread root shear deformation δ_4, and radial direction extended deformation δ_5 (nut) or radial shrinkage deformation δ_5 (screw), and calculate these deformations of the thread, respectively, and then sum them, that is, the total deformation.

2.1.1. Bending Deformation. In the threaded connection, under the action of the load, the contact surface friction coefficient is μ, when the sliding force along the inclined plane is greater than the friction force along the inclined plane, the relative sliding occurs between the two inclined planes, and the axial unit width force (shown in Figure 3) is w_z; if the influence of the lead angle is ignored, the force per unit width perpendicular to the thread surface can be expressed as

$$w = \frac{w_z}{\mu \sin \alpha + \cos \alpha} \tag{1}$$

The force per unit width perpendicular to the thread surface can be decomposed into the x-direction component force and the y-direction component force, respectively

$$w \cos \alpha = \frac{w_z \cos \alpha}{\mu \sin \alpha + \cos \alpha} \tag{2}$$

and

$$w \sin \alpha = \frac{w_z \sin \alpha}{\mu \sin \alpha + \cos \alpha} \tag{3}$$

The friction generated along the slope is $w\mu$; i.e.,

$$w\mu = \frac{w_z \mu}{\mu \sin \alpha + \cos \alpha} \tag{4}$$

The force $w\mu$ is also decomposed into x-direction force and y-direction force, which are $\mu \sin \alpha$ and $\mu \cos \alpha$, respectively.

$$w\mu \sin \alpha = \frac{w_z \mu \sin \alpha}{\mu \sin \alpha + \cos \alpha} \tag{5}$$

$$w\mu \cos \alpha = \frac{w_z \mu \cos \alpha}{\mu \sin \alpha + \cos \alpha} \tag{6}$$

In the unit width, the thread is regarded as a rectangular variable-section cantilever beam. Under the action of the

above-mentioned force, the thread undergoes bending deformation, and the virtual work done by the bending moment $\overline{E}$ on the beam dy section is

$$\overline{E}d\theta = \overline{E}\frac{M_w}{E_b I(y)}dy \tag{7}$$

According to the principle of virtual work, the deflection δ_1 (see Figure 3(a)) of the beam subjected to the load is

$$\delta_1 = \int_0^c \frac{\overline{E}M_w}{E_b I(y)}dy \tag{8}$$

where $\overline{E}$ is the bending moment of the unit load beam. M_w is the bending moment of the beam under the actual load. $I(y)$ is the area moment of inertia of the beam at y. E_b is Young's Modulus of the material. c is the length of the beam. Here, the forces are assumed as acting on the mean diameter of the thread.

As shown in Figure 5, the height $h(y)$ of the beam section per unit width and the area moment of inertia $I(y)$ of the section can be expressed by using the function interpolation.

$$\begin{aligned} h(y) &= \left[1 + \frac{(\beta_1 - 1)(c - y)}{c}\right]h, \quad (0 \le y \le c) \\ I(y) &= \frac{1}{12}bh^3\left[1 + \frac{(\beta_1 - 1)(c - y)}{c}\right]^3, \quad (0 \le y \le c) \\ \beta_1 &= \frac{a}{h} \end{aligned} \tag{9}$$

where h is the beam end section height; b is the beam section width; β_1 is the beam root section height and the beam end section height ratio; see Figure 5.

From Figure 5, the bending moment of the beam is related to the y-axis component of w and $w\mu$, and these components cause the beam to bend; therefore, the analytical solution shows that the bending moment of the unit width beam subjected to the friction force and the vertical load of the thread surface is

$$\begin{aligned} M_w = \frac{w_z}{\mu\sin\alpha + \cos\alpha} \cdot \Big[&\cos\alpha \cdot c + \mu\sin\alpha \cdot c \\ &- \sin\alpha\left(\frac{a}{2} - c\tan\alpha\right) + \mu\cos\alpha\left(\frac{a}{2} - c\tan\alpha\right)\Big] \end{aligned} \tag{10}$$

Substituting (10) and (9) to (8) and integrating to obtain the analytical expression of the deflection δ_1 (shown in Figure 3(a)) of the cantilever beam with variable cross-section under load one has

$$\delta_1 = \frac{12M_w c^2}{E_b bh^3} \cdot \left[\frac{1}{2}\left(\frac{1}{\beta_1^2} + 1\right) - \frac{1}{\beta_1}\right] \cdot \frac{1}{(\beta_1 - 1)^2} \tag{11}$$

2.1.2. Shear Deformation. Assume that the distribution of shear stress on any section is distributed according to the parabola [31] and the deformation δ_2 (see Figure 3(b)) caused by the shear force within the width of unit 1 is

$$\begin{aligned} \delta_2 = \log_e\left(\frac{a}{b}\right) \cdot \frac{6(1+\nu)(\cos\alpha + \mu\sin\alpha)\cot\alpha}{5E_b} \\ \cdot \frac{w_z}{\mu\sin\alpha + \cos\alpha} \end{aligned} \tag{12}$$

2.1.3. Inclination Deformation of the Thread Root. Under the action of the load, the thread surface is subjected to a bending moment, and the root of the thread is tilted, as shown in Figure 3(c). Due to the inclination of the thread, axial displacement occurs at the point of action of the thread surface force, and the axial displacement can be expressed as [31]

$$\begin{aligned} \delta_3 = \frac{w_z}{\mu\sin\alpha + \cos\alpha} \cdot \frac{12c(1-\nu^2)}{\pi E_b a^2} \cdot \Big[&\cos\alpha \cdot c \\ &+ \mu\sin\alpha \cdot c - \sin\alpha\left(\frac{a}{2} - c\tan\alpha\right) \\ &+ \mu\cos\alpha\left(\frac{a}{2} - c\tan\alpha\right)\Big] \end{aligned} \tag{13}$$

2.1.4. Deformation due to Radial Expansion and Radial Shrinkage. According to the static analysis, the thread is subjected to radial force $w\sin\alpha - w\mu\cos\alpha$ (shown in Figure 4), and it is known from the literature [31] that the internal and external thread radial deformation (shown in Figure 3(d)) are

$$\delta_{4b} = (1 - \nu_b)\frac{d_p}{2E_b P}\tan\alpha \cdot \frac{w_z(\sin\alpha - \mu\cos\alpha)}{\mu\sin\alpha + \cos\alpha} \tag{14}$$

and

$$\begin{aligned} \delta_{4n} = \left(\frac{D_0^2 + d_p^2}{D_0^2 - d_p^2} + \nu_n\right)\frac{d_p}{2E_n P} \cdot \tan\alpha \\ \cdot \frac{w_z(\sin\alpha - \mu\cos\alpha)}{\mu\sin\alpha + \cos\alpha} \end{aligned} \tag{15}$$

2.1.5. Shear Deformation of the Root. Assuming that the shear stress of the root section is evenly distributed, the displacement of the O point in the x direction caused by the shear deformation (shown in Figure 3(e)) is the same as the displacement of the thread in the x direction; this displacement can be expressed as [31]

$$\begin{aligned} \delta_5 = \frac{w_z}{\mu\sin\alpha + \cos\alpha} \cdot \frac{2(1-\nu^2)\cdot(\cos\alpha + \mu\sin\alpha)}{\pi E_b} \\ \cdot \left\{\frac{P}{a}\log_e\left(\frac{P + a/2}{P - a/2}\right) + \frac{1}{2}\log_e\left(\frac{4P^2}{a^2} - 1\right)\right\} \end{aligned} \tag{16}$$

For ISO internal threads, the relationship between a, b, c, and pitch P is

$$\begin{aligned} a &= 0.833P \\ b &= 0.5P \\ c &= 0.289P \end{aligned} \tag{17}$$

Substituting (17) into (9), (10), (11), (12), (13), (14), and (16) one gets the relation

$$\delta_{1b} = 3.468\frac{M_{wb}}{E_b P^2 \beta_b^3} \cdot \left[\frac{1}{2}\left(\frac{1}{\beta_b^2}+1\right) - \frac{1}{\beta_b}\right] \cdot \frac{1}{(\beta_b - 1)^2}, \quad \beta_b = 1.6684 \tag{18}$$

$$M_{wb} = \frac{w_z}{\mu \sin\alpha + \cos\alpha}\left[0.289P \cdot (\cos\alpha + \mu \cdot \sin\alpha) - (0.4165P - 0.289P \cdot \tan\alpha)(\sin\alpha - \mu \cdot \cos\alpha)\right] \tag{19}$$

$$\delta_{2b} = 0.51 \cdot \frac{6(1+\nu)(\cos\alpha + \mu\sin\alpha)\cot\alpha}{5E_b} \cdot \frac{w_z}{\mu\sin\alpha + \cos\alpha} \tag{20}$$

$$\delta_{3b} = \frac{w_z}{\mu\sin\alpha + \cos\alpha} \cdot \frac{12c\left(1-\nu^2\right)}{\pi E_b a^2} \cdot \left[0.289P \cdot (\cos\alpha + \mu\cdot\sin\alpha) - (0.4165P - 0.289P\cdot\tan\alpha) \cdot (\sin\alpha - \mu\cdot\cos\alpha)\right] \tag{21}$$

$$\delta_{4b} = (1-\nu_b)\frac{d_p}{2E_b P}(\sin\alpha - \mu\cos\alpha)\tan\alpha \cdot \frac{w_z}{\mu\sin\alpha + \cos\alpha} \tag{22}$$

$$\delta_{5b} = \frac{1.8449 w_z}{\mu\sin\alpha + \cos\alpha} \cdot \frac{2\left(1-\nu^2\right)\cdot(\cos\alpha + \mu\sin\alpha)}{\pi E_b} \tag{23}$$

For ISO internal threads, the relationship between a, b, c, and pitch P is

$$\begin{aligned} a &= 0.875P \\ b &= 0.5P \\ c &= 0.325P \end{aligned} \tag{24}$$

Substituting (24) into (9), (10), (11), (12), (13), (15), and (16) type one gets the relation

$$\delta_{1n} = 3.784\frac{M_{wn}}{E_n P^2 \beta_n^2} \cdot \left[\frac{1}{2}\left(\frac{1}{\beta_n^2}+1\right) - \frac{1}{\beta_n}\right] \cdot \frac{1}{(\beta_n - 1)^2}, \quad \beta_n = 1.751 \tag{25}$$

$$M_{wn} = \frac{w_z}{\mu\sin\alpha + \cos\alpha}\left[0.325P \cdot (\cos\alpha + \mu\cdot\sin\alpha) - (0.4375P - 0.325P\cdot\tan\alpha)(\sin\alpha - \mu\cdot\cos\alpha)\right] \tag{26}$$

$$\delta_{2n} = 0.55962 \cdot \frac{6(1+\nu)(\cos\alpha + \mu\sin\alpha)\cot\alpha}{5E_b} \cdot \frac{w_z}{\mu\sin\alpha + \cos\alpha} \tag{27}$$

$$\delta_{3n} = \frac{w_z}{\mu\sin\alpha + \cos\alpha} \cdot \frac{12c\left(1-\nu^2\right)}{\pi E_b a^2} \cdot \left[0.325P \cdot (\cos\alpha + \mu\cdot\sin\alpha) - (0.4375P - 0.325P\cdot\tan\alpha)(\sin\alpha - \mu\cdot\cos\alpha)\right] \tag{28}$$

$$\delta_{4n} = \left(\frac{D_0^2 + d_p^2}{D_0^2 - d_p^2} + \nu_n\right)\frac{d_p}{2E_n P} \cdot (\sin\alpha - \mu\cos\alpha)\tan\alpha \cdot \frac{w_z}{\mu\sin\alpha + \cos\alpha} \tag{29}$$

$$\delta_{5n} = \frac{1.7928 w_z}{\mu\sin\alpha + \cos\alpha} \cdot \frac{2\left(1-\nu^2\right)\cdot(\cos\alpha + \mu\sin\alpha)}{\pi E_b} \tag{30}$$

By adding these deformations separately, the total deformation (shown in Figure 4) of screw thread and nut thread can be obtained under the action of force w_z.

$$\delta_b = \delta_{1b} + \delta_{2b} + \delta_{3b} + \delta_{4b} + \delta_{5b} \tag{31}$$

$$\delta_n = \delta_{1n} + \delta_{2n} + \delta_{3n} + \delta_{4n} + \delta_{5n} \tag{32}$$

The unit force per unit width of the axial direction can be expressed as

$$f_\Delta = \frac{w_z}{w_z} = 1 \tag{33}$$

Under the action of unit force of axial unit width, the total deformation of external thread and internal thread is

$$\delta_{b1} = \frac{\delta_{1b} + \delta_{2b} + \delta_{3b} + \delta_{4b} + \delta_{5b}}{w_z} \tag{34}$$

and

$$\delta_{n1} = \frac{\delta_{1n} + \delta_{2n} + \delta_{3n} + \delta_{4n} + \delta_{5n}}{w_z} \tag{35}$$

For threaded connections, at the x-axis of the load F, the axial deformation of screws and nuts can be expressed as

$$z_b(r) = \delta_{b1} \cdot \frac{\partial F}{\partial r} \tag{36}$$

$$z_n(r) = \delta_{n1} \cdot \frac{\partial F}{\partial r} \tag{37}$$

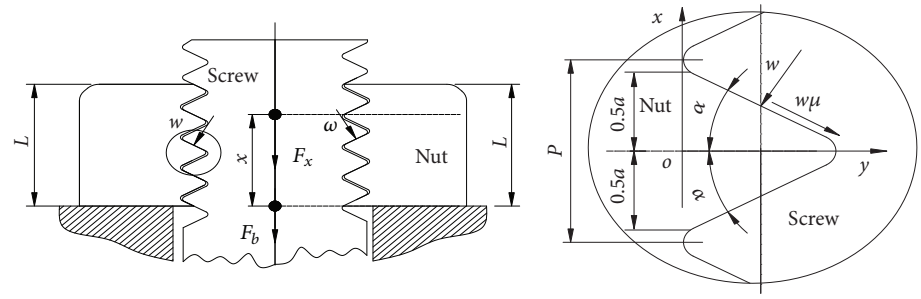

Thread axial force distribution (a) Partial view (b)

Figure 1: Thread force.

Here r is the length along the helical direction, and the relation between the axial height x and the length along the helix direction can be represented by the following formula according to the geometric relation shown in Figure 6.

$$r = \frac{x}{\sin\beta} \tag{38}$$

Here, β is the lead angle of the thread shown in Figure 6, and then

$$z_n(x) = \delta_{n1} \cdot \frac{\partial F}{\partial r} = \delta_{n1} \cdot \frac{\partial F}{\partial x} \cdot \frac{\partial x}{\partial r} = \delta_{n1} \cdot \sin\beta \cdot \frac{\partial F}{\partial x} \tag{39}$$

$$z_b(x) = \delta_{b1} \cdot \frac{\partial F}{\partial r} = \delta_{b1} \cdot \frac{\partial F}{\partial x} \cdot \frac{\partial x}{\partial r} = \delta_{b1} \cdot \sin\beta \cdot \frac{\partial F}{\partial x} \tag{40}$$

Assume

$$\frac{\partial F}{\partial x \cdot z_b(x)} = \frac{1}{\delta_{b1} \cdot \sin\beta} = k_{ubx}(x) \tag{41}$$

$$\frac{\partial F}{\partial x \cdot z_n(x)} = \frac{1}{\delta_{n1} \cdot \sin\beta} = k_{unx}(x) \tag{42}$$

Here, $k_{bx}(x)$ and $k_{nx}(x)$ represent the stiffness of the unit axial length of the nut and the screw, respectively, for the unit force.

The axial total deformation of the threaded connection at x is denoted as

$$z_x(x) = z_b(x) + z_n(x) \tag{43}$$

The stiffness of the unit axial length of the threaded connection is expressed as

$$\begin{aligned} k_{ux}(x) &= \frac{\partial F}{\partial x \cdot z_x(x)} \\ &= \frac{\partial F}{\partial x} \div \left(\delta_{b1} \cdot \sin\beta \cdot \frac{\partial F}{\partial x} + \delta_{n1} \cdot \sin\beta \cdot \frac{\partial F}{\partial x}\right) \\ &= \frac{1}{(\delta_{n1} + \delta_{b1}) \cdot \sin\beta} \end{aligned} \tag{44}$$

As shown in Figure 1(a), the threaded connection structure includes a nut body and a screw body. The nut is fixed, the screw is subjected to pulling force, the total axial force is F_b, and the axial force at the threaded connection screw x is $F(x)$. If the position of the bottom end face of the nut is the origin 0 and, at the x position, the axial force is $F(x)$, the screw elongation amount ε_b and the nut compression ε_n can be obtained from the following:

$$\varepsilon_b(x) = \frac{F(x)}{A_b(x) E_b} \tag{45}$$

$$\varepsilon_n(x) = \frac{F(x)}{A_n(x) E_n} \tag{46}$$

where $A_b(x)$ and $A_n(x)$ are the vertical cross-sectional areas of screws and nuts at the x position. E_b and E_n are, respectively, Young's modulus of the screw body and Young's modulus of the nut body. Find the displacement gradient for the expression, which is, respectively, expressed as

$$\frac{\partial z_b(x)}{\partial x} = \frac{1}{k_{ubx}(x)} \cdot \frac{\partial^2 F}{\partial x^2} \tag{47}$$

$$\frac{\partial z_n(x)}{\partial x} = \frac{1}{k_{unx}(x)} \cdot \frac{\partial^2 F}{\partial x^2} \tag{48}$$

Here, $k_{ubx}(x) = 1/(\delta_{b1} \cdot \sin\beta)$, and $k_{unx}(x) = 1/(\delta_{n1} \cdot \sin\beta)$.

As shown in Figure 1(a), the screw is subjected to the tensile force F_b, with the bottom of the nut as the coordinate origin, and the force at the x position is F_x, and then the elongation of the screw at x is $\int_x^L \varepsilon_b(x)dx = w_b$, and the compressed shortening amount of the nut at x is $\int_x^L \varepsilon_n(x)dx = w_n$. The relationship between w_b, w_n, z_b, and z_n is $\int_x^L \varepsilon_b(x)dx + \int_x^L \varepsilon_n(x)dx = [z_b(x) + z_n(x)]_{x=L} - [z_b(x) + z_n(x)]_{x=x}$ (see Figures 7 and 1(a),), and the partial derivative of this relation can be obtained by the following formula:

$$\varepsilon_b(x) + \varepsilon_n(x) = \frac{\partial z_b(x)}{\partial x} + \frac{\partial z_n(x)}{\partial x} \tag{49}$$

Substituting (45), (46), (47), and (48) into (49) and simplifying it

$$\frac{(A_n E_n + A_b E_b)}{A_b E_b A_n E_n} \cdot \frac{k_{ubx} k_{unx}}{(k_{ubx} + k_{unx})} F(x) = \frac{\partial^2 F(x)}{\partial x^2} \tag{50}$$

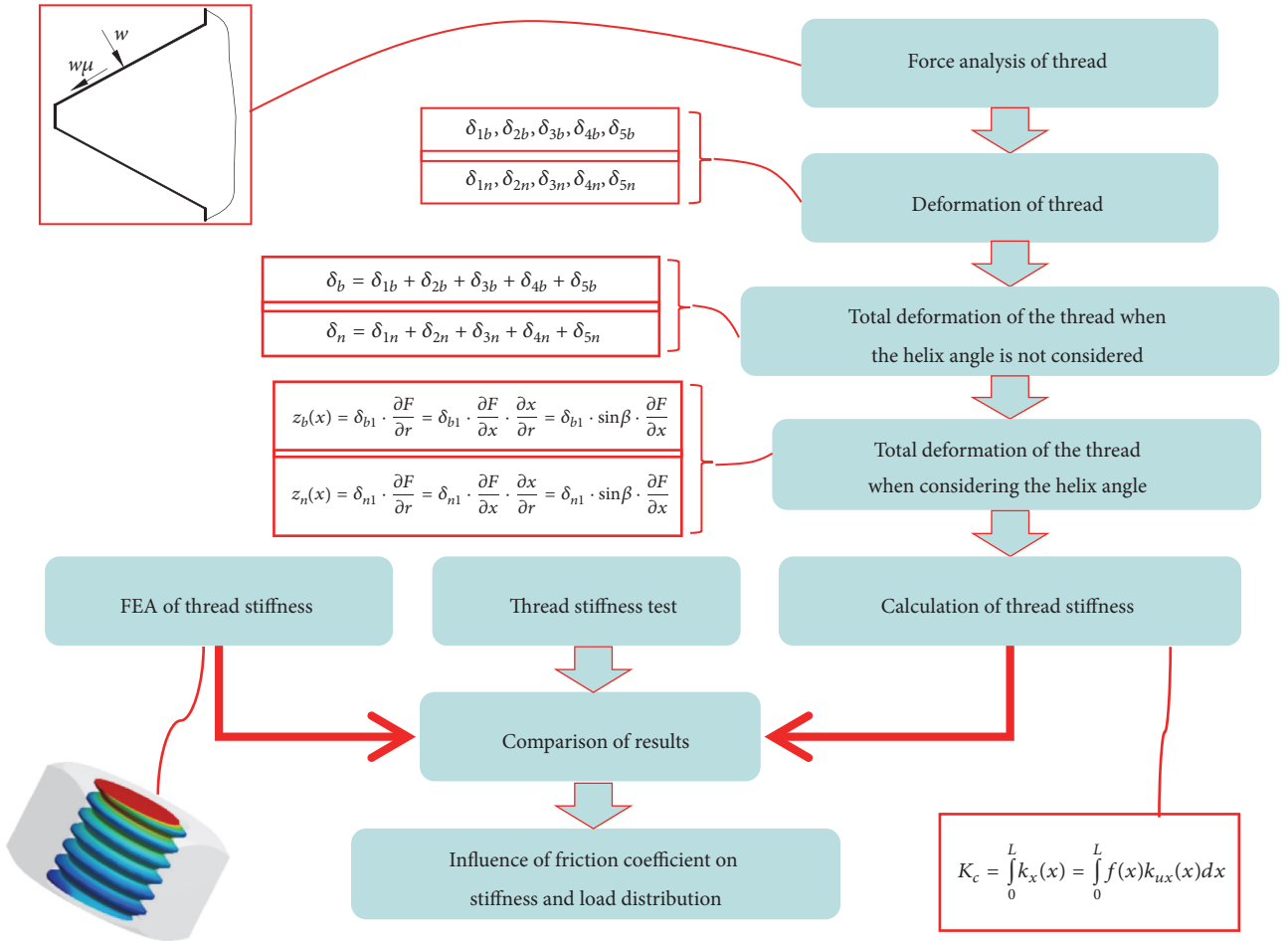

Figure 2: Schematic diagram of the article.

Let

$$n = \sqrt{\frac{(A_n E_n + A_b E_b)}{A_b E_b A_n E_n} \cdot \frac{k_{ubx} k_{unx}}{(k_{ubx} + k_{unx})}} \tag{51}$$

Then

$$n^2 F(x) = \frac{\partial^2 F(x)}{\partial x^2} \tag{52}$$

From mathematical knowledge, the equation is a differential equation. The general solution of the equation can be expressed as

$$F(x) = C_1 \sinh nx + C_2 \cosh nx \tag{53}$$

As can be seen from Figure 1, the axial force at the first thread at the connection surface of the nut and the screw is F_b, and the axial force at the last thread at the lower end of the thread joint surface of the nut and screw is 0; that is, the boundary condition is $F(x=0)=F_b$ and $F(x=L)=0$. Taking these boundary conditions into the equation will give $C_1=-F_b(\cosh(nL))/\sinh(nL)$ and $C_2=F_b$, so we get the expression of the threaded connection axial load as

$$F(x) = F_b \left(\cosh nx - \frac{\cosh nL}{\sinh nL} \sinh nx \right) \tag{54}$$

Therefore, the axial force distribution density of the thread connection along the x direction can be expressed as

$$f(x) = \frac{F(x)}{F_b} = \left(\cosh nx - \frac{\cosh nL}{\sinh nL} \sinh nx \right) \tag{55}$$

2.2. Thread Connection Stiffness. The stiffness in the axial direction x of the bolted connection is equal to the axial force distribution of the threaded connection multiplied by the unit stiffness; i.e.,

$$k_x(x) = f(x) k_{ux}(x) \tag{56}$$

The overall stiffness of the bolt connection can be expressed as

$$K_c = \int_0^L k_x(x) = \int_0^L f(x) k_{ux}(x) dx \tag{57}$$

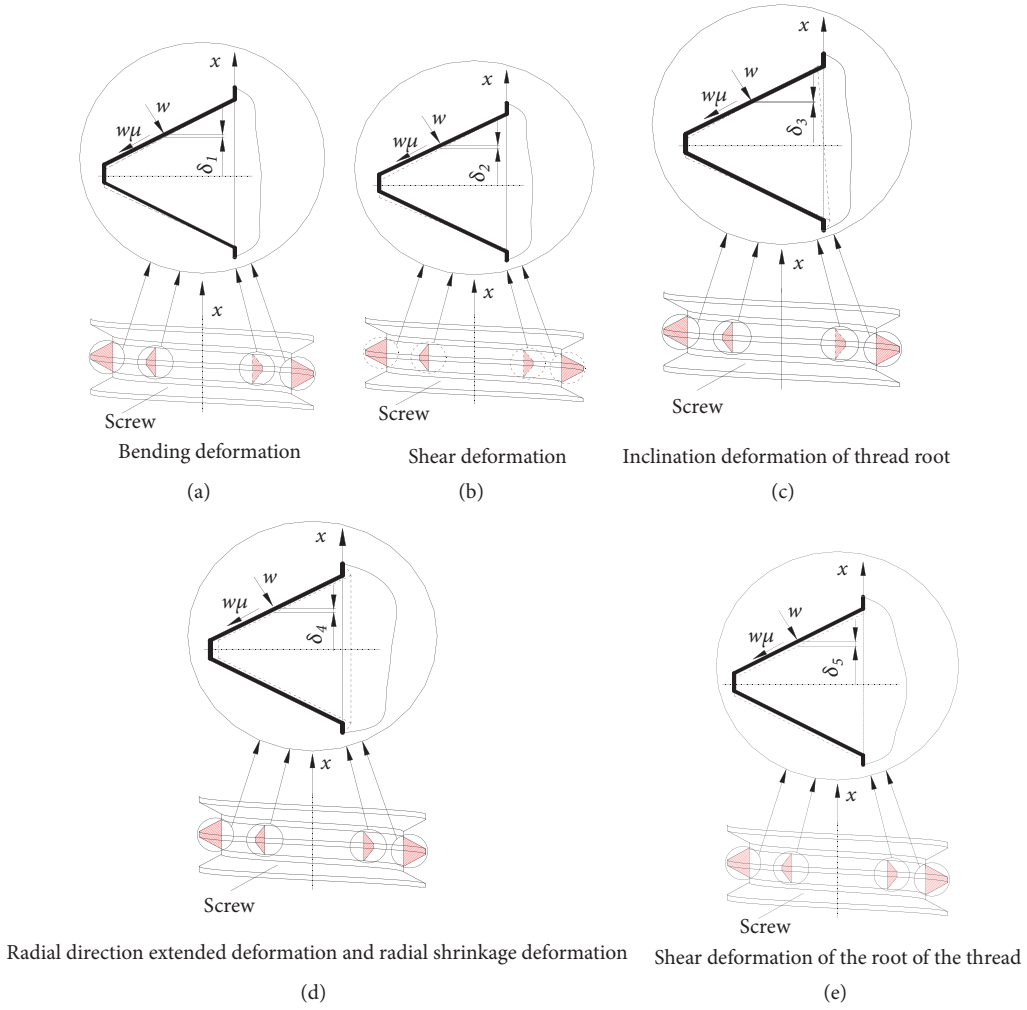

Figure 3: Thread deformation caused by various reasons.

Substituting (44) and (55) into (57), the stiffness of the bolt connection is expressed as

$$K_c = \int_0^L k_x(x) = \int_0^L f(x)\, k_{ux}(x)\, dx = \frac{1}{n(\delta_{b1} + \delta_{n1}) \cdot \sin\beta} \cdot \frac{\cosh nL - 1}{\sinh nL} \tag{58}$$

3. FEA Model

A 3D finite element model (shown in Figure 10) was established, and FEA was performed to analyze the influence of various parameters of the thread on the thread stiffness. These parameters include material, thread length, pitch, etc.

The FEA software ANSYS 14.0 was used for analysis. During the analysis, the end face of the nut was fixed (shown in Figure 9), the initial state of the model is shown in Figure 8, and an axial displacement Δ_x was forced to the end face of the screw. Then, the axial force F_x of the screw end face was extracted. The axial stiffness of the threaded connection was calculated by the FEM. The friction coefficient μ of the thread contact surface is set first. In FEA, the contact algorithm used is Augmented Lagrange. Figures 11(a)–11(c) are the force convergence curves for FEA of threaded connections. Figures 12(a)–12(c) are the effect of the reciprocal of the mesh size on the axial force obtained by FEA. We can see from Figures 12(a)–12(c) that as the mesh size decreases, the resulting axial force gradually decreases, but when the mesh size is small to a certain extent, the resulting axial force will hardly decrease. The axial force at this time is the axial force required by the author. With known displacements and axial force, the stiffness of the threaded connection can be calculated using the formula

$$K_c = \frac{F_x}{\Delta_x} \tag{59}$$

4. Tensile Test of Threaded Connections [1]

In order to verify the effectiveness of this paper method, the experimental data of the experimental device in [1] are used. In [1], the electronic universal testing machine is used to measure the load-defection data of samples, and the

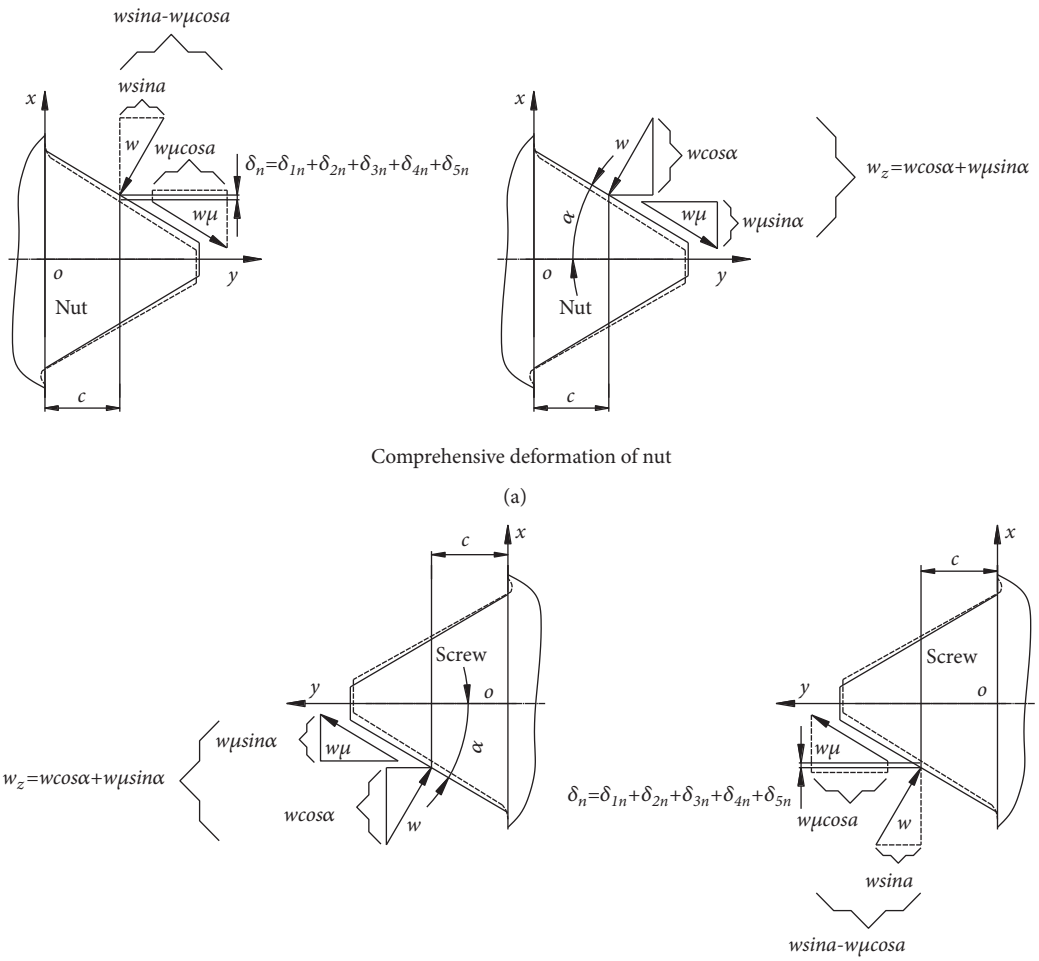

Figure 4: The comprehensive deformation of the thread.

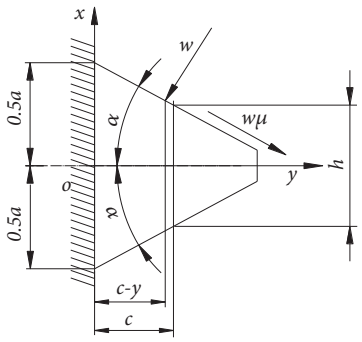

Figure 5: The force on the thread.

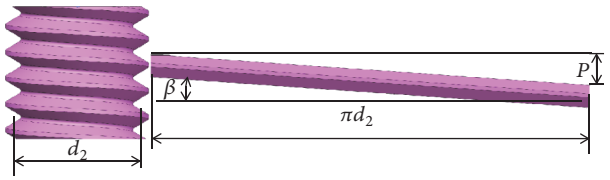

Figure 6: The lead angle of the thread.

test sample is made of brass. The tension value F_{xt} can be read from the test machine. The axial deflection of thread connection can be represented by the displacement variation δ_L between two lines as shown in Figure 14, which can be measured by a video gauge [1]. In [1], in order to obtain the most accurate data possible, each size of the thread is in a small range of deformation during the tensile test, and each size of the thread tensile test is performed 10 times, and the average value is calculated as the final calculated data. Some samples in the experiment are shown in Figure 13.

The stiffness calculation formula is

$$K_c = \frac{F_{xt}}{\delta_L}. \tag{60}$$

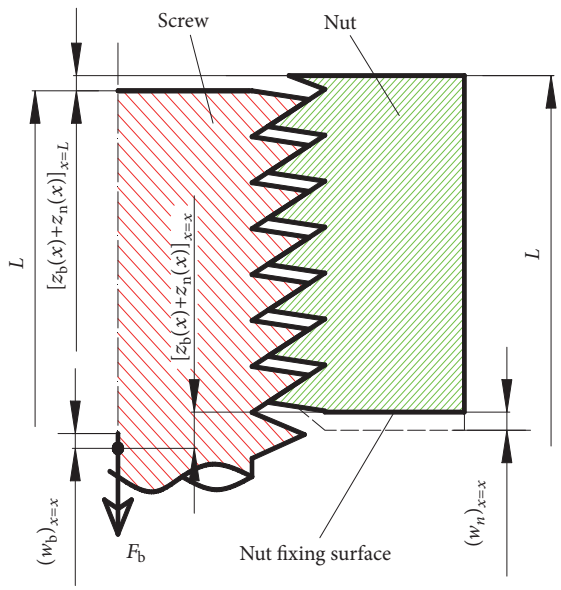

Figure 7: Illustration of the elastic deformation of the screwed portion of the threaded connection.

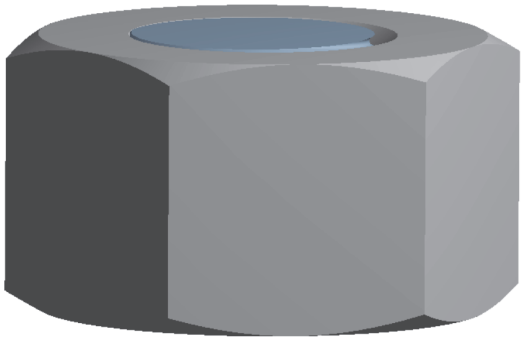

Figure 8: Initial state.

The materials used to make nuts and screws are brass. Young's modulus of brass is 107GPa, and Poisson's ratio is 0.32 [1].

5. Results and Discussion

5.1. Stiffness of Threaded Connections. Croccolo, D. [12], Nassar SA [19], and Zou Q [32] studied the coefficient of friction of the thread. According to the study by Zou Q and Nassar SA, in the case of lubricating oil on the thread surface, the friction coefficient of the steel-steel thread connection thread is 0.08, and the friction coefficient of aluminum-aluminum thread connection thread is 0.1.

In order to verify the correctness of the calculation results of the theory presented in this paper, a variety of threaded connections were used to calculate an experimental test.

In the finite element analysis and theoretical calculations of this paper, Young's modulus of steel is $E_b = E_n = 200$Gpa, and Poisson's ratio of steel is 0.3, and the friction coefficient [12, 19, 32] is set to 0.08.

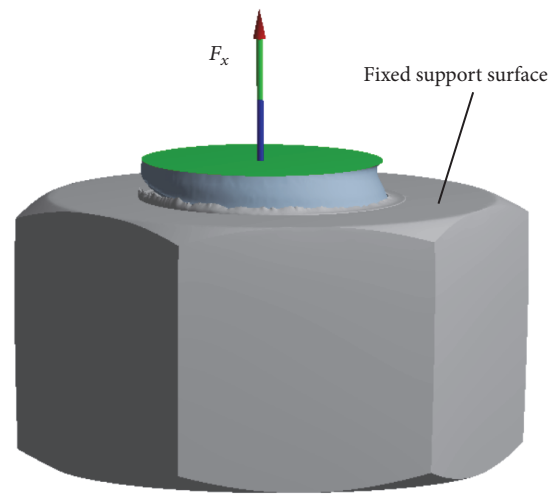

Figure 9: Threaded connection deformed by axial forces.

The experimental data, FEA data, and Yamamoto method data in Tables 1 and 5 are from literature [1]. As can be seen from Tables 1 and 5, the calculated values obtained in this paper are all higher than the experimental results. Perhaps the error is caused by the presence of a small amount of impurities on the surface of the thread and partial deformation of the thread inevitably and there is a slip between the threaded contact surfaces. The theoretical calculation results and FEA results in this paper have a small error.

In Table 2, the effect of thread length on stiffness is presented. It can be seen that when the same nominal diameter M10, the same pitch P=1.5, and the same material steel are taken, when the thread engaged length is taken as 14 mm, 9 mm, and 6 mm, respectively, it is found that the longer the thread engaged length, the greater the stiffness and the smaller the length of the bond, the smaller the stiffness.

In the FEA, the method of this paper and the Yamamoto method, Young's Modulus of aluminum alloy is E=68.9GPa; Poisson's ratio of the aluminum alloy is 0.34. The friction coefficient of the steel- steel threaded connection [12, 21, 22, 32] is set to 0.08, and the friction coefficient of aluminum-aluminum threaded connection [12, 19, 32] is set to 0.1. Table 3 shows the effect of different materials on the stiffness of threaded connections. The two types of threaded connections are made of two different materials, the steel and aluminum alloys. It can be seen from the table that, under the condition of the same pitch, the same nominal diameter, and the same engaged length, the stiffness of the steel thread connection is larger than that when the material is aluminum.

In Table 4, it also shows the influence of different pitches on the stiffness of the thread connection. It can be seen that with the same engaged length, the same material, and the same nominal diameter, the pitch P is 1.5, 1.25, and 1, respectively, and we find that the smaller the pitch, the greater the stiffness.

When using FEM to analyze the influence of friction factors on the stiffness of threaded connections, the thread

Table 1: Stiffness of threaded connections with different engaged lengths [1] (kN/mm).

No.	Size code of threads	Material	Exp.	Theory		FEA
				This study	Yamamoto method	
1	M36×4×32	Brass	3627.6	4201.9	4282.1	3630.9
2	M36×4×20		2664.3	3152.9	3946.1	2761.6
3	M36×4×12		1801.3	2074.2	3129.3	1816.8

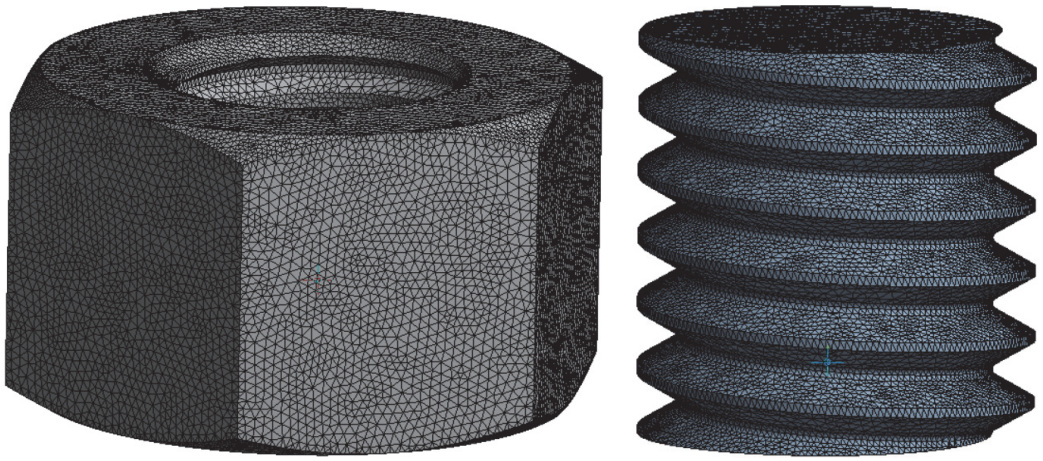

(a) Nut (b) Screw

Figure 10: Finite element meshing of thread-bonded 3D finite element models.

Table 2: Stiffness of threaded connections with different engaged lengths (kN/mm).

No.	Size code of threads	Material	Theory		FEA
			This study	Yamamoto method	
1	M10×1.5×14	Steel	2095.26	2076.6	1965.21
2	M10×1.5×9		1759.23	2006.2	1770.02
3	M10×1.5×6		1354.70	1804.6	1551.27

Table 3: Stiffness of threaded connections with different material (kN/mm).

No.	Size code of thread	Material	Theory		FEA
			This study	Yamamoto method	
1	M10×1.5×9	Steel	1759.23	2006.2	1770.02
2	M10×1.5×9	Aluminum alloy	607.51	682.11	597.99

Table 4: Stiffness of threaded connections with different pitch (kN/mm).

No.	Size code of threads	Material	Theory	
			This study	Yamamoto method
1	M10×1.5×9	Steel	1759.23	2006.2
2	M10×1.25×9		2083.17	2177.1
3	M10×1×9		2324.30	2375.2

Table 5: Stiffness of threaded connections with different engaged lengths [1] (kN/mm).

No.	Size code of threads	Material	Exp.	Theory	
				This study	Yamamoto method
1	M36×3×12	Brass	2085.3	2593.2	3525.1
2	M36×2×12	Brass	2396.2	3418.3	4008.9

specification is M6×1×6.1 and the friction coefficients are 0.01, 0.05, 0.1, 0.2, 0.25, and 0.3. (as shown in Figures 15–20)

Figures 21 and 22 show the results of stiffness calculations. The thread size is M10×1.5×9 and M6×1×6.1, the material is steel, Poisson's ratio of the material is 0.3, Young's Modulus of the material is 200 GPa, and the thread surface friction coefficient is taken as 0.01, 0.05, 0.1, 0.2, 0.25, and 0.3. Calculated using the theories of this paper, FEA and Yamamoto, respectively, and from Figures 21 and 22, we can see that the results of FEA are very similar to the results of the theoretical calculations of this paper, the variation trend of stiffness with friction coefficient is the same, and it increases with the increase of friction coefficient, and the results of the FEA are in good agreement with those of the FEA;

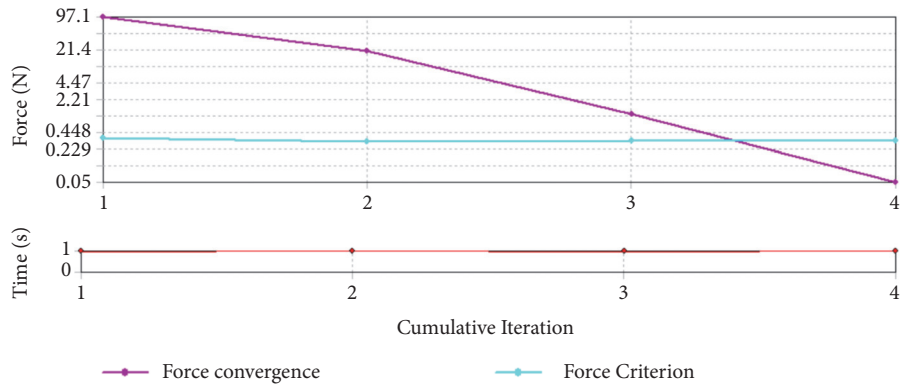

(a) M10×1.5×9, μ=0.08, Δ_x=0.001mm

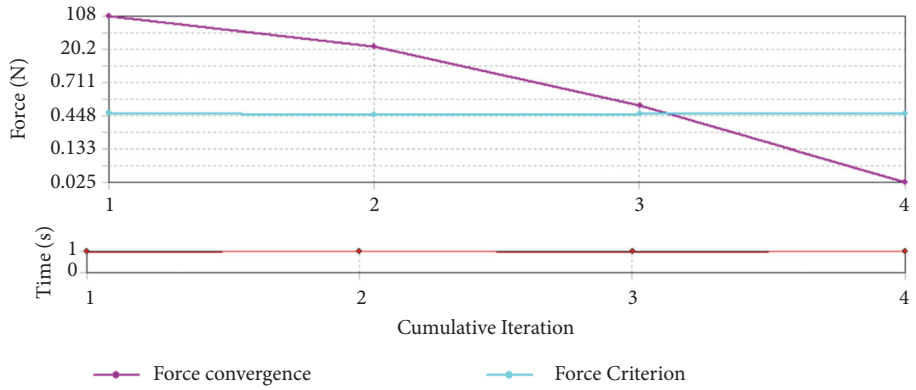

(b) M8×1.25×6.5, μ=0.08, Δ_x=0.001mm

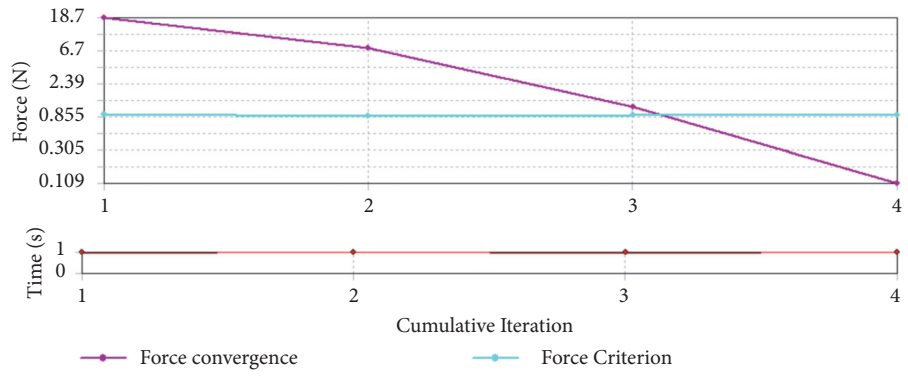

(c) M6×1.0×6.1, μ=0.08, Δ_x=0.001mm

Figure 11: FEA convergence curve.

however, Yamamoto theory does not consider the influence of the friction coefficient on stiffness, and this is obviously unreasonable.

5.2. Effect of Friction Coefficient on Axial Force Distribution. Take the thread size as M6×0.75×6.1, the axial load F_b is taken as 100N, 350N, and 550N, respectively, and take the friction coefficients 0, 0.3, 0.6, and 1, respectively, to calculate the axial force distribution of the thread. As can be seen from Figure 23, when the friction coefficient is 1, the curve bending degree is the greatest, when the friction coefficient is 0, the curve bending degree is the lightest, the curve bending degree is greater, indicating that the more uneven the distribution of axial force, the smaller the curve bending degree, indicating that the more uniform the distribution of axial force. We can see that the friction coefficient of thread surface has an effect on the distribution of axial force.

6. Conclusion

This study provides a new method of calculating the thread stiffness considering the friction coefficient and analyzes the influence of the thread geometry and material parameters on the thread stiffness and also analyzes the influence of

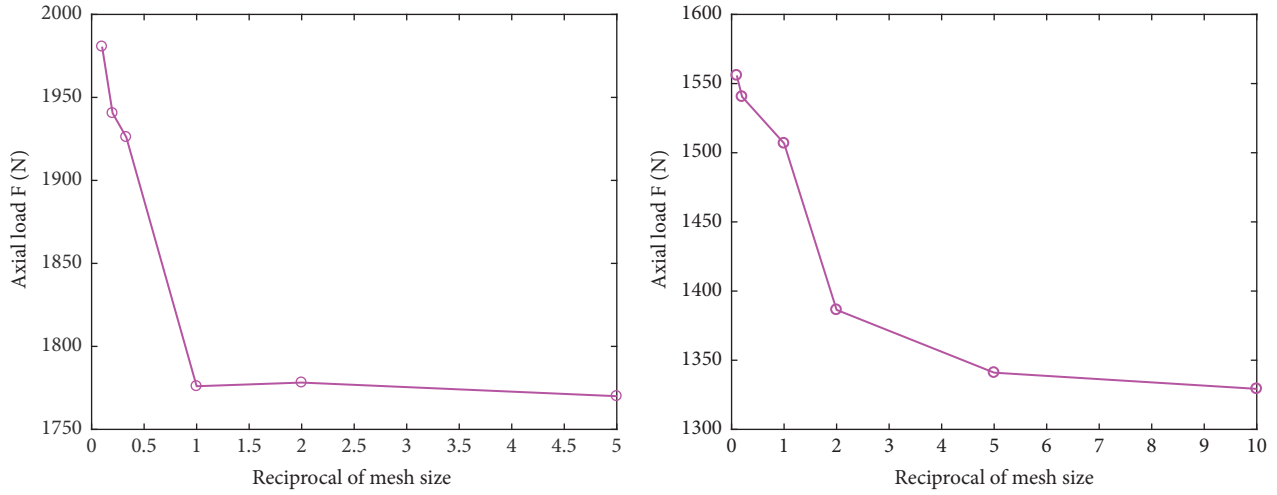

(a) M10×1.5×9, μ=0.08, Δ_x=0.001mm

(b) M8×1.25×6.5, μ=0.08, Δ_x=0.001mm

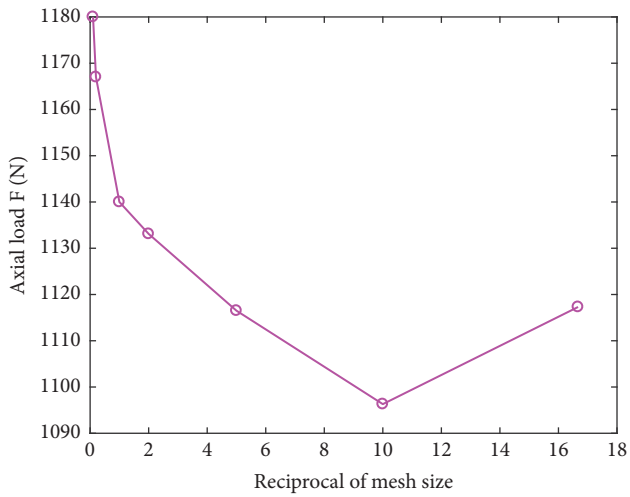

(c) M6×1.0×6.1, u=0.08, Δ_x=0.001mm

Figure 12: Influence of the reciprocal of finite element mesh size on axial force.

the friction coefficient on the thread stiffness and axial force distribution.

(1) The results of the calculation of the thread stiffness calculated by the theoretical calculation method of this study are basically consistent with the results of the FEA. The results obtained by the test are smaller than the calculated results. This is due to the influence of the thread manufacturing on the experimental results.

(2) Thread-stiffness is closely related to material properties, pitch, and thread length. We can obtain higher stiffness by increasing Young's modulus of the material, increasing the length of the thread, and reducing the pitch.

(3) We can also increase the friction coefficient of the thread joint surface to increase the stiffness of the thread connection, but we have found that using this method to increase the thread stiffness is limited.

(4) In order to make the axial load distribution of the thread uniform, we can reduce the friction coefficient of the thread surface, but we found that the use of this method to improve the distribution of the axial force of the thread has limited effectiveness.

Nomenclature

μ: Contact surface friction coefficient
w_z: Axial unit width force, N
δ_1: Thread bending deformation, mm
δ_2: Thread shear deformation, mm
δ_3: Thread root inclination deformation, mm
δ_4: Radial direction extended deformation or radial shrinkage deformation, mm
δ_5: Thread root shear deformation, mm
$\overline{E}$: Bending moment of the unit load beam, N•mm

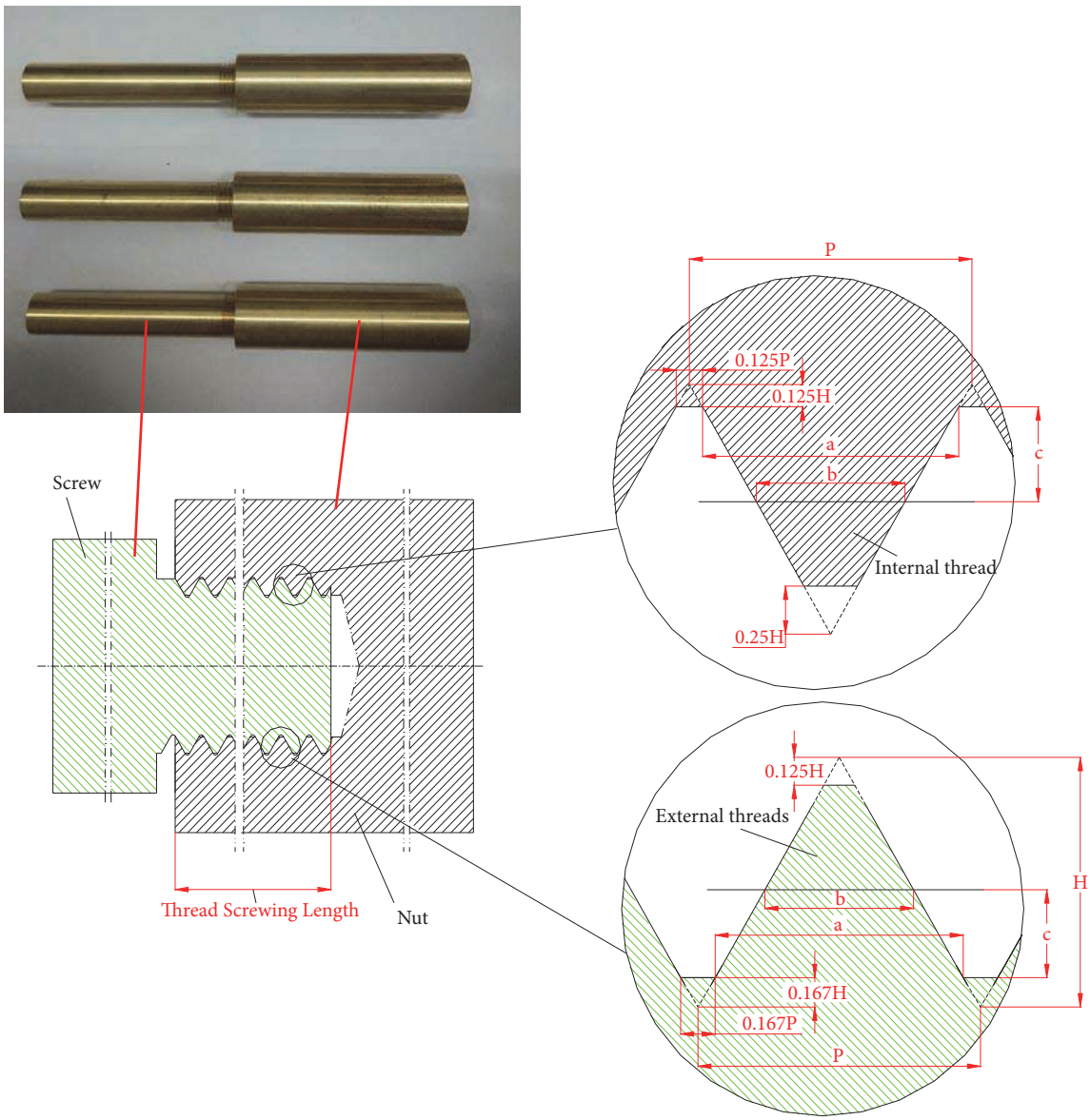

Figure 13: Part of experimental threaded connection samples and ISO internal thread and ISO external thread.

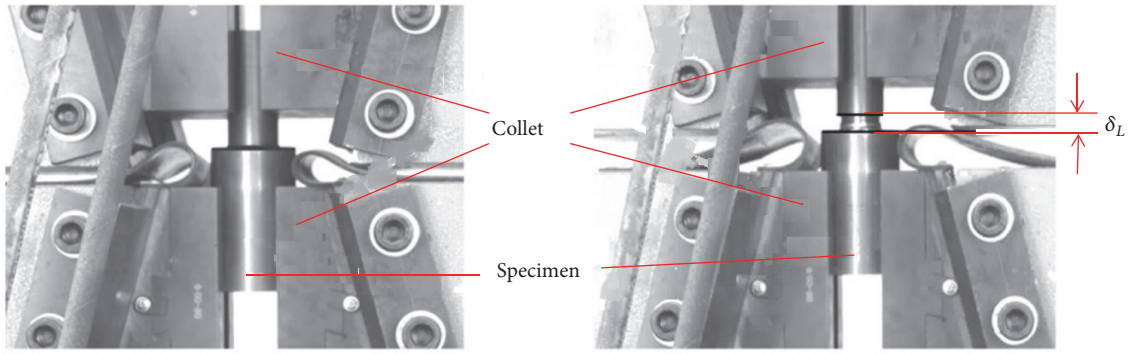

Figure 14: Tensile test [1].

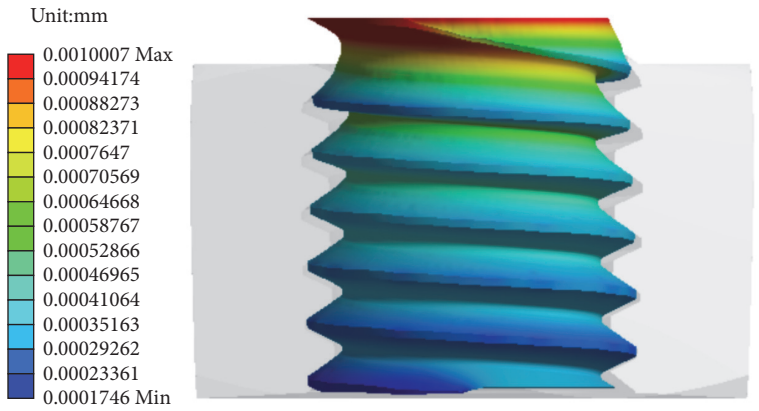

Figure 15: Axial displacement for screws with a friction coefficient of μ=0.01. Total force reaction=1086.00 N.

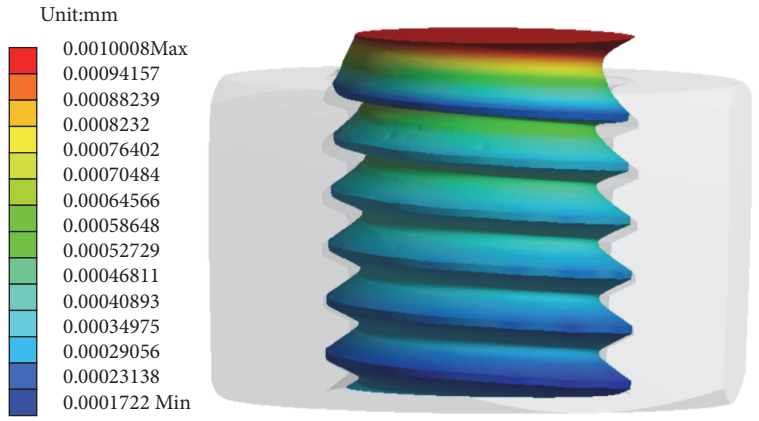

Figure 16: Axial displacement for screws with a friction coefficient of μ=0.05. Total force reaction=1092.00 N.

M_w: Bending moment of the beam under the actual load, N•mm
I: Area moment of inertia, mm^4
E_b: Young's modulus of the screw material, N/mm^2
c: Length of the beam, thread pitch line height, mm
h: Beam end section height, mm
B: Beam section width, mm
β_1: Beam root section height and the beam end section height ratio
B_b: Ratio of the height of the screw thread root section to the section height at the middiameter
B_n: Ratio of the height of the nut thread root section to the section height at the middiameter
δ_{4b}: Radial shrinkage deformation of the screw thread, mm
δ_{4n}: Radial direction extended deformation of the nut thread, mm
a: Width of the thread root, mm
D_0: Cylinder (nut) outer diameter, mm
d_p: Effective diameter of the thread, mm
ν_n: Poisson's ratio of nut material
P: Pitch, mm
M_{wb}: Bending moment of the screw thread, N•mm
δ_{1b}: Thread bending deformation of the screw thread, mm
δ_{2b}: Thread shear deformation of the screw thread, mm
δ_{3b}: Thread root inclination deformation of the screw thread, mm
δ_{4b}: Radial direction extended deformation of the screw thread, mm
δ_{5b}: Thread root shear deformation of the screw thread, mm
M_{wn}: Bending moment of the nut thread, N•mm
δ_{1n}: Thread bending deformation of the nut thread, mm
δ_{2n}: Thread shear deformation of the nut thread, mm
δ_{3n}: Thread root inclination deformation of the nut thread, mm
δ_{4n}: Radial direction extended deformation of the nut thread, mm
δ_{5n}: Thread root shear deformation of the nut thread, mm
f_Δ: Unit force per unit width of the axial direction

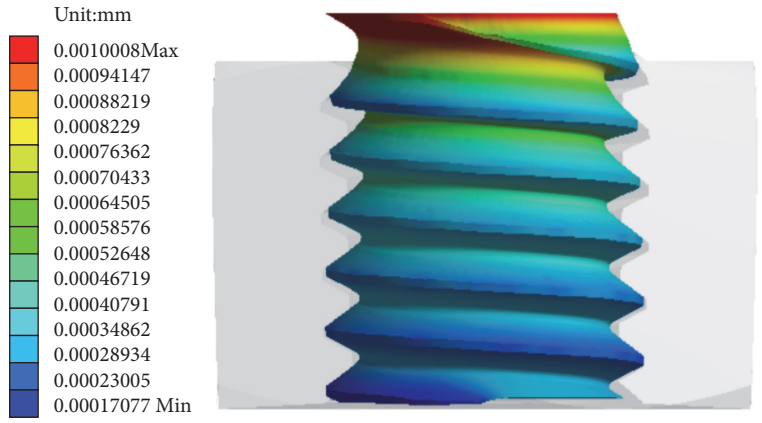

Figure 17: Axial displacement for screws with a friction coefficient of μ=0.1. Total force reaction=1098.00 N.

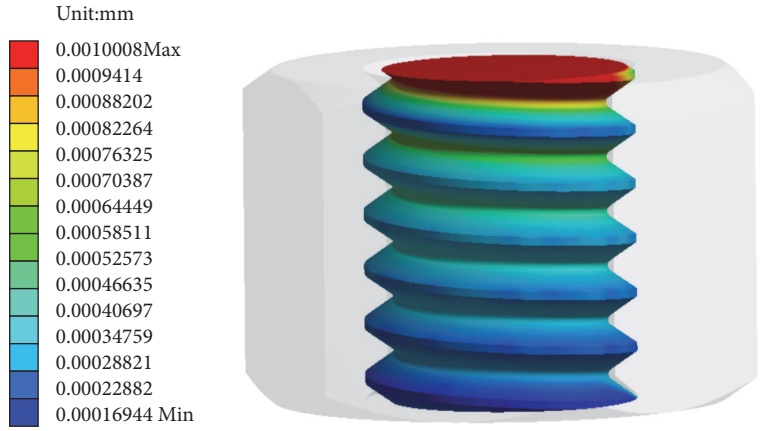

Figure 18: Axial displacement for screws with a friction coefficient of μ=0.2. Total force reaction=1108.40 N.

δ_{b1}: Total deformation of external (screw) thread, mm
δ_{n1}: Total deformation of internal (nut) thread, mm
z_b: The load on somewhere on the x-axis is F, where the screw thread axial deformation, mm
z_n: The load on somewhere on the x-axis is F, where the nut thread axial deformation, mm
r: Length along the helical direction, mm
β: Lead angle of the thread, degree
$k_{bx}(x)$: Stiffness of the unit axial length of the screw, N/mm
$k_{nx}(x)$: Stiffness of the unit axial length of the nut, N/mm^2
z_x: Axial total deformation of the threaded connection, mm
$k_{ux}(x)$: Stiffness of the unit axial length of the threaded connection, N/mm^2
F_b: Total axial force (load), N
ε_b: At the x position, the axial force is $F(x)$, the screw elongation amount
ε_n: At the x position, the axial force is $F(x)$, the nut compression amount
$A_b(x)$: Vertical cross-sectional areas of screw at the x position, mm^2
$A_n(x)$: Vertical cross-sectional areas of nut at the x position, mm^2
E_b: Young's modulus of the screw body, N/mm^2
E_n: Young's modulus of the nut body, N/mm^2
$k_x(x)$: Stiffness in the axial direction x, N/mm
K_c: Overall stiffness of the threaded connection, N/mm
Δ_x: Axial displacement, mm
F_x: Total axial force, N
F_{xt}: Axial tension load, N
K_t: Overall stiffness of the threaded connection, N/mm

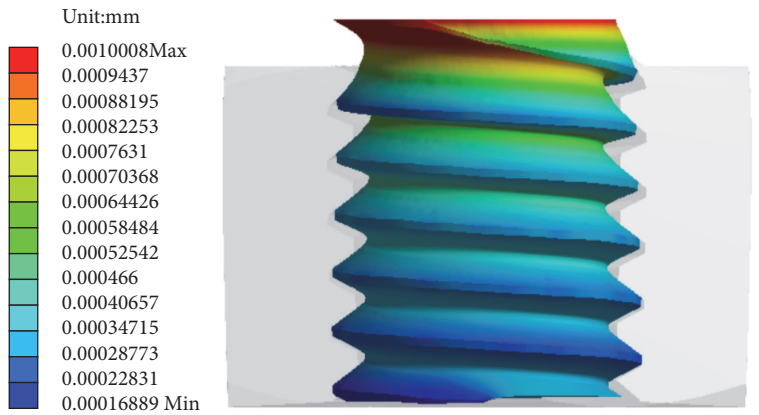

Figure 19: Axial displacement for screws with a friction coefficient of μ=0.25. Total force reaction=1110.6 N.

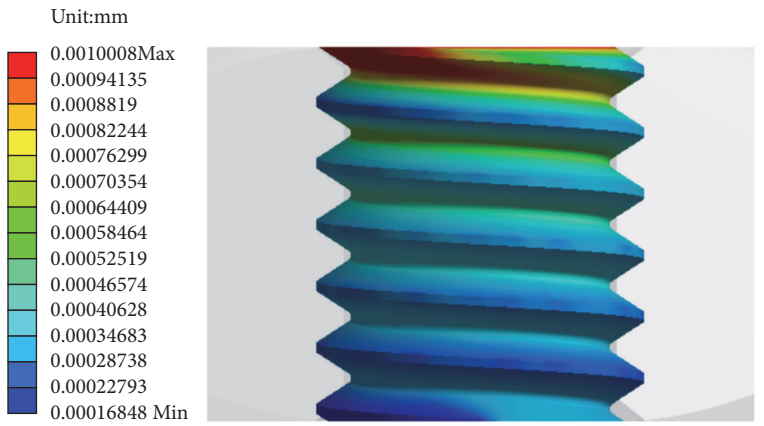

Figure 20: Axial displacement for screws with a friction coefficient of μ=0.3. Total force reaction=1114.2 N.

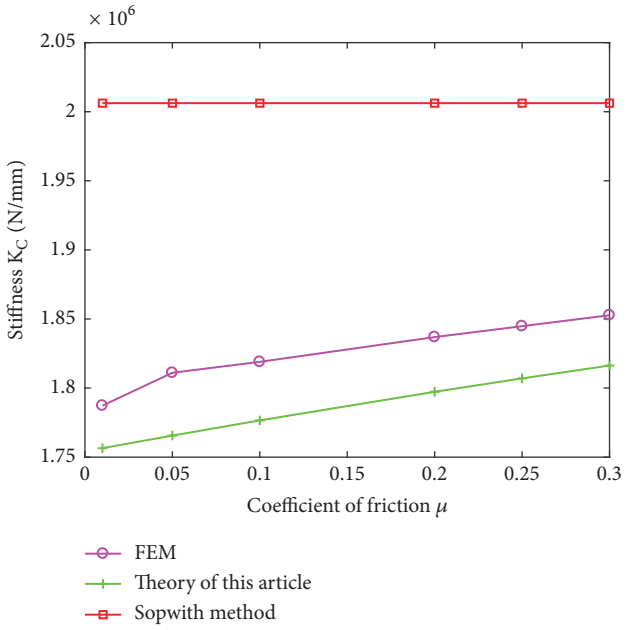

Figure 21: Effect of friction coefficient on stiffness. M10×1.5×9.

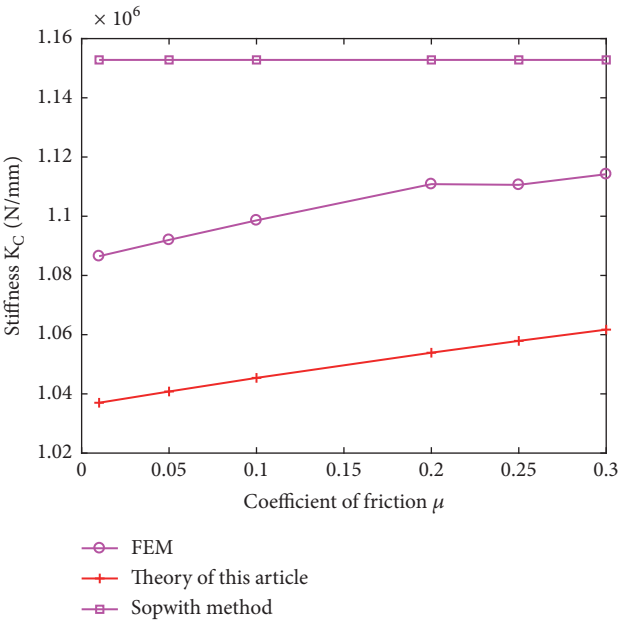

Figure 22: Effect of friction coefficient on stiffness. M6×1×6.1.

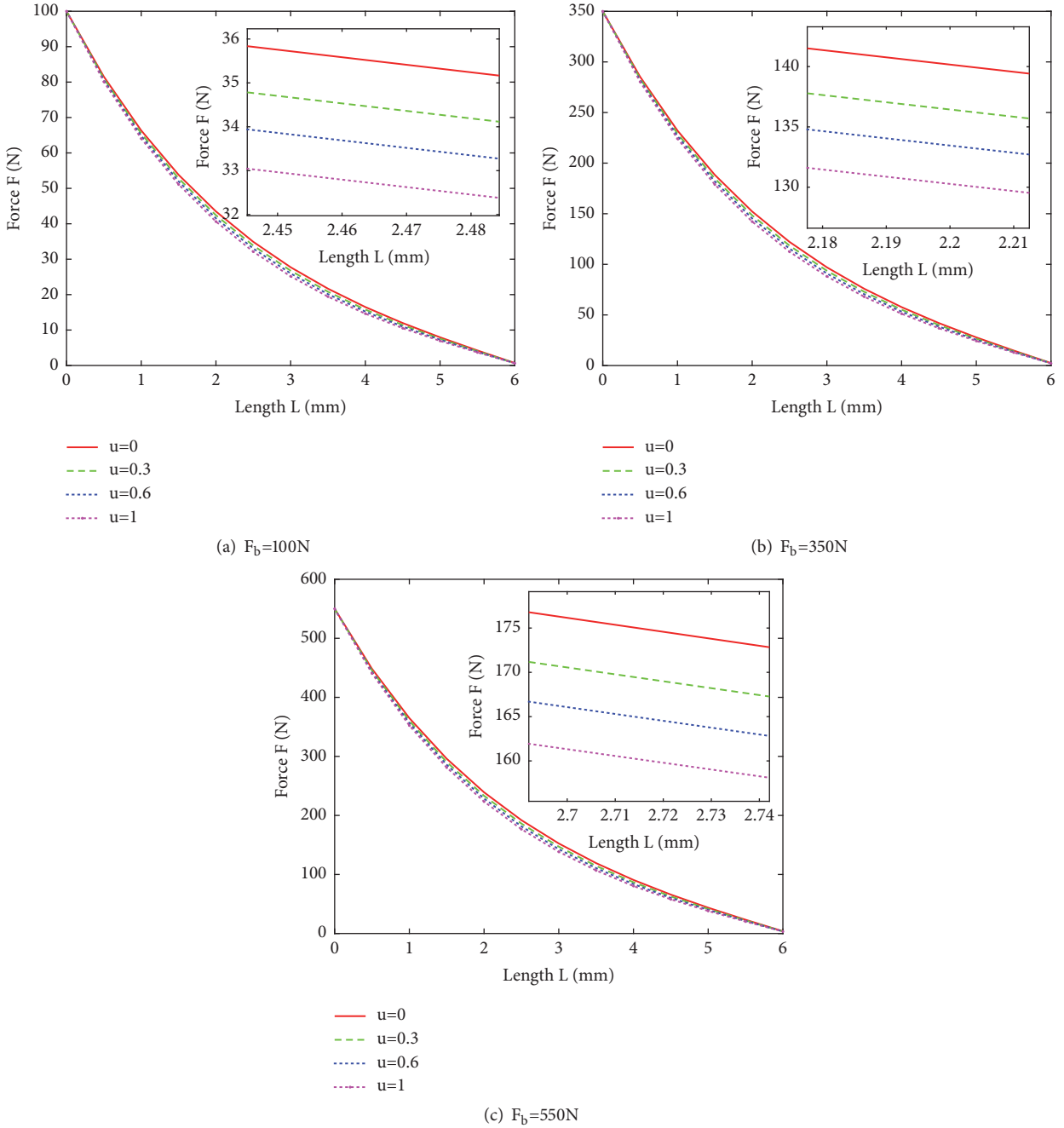

(a) F_b=100N

(b) F_b=350N

(c) F_b=550N

Figure 23: Effect of Friction Coefficient on Axial Force Distribution.

δ_L: Axial deformation of the thread, mm
H: Thread original triangle high, mm.

Data Availability

The data used to support the findings of this study are included within the article.

Conflicts of Interest

The authors declare that they have no conflicts of interest.

Acknowledgments

The authors would like to acknowledge support from the National Natural Science Foundation of China [Grant nos. 51675422, 51475366, and 51475146] and Science &

Technology Planning Project of Shaanxi Province [Grant no. 2016JM5074].

References

[1] D. Zhang, S. Gao, and X. Xu, "A new computational method for threaded connection stiffness," *Advances in Mechanical Engineering*, vol. 8, no. 12, 2016.

[2] K. Murayama, I. Yoshimoto, and Y. Nakano, "On spring constant of bolted joints," *Transactions of the Japan Society of Mechanical Engineers*, vol. 41, no. 344, pp. 1289–1297, 1975.

[3] I. Fernlund, *A Method to Calculate the Pressure Between Bolted or TU, 1962. Riveted Plates*, Chalmers University of Technology, 1961.

[4] N. Motosh, "Determination of joint stiffness in bolted connections," *Journal of Engineering for Industry*, vol. 98, no. 3, pp. 858–861, 1976.

[5] B. Kenny and E. A. Patterson, "Load and stress distribution in screw threads," *Experimental Mechanics*, vol. 25, no. 3, pp. 208–213, 1985.

[6] B. Kenny and E. A. Patterson, "The distribution of load and stress in the threads of fasteners - a review," *Journal of the Mechanical Behavior of Materials*, vol. 2, no. 1-2, pp. 87–106, 1989.

[7] D. L. Miller, K. M. Marshek, and M. R. Naji, "Determination of load distribution in a threaded connection," *Mechanism and Machine Theory*, vol. 18, no. 6, pp. 421–430, 1983.

[8] W. Wang and K. M. Marshek, "Determination of load distribution in a threaded connector with yielding threads," *Mechanism and Machine Theory*, vol. 31, no. 2, pp. 229–244, 1996.

[9] J. Wileman, M. Choudhury, and I. Green, "Computation of member stiffness in bolted connections," *Journal of Mechanical Design*, vol. 113, no. 4, pp. 432–437, 1991.

[10] M. De Agostinis, S. Fini, and G. Olmi, "The influence of lubrication on the frictional characteristics of threaded joints for planetary gearboxes," *Proceedings of the Institution of Mechanical Engineers, Part C: Journal of Mechanical Engineering Science*, vol. 230, no. 15, pp. 2553–2563, 2016.

[11] D. Croccolo, M. De Agostinis, S. Fini, and G. Olmi, "Tribological properties of bolts depending on different screw coatings and lubrications: An experimental study," *Tribology International*, vol. 107, pp. 199–205, 2017.

[12] D. Croccolo, M. De Agostinis, S. Fini, and G. Olmi, "An experimental study on the response of a threadlocker, involving different materials, screw dimensions and thread proportioning," *International Journal of Adhesion and Adhesives*, 2018.

[13] D. Croccolo, M. De Agostinis, and N. Vincenzi, "Failure analysis of bolted joints: Effect of friction coefficients in torque-preloading relationship," *Engineering Failure Analysis*, vol. 18, no. 1, pp. 364–373, 2011.

[14] Q. Zou, T. S. Sun, S. A. Nassar, G. C. Barber, and A. K. Gumul, "Effect of lubrication on friction and torque-tension relationship in threaded fasteners," in *Proceedings of the STLE/ASME International Joint Tribology Conference (IJTC '06)*, San Antonio, TX, USA, October 2006.

[15] Q. Zou, T. S. Sun, S. Nassar, G. C. Barber, H. El-Khiamy, and D. Zhu, "Contact mechanics approach to determine effective radius in bolted joints," *Journal of Tribology*, vol. 127, no. 1, pp. 30–36, 2005.

[16] S. A. Nassar, P. H. Matin, and G. C. Barber, "Thread friction torque in bolted joints," *Journal of Pressure Vessel Technology*, vol. 127, no. 4, pp. 387–393, 2005.

[17] S. A. Nassar, H. El-Khiamy, G. C. Barber, Q. Zou, and T. S. Sun, "An experimental study of bearing and thread friction in fasteners," *Journal of Tribology*, vol. 127, no. 2, pp. 263–272, 2005.

[18] S. A. Nassar, G. C. Barber, and D. Zuo, "Bearing friction torque in bolted joints," *Tribology Transactions*, vol. 48, no. 1, pp. 69–75, 2005.

[19] S. Nassar A, S. Ganeshmurthy, R. Ranganathan M et al., "Effect of tightening speed on the torque-tension and wear pattern in bolted connections," *Journal of Pressure Vessel Technology*, vol. 129, no. 3, pp. 1669–1681, 2007.

[20] H. Kopfer, C. Friedrich, M. De Agostinis, and D. Croccolo, "Friction characteristics in light weight design focusing bolted joints," in *Proceedings of the ASME International Mechanical Engineering Congress and Exposition (IMECE '12)*, pp. 839–846, November 2012.

[21] B. Kenny and E. A. Patterson, "The distribution of load and stress in the threads of fasteners - a review," *Journal of the Mechanical Behavior of Materials*, vol. 2, no. 1-2, pp. 87–105, 1989.

[22] J. E. Shigley, C. R. Mischke, and R. G. Budynas, *Mechanical Engineering Design*, McGraw-Hill, New York, NY, USA, 2004.

[23] T. F. Lehnhoff and W. E. Wistehuff, "Nonlinear effects on the stresses and deformations of bolted joints," *Journal of Pressure Vessel Technology, Transactions of the ASME*, vol. 118, no. 1, pp. 54–58, 1996.

[24] N. S. Al-Huniti, "Computation of member stiffness in bolted connections using the finite element analysis," *Mechanics Based Design of Structures and Machines*, vol. 33, no. 3-4, pp. 331–342, 2005.

[25] J. C. Musto and N. R. Konkle, "Computation of member stiffness in the design of bolted joints," *Journal of Mechanical Design*, vol. 128, no. 6, pp. 1357–1360, 2006.

[26] N. Haidar, S. Obeed, and M. Jawad, "Mathematical representation of bolted-joint stiffness: A new suggested model," *Journal of Mechanical Science and Technology*, vol. 25, no. 11, pp. 2827–2834, 2011.

[27] S. A. Nassar and A. Abboud, "An improved stiffness model for bolted joints," *Journal of Mechanical Design*, vol. 131, no. 12, Article ID 121001, 2009.

[28] Z. Y. Qin, Q. K. Han, and F. L. Chu, "Analytical model of bolted disk-drum joints and its application to dynamic analysis of jointed rotor," *Proceedings of the Institution of Mechanical Engineers, Part C: Journal of Mechanical Engineering Science*, vol. 228, no. 4, pp. 646–663, 2014.

[29] J. Liu, H. Ouyang, J. Peng et al., "Experimental and numerical studies of bolted joints subjected to axial excitation," *Wear*, vol. 346-347, pp. 66–77, 2016.

[30] D. G. Sopwith, "The distribution of load in screw threads," *Proceedings of the Institution of Mechanical Engineers*, vol. 159, no. 1, pp. 373–383, 2006.

[31] A. Yamamoto, *The Theory and Computation of Threads Connection*, Yokendo, Tokyo, Japan, 1980.

[32] Q. Zou, T. S. Sun, S. A. Nassar, G. C. Barber, and A. K. Gumul, "Effect of lubrication on friction and torque-tension relationship in threaded fasteners," *Tribology Transactions*, vol. 50, no. 1, pp. 127–136, 2007.

Hindawi
Mathematical Problems in Engineering
Volume 2019, Article ID 1378783, 11 pages
https://doi.org/10.1155/2019/1378783

Research Article

An MEA-Tuning Method for Design of the PID Controller

Yongli Zhang,[1] **Lijun Zhang**,[2] **and Zhiliang Dong**[1]

[1]*School of Management Science and Engineering, Hebei GEO University, Shijiazhuang, Hebei, China*
[2]*Earth Sciences Museum, Hebei GEO University, Shijiazhuang, Hebei, China*

Correspondence should be addressed to Yongli Zhang; zhangyongli086@163.com

Received 1 November 2018; Revised 3 December 2018; Accepted 8 January 2019; Published 20 January 2019

Guest Editor: Anders E. W. Jarfors

The optimization and tuning of parameters is very important for the performance of the PID controller. In this paper, a novel parameter tuning method based on the mind evolutionary algorithm (MEA) was presented. The MEA firstly transformed the problem solutions into the population individuals embodied by code and then divided the population into superior subpopulations and temporary subpopulations and used the similar taxis and dissimilation operations for searching the global optimal solution. In order to verify the control performance of the MEA, three classical functions and five typical industrial process control models were adopted for testing experiments. Experimental results indicated that the proposed approach was feasible and valid: the MEA with the superior design feature and parallel structure could memorize more evolutionary information, generate superior genes, and enhance the efficiency and effectiveness for searching global optimal parameters. In addition, the MEA-tuning method can be easily applied to real industrial practices and provides a novel and convenient solution for the optimization and tuning of the PID controller.

1. Introduction

The proportional integral derivative (PID) controller is the most widely used and most mature in industrial production [1, 2]. So far, the vast majority of industrial controllers are PID controllers or their second generations owing to the advantages of simple structure, strong robustness, and easy realization [3–5]. However, once the controller characteristics, control scheme, interference form, and size are basically fixed, the quality of the control system depends on the setting of the controller parameters. Therefore, PID parameter tuning and optimizing is one core issue for PID controller design [6, 7].

The parameter tuning methods for PID controller design fall into two basic categories: conventional parameter tuning methods and intelligent optimization algorithms. Conventional parameter tuning methods include the empirical method, upwards curve method, critical ratio method, damping oscillatory method, and relay feedback method [8]. The Z-N method as an empirical parameter tuning method had a very strong impact on the actual control system; practically all vendors and users of the PID controller apply it or its simple modifications in controller tuning. The Z-N method was developed by Ziegler and Nichols in seminal paper [9], which was based on two ideas: to characterize process dynamics by two parameters, which are easily determined experimentally, and to calculate controller parameters from the process characteristics by a simple formula. Although widely used in practice, conventional parameter tuning methods have large overshoot, poor correction accuracy, and time-consuming tuning process [10–13].

With the development of the intelligent control theory, intelligent optimization algorithms started to be applied in PID parameter tuning and optimizing and achieved incomparable results that the conventional parameter tuning methods cannot obtain. For example, the genetic algorithm (GA) [14–16], particle swarm optimization (PSO) [17–19], tabu search algorithm (TSA) [20–22], bacterial foraging algorithm (BFA) [23–25], ant colony algorithm (ACA) [26], artificial bee colony (ABC) algorithm [27], and BAT search algorithm [28] were adopted to optimize PID controller parameters and had achieved much better performances.

Although intelligent optimization algorithms possess merits of strong robustness, good universality, and few limited conditions for use, some intelligent algorithms still have defects such as premature convergence and slow convergence

rate. For example, the GA, PSO, and TSA are all stochastic search algorithms. Their search processes are nondeterministic, suffer from slow convergence, and easily fall into the local optimal solution [29, 30]. The parameter settings of the GA and ACA have not clear theoretical basis, and most parameters still need to be determined by experience and experiment. The population individual of the PSO and BAT search algorithm lacks the mutation mechanism; once trapped in the local extreme, it is difficult to get rid of [31]. The complexity of the ABC algorithm programming limits its application to a certain extent. In addition, there are few controlled process models that adopt the ABC algorithm for PID parameter tuning, and its generality is not high [32, 33]. To further improve the optimization performance and overcome the defects of traditional algorithms, Chinese scholar Sun Cheng-Yi et al. raised the mind evolutionary algorithm (MEA) based on the genetic algorithm in 1998 [34]. The MEA is an evolutionary algorithm simulating the progress of human mind and has the positive and negative feedback mechanism, wherein the positive feedback mechanism improves toward being more beneficial to the population survival, so as to consolidate and develop the evolution achievement. The negative feedback mechanism prevents the premature convergence of the algorithm, so as to avoid the situation in which the algorithm is caught in the local optimal solution. The structural parallelism of the MEA guarantees the high search efficiency of the algorithm, overcomes the defects of the GA such as time-consuming computation and premature convergence, and also has extremely strong robustness on interference [35, 36].

While theory application and engineering practices have proved that the MEA has very high search efficiency and convergence performance [37–39], few researches apply it to the PID parameter tuning and optimizing. Therefore, this paper is undertaken to establish a parameter tuning method using the MEA for PID controller design to fill the research gap.

The rest of this article is organized as follows. The principle of the MEA and MEA-tuning process for PID controller design are described in Section 2. Three classical functions are used to test the performance of the MEA and compare it with the GA in Section 3. The MEA is applied to the parameters tuning of five classical PID controllers and compared with the GA and traditional Z-N method in optimization performance, convergence time, and robustness in Section 4. Finally, conclusions are drawn and future researches are suggested in Section 5.

2. Mind Evolutionary Algorithm

2.1. Algorithm Principle. The mind evolutionary algorithm (MEA) is a kind of evolutionary algorithm simulating the progress of the human mind, developed on the basis of the GA. The MEA uses two types of operation, similar taxis and dissimilation, and uses population optimizing instead of individual optimizing, which avoids the defects of the GA. The similar taxis operation is a process in which the individual competes to be a winner, which happens within the scope of a subpopulation. The dissimilation operation is the process in which a subpopulation competes to be a winner and continuously explores the new point of solution space, which happens within the whole solution space. In the course of the algorithm running, the similar taxis and dissimilation operation is executed repeatedly until the condition of terminating the running of algorithm is satisfied.

Compared with the GA, the MEA has following advantages: the crossover and mutation operations of the GA generate not only superior genes, but also inferior destructive genes, and those operations have duality, but the MEA uses the similar taxis and dissimilation operations, which amend the defects of the GA; the similar taxis and dissimilation operations of the MEA are coordinated mutually but also independent mutually, and any improvement on any aspect will raise the algorithm's prediction accuracy; the similar taxis and dissimilation operations have parallelism on structure, which raises the algorithm's search efficiency and computation speed; the MEA divides the populations into superior subpopulations and temporary subpopulations, which can memorize evolutionary information more than one generation.

2.2. Basic Concepts. The MEA follows some basic concepts of the GA such as "population," "individual," and "environment," but meanwhile it also adds some new concepts.

2.2.1. Population and Subpopulation. The MEA is a kind of learning method making optimization through iteration, and all individuals in every generation of the evolutionary process gather into one population. A population is divided into several subpopulations. The subpopulation contains two classes: superior subpopulation and temporary subpopulation. The superior subpopulation records the information of the winners in the global competition, and the temporary subpopulation records the process of the global competition.

2.2.2. Billboard. The billboard is equivalent to an information platform, which provides chances of information communication between the individuals or the subpopulations. The billboard records three types of effective information: the serial number of individual or subpopulation, the action, and the score. By utilizing the serial number of the individual or subpopulation, it is convenient to distinguish different individuals or subpopulations; the description of action varies from different research fields, and since this article is researching the problem of parameter optimization, the action is used to record the exact position of the individual and subpopulation; the score is the evaluation of environment on the individual action, and, in the optimization process by utilizing the MEA, it can rapidly find out the optimized individuals and populations only if the scores of every individual and subpopulation are recorded all the time. The individuals in the subpopulation post up their own information on the local billboard, and the information of each subpopulation is posted up on the global billboard.

2.2.3. Similar Taxis. Within the scope of a subpopulation, the process in which an individual competes to be a winner is called similar taxis. In the process of a subpopulation's

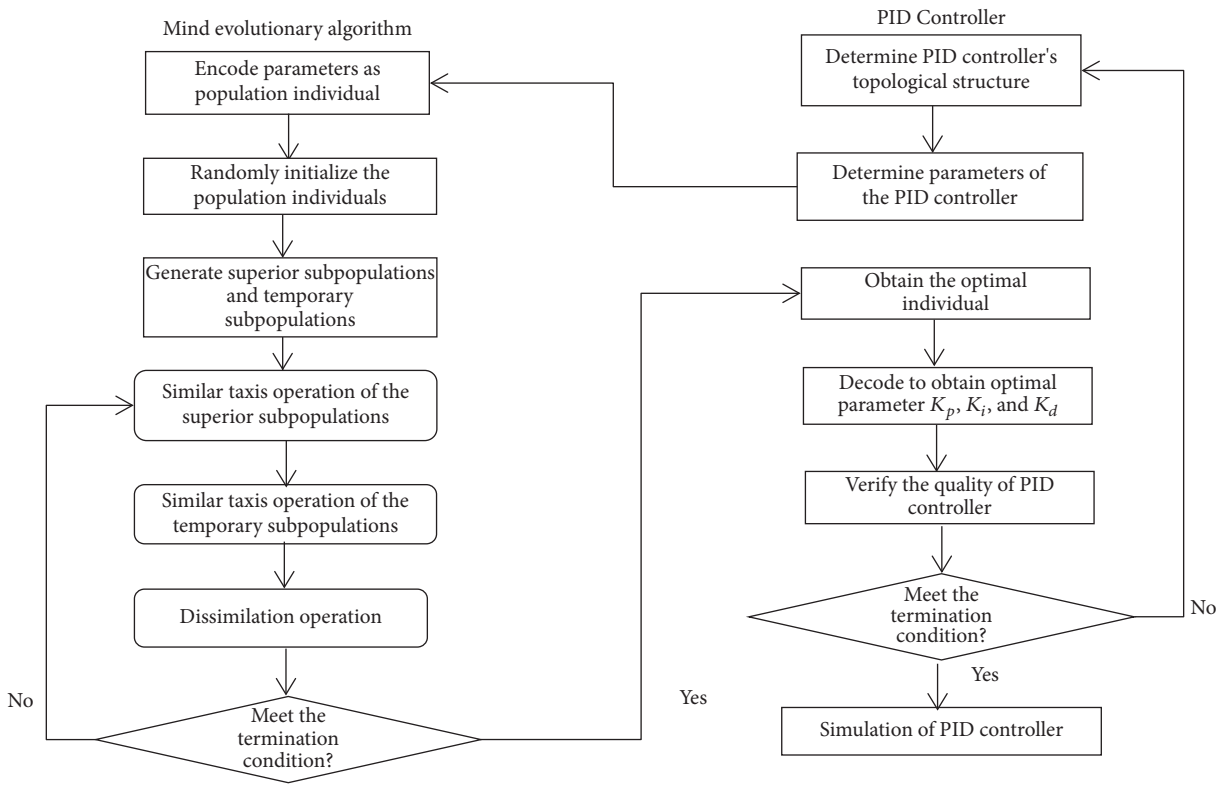

Figure 1: Parameter tuning process of the PID controller by the MEA.

similar taxis, if a new winner cannot be generated, this means that such subpopulation has matured. When a subpopulation matures, the similar taxis process of such subpopulation comes to an end. The period of a subpopulation from its birth to maturity is called as lifetime.

2.2.4. Dissimilation. In the whole solution space, each subpopulation competes to be a winner and continuously explores a new solution space point; this process is known as dissimilation. Dissimilation has two definitions: each subpopulation makes global competition, and if the score of a temporary subpopulation is higher than the score of a certain matured superior subpopulation, such superior subpopulation will be replaced by the winning temporary subpopulation, and the individuals of the original superior subpopulation will be released; if the score of a matured temporary subpopulation is lower than the score of any superior subpopulation, such temporary subpopulation will be abandoned, and the individuals therein will be released; the released individuals will re-search and form a new temporary subpopulation.

2.3. Calculation Procedure. The quality of the PID controller depends on the tuning and optimizing of parameters K_p, K_i, and K_d. To obtain the optimal PID controller, the parameters K_p, K_i, and K_d are encoded and taken as the population individual, the integral of time absolute errors (*ITAE*) obtained from the PID controller is regarded as the individual fitness value, and then the MEA begins to evolve. Through continuous iterative evolution of the similar taxis and dissimilation operation, the optimal individual of the population is finally obtained, which is taken as the parameter of the PID controller after being decoded; the optimal PID controller is established.

The tuning process of the PID controller by using the MEA is shown as Figure 1.

Step 1 (initialization of the population's individual). The parameters K_p, K_i, and K_d of PID controller coding in the real number are taken as the population individual and the integral of time absolute errors (*ITAE*) is regarded as the individual fitness value, and then N initial population's individuals are generated randomly.

Step 2 (generation of the superior subpopulation and temporary subpopulation). According to the individual fitness value, the N_s superior individuals with the highest scores and N_t temporary individuals with the next highest scores are picked out. Taking each superior individual or temporary individual as center, new individuals are produced and N_s superior subpopulations and N_t temporary subpopulations are formed, named as G_s and N_t, respectively. The number of individuals in the subpopulation is $N_p = N/(N_s + N_t)$.

Step 3 (similar taxis). To compute the fitness values of all individuals in the superior subpopulation and temporary subpopulation, the optimal population g_s^* or g_t^* (namely, the center) in the subpopulation is taken as the center of the subpopulation, and the score of the optimal individual is

taken as the score of such subpopulation. The fitness values of g_s^* and g_t^* are described as below:

$$f_s^* = \min\{(f(g) : g \in G_s),\ 1 \le s \le N_s\} \quad (1)$$

$$f_t^* = \min\{(f(g) : g \in G_t),\ 1 \le t \le N_t\}. \quad (2)$$

Step 4 (judgment of subpopulation's maturity). In the process of subpopulation similar taxis, when the population center is the optimal individual, and no new superior individual is generated any more, then such subpopulation matures and turns into the next step; otherwise it turns into the previous step and executes the similar taxis operation again.

Step 5 (dissimilation). After the subpopulation matures, the score of each subpopulation will be posted up on the global billboard, and if the score of any temporary subpopulation G_t is higher than the score of any matured superior subpopulation G_s, such superior subpopulation G_s will be replaced by the winning temporary subpopulation G_t, the individuals in the original superior subpopulation G_s will be released, the originally winning temporary subpopulation G_t will be replaced by the new temporary subpopulation G_t', and the individuals in G_t' will be evenly distributed in the solution space.

Step 6 (iterative evolution). The superior subpopulation with the highest fitness value in all superior subpopulations or temporary subpopulations is selected to judge whether the termination condition is satisfied. If yes, the evolution will be terminated, and if not, the operation of Steps 3~5 will be repeated.

Step 7 (decoding of the optimal individual and establishing of the PID controller optimized by the MEA). When the termination condition of the MEA is met, the superior subpopulation center as the optimal population individual will be decoded to obtain the parameters K_p, K_i, and K_d of the PID controller, and the optimized PID controller is established.

3. Classical Test Functions Verification

In order to verify the validity of the MEA, 3 classical functions are selected for testing and compared with the GA. The test functions are the Sphere function, Rastrigin function, and Rosenbrock function.

(1) The Sphere Function

$$f(x, y) = x^2 + y^2. \quad (3)$$

In formula (3), $x, y \in [-10, 10]$; when $(x,y)=(0,0)$, the Sphere function reaches its minimum 0 (Figure 2).

(2) The Rastrigin Function

$$f(x, y) = 20 + x^2 - 10\cos(2\pi x) + y^2 - 10\cos(2\pi y). \quad (4)$$

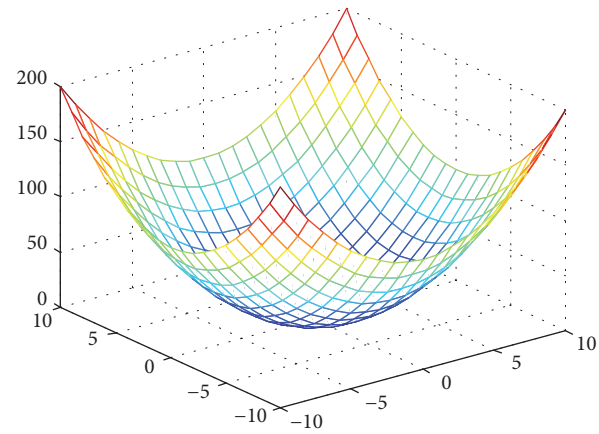

Figure 2: Sphere function graph.

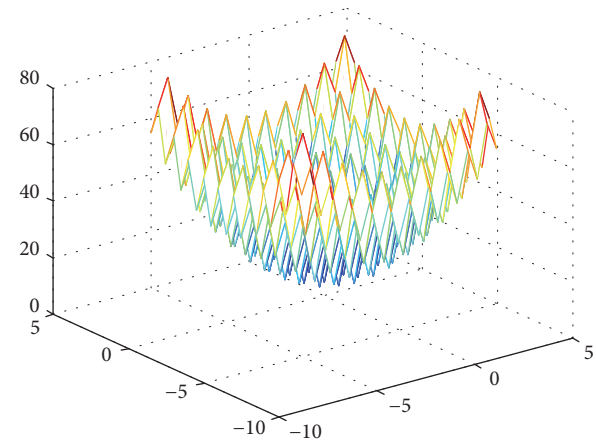

Figure 3: Rastrigin function graph.

In formula (4), $x, y \in [-5.12, 5.12]$; the global optimal solution of the Rastrigin function is 0, distributed at (0,0) (Figure 3).

(3) The Rosenbrock Function

$$f(x) = \sum_{i=1}^{N-1} \left(x_i^2 - x_{i+1}\right)^2 + \left(1 - x_i\right)^2. \quad (5)$$

In formula (5), $x, y \in [-10, 10]$; the Rosenbrock function is a pathological function that is hard to minimize, and the theoretical global minimum is 0 (Figure 4).

The MEA is established due to the defect of the GA, so this paper makes a comparative test between the MEA and GA to verify the superiority of the MEA. In the test, parameters of the MEA and GA are set as follows: evolution generations $iter_{max}$=10, population size N=200, number of superior subpopulation N_s=5, number of temporary subpopulation N_t=5, subpopulation size N_p=20, crossover probability C=0.2, and mutation probability M=0.1. The testing results are displayed in Table 1.

As shown in Table 1, the test results of three classical functions prove that the optimization performance of the MEA is better than the GA. In Figure 5, the fitness evolution

Table 1: Optimization results and comparison for the MEA and GA.

Function	Theoretical extreme	MEA			GA		
		Mean value	Optimal value	Worst value	Mean value	Optimal value	Worst value
Sphere	0	1.3396	0.0004	4.7535	2.1702	0.1306	2.2877
Rastrigin	0	5.9375	0.1557	10.2223	5.9935	2.0612	17.6934
Rosenbrock	0	1.0562	0.0010	9.2253	2.5015	6.5593	5.6020

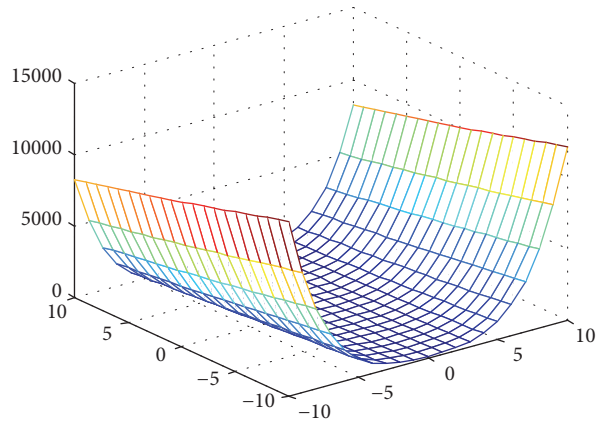

Figure 4: Rosenbrock function graph.

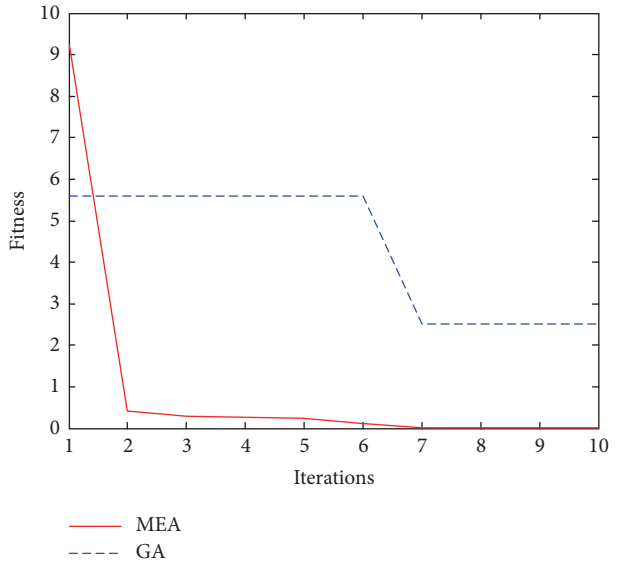

Figure 5: Evolutionary curves of optimal fitness for the Rosenbrock function.

curves of the Rosenbrock function show that, compared with the GA, the MEA has faster convergence speed and higher convergence precision. The experimental results indicated that, due to its superior design feature and parallel structure, the MEA could memorize more evolutionary information and search the optimal solution more efficiently and effectively, overcoming the defects of the GA, such as precociousness, easiness of falling into the local extremum, and time-consuming computation.

Figure 6: PID control system.

4. Simulation Studies

4.1. PID Controller and Performance Index. The proportional integral derivative (PID) controller is widely applied in industrial processes. The system structure of the PID controller is shown in Figure 6.

The general form of one PID controller is shown as below.

$$u(t) = K_p e(t) + K_i \int_0^t e(\tau)\, d\tau + K_d \frac{de(t)}{dt}. \quad (6)$$

In formula (6), $u(t)$ and $e(t)$ represent the control signal and error signal and K_p, K_i, and K_d are the proportional gain, integral gain, and derivative gain, respectively. By entering parameters K_p, K_i, and K_d, the control signal is calculated and then sent to the controlling module; the controlled object is driven. If the controller is designed properly, the control signal will make the output error converge to a small neighborhood of the origin to achieve the control requirement. Therefore, the optimization objective of the PID controller is to obtain an optimal set of parameters (K_p, K_i, K_d), which will minimize the performance function by searching the given controller parameters space.

In general, integration error indexes include the integral of squared errors (*ISE*), integrated absolute errors (*IAE*), and integral of time absolute errors (*ITAE*) [40]. In this paper, the *ITAE* is chosen as the performance indicator of the PID controller. The formula for calculation is as follows:

$$ITAE = \int_0^T t\,|e(t)|\, dt. \quad (7)$$

If the functional model on error is regarded as a loss function, the integral index of formula (7) can be regarded as the control goal of a control system when it is transferred from one state to another; then it is considered that the system has the optimal control law with a minimal performance index. Generally, the adjustment time t_s corresponding to 5% or 2% error is taken as the upper bound T parameter of the integral.

Due to the existence of absolute error $|e(t)|$, formula (7) is difficult to solve by the analytic method, and the numerical methods are usually chosen to solve it; the specific steps are as follows: the continuous time is discretized with time step Δt; meanwhile, when the time $T = m\Delta t$ and m are

Table 2: Models for general controlled processes.

Type	Mathematical model	Model features
I	$\frac{e^{-\tau s}}{1+s}$ τ=0.5,1,2	First-order time-delay process τ=0.5 in this study
II	$\frac{e^{-\tau s}}{(1+s)^2}$ τ=0.5,1,2	Second-order time-delay process τ=1 in this study
III	$\frac{e^{-s}}{s(1+s)}$	Nonoscillating process
IV	$\frac{1-as}{(1+s)^2}$ a=0.5,1	Nonminimum phase process a=0.5 in this study
V	$\frac{1}{(1+s)^n}$ n=4,6,8	High-order process n=6 in this study

the integers of the appropriate size, the discrete time vector $t[n](n=1,2,\ldots,m)$ is obtained. When t is small enough, the *ITAE* can be calculated according to

$$ITAE = \sum_{i=0}^{m} t\,[i]\,|e\,[i]|\,\Delta t. \tag{8}$$

The process of PID parameter tuning using the MEA is actually an optimization problem. The parameter set (K_p, K_i, K_d) is regarded as the particle position vector $P(K_p,K_i,K_d)$ in the optimization space, K_p, K_i, and K_d are restricted to [0, K_{pm}], [0, K_{im}], and [0, K_{dm}], respectively, and the *ITAE* performance index is chosen as the fitness function of the algorithm. Through the iteration of the MEA, a set of parameters that minimize the *ITAE* value of the system response is found.

4.2. Simulation Experiment. In order to verify the control performance of the MEA, 5 typical industrial process control models $G_p(s)$ are selected as the research models, as shown in Table 2. Five typical industrial process control models are self-balanced and nonoscillating process with time lag of the first order, self-balanced and nonoscillating process with time lag of the second order, nonoscillating process without self-balance, nonminimum phase process with reverse characteristics, and high-order process.

According to the structural characteristics of the PID controller, the parameters to be optimized are K_p, K_i, and K_d. Then the parameters K_p, K_i, and K_d are encoded as the population individual; the individual length is 3, equal to parameter number. In order to compare algorithm performance, different algorithms need to set the same experimental conditions, so the population size is set to 200, the number of superior population or temporary population size is 5, the subpopulation size is 20, the evolution generations are set to 10, the crossover probability is set to 0.2, and the mutation probability is set to 0.1.

(1) Industrial Process Control Model I. The MEA, GA, and Z-N methods were adopted to search the optimal PID parameters of industrial process control model I, respectively; the PID parameters (K_p, K_i, K_d) and performance indexes (*ITAE*, t_s) obtained were listed in Table 3.

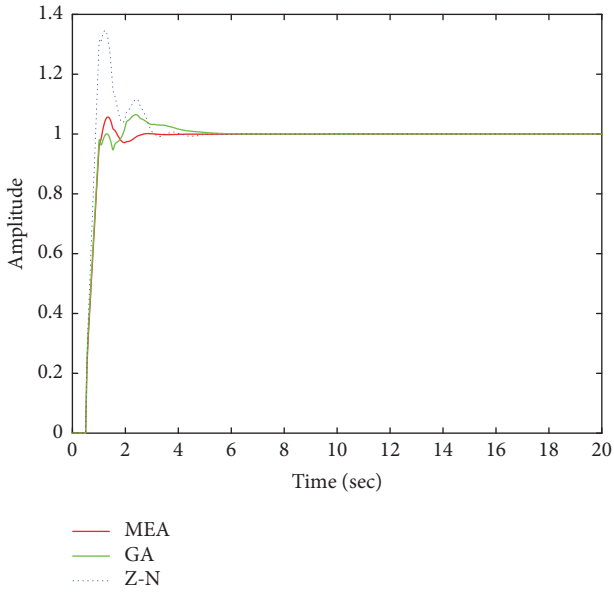

Figure 7: Closed-loop step response with process I.

Table 3 shows that the MEA-tuning method has the best fitting performance (*ITAE*=0.3463) and the fastest convergence speed (t_s=2.6910), followed by the GA-tuning method (*ITAE*=0.5758, t_s=5.6440) and the Z-N-tuning method (*ITAE*=0.7332, t_s=6.2987).

The obtained PID parameters (K_p, K_i, K_d) were brought into process model I, and the unit step responses of the MEA, GA, and Z-N methods are obtained, respectively, through Simulink (Figure 7). Figure 7 also proves that the MEA-tuning method controls process control model I more stably and faster.

(2) Industrial Process Control Model II. The optimal PID parameters (K_p, K_i, K_d) and performance indexes (*ITAE*,

Table 3: PID parameters and performances of industrial process control model I.

Parameter	MEA	GA	Z-N
K_p	1.7898	1.7449	2.2800
K_i	1.3770	1.5492	2.6576
K_d	0.2788	0.4228	0.4890
t_s	2.6910	5.6440	6.2987
ITAE	0.3463	0.5758	0.7332

Table 4: PID parameters and performances of industrial process control model II.

Parameter	MEA	GA	Z-N
K_p	1.3525	1.5441	1.6200
K_i	0.4982	0.5752	0.6707
K_d	0.8345	1.0517	0.9782
t_s	9.0798	9.5050	13.5319
ITAE	2.8671	3.2592	3.9535

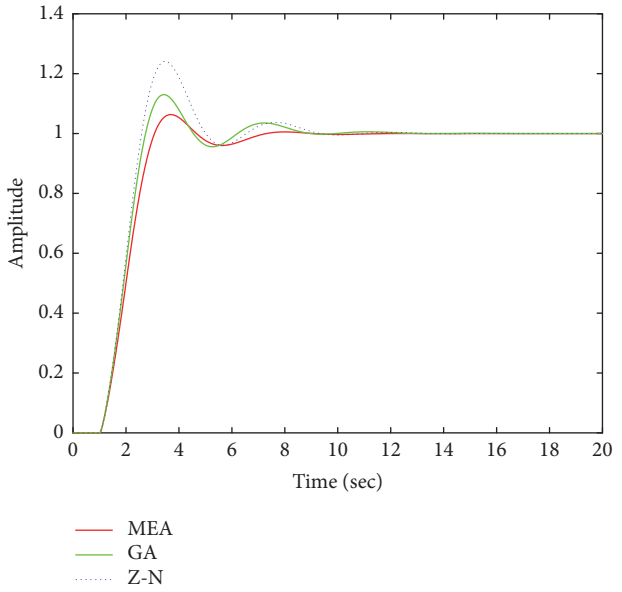

Figure 8: Closed-loop step response with process II.

t_s) tuned by the MEA, GA, and Z-N methods are obtained, as shown in Table 4. The performance indexes (*ITAE*, t_s) obtained by the MEA, GA, and Z-N methods are (*ITAE*=2.8671, t_s=9.0798), (*ITAE*=3.2592, t_s=9.5050), and (*ITAE*=3.9535, t_s=13.5319), respectively. Obviously, the MEA-tuning method has the least *ITAE* and the fastest search speed.

In order to further verify the effectiveness of the MEA, Simulink was used to investigate the unit step response of typical model control system II. The results show that, compared with the GA and Z-N methods, the MEA can make process control model II reach a stable state more quickly (Figure 8).

(3) Industrial Process Control Model III. The optimal PID parameters (K_p, K_i, K_d) and performance indexes (*ITAE*, t_s) of industrial process control model III were obtained by the MEA, GA, and Z-N methods and listed in Table 5. Compared with the GA method (*ITAE*=23.7167) and Z-N method (*ITAE*=23.7657), the MEA method can greatly improve the control performance (*ITAE*=11.2763), and the search speed of the MEA method is also improved slightly (t_s=15.2005). The unit step responses also show that the MEA method tunes process control model III with a smaller fluctuation range and faster convergence speed (Figure 9).

(4) Industrial Process Control Model V. The optimal PID parameters (K_p, K_i, K_d) and performance indexes (*ITAE*, t_s) of industrial process control model V were obtained by the MEA, GA, and Z-N methods and listed in Table 6. Compared with the GA method (*ITAE*=2.4037, t_s=7.2594) and Z-N method (*ITAE*=2.4623, t_s=8.7442), the MEA method has less *ITAE* and shorter calculation time, greatly improving the control performance (*ITAE*=0.7536) and search speed (t_s=3.3309). The GA has a slight advantage over the Z-N method, but it is not significant. The unit step responses also show that the MEA method tunes process control model V with a smaller fluctuation range and faster convergence speed (Figure 10).

(5) Industrial Process Control Model IV. The MEA, GA, and Z-N methods were used to search the optimal PID parameters of industrial process control model IV, respectively; then the PID parameters (K_p, K_i, K_d) were obtained and put into process control model IV through Simulink; the performance indexes (*ITAE*, t_s) were obtained and listed in Table 7.

Compared with the GA (*ITAE*=19.4274, t_s=18.1772) and Z-N method (*ITAE*=21.3847, t_s=20.0000), the MEA improves the control performance and computing speed, but not by much (*ITAE*=15.7474, t_s=16.1596). The unit step responses also show that none of the three methods achieve complete control of process control model IV within 20 seconds, but the MEA method has the smallest fluctuation range and the best performance (Figure 11).

The above simulation results show that, during the optimization process, the MEA constantly searches for better parameters, and the *ITAE* index decreases continuously;

Table 5: PID parameters and performances of industrial process control model III.

Parameter	MEA	GA	Z-N
K_p	0.9941	0.7477	0.6780
K_i	0.2601	0.2558	0.1855
K_d	0.9224	0.8571	0.6169
t_s	15.2005	18.4473	20.0000
ITAE	11.2763	23.7167	23.7657

Table 6: PID parameters and performances of industrial process control model V.

Parameter	MEA	GA	Z-N
K_p	2.6303	3.1253	2.3880
K_i	0.9459	1.829	1.6959
K_d	0.9984	1.7222	0.8406
t_s	3.3309	7.2594	8.7442
ITAE	0.7536	2.4037	2.4623

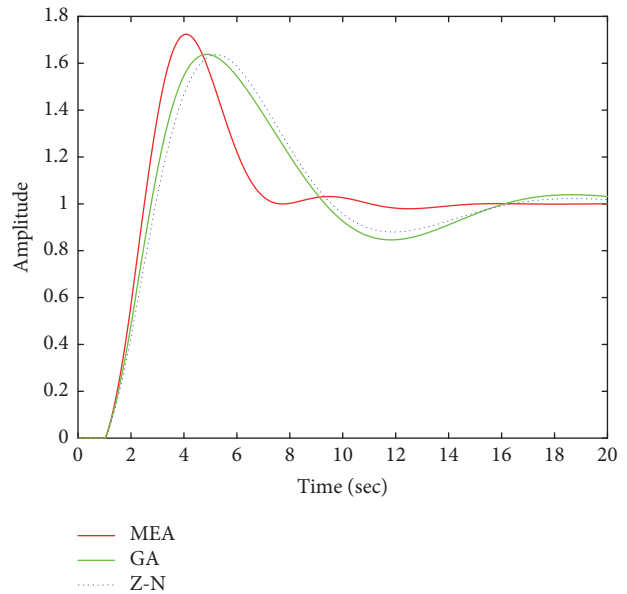

Figure 9: Closed-loop step response with process III.

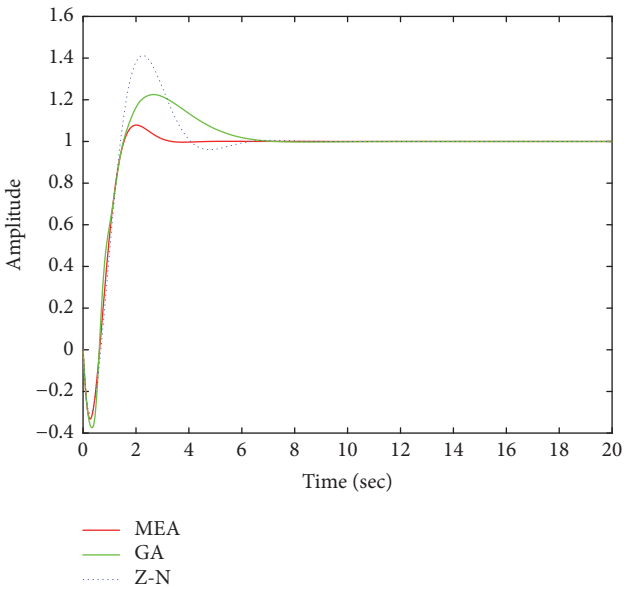

Figure 10: Closed-loop step response with process V.

finally, the unstable controlled object gradually reaches a steady state; this proves that the MEA-tuning PID controller well realizes the tuning and optimization of the controlled object. Compared with the GA and Z-N methods, the MEA can obtain satisfactory PID parameters for control systems within a few generations, the *ITAE* obtained is lower, and the convergence speed is faster. Therefore, the MEA is superior to the GA and Z-N methods.

5. Conclusion

The performance of the traditional PID control depends on the set of the parameters; therefore, an MEA-tuning method is proposed to search globally the optimal controller parameters. The MEA approach has superior design features and parallelism on structure, which raises the efficiency and effectiveness for searching global optimal parameters. In order to verify the performance of the MEA, three classical functions and five typical industrial process control models are employed for simulation and testing; the simulation results were compared with those of the GA and Z-N methods. The main results and conclusions are summarized as follows.

The experimental results of three classical functions (Sphere function, Rastrigin function, and Rosenbrock function) indicate that the MEA has faster convergence speed and higher convergence precision than the GA; due to the superior design feature and parallel structure, the MEA can memorize more evolutionary information and search the optimal solution more efficiently and effectively, overcoming the defects of the GA, such as precociousness, easiness of falling into the local extremum, and time-consuming computation.

Table 7: PID parameters and performances of industrial process control model IV.

Parameter	MEA	GA	Z-N
K_p	1.0968	1.2785	1.4220
K_i	0.2103	0.2769	0.2613
K_d	1.7656	1.9265	1.9346
t_s	16.1596	18.1772	20.0000
ITAE	15.7474	19.4274	21.3847

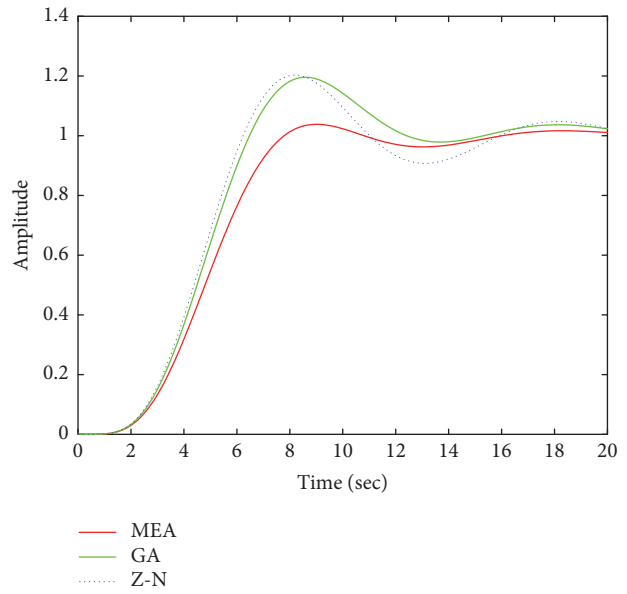

Figure 11: Closed-loop step response with process IV.

The simulation experiments of five typical industrial process control models also show that the MEA can capture better PID parameters (K_p, K_i, K_d) and lower *ITAE*; the MEA-tuning PID controller well realizes the tuning and optimization of the controlled object; the unstable controlled object gradually reaches a steady state; meanwhile, the MEA is superior to the GA and Z-N methods in speed and optimization performance.

Experiments indicated that the MEA-tuning method proposed in this study is feasible and valid, which offers a practical and novel approach for the design of the traditional PID controller. However, future work should focus on the comparison researches between the MEA and other intelligent algorithms; other PID controllers such as the PSO-PID controller, TSA-PID controller, BFA-PID controller, ACA-PID controller, and ABC-PID controller should be introduced into the tuning and optimization of the traditional PID controller and compared with the MEA-PID controller to verify its effectiveness and advantage. Moreover, the MEA approach should be further tested and developed through other practical application fields such as regression fitting, pattern recognition, and job planning and scheduling.

Abbreviations

PID: Proportional integral derivative
MEA: Mind evolutionary algorithm
Z-N: Ziegler and Nichols
GA: Genetic algorithm
PSO: Particle swarm optimization
TSA: Tabu search algorithm
BFA: Bacterial foraging algorithm
ACA: Ant colony algorithm
ITAE: Integral of time absolute errors
ISE: Integral of squared errors.

Data Availability

The data used to support the findings of this study are available from the corresponding author upon request.

Conflicts of Interest

The authors declare no conflicts of interest.

Acknowledgments

This research was funded by the National Social Science Fund of China (Grant No. 17BGL202).

References

[1] S. Bennett, "The past of PID controllers," *Annual Reviews in Control*, vol. 25, pp. 43–53, 2001.

[2] V. Chopra, S. K. Singla, and L. Dewan, "Comparative analysis of tuning a PID controller using intelligent methods," *Acta Polytechnica Hungarica*, vol. 11, no. 8, pp. 235–249, 2014.

[3] M. J. Er and Y. L. Sun, "Hybrid fuzzy proportional-integral plus conventional derivative control of linear and nonlinear systems," *IEEE Transactions on Industrial Electronics*, vol. 48, no. 6, pp. 1109–1117, 2001.

[4] M. Kushwah and A. Patra, "Tuning PID controller for speed control of DC motor using soft computing techniques-A review," *Advance in Electronic and Electric Engineering*, vol. 4, no. 2, pp. 141–148, 2014.

[5] C. Zou, C. Manzie, and D. Nesic, "A Framework for Simplification of PDE-Based Lithium-Ion Battery Models," *IEEE Transactions on Control Systems Technology*, vol. 24, no. 5, pp. 1594–1609, 2016.

[6] J. B. Odili, M. N. M. Kahar, and A. Noraziah, "Parameters-Tuning of PID controller for automatic voltage regulators using the African buffalo optimization," *PLoS ONE*, vol. 12, no. 4, p. e0175901, 2017.

[7] Y. Luo and Z. Chen, "Optimization for PID control parameters on hydraulic servo control system based on the novel compound evolutionary algorithm," in *Proceedings of the 2nd International Conference on Computer Modeling and Simulation (ICCMS '10)*, pp. 40–43, IEEE, January 2010.

[8] T. Hagglund and K. J. Astrom, "Revisiting the Ziegler-Nichols tuning rules for PI control," *Asian Journal of Control*, vol. 4, no. 4, pp. 364–380, 2002.

[9] J. G. Ziegler and N. B. Nichols, "Optimum settings for automatic controllers," *Journal of Dynamic Systems, Measurement, and Control*, vol. 46, no. 2B, pp. 220–222, 1993.

[10] A. Giwa and S. Karacan, "Decoupling PID control of a reactive packed distillation column," *International Journal of Engineering & Technical Research*, vol. 1, no. 6, 2012.

[11] M. Korkmaz, O. Aydogdu, and H. Dogan, "Design and performance comparison of variable parameter nonlinear PID controller and genetic algorithm based PID controller," in *Proceedings of the 2012 International Symposium on Innovations in Intelligent Systems and Applications (INISTA)*, pp. 1–5, IEEE, Trabzon, Turkey, July 2012.

[12] S. Y. S. Hussien, H. I. Jaafar, N. A. Selamat, F. S. Daud, and A. F. Z. Abidin, "PID control tuning via Particle Swarm Optimization for coupled tank system," *International Journal of Soft Computing & Engineering*, vol. 4, no. 2, pp. 202–206, 2014.

[13] M. W. Foley, R. H. Julien, and B. R. Copeland, "A comparison of PID controller tuning methods," *The Canadian Journal of Chemical Engineering*, vol. 83, no. 4, pp. 712–722, 2010.

[14] A. Harrag and S. Messalti, "Variable step size modified P&O MPPT algorithm using GA-based hybrid offline/online PID controller," *Renewable & Sustainable Energy Reviews*, vol. 49, pp. 1247–1260, 2015.

[15] X. H. Liu, X. H. Chen, X. H. Zheng, S. P. Li, and Z. B. Wang, "Development of a GA-Fuzzy-Immune PID Controller with Incomplete Derivation for Robot Dexterous Hand," *The Scientific World Journal*, vol. 2014, Article ID 564137, 10 pages, 2014.

[16] C.-H. Cheng, P.-J. Cheng, and M.-J. Xie, "Current sharing of paralleled DC-DC converters using GA-based PID controllers," *Expert Systems with Applications*, vol. 37, no. 1, pp. 733–740, 2010.

[17] S. Ahmadi, S. Abdi, and M. Kakavand, "Maximum power point tracking of a proton exchange membrane fuel cell system using PSO-PID controller," *International Journal of Hydrogen Energy*, vol. 42, no. 32, pp. 20430–20443, 2017.

[18] I. Atacak and B. Küçük, "PSO-based PID controller design for an energy conversion system using compressed air," *Tehnički vjesnik*, vol. 24, no. 3, pp. 671–679, 2017.

[19] Y. Ye, C.-B. Yin, Y. Gong, and J.-J. Zhou, "Position control of nonlinear hydraulic system using an improved PSO based PID controller," *Mechanical Systems and Signal Processing*, vol. 83, pp. 241–259, 2017.

[20] A. Ateş and C. Yeroglu, "Optimal fractional order PID design via Tabu Search based algorithm," *ISA Transactions*, no. 60, pp. 109–118, 2016.

[21] O. Roeva and T. Slavov, "PID controller tuning based on metaheuristic algorithms for bioprocess control," *Biotechnology & Biotechnological Equipment*, vol. 26, no. 5, pp. 3267–3277, 2012.

[22] A. Bagis, "Tabu search algorithm based PID controller tuning for desired system specifications," *Journal of The Franklin Institute*, vol. 348, no. 10, pp. 2795–2812, 2011.

[23] D. H. Kim, "Hybrid GA-BF based intelligent PID controller tuning for AVR system," *Applied Soft Computing*, vol. 11, no. 1, pp. 11–22, 2011.

[24] A. Shamel and N. Ghadimi, "Hybrid PSOTVAC/BFA technique for tuning of robust PID controller of fuel cell voltage," *Indian Journal of Chemical Technology*, no. 23, pp. 171–178, 2016.

[25] E. S. Ali and S. M. Abd-Elazim, "BFOA based design of PID controller for two area Load Frequency Control with nonlinearities," *International Journal of Electrical Power & Energy Systems*, no. 51, pp. 224–231, 2013.

[26] M. Ünal, H. Erdal, and V. Topuz, "Trajectory tracking performance comparison between genetic algorithm and ant colony optimization for PID controller tuning on pressure process," *Computer Applications in Engineering Education*, vol. 20, no. 3, pp. 518–528, 2012.

[27] A. S. Oshaba, E. S. Ali, and S. M. Abd Elazim, "PI controller design using ABC algorithm for MPPT of PV system supplying DC motor pump load," *Neural Computing and Applications*, vol. 28, no. 2, pp. 353–364, 2017.

[28] A. S. Oshaba, E. S. Ali, and S. M. Abd Elazim, "PI controller design for MPPT of photovoltaic system supplying SRM via BAT search algorithm," *Neural Computing and Applications*, vol. 28, no. 4, pp. 651–667, 2017.

[29] N. Yusup, A. M. Zain, and S. Z. M. Hashim, "Evolutionary techniques in optimizing machining parameters: review and recent applications (2007–2011)," *Expert Systems with Applications*, vol. 39, no. 10, pp. 9909–9927, 2012.

[30] A. K. Dwivedi, S. Ghosh, and N. D. Londhe, "Review and Analysis of Evolutionary Optimization-Based Techniques for FIR Filter Design," *Circuits, Systems and Signal Processing*, pp. 1–22, 2018.

[31] B. J. Saharia, H. Brahma, and N. Sarmah, "A review of algorithms for control and optimization for energy management of hybrid renewable energy systems," *Journal of Renewable and Sustainable Energy*, vol. 10, no. 5, p. 053502, 2018.

[32] D. Karaboga, B. Gorkemli, C. Ozturk, and N. Karaboga, "A comprehensive survey: artificial bee colony (ABC) algorithm and applications," *Artificial Intelligence Review*, vol. 42, pp. 21–57, 2014.

[33] Z. Li, W. Wang, Y. Yan, and Z. Li, "PS-ABC: A hybrid algorithm based on particle swarm and artificial bee colony for high-dimensional optimization problems," *Expert Systems with Applications*, vol. 42, no. 22, pp. 8881–8895, 2015.

[34] C. Sun, Y. Sun, and L. Wei, "Mind-evolution-based machine learning: framework and the implementation of optimization," in *Proceedings of the IEEE International Conference on Intelligent Engineering Systems (INES'98)*, pp. 355–359, 1998.

[35] C. Sun, X. Zhou, and W. Wang, "Mind evolutionary computation and applications," *Journal of Communication and Computer*, vol. 1, no. 1, pp. 13–21, 2004.

[36] X. Zhou and C. Sun, "Pareto-MEC and its convergence analysis," *Jisuanji Gongcheng/Computer Engineering*, vol. 33, no. 10, pp. 233–236, 2007.

[37] H. Liu, H. Tian, X. Liang, and Y. Li, "New wind speed forecasting approaches using fast ensemble empirical model decomposition, genetic algorithm, Mind Evolutionary Algorithm and Artificial Neural Networks," *Journal of Renewable Energy*, vol. 83, pp. 1066–1075, 2015.

[38] G. Yan, G. Xie, Y. Qiu, and Z. Chen, "MEA based nonlinearity correction algorithm for the VCO of LFMCW radar level gauge," in *Rough Sets, Fuzzy Sets, Data Mining, and Granular Computing*, Springer, Berlin, Germany, 2005.

[39] G. Li and W. H. Li, "Face occlusion recognition based on MEBML," *Journal of Jilin University*, vol. 44, no. 5, pp. 1410–1416, 2014.

[40] K. J. Åström and T. Hägglund, *PID Controllers: Theory, Design And Tuning*, Instrument society of America, Research Triangle Park, NC, USA, 1995.

Hindawi
Mathematical Problems in Engineering
Volume 2019, Article ID 4323127, 8 pages
https://doi.org/10.1155/2019/4323127

Research Article

Ultimate Strength of Pit Corrosion Damnification on Pressure-Resistant Shells of Underwater Glider

Shaojuan Su, Tianlin Wang, Chunbo Zhen, and Fan Zhang

Naval Architecture and Ocean Engineering College, Dalian Maritime University, Dalian, Liaoning, China

Correspondence should be addressed to Shaojuan Su; 32248522@qq.com

Received 31 October 2018; Revised 10 December 2018; Accepted 27 December 2018; Published 15 January 2019

Guest Editor: Yingyot Aue-u-lan

The ultimate strength of the pressure-resistant shells is degraded due to corrosion pit on the surface of the shells. The underwater glider is prone to pit corrosion damage after working in the water for a long time. This study is aimed at development of an assessing formula for ultimate strength of pressure-resistant shells with pit damage. Firstly, a parameterized geometry model of the pit is determined under the assumption that the pits are elliptical. Secondly, a finite element numerical simulation model is established and the numerical simulation results are analyzed to find that the effect of pit damage on the pressure-resistant shell is obvious. Thirdly, the influences of some parameters (relative length, relative width, and relative depth) of pit on the ultimate strength are studied. The regular curve of the influence of geometric parameters on ultimate strength is drawn. Lastly, the ultimate strength assessment formula of pressure-resistant shells was obtained from the data by nonlinear FEM based on the regression function of multiple nonlinear regression analysis by nonlinear regression analysis function regress which can provide the foundation to assess the ultimate strength of damaged pressure-resistant shells.

1. Introduction

Due to the particularity of the underwater glider, the rest of the time will be in seawater except for charging or maintenance. Therefore, its pressure-resistant shell will face a strong external environmental damage. In general, pit corrosion damage is the most common type to pressure-resistant shell. There are many factors that cause pit corrosion damage. For example, the destruction of seawater and marine life will cause electrochemical reactions of glider pressure-resistant shells and direct external damage of pressure-resistant shells in the marine environment, which will lead to pit corrosion damage. Although we will apply paint and other anticorrosion measures to protect the pressure-resistant shell, it is inevitable that the glider pressure-resistant shell working in a very harsh environment is destroyed. The pit damage causes the thickness of the pressure-resistant shell to become thinner, which has great safety risks and has serious impact on the safety of the entire underwater glider structure. The evaluation of the ultimate strength of the pressure-resistant shell with pit corrosion damage is the basis of the safety assessment for the overall structure.

Because of the complexity of geometrical nonlinearity and constitutive relations, it is difficult to find an exact solution by analytical method. For the calculation of the ultimate strength of pitting damage, a more representative study is Sadovsky and Drdacky [1]. Using statistical data from experimental studies, the critical buckling load of locally corroded slabs is obtained by statistical methods. Dunbar et al. combined finite element simulation analysis and experimental methods to discuss the effect of corrosion on the stability of the square plate [2]. Nakai et al. conducted a series of experiments and finite element tests on the ultimate strength of bulk carriers with local pitting corrosion; the ultimate strength is related to pitting distribution, pitting location, and plate thickness [3–5]. Duo Ok et al. calculated the knot with 256 nonlinear finite elements for two cases where there is corrosion in the edge region. An empirical formula for predicting the ultimate strength of locally corroded nonreinforced plates is obtained [6, 7]. Yan Zhang et al. got the ultimate strength calculation of pitted stiffened plates under uniaxial compression by the data analysis from lots of nonlinear finite element analyses [8]. Ahmad Rahbar-Ranji et al. employed a series of nonlinear finite element method

Table 1: 7075 performance parameters of aviation aluminum.

Density (kg/m^3)	Young's Modulus (Mpa)	Poisson's ratio	Conditional yield strength (Mpa)	Allowable stress (Mpa)
2800	717000	0.33	505	328

Table 2: Geometrical parameters of pressure shell and corrosion pit.

a	R	b	L	h	t
Pit long axis	Pit center circle radius	Pit short axis	Pit center busbar length	Depth of pit	Shell thickness

for ultimate strength analysis of stiffened plates with pitting corrosion [9].

In this paper, the ultimate strength of the pressure-resistant shell with pit corrosion damage is calculated by numerical simulation technology. It is assumed that the pits are elliptical and the effects of relative length, relative width, and relative depth of pit on the ultimate strength of the pressure-resistant shell are studied. Finally, the calculation results are regressed and analyzed by Matlab software, and the empirical formula of the ultimate strength of the pressure-resistant shell with pit corrosion damage is obtained.

2. Geometric Parametric Model

In general, there are local corrosion damage and total corrosion damage to the glider's pressure-resistant shell. And the local corrosion to the pressure shell is far greater more complex than the other corrosions because the local corrosion has many sources of influence on the pressure shell, and it is difficult to determine it. In this paper, pits corrosion is considered as the object of local corrosion.

In terms of pit corrosion, the length, width, and depth of the corrosion pit are called damage parameters. Solidworks is used to model the pressure-resistant shells with different defect parameters, and then it is imported into finite element analysis software to perform parametric analysis to the ultimate strength of pressure-resistant shells with corrosion pits. The remaining ultimate strength of the shell is solved. Analyze all the result data obtained and plot the influence of different defect levels on the ultimate strength of the pressure shell and analyze the regular.

2.1. Assumptions . In order to better ensure the quality and accuracy of meshing, we make the following assumptions about the pressure-resistant shell of the glider:

(1) The material used in the aluminum alloy is an ideal plastic unit and is isotropic.

(2) The outline of the corrosion pit is a regular ellipse.

2.2. Determining the Geometric Model. For the finite element analysis of the pressure-resistant shell with corrosion pits after the assumption is simplified, the boundary conditions and the load application method are set, and the accurate calculation is obtained and the accurate result is obtained.

2.2.1. Material Parameters. The material used in the pressure shell is 7075 aluminum alloy. The parameters are as shown in Table 1.

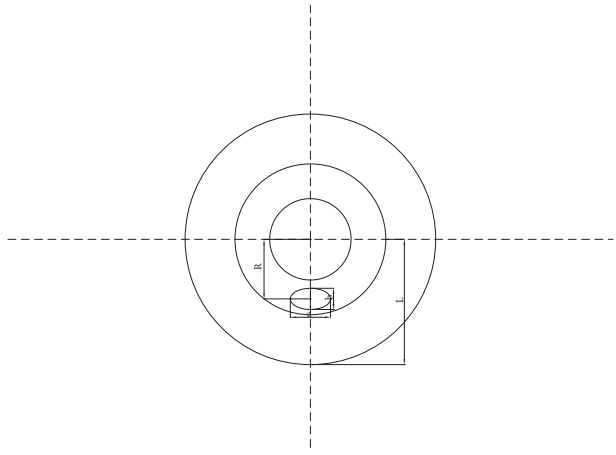

Figure 1: Corrosion pit.

Table 3: Dimensionless table of geometric parameters and ultimate strength.

$\alpha = a/2\pi R$	$\beta = b/L$	$\gamma = h/t$	$\lambda = \sigma_I/\sigma_{II}$
Relative length	Relative width	Relative depth	Ultimate strength factor

2.2.2. Geometric Model. The ellipsoidal shape pit is used for parametric analysis. The geometric data of the pressure-resistant shell with corrosion pit is shown in Figures 1 and 2, in which the corrosion pit is located between the 2nd and 3rd reinforcement rings of the pressure-resistant shell.

To quantitatively describe corrosion pits, introduce the following parameters, shown in Table 2.

In order to make the nondimensionalization between the ultimate strength and the geometrical parameters of the pressure-resistant shell with corrosion pits, the definitions are made in Table 3.

Among them, σ_I is the residual ultimate strength of the pressure-resistant shell with corrosion pits, and σ_{II} is the ultimate strength of the pressure-resistant shell without corrosion.

2.2.3. Load Application and Determination Ultimate Strength. The working environment of the circular dish underwater glider is mainly for various sea areas, so the external load is mainly deep-water hydrostatic pressure and the dynamic pressure and static pressure produced by the current on the

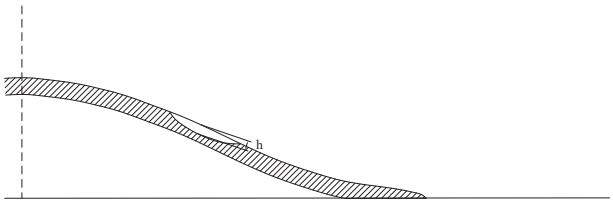

Figure 2: Corrosion pit pressure shell profile.

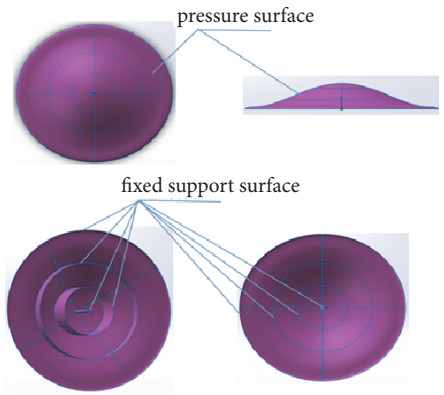

Figure 3: Sketch of boundary conditions.

pressure-resistant shell is negligible. Therefore, taking the edge of the pressure shell and the three reinforcement ring contact surfaces as a fixed support, the pressure surface is the entire outer surface of the pressure shell, as shown in Figure 3, and the pit surface also acts as a pressure surface to determine the mechanical properties of the pressure shell.

In the process of loading the load, the time displacement curve of the pressure-resistant shell can be obtained through calculation, and the load value corresponding to the abrupt change position of the curve is the ultimate strength of the pressure-resistant shell.

3. Finite Element Model

3.1. Establish Finite Element Model. Taking the corrosion pit pressure-resistant shell with the parameters $a = 106.1mm$, $b = 32.8mm$, and $h = 0.9mm$ as an example, the ultimate strength is calculated. The three-dimensional model of the pressure-resistant shell is shown in Figure 4.

3.2. Model Grid Division and Solution Settings. When meshing the model, in order to get more accurate calculation results, we encrypt the meshes of the cells near the damaged pits by creating a new coordinate system in the center of the ellipse and inserting the influence ball. The refined mesh size is set to 2.5 mm, and for other areas far away from the damaged pits, the mesh size is 10 mm. The finite element model is shown in Figure 5.

When solving the ultimate strength of pressure-resistant shells with damaged pits, nonlinear static analysis is adopted to solve the ultimate strength of the model, and arc length method is introduced to control convergence.

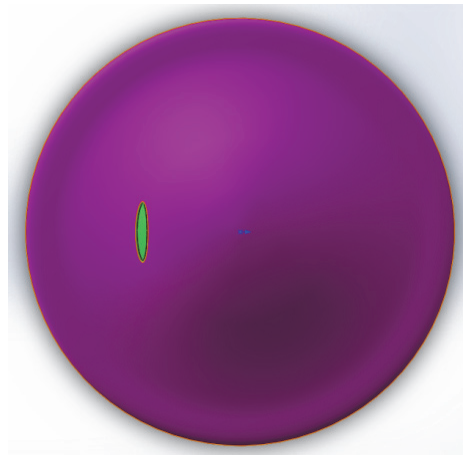

Figure 4: Pressure hull model with corrosion pits.

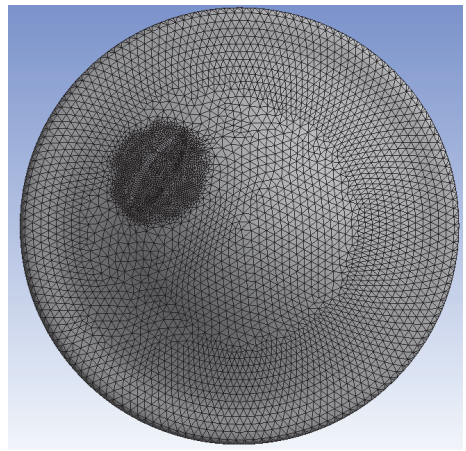

Figure 5: Meshing diagram of pressure hull with corrosion pits.

3.3. Result Analysis. From the overall deformation nephogram obtained by finite element analysis, it is found that large deformation occurs at first in the area near the corrosion pit, which indicates that the influence of the corrosion pit on the pressure-resistant shell is obvious. The overall deformation nephogram is shown in Figure 6.

After further calculation and analysis, we found that the pressure-resistant shell with corrosion pits was obviously influenced by the position of the second reinforcing ring near the corrosion pits, which significantly reduced the ultimate strength. The deformation nephogram and time displacement curve of the shell are shown in Figure 7.

The hydrostatic pressure of 2 MPa is gradually applied to the outer surface of the shell for 20 seconds. From the time displacement curve in Figure 8, it can be found that the structure suddenly changes in 12.304 seconds; that is, the ultimate strength of the pressure-resistant shell is 1.2304 MPa at this time.

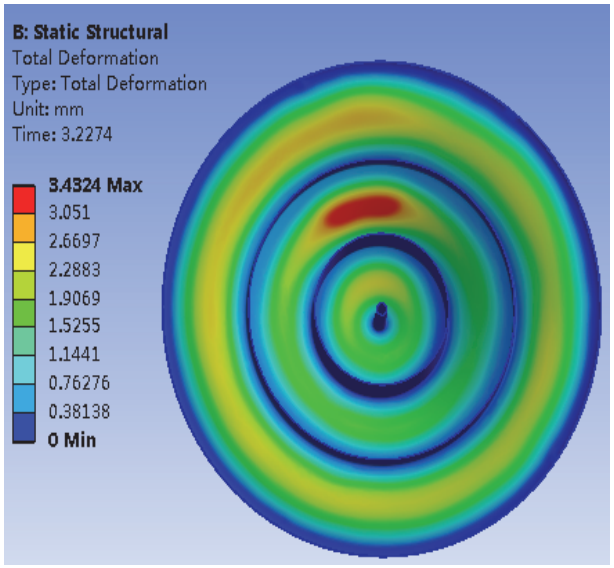

Figure 6: Overall deformation nephogram of pit corrosion resistant shell.

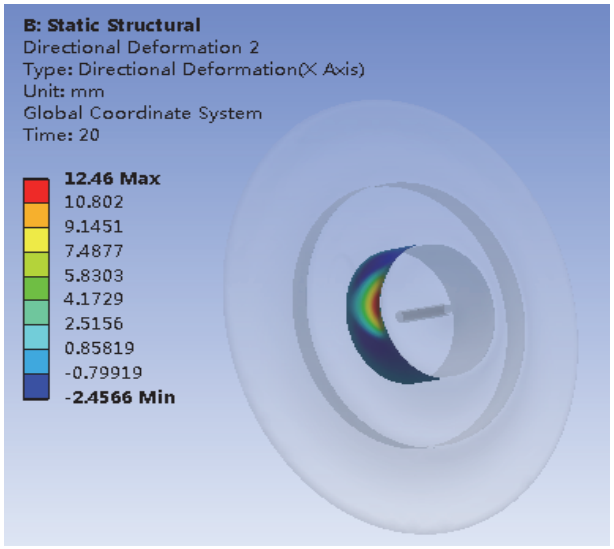

Figure 7: Deformation nephogram of the second ring region.

4. Parametric Analysis

Considering the actual use, the length direction shall not exceed half of the circumference of the water glider at the center of the pit, the width shall not exceed the edge of the glider, and the depth shall not exceed 0.75 times the thickness of the plate. So the range of relative length $\alpha \in [0, 0.5]$, the relative width $\beta \in [0, 1]$, and the relative depth $\gamma \in [0, 0.75]$. In order to obtain the influence of geometric parameters on ultimate strength of pressure hull, we discretize the parameters. Here α takes a value of 0.1, 0.2, 0.3, 0.4, 0.5, β takes a value of 0.1, 0.2, 0.3, 0.4, 0.5, 0.6, 0.7, 0.8, 0.9, 1.0, and γ takes a value of 0.15, 0.3, 0.45, 0.6, 0.75.

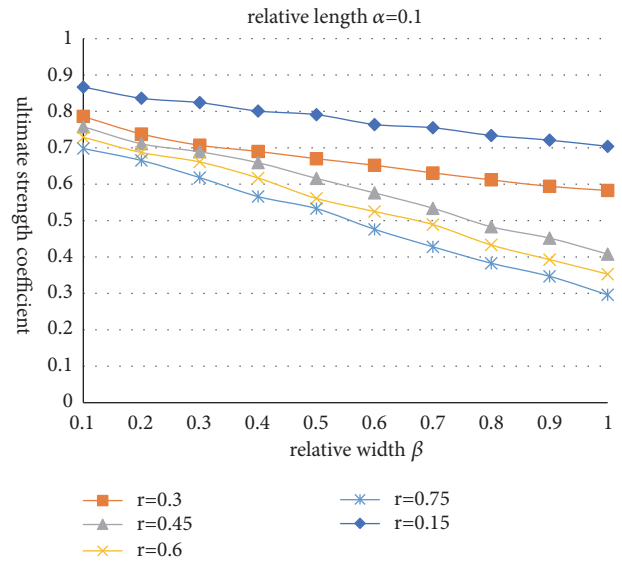

Figure 8: The graph of relative width on ultimate strength.

Table 4: Effect of relative width on ultimate strength coefficient.

α		0.1				
γ		0.15	0.30	0.45	0.60	0.75
β	0.1	0.867	0.786	0.758	0.729	0.698
	0.2	0.836	0.738	0.711	0.687	0.665
	0.3	0.824	0.707	0.689	0.661	0.618
	0.4	0.801	0.69	0.659	0.617	0.566
	0.5	0.791	0.67	0.616	0.561	0.533
	0.6	0.764	0.652	0.576	0.525	0.476
	0.7	0.755	0.631	0.534	0.489	0.428
	0.8	0.734	0.612	0.483	0.433	0.383
	0.9	0.721	0.594	0.452	0.393	0.347
	1.0	0.704	0.583	0.408	0.353	0.296

By means of second chapters, the ultimate strength of the pressure-resistant shells without pits is 1.6691MPa. The ultimate strength coefficient of the damaged shell is 1.2304/1.6691=0.737.

After finite element calculation, the calculation results of the ultimate strength coefficient of pressure-resistant shell with different dent parameters are summarized in Tables 4, 5, and 6. From these tables, it is found that the three parameters of the damaged pits have a direct impact on the ultimate strength of the pressure-resistant shell, and the specific influence rules are shown as follows.

4.1. Effects of Relative Width on Ultimate Strength. According to the calculation results of the ultimate strength of the pressure-resistant shell with the corrosion pit, the calculation results of the limit strength coefficients are summarized in Table 4 in which relative length $\alpha = 0.1$ and relative depth γ is 0.15, 0.3, 0.45, 0.6, 0.75

According to Table 4, draw a regular graph of the ultimate strength with relative width β, as shown in Figure 8.

Table 5: Effect of relative depth on ultimate strength.

β		0.3				
α		0.1	0.2	0.3	0.4	0.5
γ	0.15	0.874	0.868	0.857	0.845	0.823
	0.3	0.849	0.835	0.826	0.816	0.801
	0.45	0.838	0.829	0.817	0.803	0.791
	0.6	0.83	0.822	0.809	0.798	0.783
	0.75	0.828	0.818	0.805	0.795	0.779

Table 6: Effect of relative length alpha on the ultimate strength.

γ		0.3				
α		0.1	0.2	0.3	0.4	0.5
β	0.1	0.876	0.872	0.867	0.861	0.856
	0.2	0.851	0.849	0.846	0.843	0.839
	0.3	0.834	0.831	0.828	0.825	0.819
	0.4	0.825	0.819	0.815	0.811	0.806
	0.5	0.817	0.809	0.803	0.797	0.788
	0.6	0.791	0.788	0.785	0.780	0.766
	0.7	0.779	0.773	0.769	0.765	0.761
	0.8	0.769	0.764	0.758	0.753	0.747
	0.9	0.758	0.752	0.749	0.745	0.741
	1.0	0.755	0.748	0.743	0.738	0.730

From Figure 8, the width of the damaged pit has a significant effect on the ultimate strength of the pressure-resistant shell, because, with the increase of the width of the pit, the strength of the inner ring 2 of the pressure-resistant shell is greatly affected, which directly leads to the reduction of the overall ultimate strength of the pressure-resistant shell. At the same time, it can also be found that the limit strength of the pressure-resistant shell varies linearly with the relative width of the corrosion pit. When the width of the corrosion pit increases, the limit strength of the pressure-resistant shell decreases significantly and increases with the relative depth γ. The reduction of ultimate strength of pressure-resistant shell is more significant.

4.2. Effect of Relative Depth on Ultimate Strength. According to the calculation results of the ultimate strength of the pressure-resistant shell with the corrosion pit, the calculation results of the limit strength coefficients are summarized in Table 5 in which relative width $\beta = 0.3$ and relative length α is 0.1, 0.2, 0.3, 0.4, 0.5

According to Table 5, draw a regular graph of the limit strength with relative depth γ, as shown in Figure 9.

From Figure 9, we can see that when the relative width β and relative length α of the damaged pit remain unchanged, the ultimate strength of the pressure-resistant shell decreases significantly with the increase of relative depth γ. At the same time, from the changing regular of the curve, it can be seen that in the first half of the relative depth γ gradually increasing, the limit strength of the pressure-resistant shell decreased sharply, and in the second half of the relative depth

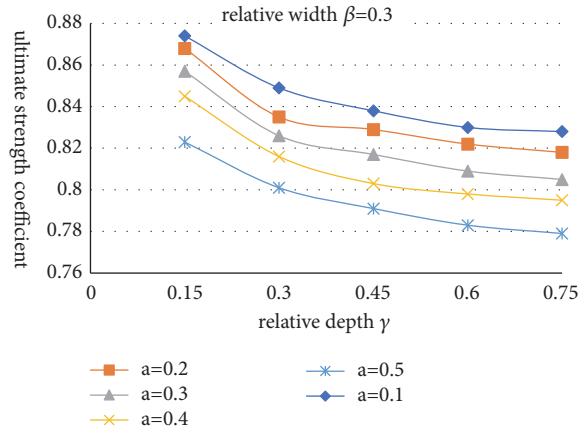

Figure 9: The graph of relative depth on ultimate strength.

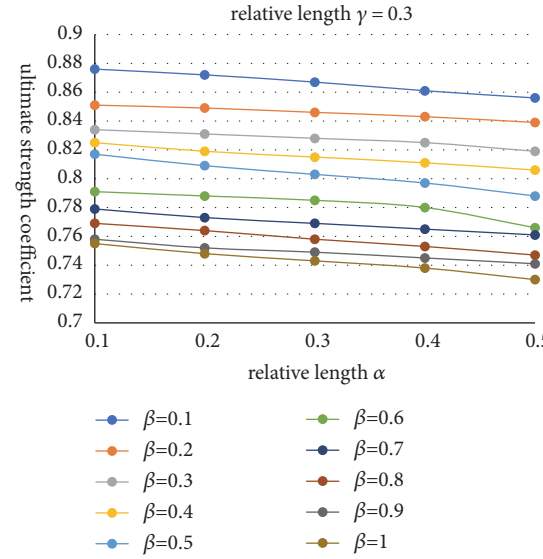

Figure 10: The graph of relative length on ultimate strength.

γ gradually increasing, the limit strength of the pressure-resistant shell gradually decreased. On the whole, with the increase of relative depth, the linear characteristics of the ultimate strength of the pressure-resistant shell are not strong, and it can be approximated as nonlinear.

4.3. Effect of Relative Length on Ultimate Strength. According to the calculation results of the ultimate strength of the pressure-resistant shell with the corrosion pit, the calculation results of the limit strength coefficients are summarized in Table 6 in which relative width $\gamma = 0.3$ and relative length β is 0.1, 0.2, 0.3, 0.4, 0.5, 0.6, 0.7, 0.8, 0.9, 1.0.

According to Table 6, a regular graph of the ultimate strength with the relative length α is drawn, as shown in Figure 10.

From Figure 10, it can be found that the ultimate strength of the pressure-resistant shell containing the damaged pit is approximately linear to the relative length α under different relative widths. When the corrosion pit width is certain,

Table 7: The optimal fitting results.

Geometric parameters	Fitting curve equation	Correlation coefficient
α	$y = 0.9062\gamma^3 + 1.7665\gamma^2 - 1.424\gamma - 0.33\beta + 1.1386$	0.9714
β	$y = -0.3852\gamma^3 + 0.6825\gamma^2 - 0.4263\gamma - 0.121\alpha + 0.9394$	0.9954
γ	$y = -0.0471\alpha - 0.1388\beta + 0.8866$	0.9920

the ultimate strength of the pressure-resistant shell gradually decreases with the relative length α. At the same time, when the relative width of the corrosion pit continues to increase, the residual ultimate strength of the pressure-resistant shell decreases not significantly with the increase of the relative length. To sum up, the effect of the corrosion pit length on the residual limit strength of the shell is minimal compared with the width and depth.

5. Formula on Ultimate Strength of Pressure-Resistant Shell with Corrosion Pit

The results of finite element analysis show that the relative length α, relative width β, and relative depth γ of the damaged pit have different degrees of influence on the ultimate strength of the glider's pressure-resistant shell, and the degree of influence varies with the changing trend of pit parameters. The finite element software is used to simulate the ultimate strength of the pressure-resistant shell damage. Although it is relatively scientific and perfect, the calculation process is quite complicated and time-consuming, and it can not be well applied to engineering practice. Therefore, it is very important to fit the empirical formula between the limit strength and the damage parameters in order to calculate the limit strength of the shell with the corrosion pit more easily and accurately.

5.1. Curve Formula Fitting between the Geometric Parameters. From Figures 8, 9 and 10, we can clearly find that the limit strength of the pressure-resistant shell damage has a clear linear relationship with the relative length α, a clear linear relationship with the relative width β, and an approximate nonlinear relationship with the relative depth γ relationship.

The above is only a qualitative analysis of the impact of the pit geometry parameters on the ultimate strength. In order to realize the simple and accurate prediction of the limit strength of the pressure-resistant shell pit in the same type of underwater glider, the geometrical parameters of the corresponding corrosion pit must be quantitatively analyzed. Matlab software is used to fit the curve formula between the finite element results and the geometric parameters of each corrosion pit. The curves and scattered points shown in Figures 11, 12, and 13 are obtained.

The optimal curve fitting equation is obtained by multiple fitting as shown in Table 7.

The fitting curve of single geometric parameters and pit limit strength coefficient can not comprehensively reflect the effect of limit strength coefficient and relative value of geometry parameter. However, it can reflect the influence of the geometric parameters of the single damage on the ultimate strength coefficient of the pressure-resistant shell. According

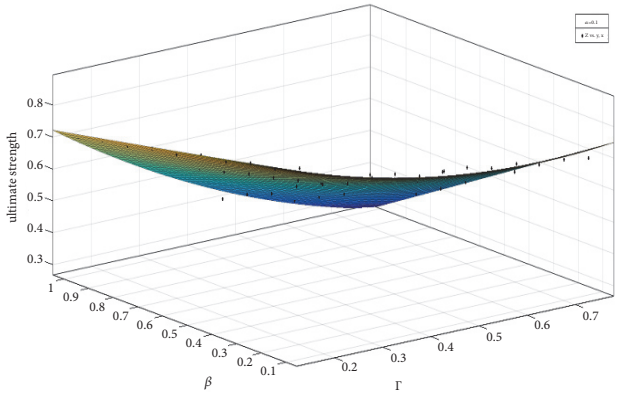

Figure 11: The formula fit graph of ultimate strength with β and γ.

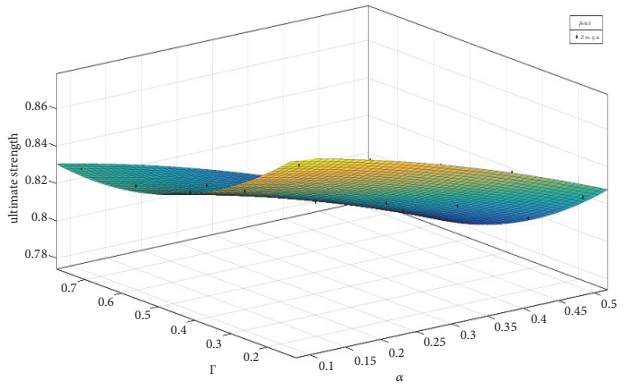

Figure 12: The formula fit graph of ultimate strength with α and γ.

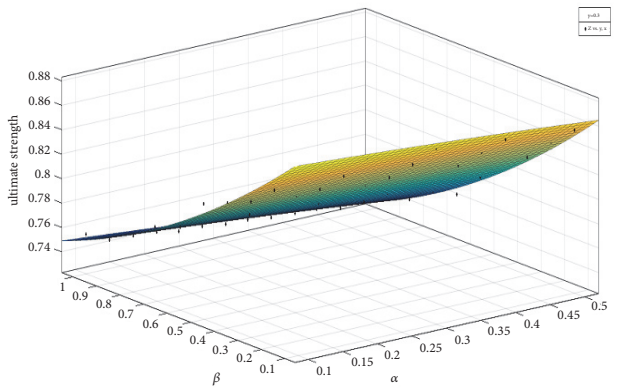

Figure 13: The formula fit graph of ultimate strength with α and β.

to Table 7, it can be seen that the limit strength coefficient of the pressure-resistant shell has a linear relationship with the pit-shaped geometric parameters α and β and a nonlinear relationship with γ.

5.2. Regression Analysis and Validity Verification. In order to analyze the relationship between the limit strength coefficient and the nonquantized geometrical parameters α, β, and γ, the multiple nonlinear regression analysis function in Matlab software is used to analyze the finite element calculation results of the ultimate strength of the pressure-resistant shell.

According to Table 7, the relationship between the nonquantized geometric parameters and the ultimate strength can be seen, and the relationship is drawn as

$$\mathrm{y} = A + B\alpha + C\beta + D\gamma + E\gamma^2 + F\gamma^3 \tag{1}$$

Combined with Tables 4, 5, and 6, regression analysis based on multivariate nonlinear regression analysis function regress is done.

According to Table 4, the vector is as follows. Similarly, the vectors of Tables 5 and 6 can be made.

α = [0.1 0.1 0.1 0.1 0.1 0.1 0.1 0.1 0.1 0.1 0.1 0.1 0.1 0.1 0.1 0.1 0.1 0.1 0.1 0.1 0.1 0.1 0.1 0.1 0.1 0.1 0.1 0.1 0.1 0.1 0.1 0.1 0.1 0.1 0.1 0.1 0.1 0.1 0.1 0.1 0.1 0.1 0.1 0.1 0.1 0.1 0.1 0.1 0.1 0.1]

β = [0.1 0.2 0.3 0.4 0.5 0.6 0.7 0.8 0.9 1.0 0.1 0.2 0.3 0.4 0.5 0.6 0.7 0.8 0.9 1.0 0.1 0.2 0.3 0.4 0.5 0.6 0.7 0.8 0.9 1.0 0.1 0.2 0.3 0.4 0.5 0.6 0.7 0.8 0.9 1.0 0.1 0.2 0.3 0.4 0.5 0.6 0.7 0.8 0.9 1.0]

γ = [0.15 0.15 0.15 0.15 0.15 0.15 0.15 0.15 0.15 0.15 0.3 0.3 0.3 0.3 0.3 0.3 0.3 0.3 0.3 0.3 0.45 0.45 0.45 0.45 0.45 0.45 0.45 0.45 0.45 0.45 0.60 0.60 0.60 0.60 0.60 0.60 0.60 0.60 0.60 0.60 0.75 0.75 0.75 0.75 0.75 0.75 0.75 0.75 0.75 0.75]

y = [0.867 0.836 0.824 0.801 0.791 0.764 0.755 0.734 0.721 0.704 0.786 0.738 0.707 0.69 0.67 0.652 0.631 0.612 0.594 0.583 0.758 0.711 0.689 0.659 0.616 0.576 0.534 0.483 0.452 0.408 0.729 0.687 0.661 0.617 0.561 0.525 0.489 0.433 0.393 0.353 0.698 0.665 0.618 0.566 0.533 0.476 0.428 0.383 0.347 0.296]

The 125-dimensional vectors of α, β, γ, and y can be got by combining Tables 4, 5, and 6. According to the multivariate nonlinear regression analysis function regress formula (2) is obtained.

The code in Matlab is as follows.

```
y = [ones(125, 1) x1' x2' x3' (x3.^2)' (x3.^3)'];
[b,bint,r,rint,stats]=regress(y,X);
```

where x1′ x2′ x3′ is α, β, γ.

$$\begin{aligned} y = {} & -0.585\gamma^3 + 1.1959\gamma^2 - 1.003\gamma - 0.2743\beta \\ & - 0.0562\alpha + 1.0989 \end{aligned} \tag{2}$$

After the regression analysis formula is obtained, its results need to be evaluated to determine its credibility. The correlation coefficient can be used as the basis for judging the results. The closer the correlation coefficient is to 1, the higher the credibility of the results of regression analysis. According to the calculation results, when the curve fitting equation is formula (2), the correlation coefficient R2 = 0.9753, and the result is closer to 1, so it has a higher credibility.

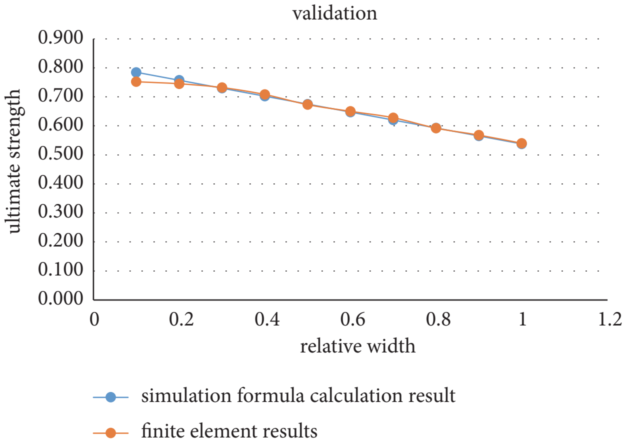

Figure 14: Comparison of the fitting formula and finite element results at different width.

The ultimate strength with $\alpha = 0.2$, $\gamma = 0.5$ corrosion pit is calculated using the finite element method at different width β.

At the same time, in order to verify the accuracy of the resulting regression formula (2), pick more points for analysis. The ultimate strength with different depth and different length are simulated to verify the accuracy of the regression formula, due to space reasons not listed in the paper. From Figure 14, we can find that the result of the fitting regression formula is very consistent with the finite element calculation result, which shows that the fitting regression formula is accurate.

6. Conclusion

Ultimate strength is calculated by finite element software in this paper. The effects of corrosion pit on the ultimate strength with different parameters (relative length α, relative width β, and relative depth γ) are studied qualitatively and quantitatively. The regression analysis is carried out by using the regress function in Matlab software and fitting formula on ultimate strength of pressure-resistant shell with pit is obtained. The analysis shows that the ultimate strength of the disc shell is obviously affected by the width and depth. However, the effect of pit length on the ultimate strength of the pressure-resistant shell is not obvious. At the same time, we can also know that the length and width of the pit have a linear relationship with the ultimate strength and a nonlinear relationship with the depth.

In this paper, the pit defects which have the most obvious influence on the pressure-resistant shell were analyzed. But only the effects of single pit damage on the ultimate strength are studied. The actual pit distribution is randomly distributed, and the size and shape are also uncertain. The situation is more complicated. Analysis has great limitations

in the paper. But it also provides a research idea for the next study of pressure-resistant shell damage. In the next research, we can use the research ideas proposed in this paper to analyze the ultimate strength of the pressure-resistant shell with multiple pits to get the analysis regular and fit the empirical formula so as to simplify the damage analysis of the pressure-resistant shell in the future.

Data Availability

(1) The nondimensionalization calculation data used to support the findings of this study are included within the article. (2) The water glider pressure shell structure data used to support the findings of this study have not been made available because this product is currently under patent protection and has not been published yet. But the nondimensionalization calculation data is enough and does not affect the calculation results.

Conflicts of Interest

The authors declare that they have no conflicts of interest.

Acknowledgments

This work is supported by Natural Science Foundation of China (51609031), National Key Research and Development Plan (2016YFC0301500), The Research Fund of the Fundamental Research Funds for the Central Universities (3132018306), and Chia Scholarship Council (No.201806575010)

References

[1] Z. Sadovský and M. Drdácký, "Buckling of plate strip subjected to localized corrosion-a stochastic model," *Thin-Walled Structures*, vol. 39, no. 3, pp. 247–259, 2001.

[2] T. E. Dunbar, N. Pegg, F. Taheri, and L. Jiang, "A computational investigation of the effects of localized corrosion on plates and stiffened panels," *Marine Structures*, vol. 17, no. 5, pp. 385–402, 2004.

[3] T. Nakai, H. Matsushita, N. Yamamoto, and H. Arai, "Effect of pitting corrosion on local strength of hold frames of bulk carriers (1st report)," *Marine Structures*, vol. 17, no. 5, pp. 403–432, 2004.

[4] H. Matsushita, T. Nakai, N. Yamamoto, and H. Arai, "Effect of corrosion on static strength of hull structural members (1st report)," *Journal of the Society of Naval Architects of Japan*, vol. 2002, no. 192, pp. 357–365, 2002.

[5] T. Nakai, H. Matsushita, N. Yamamoto, and H. Arai, "Effect of corrosion on static strength of hull structural members (2nd report)," *Journal of the Society of Naval Architects of Japan*, vol. 2004, no. 195, pp. 221–231, 2004.

[6] D. Ok, Y. Pu, and A. Incecik, "Computation of ultimate strength of locally corroded unstiffened plates under uniaxial compression," *Marine Structures*, vol. 20, no. 1-2, pp. 100–114, 2007.

[7] D. Ok, Y. Pu, and A. Incecik, "Artificial neural networks and their application to assessment of ultimate strength of plates with pitting corrosion," *Ocean Engineering*, vol. 34, no. 17-18, pp. 2222–2230, 2007.

[8] Y. Zhang, Y. Huang, and F. Meng, "Ultimate strength of hull structural stiffened plate with pitting corrosion damage under unaxial compression," *Marine Structures*, vol. 56, pp. 117–136, 2017.

[9] A. Rahbar-Ranji, N. Niamir, and A. Zarookian, "Ultimate strength of stiffened plates with pitting corrosion," *International Journal of Naval Architecture and Ocean Engineering*, vol. 7, no. 3, pp. 509–525, 2015.

Hindawi
Mathematical Problems in Engineering
Volume 2018, Article ID 5153292, 12 pages
https://doi.org/10.1155/2018/5153292

Research Article

Modeling and Analysis of Effective Case Depth on Meshing Strength of Internal Gear Transmissions

Dezheng Liu,[1] **Yan Li**,[1] **Zhongren Wang**,[1] **You Wang**,[1] **and Yu Wang**[2]

[1]*Department of Mechanical Engineering, Hubei University of Arts and Science, Xiangyang, Hubei 441053, China*
[2]*Shanghai Institute of Applied Physics, Chinese Academy of Sciences, Shanghai 201800, China*

Correspondence should be addressed to Zhongren Wang; wzrvision@hbuas.edu.cn

Received 18 July 2018; Revised 27 November 2018; Accepted 17 December 2018; Published 30 December 2018

Guest Editor: Yingyot Aue-u-lan

The effective case depth (ECD) plays an important role in the meshing strength of internal gear transmissions. Carburizing quenching heat treatment is commonly used to enhance gear strength and wear resistance. However, the different ECDs in internal and external gears caused by heat treatment significantly affect the meshing strength, causing vibration, reducing gear service life, and hastening malfunction in internal gear transmission. In this study, we conducted an investigation of different ECDs by the heat treatment of carburized gear pairs by numerical simulation with the finite element method (FEM) and experiment tests. We analyzed three different carburized layer models, with the ECD in the internal gear being greater than, less than, and equal to the ECD in the external gear. In addition, we investigated the ability to distinguish between hardness gradients in gear teeth by dividing the carburized depth into seven layers to improve modeling accuracy. Results revealed that the meshing strength of internal gear transmission could be significantly enhanced by adopting the model with the ECD in the internal gear being less than the ECD in the external gear, and moreover, the shear stress of carburized gears initially increased and then decreased along with depth direction, and the maximum value appeared in the middle of the lower surface.

1. Introduction

With the overall development of science and technology, gear transmission has been progressively developed toward light weight, high load capacity, and low energy consumption. Carburizing and quenching heat treatment have been widely adopted to enhance gear strength and wear resistance. The use of a carburizing process in gear transmission systems is an important means of achieving a lightweight gear design because the carburized gear teeth usually acquire sufficient toughness, hardness, and wear resistance [1, 2]. It is well known that the increase of carburizing depth can improve the strength of gears and prevent failure. However, the increases in production and energy consumption may result from carburizing depths that are too large, which may lead to high-difficulty processes and the growth of the process cycle. ECD is closely related to the meshing strength and reliability of gears; thus, the design of an optimum ECD can not only improve the strength of gears but also avoid high cost and wasted energy.

Most current studies on carburized gears are limited to the theory of carburizing and quenching heat treatment and strength analysis for fatigue failure and rarely involve the accurate modeling and analysis of the effects of ECD on meshing strength of internal gear transmission. The distribution of hardness and shear stress under the tooth surface is closely related to the failure of internal gear transmission and thus has attracted significant attention from many researchers studying the evolution of shear stress in meshing gears. Li *et al.* [3] investigated different forms of failure of carburized gears using finite element (FE) simulation analysis by ANSYS; however, Li *et al.* [4] demonstrated that the modeling process and performance analysis of carburized gears were not detailed. Jiang [5] proposed a calculation method for maximum shear stress of gear contact surfaces and demonstrated that the most sensitive parameter of the largest stress is the maximum Hertz stress. Chen and Shao [6] proposed the mesh stiffness calculation method of external spur gear pairs based on applying the potential energy theory to the calculation of internal gear tooth deformation. Tang

and Liu [7] proposed a new simulation method and built a loaded multitooth contact model to investigate the contact stress of face-gear drives, proving that the adoption of the FEM in analyzing contact stress of face-gear drives is reliable. Nevertheless, these methods cannot meet the requirement of comprehensive analysis of carburized gear strength.

The hardness and elastic modulus at each point on and inside the gear surface are different after carburization, such that a carburized gear can be regarded as a heterogeneous material [8, 9]. Thus, the strengths and shear stresses at different ECDs are nonlinear in gear meshing. Kim and Bae [10] studied gear deformation at different quenching temperatures during carburizing-quenching simulation and proposed process parameters for practical manufacturing. Sugimoto [11] investigated the distortion in axial contraction of a carburized-quenched helical gear. Rajesh *et al.* [12] analyzed load sharing and bending strength for altered tooth-sum gears in which the tooth-profile shift greatly affected performance. In these studies, however, the strength and failure analysis based on experimental testing was discussed, and the related processes are usually expensive and time-consuming. Kim *et al.* [10] and Nojima *et al.* [13] proposed calculation methods for the ECD of carburized gears that, while involving only a few process parameters, did not analyze the strength of carburized gears.

From the publicly available literature, it is evident that work on the effects of ECD on meshing strength is limited, especially regarding internal gear transmission. Actually, the ECD has a great impact on the meshing strength, including not only the shear stress distribution but also the wear resistance, thus resulting in the possibility of meshing performance variation of the internal gear transmission [14, 15]. In this paper, we established an analytical calculation model for meshing shear stresses of an internal gear pair with a shifted tooth profile based on previous work [4, 16, 17] with consideration for the friction factor. The proposed model made it possible to reveal the effect of ECD on the meshing strength of an internal gear pair via the different ECDs achieved by heat treatment of a carburized gear pair made of 805M20 steel through numerical simulation using FEM and experiment. We analyzed three different carburized layer models, with the ECD of an internal gear being greater than, less than, and equal to the ECD in an external gear. We realized the distinguishing of hardness gradients in gear teeth by dividing the ECD into seven layers to improve the analysis accuracy.

This paper is organized as follows. Reviews of the previous literature on gear ECD and the meshing strength calculation method were presented previously. Thus, in Section 2, an analytical meshing formulation of a carburized gear pair is derived, followed by the construction of an internal gear transmission model. The results and discussion of the investigation of the effect of ECD on the meshing strength of internal gear transmissions are presented in Section 3. Conclusions are drawn in Section 4.

2. Materials and Methods

2.1. Analytical Meshing Formulation of Carburized Gear. The meshing strength performance of a gear is determined by the shear strength of the gear material and shear stress distribution under the tooth surface [18]. Reasonable selection of the depth of the carburizing layer can improve the strength and the rolling contact durability of powder metallurgical gears. The radius of curvature of the involute surface of the gear can be regarded as the radius of the cylinder when a pair of involute gears is engaged. Therefore, the contact problem of the two meshing teeth can be simplified as the contact problem of two cylinders. The meshing-tooth model is illustrated in Figure 1(a) and the stress state under the contact surface is shown in Figure 1(b), in which the vertical direction of the contact surface is the Z axis and the horizontal direction is the Y axis. The contact surface is affected by the normal load P, and the friction between the two contact surfaces is q.

The maximum contact stress $P_{\max}$ and the half-width of Hertz contact zone b can be expressed as follows:

$$P_{\max} = \sqrt{\frac{W}{\pi} \cdot \frac{(R_1 + R_2)/R_1R_2}{[(1-\nu_1^2)/E_1 + (1-\nu_2^2)/E_2]}} \tag{1}$$

$$b = \sqrt{\frac{4W}{\pi} \cdot \frac{R_1R_2}{R_1 + R_2}\left[\frac{1-\nu_1^2}{E_1} + \frac{1-\nu_2^2}{E_2}\right]} \tag{2}$$

where W is the load per unit length of gear teeth, R_1 and R_2 are the curvature radii at the contact point, E_1 and E_2 are Young's moduli, and ν_1 and ν_2 are Poisson's ratios.

In gear meshing, the carburized layer involves alternating shear stress. Spalling will occur when the shear stress exceeds the ultimate strength of the material [19]. By ignoring the friction, the stress at an arbitrary point under the gear surface can be calculated by the following formulas:

$$\sigma_{yy} = \frac{\left[\left(\sqrt{1 + (z/b)^2} - z/b\right)^2 / \sqrt{1 + (z/b)^2}\right] b}{\Delta} \tag{3}$$

$$\sigma_{zz} = -\frac{\left[1/\sqrt{1 + (z/b)^2}\right] b}{\Delta} \tag{4}$$

$$\sigma_{xx} = -\frac{2\nu\left[\sqrt{1 + (z/b)^2} - z/b\right] b}{\Delta} \tag{5}$$

$$\Delta = \frac{2}{1/R_1 + 1/R_2}\left[\frac{1-{\nu_1}^2}{E_1} + \frac{1-{\nu_2}^2}{E_2}\right] \tag{6}$$

where b is the half-width of the Hertz contact zone and z the distance beneath the tooth surface. The maximum shear stress can be expressed as follows:

$$\tau_{\max} = \frac{1}{2}(\sigma_{\max} - \sigma_{\min}) \tag{7}$$

$\sigma_{\max}$ takes the maximum value of σ_{xx}, σ_{yy}, and σ_{zz}, and $\sigma_{\min}$ takes the minimum value of σ_{xx}, σ_{yy}, and σ_{zz}.

In practical engineering application, the calculation of gear-meshing strength analytically always can be achieved by considering the friction influence. In addition to the panel

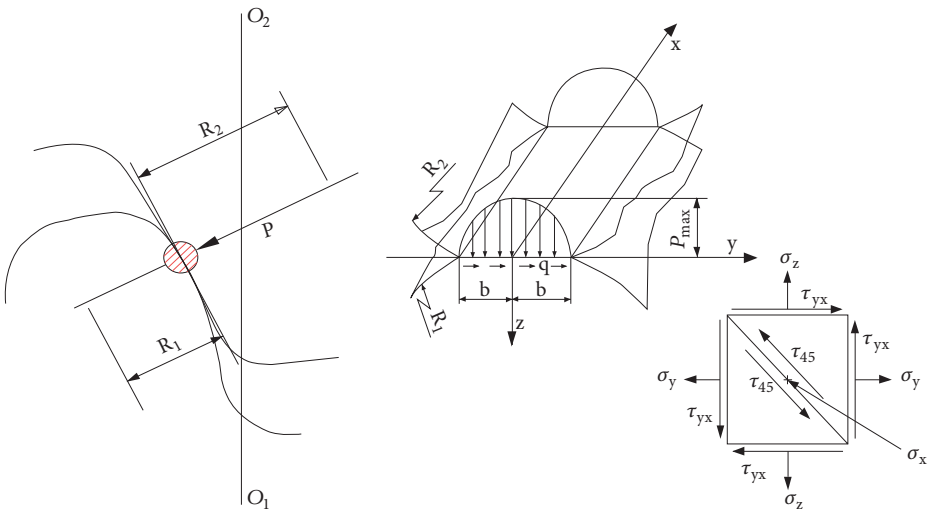

(a) (b)

Figure 1: Stress state under the contact surface of gear teeth: (a) involute gear meshing and (b) stress distribution on gear surface.

node, the rest of the meshing points experience both rolling and sliding. Therefore, the contact area simultaneously bears the normal force and tangential force [20]. According to Hertz theory [21], the stress at an arbitrary point under the combined effect of normal pressure and shear stress can be calculated by the following formulas:

$$\sigma_{yy} = -\frac{b}{\pi\Delta}\left\{z\left(\frac{b^2+2z^2+2y^2}{b}\Phi_1 - \frac{2\pi}{b} - 3y\Phi_2\right) + f\left[\left(2y^2-2b^2-3z^2\right)\Phi_2 + \frac{2\pi y}{b} + 2\left(b^2-x^2-z^2\right)\frac{y}{b}\Phi_1\right]\right\} \tag{8}$$

$$\sigma_{xx} = -\frac{2vb}{\pi\Delta}\left\{z\left(\frac{b^2+z^2+y^2}{b}\Phi_1 - \frac{\pi}{b} - 2y\Phi_2\right) + f\left[\left(y^2-b^2-z^2\right)\Phi_2 + \frac{\pi y}{b} + \left(b^2-x^2-z^2\right)\frac{y}{b}\Phi_1\right]\right\} \tag{9}$$

$$\sigma_{zz} = -\frac{b}{\pi\Delta}\left[z\left(b\Phi_1 - y\Phi_2\right) + {f_z}^2\Phi_2\right] \tag{10}$$

$$\tau_{yz} = -\frac{b}{\pi\Delta}\left\{z^2\Phi_2 + f\left[\left(c^2+2y^2+2z^2\right)\frac{z}{b}\Phi_1 - \frac{2\pi z}{b} - 3yz\Phi_2\right]\right\} \tag{11}$$

where f is the friction coefficient and v Poisson's ratio:

$$\Phi_1 = \frac{\pi\left(M+N\right)}{MN\sqrt{2MN+2y^2+2z^2-2b^2}} \tag{12}$$

$$\Phi_2 = \frac{\pi\left(M-N\right)}{MN\sqrt{2MN+2y^2+2z^2-2b^2}} \tag{13}$$

$$M = \sqrt{\left(b+y\right)^2+z^2} \tag{14}$$

$$N = \sqrt{\left(b-y\right)^2+z^2} \tag{15}$$

The formulas for the three principal stresses can be expressed as follows:

$$\sigma_1 = \frac{\sigma_{yy}+\sigma_{zz}}{2} + \sqrt{\left(\frac{\sigma_{yy}-\sigma_{zz}}{2}\right)^2 + {\tau_{yz}}^2} \tag{16}$$

$$\sigma_2 = v\left(\sigma_{yy}+\sigma_{zz}\right) \tag{17}$$

$$\sigma_3 = \frac{\sigma_{yy}+\sigma_{zz}}{2} - \sqrt{\left(\frac{\sigma_{yy}-\sigma_{zz}}{2}\right)^2 + {\tau_{yz}}^2} \tag{18}$$

According to the third strength theory, the maximum shear stress value on the principal shear stress plane can be expressed as follows:

$$\tau_{\max} = \frac{1}{2}\left(\sigma_1 - \sigma_3\right) \tag{19}$$

where σ_1 and σ_3 are the maximum and minimum algebraic values of the principal stress, respectively. On the basis of the Tresca criterion [22], the relationship between the yield strength (YS) and the critical shear fracture stress has been described by Ashby and Jones [23]. The formula of the critical shear fracture stress can be written as follows:

$$2\tau_0 = 1.15\sigma_y \tag{20}$$

where τ_0 is the critical fracture stress in MPa and σ_y the yield stress in MPa.

The spalling failure of a gear is related to the loads, ECD, and hardness in the tooth heart [24]. Under certain assumptions concerning the loads, the crack that originates from the transition layer will cause deep spalling if the ECD is too shallow or the hardness in the tooth heart is low. When the hardness in the gear-tooth center meets the requirement of strength, the crack that originates from the hardness layer will cause shallow spalling if the defects exist in the structure of the hardness layer.

The junction between the hardness layer and tooth heart is a weak region [4]. To avoid spalling produced by the transition layer, it is essential to design a reasonable ECD. Ding and Rieger [25] indicated that the spalling failure of a gear is caused by orthonormal shear stress and proposed the conditions in which the hardness and transition layers do not produce spalling cracks:

$$A\left(\frac{\tau_{yz}}{\mathrm{HV}}\right)_t \le 0.6A\left(\frac{\tau_{yz}}{\mathrm{HV}}\right)_{\mathrm{lim}} \tag{21}$$

$$A\left(\frac{\tau_{yz}}{\mathrm{HV}}\right)_H \le 0.6A\left(\frac{\tau_{yz}}{\mathrm{HV}}\right)_{\mathrm{lim}} \tag{22}$$

where τ_{yz} is the orthonormal shear stress, $A(\tau_{yz}/\mathrm{HV})_t$ is the extreme value in the transition layer, $A(\tau_{yz}/\mathrm{HV})_H$ is the extreme value in the hardness layer, and $A(\tau_{yz}/\mathrm{HV})_{\mathrm{lim}}$ is the limit amplitude.

Some researchers [4, 26, 27] have indicated that the spalling failure of a gear is caused by the maximum shear stress and proposed that the ratio of the shear stress in the transition layer and the shear strength of the gear material should not be larger than 0.55, which is expressed as follows:

$$\varepsilon = \frac{\tau_{\max}}{[\tau]} \le 0.55 \tag{23}$$

where ε is the ratio of the shear stress in the transition layer and shear-strength resistance, $\tau_{\max}$ is the maximum shear stress, and $[\tau]$ is a material property of the shear strength for gear.

The depth of the hardness layer is an important technical index in the carburizing and quenching heat treatment of gears. Calculation of the depth of the hardness layer could be achieved analytically by regarding the gear teeth as nonuniform cantilever beams [28, 29], which has been employed in previously published papers to give the recommended value of the depth of the hardness layer to prevent spalling failure based on the maximum shear stress caused by gear meshing. The formula [30] for calculating the minimum depth of the hardness layer at the pitch circles of the gear tooth can be expressed as follows:

$$h_e = \frac{S_C \cdot d \cdot \sin\alpha}{U_H \cdot \cos\beta} \mathrm{C_G} \tag{24}$$

where h_e is the minimum depth of the hardness layer at the pitch circles, S_c is the contact stress, α is the pressure angle of the end surface of the pitch circle, d is the diameter of the pitch circle, β is the base helix angle, U_H is the hardening process coefficient, and C_G is the transmission ratio coefficient.

Heat treatment parameters			
Model	Gear type	a(min)	b(min)
EH	Internal	200	60
EH	External	190	60
IH	Internal	120	60
IH	External	180	60
HH	Internal	170	60
HH	External	170	60

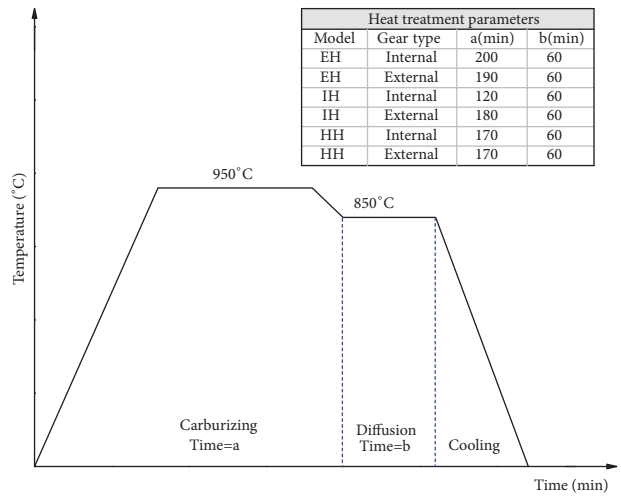

Figure 2: Process curve for heat treatment of gear.

More detailed expressions of the empirical formula [31] for the depth of the hardness layer at each meshing point of the tooth surface can be derived and expressed as follows:

$$t_i = 1.66 \times 10^3 \times \left(1 + \frac{w(C_i) - w(C_{\mathrm{inner}})}{w(C_{\mathrm{outer}}) - w(C_i)}\right) \times \left[\frac{T_1 \times z_2 \tan\alpha}{z_1 + z_2}\right]^{1/2} \tag{25}$$

where t_i is the thickness of each point of the carburized layer, $w(C_{\mathrm{outer}})$ is the carbon intensity of the gear surface, $w(C_{\mathrm{inner}})$ is the carbon intensity of the gear heart, $w(C_i)$ is the carbon intensity of each point of the carburized layer, T_1 is the torque of the driving gear, z_1 is the number of driving-gear teeth, and z_2 is the number of driven-gear teeth.

The empirical formula [31] for the calculation of the minimum depth of the carburized layer can be written as follows:

$$t \ge \frac{31a \times \sin\alpha_t \times \delta_{\max} \times u}{Hv \times \cos\beta_h \times (u \pm 1)^2} \tag{26}$$

where t is the minimum depth of the carburized layer, a is the center distance of the gear pair, a_t is the engaged angle of the gear transverse plane, $\delta_{\max}$ is the maximum contact stress, u is the gear transmission ratio, Hv is the Vickers hardness of the carburized layer of the gear surface in kg/mm^2, β_h is the base helix angle, and "+" and "−" represent external meshing and internal meshing, respectively.

2.2. Internal Gear Transmission Model. The complete die-quenching process for a gear pair includes carburizing, die quenching, and air cooling. The complete technical curve is shown in Figure 2. The gear pairs made of 805M20 steel were carburized in a double-ring hearth furnace consisting of carburizing and diffusion units. We applied load to the gear before the quenching process and removed load after the quenching process. To investigate the effects of ECD on the

Table 1: Parameters for external and internal gears.

Gear pair	Tooth number	Modulus (mm)	Tooth width (mm)	Pressure angle (°)	Pitch diameter (mm)
External gear	35	1.60	3.5	33.94	45.54
Internal gear	36	1.63	3.5	33.94	46.84

meshing strength of internal gear transmission, we devised three different carburized layer models, with the carburized-layer depth in the internal gear being greater than, less than, and equal to the carburized-layer depth in the external gear.

The hardness-gradient measurement was carried out by Vickers microhardness measurements after gear-tooth cutting. A 300-g load was used for the microhardness tests. The ECD was defined as the distance from the surface to the point at which the microhardness was 550 HV, and it was dependent on the carbon potential and the duration of the carburizing process [32]. The variation of hardness values with the carburized depth is shown in Figure 3. We built three mechanical models, (1) EH, (2) IH, and (3) HH, corresponding to the ECD in the internal gear being greater than, less than, and equal to the ECD in the external gear, in the static strength tests. The ECDs in the three mechanical models are shown in Figure 4.

Zhang *et al.* [22] described the physical relationship between hardness and strength and developed the correlations that allow for calculation of expected YSs from measured hardness. For a Vickers indenter, the relationship between hardness and strength through the pressure normal to the surface of the indenter tip can be calculated as follows:

$$\sigma_y = 3.12H_V, \tag{27}$$

$$\sigma_{UTS} = 3.26H_V, \tag{28}$$

where σ_y is the yield stress (YS) in MPa, H_V is the Vickers hardness of the carburized layer of the gear surface in kg/mm^2, and σ_{UTS} is the ultimate tensile strength (UTS) in MPa. In this study, we calculated the mechanical properties of three different carburized-layer models using (27) and (28); the relationship between strength and carburized-layer depth is plotted in Figure 5.

The parameters for external and internal gears are shown in Table 1. Under normal circumstances, gear failure usually occurs in the gear teeth and rarely in a part of the hub. To achieve high calculation accuracy, the hexahedron element is used in the mesh of the FEM model. We used a geometric model of the external and internal gears to represent the entire gear pair. There were 817906 nodes and 806721 elements in the FE mesh, as shown in Figure 6(a). We determined the hardness gradient in the gear teeth by dividing the carburized depth into seven layers, as shown in Figure 6(b).

We devised three different carburized-layer models, with the ECD in the internal gear being greater than, less than, and equal to the ECD in the external gear. In addition, we determined the hardness gradient in the gear teeth by dividing the carburized depth into seven layers to improve the modeling accuracy.

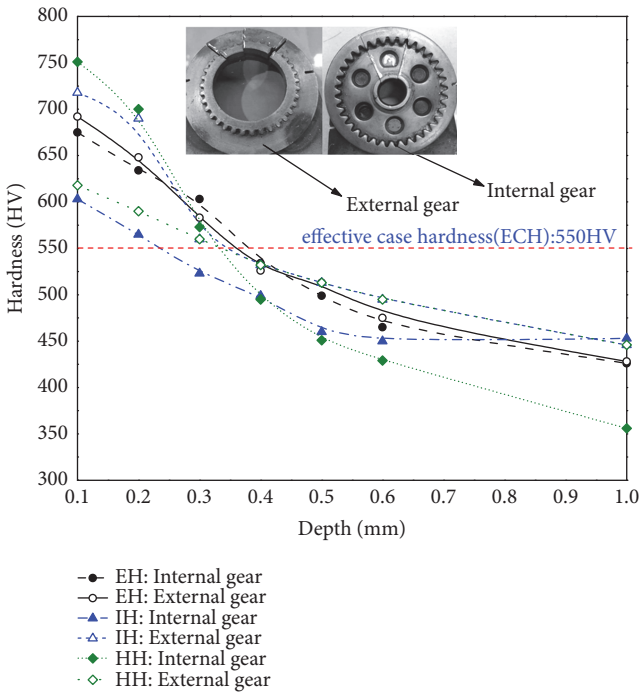

Figure 3: Variation of hardness value with carburized-layer depth.

3. Results and Discussion

In this study, we used three carburized gear-pair models (EH, IH, and HH models) for the static strength test. The external gear was fixed on a pedestal and the internal gear connected to a steel frame. The steel frame and a hydraulic drawing machine were connected flexibly through a steel cable; the piston of the hydraulic drawing machine was uniformly contracted in the cylinder, as shown in Figure 7. We recorded the displacement curve of the piston and the force of hydraulic cylinder to achieve the strength of carburized gear pair. The variation of maximum strength with gear rotation angle is shown in Figure 8.

The stress and displacement distribution of the carburized gear pair in any position can be achieved through transient analysis of the FEM models of the carburized gear pair using (1) to (19). The maximum stress can be obtained by reading the maximum contact stress on the surface of the tooth root of the carburized gear using (1). Furthermore, we calculated the maximum shear stress in the carburized layer

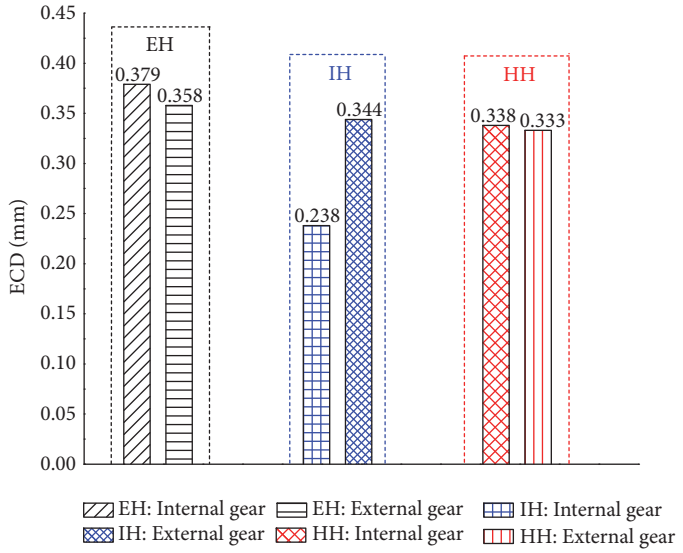

Figure 4: ECD in three mechanical models.

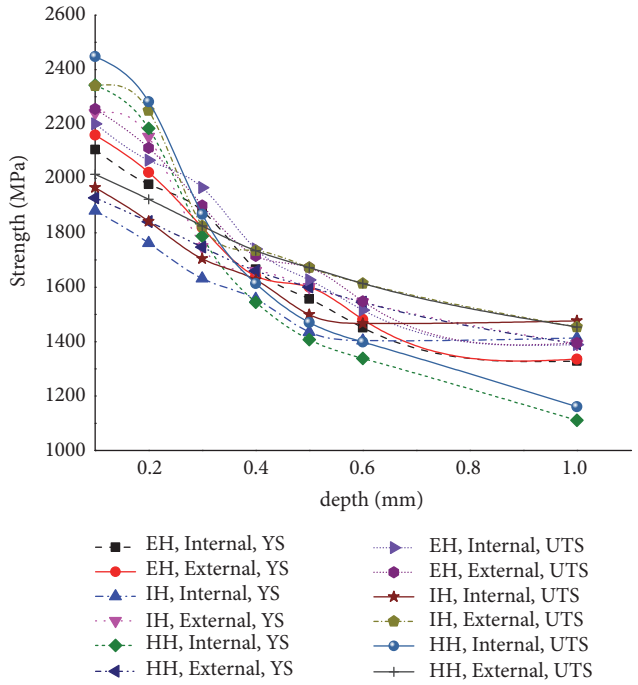

Figure 5: Relationship between strength and carburized-layer depth.

and obtained the worst meshing point and corresponding meshing-gear number. The maximum shear stress value and the maximum stress on the principal shear stress plane can be calculated by (7) and (19), respectively. The calculations were conducted through the use of the platform of ABAQUS software. The displacement distribution of the external gear teeth at the maximum meshing strength of three different gear pairs is shown in Figure 9.

The stress and displacement were zero at the beginning of engagement, but the stress increased significantly for the shock in the 24th pair of gear teeth and reduced with rotation. The maximum displacements in the EH, IH, and HH models were 1.594, 1.54, and 1.571 mm, respectively. The shear stress increased simultaneously upon engagement of a single tooth. Furthermore, the maximum shear stress was observed when the 24th pair of teeth meshed. By reading the maximum strength of the carburized gear-pair models, the variation of the maximum strength with gear rotation angle in the three models is shown in Figure 10.

According to Figure 10, the maximum strengths in the EH, IH, and HH models are 4322 N·m, 4609 N·m, and 4480 N·m, respectively. Thus, the highest strength of a carburized gear pair can be obtained when the carburized-layer depth in the internal gear is less than that in the external gear. The

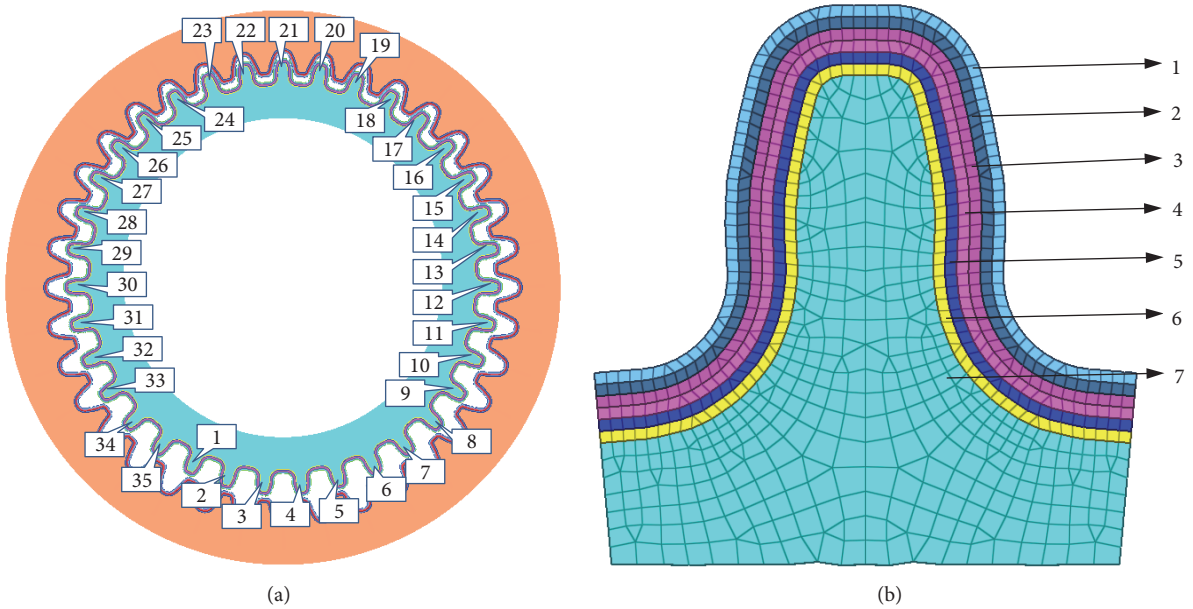

(a) (b)

Figure 6: Geometry and mesh of gear-pair model: (a) FE mesh model and (b) distinction of hardness gradient.

Figure 7: The loading apparatus for testing the maximum strength value of gear pairs.

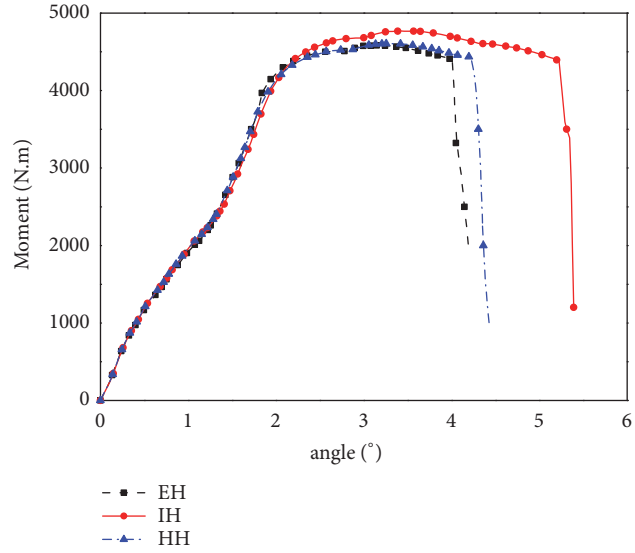

Figure 8: Variation of maximum strength with gear rotation angle based on experimental test.

maximum meshing strength predicted by the FEM is in good agreement with that determined from experiment. According to the von Mises criterion [33], the ductility of the different carburized gear pairs can be achieved based on the ability of the gear to absorb deformation energy before the failure of the gear pair; the deformation energies of the three gear-pair models studied before failure are shown in Figure 11.

In this study, we defined the ductility of different carburized gear pairs as the ratios of the total energy that the gear pairs can absorb before failure. For a volume of the gear pair of 3280 mm^3, we calculated the total energy by integration of the torque by rotation angle. The total deformation energies in different models are represented by the dashed area in Figure 12 and the strength and ductility of the three carburized gear-pair models studied are given in Table 2.

The strength and ductility of the IH gear-pair model are the highest of the three carburized gear-pair models studied. The results for the hardness gradients of the carburized gear pairs show that the meshing strength of internal gear transmission could be enhanced by adopting the IH gear-pair model with the ECD in the internal gear being less than the ECD in the external gear. The meshing strength performance of a gear is determined by the shear strength property of the gear material and shear stress distribution under the tooth surface. Selecting the IH gear-pair model, the shear stress and plastic strain of internal gear transmission are shown in Figure 12.

It can be seen from Figure 12 that the shear stress and plastic strain values for the external gear are obviously higher than those for the internal gear in gear engagement and

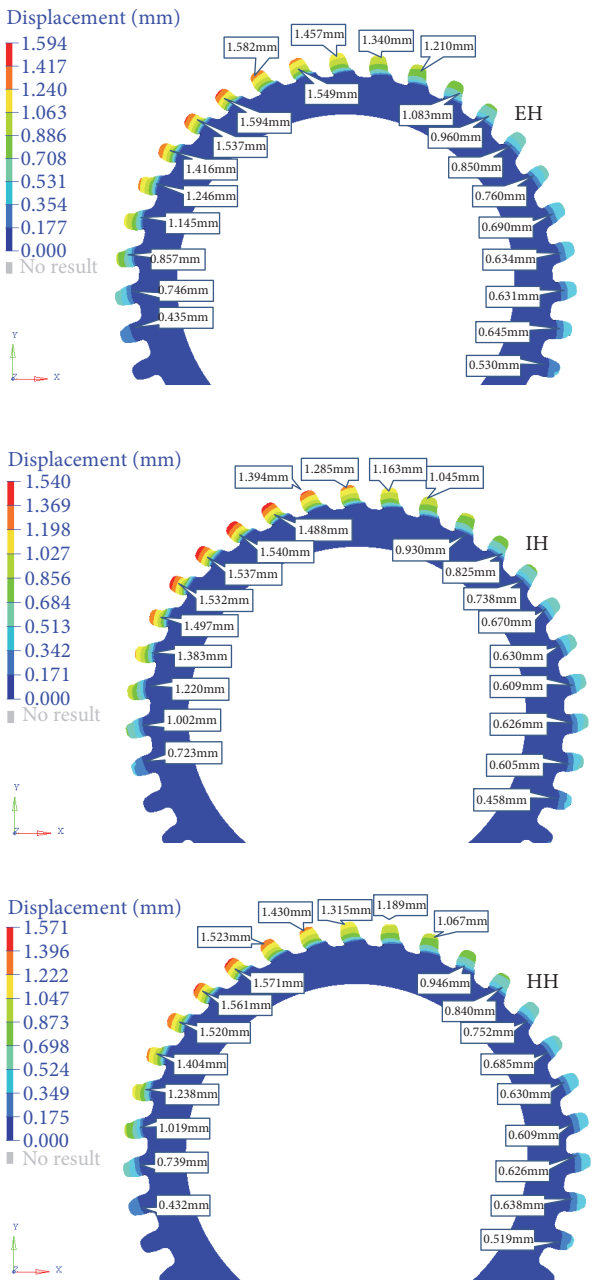

FIGURE 9: Displacement distribution of external gear teeth at maximum meshing strength of three different gear pairs.

the ECD in the internal gear has a limited influence on the strength and ductility of internal gear transmission. With an increasing number of engaged gears, the external gear will fail earlier than the internal gear.

On the basis of the Tresca criterion [22], we calculated the fracture stresses of the external gear in seven layers for the three mechanical models using (20) and the results are summarized in Table 3.

The strength of the IH gear-pair model is the highest of the three carburized gear-pair models. Using the maximum shear stress value, the maximum shear stress in each hardness layer for the external gear is presented in Figure 13.

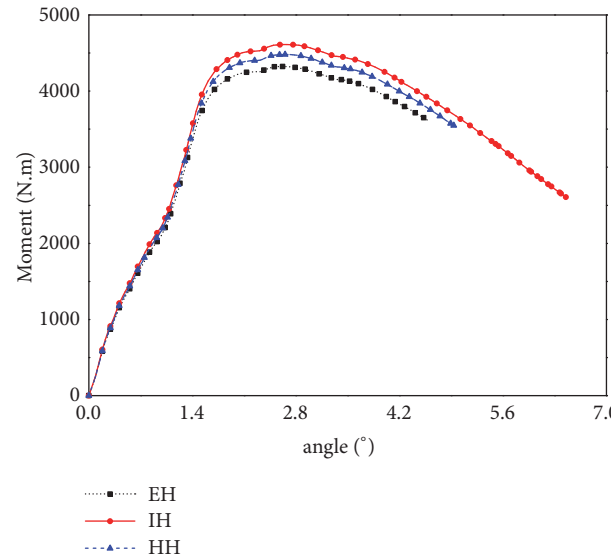

FIGURE 10: Variation of maximum strength with gear rotation angle based on FEM.

Figure 13 shows the maximum shear stress in each of seven hardness layers for the external gear and the speed sequence of the shear stress value in all seven layers that reaches the value of the fracture stress as follows: layer 4 > layer 3 > layer 7 > layer 5 > layer 6 > layer 2 > layer 1. Thus, the speed sequence of the shear stress value in all seven layers that reaches the value of the fracture stress indicates that the crack grows from the inside to the outside of the gear tooth. By selecting four points on the engaged tooth surface of the external gear in the IH model, the shear stresses on the engaged-tooth surface are shown in Figure 14.

Figure 14 shows the shear stresses on the engaged-tooth surface and that the growth sequence of the shear-stress value on the engaged tooth surface is P4 > P3 > P2 > P1, thus indicating that the crack grows from the middle to the sides of the gear-tooth surface.

4. Conclusions

We investigated the ECD of the internal carburized gear pairs using the FEM and experimental tests. We also analyzed three different carburized-layer models, with the ECD in the internal gear being greater than, less than, and equal to the ECD in the external gear. We derived the empirical formula for the calculation of the minimum depth of the carburized layer and then studied the specific process of establishing the FEM of a carburized gear pair. Finally, for the three carburized internal gear pairs studied, we performed numerical investigation of the meshing strength and compared the results with those of the experimental strength test. The following conclusions were drawn:

(1) The strength and ductility of the IH gear-pair model are the highest of the three carburized gear-pair models studied, and thus the ECD in the internal gear being less than the ECD in the external gear is the optimum configuration

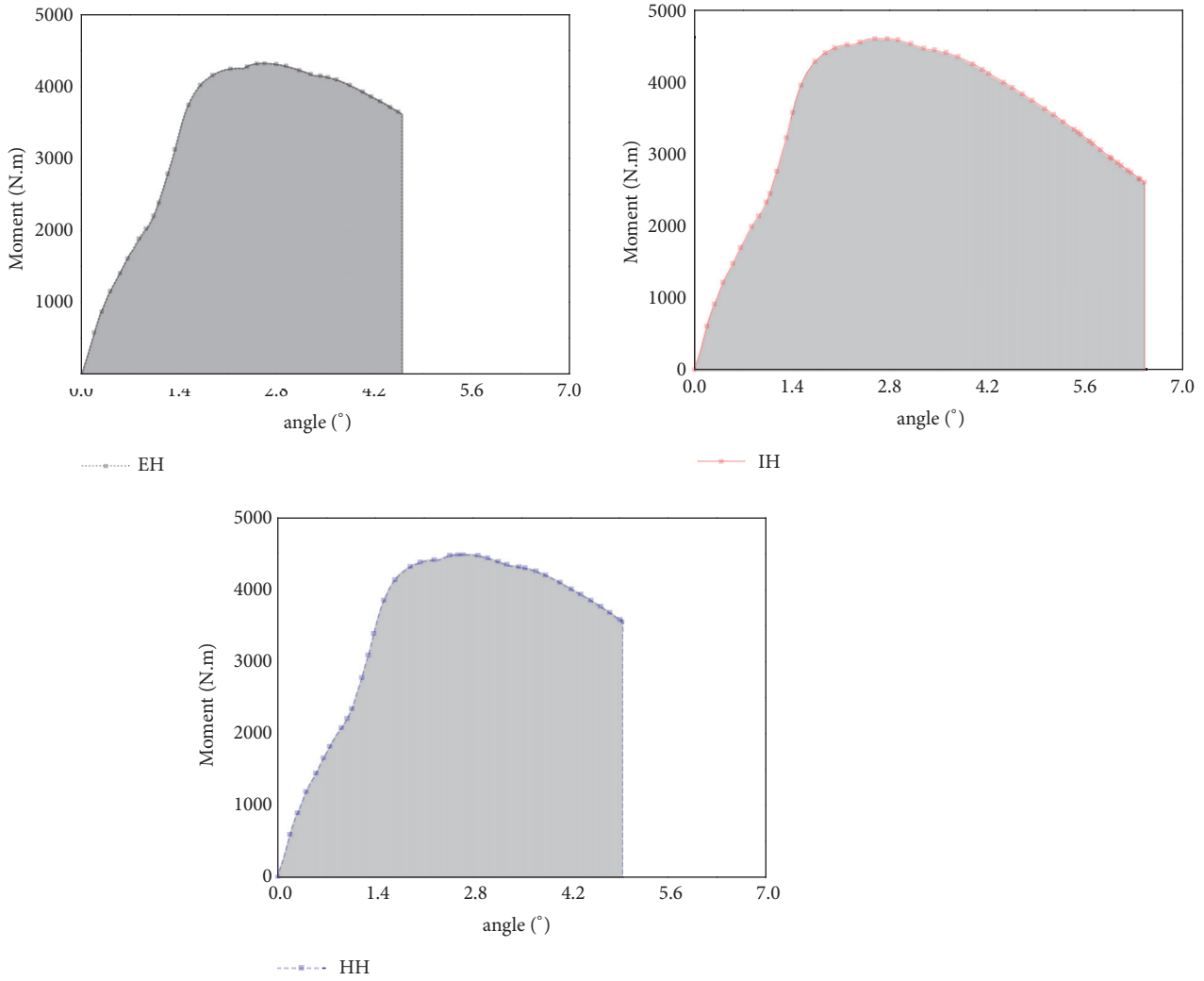

Figure 11: Deformation energies of three gear-pair models under study before failure.

Table 2: Strength and ductility of three carburized gear-pair models studied.

Carburized gear teeth	Gear-pair strength (N.m)	Strength ratio (based on EH model)	Gear-pair ductility (×100 kJ/mm^3)	Ductility ratio (based on EH model)
EH model	4322	1	814	1
IH model	4609	1.066	1195	1.468
HH model	4480	1.037	912	1.120

Table 3: Fracture stresses of external gears in seven layers for three mechanical models studied.

Layer number	Tresca criterion fracture stress (MPa)		
	EH	IH	HH
1	1241.448	1288.092	1108.692
2	1162.512	1237.86	1058.46
3	1045.902	1004.64	1004.64
4	943.644	954.408	954.408
5	920.322	920.322	920.322
6	852.15	888.03	888.03
7	767.832	800.124	800.124

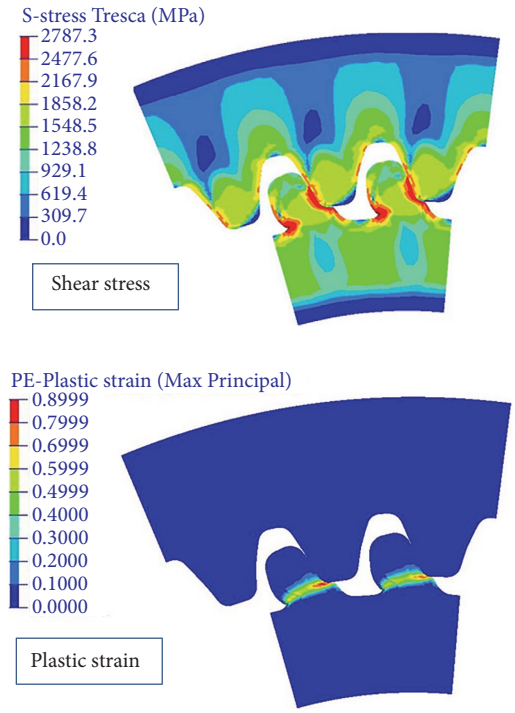

FIGURE 12: Shear stress and plastic strain of internal gear transmission.

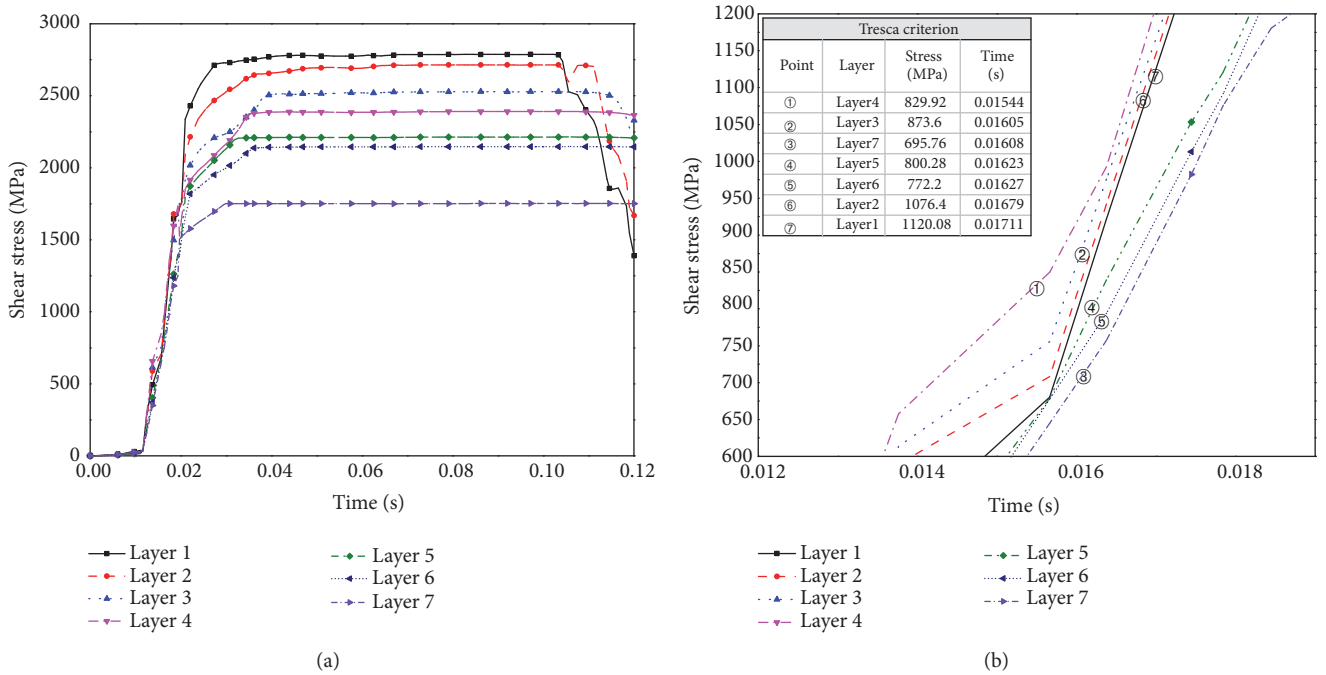

FIGURE 13: Maximum shear stress in each hardness layer for external gear: (a) evolution of maximum shear stress in seven layers; (b) sequence of shear stress in seven layers that reaches fracture stress from first to last.

in the design of the carburizing process for internal gear transmissions.

(2) The meshing strength of internal gear transmission is significantly affected by the shear strength of the gear material and shear stress distribution under the tooth surface; the shear stress of carburized gears initially increases and then decreases along with depth direction, and the maximum value appears in the middle of the lower surface.

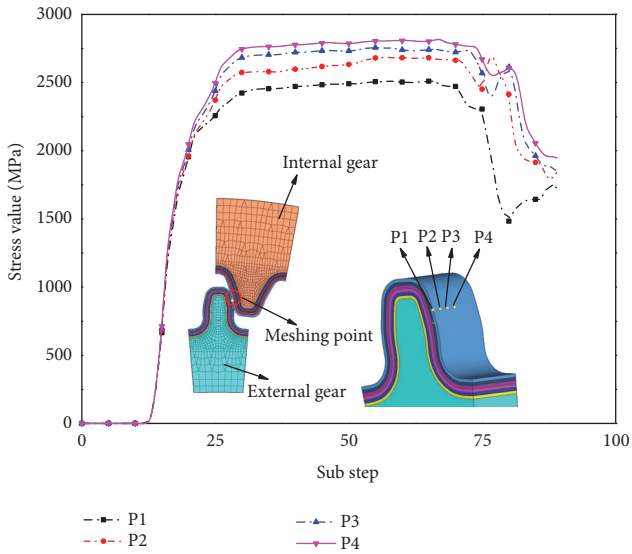

Figure 14: Shear stresses on engaged-tooth surface.

Data Availability

(1) The FE model catalysts data of the EH carburized gear-pair model used to support the findings of this study have been deposited in the FAIRsharing (https://fairsharing.org/) repository (DOI: https://doi.org/10.6084/m9.figshare.6875450.v1). (2) The FE model catalysts data of the HH carburized gear-pair model used to support the findings of this study have been deposited in the FAIRsharing (https://fairsharing.org/) repository (DOI: https://doi.org/10.6084/m9.figshare.6875456.v1). (3) The FE model catalysts data of the IH carburized gear-pair model used to support the findings of this study have been deposited in the FAIRsharing (https://fairsharing.org/) repository (DOI: https://doi.org/10.6084/m9.figshare.6875462.v1). (4) The experimental catalysts data of the hardness gradients of the three carburized gear-pair models used to support the findings of this study have been deposited in the FAIRsharing (https://fairsharing.org/repository) repository (DOI: https://doi.org/10.6084/m9.figshare.6875477.v1). (5) The experimental catalysts data for the maximum strength values and deformation energies used to support the findings of this study are currently under embargo while the research findings are commercialized. Requests for data, 12 months after publication of this article, will be considered by the corresponding author (Zhongren Wang; wzrvision@hbuas.edu.cn).

Conflicts of Interest

The authors declare that there are no conflicts of interest regarding the publication of this paper.

Acknowledgments

The authors gratefully acknowledge the use of the services and facilities of AVIC Hubei Aviation Precision Machinery Technology Co., Ltd., and Hubei Key Laboratory of Power System Design and Test for Electrical Vehicle. This research was funded by the Youth Project of Hubei Provincial Department of Education (No. Q20172603), Hubei Superior and Distinctive Discipline Group of Mechatronics and Automobiles (No. XKQ2018065), and Hubei Superior and Distinctive Discipline Group of Mechatronics and Automobiles (No. XKQ2018009).

References

[1] L. Xie, D. Palmer, F. Otto, Z. Wang, and Q. Jane Wang, "Effect of Surface Hardening Technique and Case Depth on Rolling Contact Fatigue Behavior of Alloy Steels," *Tribology Transactions*, vol. 58, no. 2, pp. 215–224, 2015.

[2] A. Emamian, "A Study on Wear Resistance, Hardness and Impact Behaviour of Carburized Fe-Based Powder Metallurgy Parts for Automotive Applications," *Materials Sciences and Applications*, vol. 03, no. 08, pp. 519–522, 2012.

[3] X. Y. Li, S. S. Li, and Q. L. Ceng, "Study on strength of carburized gear for mining gearbox based on dynamics," *Journal of China Coal Society*, vol. 36, no. 7, pp. 1227–1231, 2011.

[4] X. Y. Li, Q. X. Zhang, N. N. Wang, Q. L. Zeng, and K. Hidenori, "Meshing simulation and strength calculation of a carburized gear pair," *International Journal of Simulation Modelling*, vol. 16, no. 1, pp. 121–132, 2017.

[5] B. Jiang, X. Zheng, and L. Wu, "Estimate by fracture mechanics theory for rolling contact fatigue life and strength of case-hardened gear materials with computer," *Engineering Fracture Mechanics*, vol. 39, no. 5, pp. 867–874, 1991.

[6] Z. Chen and Y. Shao, "Mesh stiffness calculation of a spur gear pair with tooth profile modification and tooth root crack," *Mechanism and Machine Theory*, vol. 62, pp. 63–74, 2013.

[7] J.-Y. Tang and Y.-P. Liu, "Loaded multi-tooth contact analysis and calculation for contact stress of face-gear drive with spur involute pinion," *Journal of Central South University*, vol. 20, no. 2, pp. 354–362, 2013.

[8] F. O. Aramidea, S. A. Ibitoye, I. O. Oladele, and J. O. Borode, "Effects of carburization time and temperature on the mechanical properties of carburized mild steel, using activated carbon as carburizer," *Materials Research*, vol. 12, no. 4, pp. 483–487, 2009.

[9] J. John, K. Li, and H. Li, "Fatigue performance and residual stress of carburized gear steels Part I: Residual stress," *SAE International Journal of Materials and Manufacturing*, vol. 1, no. 1, pp. 718–724, 2009.

[10] N.-K. Kim and K.-Y. Bae, "Analysis of deformation in the carburizing-quenching heat treatment of helical gears made of SCM415H steel," *International Journal of Precision Engineering and Manufacturing*, vol. 16, no. 1, pp. 73–79, 2015.

[11] A. Sugianto, M. Narazaki, M. Kogawara, S. Y. Kim, and S. Kubota, "Distortion analysis of axial contraction of carburized-quenched helical gear," *Journal of Materials Engineering and Performance*, vol. 19, no. 2, pp. 194–206, 2010.

[12] A. R. Rajesh, G. Joseph, and K. A. Venugopal, "Design and Testing of Gears Operating between a Specified Center Distance Using Altered Tooth-sum Gearing (Z± Gearing)," *Journal of Mechanical Engineering and Automation*, vol. 6, no. 5A, pp. 102–108, 2016.

[13] K. Nojima, K. Ogata, M. Tanaka, R. Nishi, Y. Ono, and T. Koide, "Bending fatigue strength of case-carburized helical gears (In the case of large helix angles)," *Journal of Mechanical Science and Technology*, vol. 31, no. 12, pp. 5657–5663, 2017.

[14] G.-J. Du, Z.-Q. Yang, and X.-M. Liu, "Quenching process simulation of carburized cylindrical gear," *Gongcheng Lixue/Engineering Mechanics*, vol. 30, no. 1, pp. 407–412, 2013.

[15] Y. Zhang, W. Shi, L. Yang, Z. Gu, and Z. Li, "The Effect of Hardenability Variation on Phase Transformation of Spiral Bevel Gear in Quenching Process," *Journal of Materials Engineering and Performance*, vol. 25, no. 7, pp. 2727–2735, 2016.

[16] G. Deng, K. Inoue, N. Takatsu, and M. Kato, "Evaluation of the Strength of Carburized Spur Gear Teeth Based on Fracture Mechanics: (3rd Report, The Crack Growth in Carburized Gear)," *Transactions of The Japan Society of Mechanical Engineers Series C*, vol. 57, no. 535, pp. 909–913, 1991.

[17] K. Miyachika, B. D. I. Daing Mohamad Nafiz, T. Koide, B. W. N. Imadjiddin Helmi, and K. Ando, "Effects of rim and web thicknesses on root stresses of thin-rimmed helical gears," *Nihon Kikai Gakkai Ronbunshu, C Hen/Transactions of the Japan Society of Mechanical Engineers, Part C*, vol. 77, no. 775, pp. 597–603, 2011.

[18] C. Han, "The prediction research on fatigue failure under gear tooth surface," *Journal of Mechanical Transmission*, vol. 37, no. 8, pp. 1–5, 2011.

[19] H. Jiang, Y. Shao, and C. K. Mechefske, "Dynamic characteristics of helical gears under sliding friction with spalling defect," *Engineering Failure Analysis*, vol. 39, pp. 92–107, 2014.

[20] T. Xiang, L. Gu, and J. Xu, "The meshing angular velocity and tangential contact force simulation for logarithmic spiral bevel gear based on Hertz elastic contact theory," *Journal of Mechanical Science and Technology*, vol. 30, no. 8, pp. 3441–3452, 2016.

[21] I. Gonzalez-Perez, J. L. Iserte, and A. Fuentes, "Implementation of Hertz theory and validation of a finite element model for stress analysis of gear drives with localized bearing contact," *Mechanism and Machine Theory*, vol. 46, no. 6, pp. 765–783, 2011.

[22] P. Zhang, S. X. Li, and Z. F. Zhang, "General relationship between strength and hardness," *Materials Science and Engineering: A Structural Materials: Properties, Microstructure and Processing*, vol. 529, no. 1, pp. 62–73, 2011.

[23] M. F. Ashby and H. D. R. Jones, *Engineering Materials*, Pergamon, Oxford, UK, 1980.

[24] A. Saxena, A. Parey, and M. Chouksey, "Time varying mesh stiffness calculation of spur gear pair considering sliding friction and spalling defects," *Engineering Failure Analysis*, vol. 70, pp. 200–211, 2016.

[25] Y. Ding and N. F. Rieger, "Spalling formation mechanism for gears," *Wear*, vol. 254, no. 12, pp. 1307–1317, 2003.

[26] J. M. Gere and B. J. Goodno, *International Journal of Strength of Materials*, China machine press, Beijing, China, 2011.

[27] M. A. Muraro, F. Koda, U. Reisdorfer Jr., and C. H. da Silva, "The influence of contact stress distribution and specific film thickness on the wear of spur gears during pitting tests," *Journal of the Brazilian Society of Mechanical Sciences and Engineering*, vol. 34, no. 2, pp. 135–144, 2012.

[28] Z. Ren, S. Zhou, C. Li, and B. Wen, "Dynamic characteristics of multi-degrees of freedom system rotor-bearing system with coupling faults of rub-impact and crack," *Chinese Journal of Mechanical Engineering*, vol. 27, no. 4, pp. 785–792, 2014.

[29] H. Ma, X. Pang, R. Feng, R. Song, and B. Wen, "Fault features analysis of cracked gear considering the effects of the extended tooth contact," *Engineering Failure Analysis*, vol. 48, pp. 105–120, 2015.

[30] J. Shi, Z. S. Dai, Q. L. Deng, and B. Shen, "The available hardened depth of laser quenching of large module gears," *Journal of Mechanical Transmission*, vol. 30, no. 3, pp. 84–87, 2006.

[31] W. Xiao, Z. Liu, and Y. Yuan, "Design method of hardened depth for carburized gear," *Jinshu Rechuli/Heat Treatment of Metals*, vol. 39, no. 6, pp. 147–150, 2014.

[32] C. F. Yang, L. H. Chiu, and J. K. Wu, "Effects of carburization and hydrogenation on the impact toughness of AISI 4118 steel," *Surface and Coatings Technology*, vol. 73, no. 1-2, pp. 18–22, 1995.

[33] W. H. Yang, "A generalized von Mises criterion for yield and fracture," *Journal of Applied Mechanics*, vol. 47, no. 2, pp. 297–300, 1980.

Hindawi
Mathematical Problems in Engineering
Volume 2018, Article ID 9168014, 12 pages
https://doi.org/10.1155/2018/9168014

Research Article

Genetic-Based Optimization of the Manufacturing Process of a Robotic Arm under Fuzziness

Paraskevi T. Zacharia, Sotirios A. Tsirkas, Georgios Kabouridis, Andreas Ch. Yiannopoulos, and Georgios I. Giannopoulos

Department of Mechanical Engineering, Technological Educational Institute of Western Greece, Megalou Alexandrou 1, 26334 Patras, Greece

Correspondence should be addressed to Georgios I. Giannopoulos; ggiannopoulos@teiwest.gr

Received 21 September 2018; Revised 16 November 2018; Accepted 9 December 2018; Published 24 December 2018

Guest Editor: Anders E. W. Jarfors

Fuzziness is a key concern in modern industry and, thus, its implementation in manufacturing process modeling is of high practical importance for a wide industrial audience. The scientific contribution of the present attempt lies on the fact that the assembly line balancing problem of type 2 (SALBP-2) is approached for a real manufacturing process by introducing fuzzy processing times. The main scope of this work is the solution of the SALBP-2, which is an NP-hard problem, for a real manufacturing process considering fuzziness in the processing times. Since the data obtained from realistic situations are imprecise and uncertain, the consideration of fuzziness for the solution of SALBP-2 is of great interest. Thus, real data values for the processing times are gathered and estimated with uncertainty. Then, fuzzy processing times are used for finding the optimum cycle time. The optimization tool for the solution of the fuzzy SALBP-2 is a Genetic Algorithm (GA). The validity of the proposed approach is tested on the construction process of a metallic robotic arm. The experimental results demonstrate the effectiveness and efficiency of the proposed GA in determining the optimum sequence of the tasks assigned to workstations which provides the optimum fuzzy cycle time.

1. Introduction

In mass production systems, an important problem is the assembly line problem. An assembly line is a manufacturing technique according to which parts are added in sequence from workstation to workstation until the final assembly is produced. Each station has to complete a set of tasks on parts moving along the line. There are numerous studies related with assembly line systems which focus on the determination of the set of tasks which have to be assigned to each workstation under a given cycle and the constraints of precedence relationships. This kind of problem is well known as the simple assembly line balancing problem (SALBP) [1].

The most famous versions of the abovementioned problem are the SALBP type 1 (SALBP-1) and the SALBP type 2 (SALBP-2). SALBP-1 [2–15] is present when the aim is to effectively assign tasks to workstations by minimizing the number of stations for a prespecified cycle time. This problem commonly arises when new assembly lines are to be designed by a company. On the other hand, SALBP-2 [16–22] is present when the aim is to minimize the cycle time for a specific number of stations. This kind of problem usually arises when changes in the production process of a product are to take place in the effort to improve the line efficiency. Several methods have been proposed for the solution of SALBP problems such as genetic algorithms (GAs) [2, 5, 17], ant colony optimization [5, 9, 22], particle swarm optimization [10, 11, 14], Petri net [4, 10, 18], tabu search [3], bacterial foraging optimization [15], or other heuristic algorithms [8, 12, 13, 19–21]. Battaïa and Dolgui [23] have provided a very interesting survey, covering about 300 studies, which analyzes relevant research on balancing flow lines within many different industrial contexts. A more recent review regarding the assembly line balancing problem (ALBP) has been provided by Sivasankaran and Shahabudeen [24].

In a realistic manufacturing environment, the task time may be random due to worker fatigue, low skill levels, job dissatisfaction, poorly maintained equipment, defects in raw materials, etc. Since data in real-world problems are often afflicted with uncertainty, imprecision, and vagueness due

to both machine and human factors, they can only be estimated with uncertainty. Several researchers [25] have been attempted to incorporate fuzzy information in their effort to solve SALBP through various types of algorithms. Kalender et al. [26] have been developed to solve traditional ALBP with fuzzy operation times. Ozcan and Toklu [27] have presented a fuzzy goal programming model for imprecise goals for two-sided assembly line balancing. Tapkan et al. [28] have solved two-sided ALPB by employing positional, zoning, and synchronous task constraints via a bees algorithm. Mutlu and Ozgormus [29] have considered the physical workload of a task as a fuzzy concept and proposed a fuzzy linear programming model to solve ALPB. La Scalia et al. [30] have used fuzzy set theory as a viable alternative method for modelling and solving the stochastic ALPB. In several attempts, GAs have been adopted to solve SALBP in conjunction with fuzzy logic. Tsujimura et al. [31] have illustrated via a numerical experiment that a GA is an appropriate tool to solve fuzzy scheduling problems. In another attempt, Gen et al. [32] have used a numerical example to solve ALPB with fuzzy processing time by using GAs with the objective of minimizing the total operation time in each workstation. Similarly, a GA based approach for both types of fuzzy ALPB has been presented by Khoshalhan and Zegordi [33]. Zacharia and Nearchou [34] have presented a fuzzy extension of the SALBP-2 with fuzzy job processing times to deal with the uncertainty occurring in production systems. In an interesting study [35], ALBP has been modeled through a multicriteria fuzzy GA.

Few are the very recent attempts regarding line balancing problems which incorporate fuzzy considerations. Characteristically, Alavidoost et al. [36] have formulated multiobjective straight and U-shaped ALBPs with the fuzzy task processing times. In another attempt, a new approach based on queuing theory has been demonstrated by Khalili et al. [37] for solving the ALBP using fuzzy prioritization techniques. On the other hand, a heuristic has been proposed by Avikal et al. [38] to assign the disassembly, though, tasks to the workstations under its precedence constraints incorporating fuzzy analytic hierarchy process. Nevertheless, the latest attention-grabbing studies associated with the ALBP commonly do not utilize fuzzy concepts. In an interesting effort, Su et al. [39] have conducted study on balancing a mixed-model assembly line of Type E based on a Petri net model. More recently, new lower bounds for the SALBP have been introduced and empirically evaluated [40]. Additionally, a mixed integer programming model has been developed for the parallel two-sided ALBP [41]. Furthermore, an innovative parallel assembly line configuration has been introduced for U-shaped lines [42]. Finally, Roshani and Giglio [43] have addressed the multimanned ALPB, with the objective of minimizing the cycle time.

In the present paper, the SALBP-2 regarding the construction of a real robotic arm is under investigation. The metal parts of the robotic arm are manufactured in four machining workstations. In order to deal with the variability of the task operation times, fuzzy set theory [44] is adopted as a very promising approach for modeling and solving stochastic problems. The fuzzy theory is then combined with an appropriate GA [45, 46] for solving the fuzzy SALBP-2 of the robot's metal frame. To handle more realistically the manufacturing of the robot's metal frame, the processing time for each job is considered as fuzzy and is represented by triangular fuzzy membership functions. In an attempt to treat relevant imprecise data, fuzzy numbers are introduced to represent the processing time of each job, where the membership function of a fuzzy data represents the grade of satisfaction of a decision maker. The main contribution of this paper is to enhance the real manufacturing process of a robotic arm in terms of time reduction, using an optimization algorithm (GA) by simultaneously considering the variability and ambiguity associated with real situations. To the authors' best knowledge, this is the first time that the SALBP-2 combined with GA and fuzziness is applied in the manufacturing process of a robotic structure.

The rest of the paper is organized as follows: Section 2 summarizes the arithmetics of fuzzy numbers, gives the background of the fuzzy assembly line balancing of type 2, and presents the practical problem of manufacturing the robot components. Section 3 presents the proposed optimization approach applied for the fuzzy ALBP of the robotic arm. Computational results concerning the performance of the GA are presented in Section 4, while conclusions and directions for future work are pointed out and discussed in Section 5.

2. The Fuzzy Assembly Line Balancing Problem

2.1. Arithmetic and Ranking Fuzzy Number. Compared to traditional binary sets (where variables may take on true or false values), fuzzy logic variables may have a truth value that ranges in degree between 0 and 1. Fuzzy logic has been extended to handle the concept of partial truth, where the truth value may range between completely true and completely false.

A fuzzy set is a class of objects with a continuum of grades of membership. Such a set is characterized by a membership (characteristic) function which assigns to each object a grade of membership ranging between zero and one. The membership function which represents a fuzzy set $\widetilde{A}$ is usually denoted by μ_A. For an element x, the value $\mu_A(A)$ is called the membership degree of x in the fuzzy set $\widetilde{A}$. The membership degree $\mu_A(A)$ quantifies the grade of membership of the element x to the fuzzy set $\widetilde{A}$. The value 0 means that x is not a member of the fuzzy set; the value 1 means that x is fully a member of the fuzzy set. The values between 0 and 1 characterize fuzzy members, which belong to the fuzzy set only partially.

Due to the nature of processing times, the most commonly used fuzzy sets in depicting these values are triangular fuzzy numbers (TFNs) [47] that establish extreme points to represent the most likely and least likely values for the individual variables. In this work, the time variables will be represented as TFNs. TFN $\widetilde{A}$ is denoted as a triplet of points, i.e., $\widetilde{A} = (\alpha_1, \alpha_2, \alpha_3)$, where $\alpha_1 < \alpha_2 < \alpha_3$. In the adapted fuzzy heuristics, the tasks' fuzzy processing times are accumulated using the fuzzy addition operator. In particular, by assuming

a second TFN $\widetilde{B} = (\beta_1, \beta_2, \beta_3)$, where $\beta_1 < \beta_2 < \beta_3$, then the following arithmetics between $\widetilde{A}$ and $\widetilde{B}$ may be performed [48]:

$$\begin{aligned}
\widetilde{A} + \widetilde{B} &= (\alpha_1 + \beta_1, \alpha_2 + \beta_2, \alpha_3 + \beta_3) \\
\widetilde{A} - \widetilde{B} &= (\alpha_1 - \beta_3, \alpha_2 - \beta_2, \alpha_3 - \beta_1) \\
\widetilde{A} \times \widetilde{B} &= (\alpha_1 \cdot \beta_1, \alpha_2 \cdot \beta_2, \alpha_3 \cdot \beta_3) \\
\frac{\widetilde{A}}{\widetilde{B}} &= \left(\frac{\alpha_1}{\beta_3}, \frac{\alpha_2}{\beta_2}, \frac{\alpha_3}{\beta_1}\right)
\end{aligned} \tag{1}$$

To compare the fuzzy numbers, some criteria to rank the fuzzy sets should be presented. The ranking method in this work involves three ordered criteria [49] which are explained in the following.

The greatest associate ordinary number F_1 is used as a first criterion for ranking:

$$F_1\left(\widetilde{A}\right) = \frac{\alpha_1 + 2\alpha_2 + \alpha_3}{4} \tag{2}$$

If F_1 does not rank the fuzzy numbers, then those which have the best maximum presumption F_2 (the mode) will be chosen:

$$F_2\left(\widetilde{A}\right) = \alpha_2 \tag{3}$$

If F_1 and F_2 do not rank the fuzzy numbers, then the divergence F_3 (the distance between two end-points) will be used as third criterion:

$$F_3\left(\widetilde{A}\right) = \alpha_3 - \alpha_1 \tag{4}$$

Consider a set Q composed of the TFNs $\widetilde{A}_i$ with $i = 1, 2, \ldots, n$. A TFN is called major and denoted as $\widetilde{A}^*$ when dominates all the others in some criterion, in Q, that is, $\widetilde{A}^* = \max Q$ (the operator max is the discrete maximum). The decision maker chooses some criteria and determines its order of dominance. If the first criterion can not determine the major TFN, then the second criterion follows and so on. On the contrary, a TFN is called minor when dominated by all others in Q and this operation is represented as min.

2.2. Fundamentals of Fuzzy Assembly Line Balancing of Type 2. The fuzzy SALBP can be stated as follows: m workstations are arranged along an assembly line. Manufacturing a single product on the line requires the partitioning of the total work into a set $V = \{1, \ldots, n\}$ of n elementary operations called tasks. Each task j is performed on exactly one station and requires a fuzzy processing time $\widetilde{t}_j$. Let $S_z (z = 1, \ldots, m)$ be the station load of station z (i.e., the set of tasks assigned to z), with a cumulated fuzzy task time $\widetilde{tS_z} = \sum_{j \in S_z} \widetilde{t}_j$ $(z = 1, \ldots, m)$. The tasks are partially ordered by precedence relations defining a directed acyclic graph (DAG) $G = (V, E)$ with V being the set of the nodes denoting the tasks in V and E being the set of the edges representing the precedence constraints among these tasks. The assembly line is associated with a fuzzy cycle time $\widetilde{c}$ denoting the maximum processing time available for each station. The aim of SALBP-2 is the minimization of the fuzzy cycle time $\widetilde{c}$ (i.e., the maximization of the production rate) given the number of workstations m.

3. The Proposed Optimization Approach

GAs [45, 46] are optimization techniques which simulate the natural selection mechanism observed in the biological evolution process. A GA has global and parallel search capability which is suitable for solving demanding problems of high nonlinearity. A GA, in contrast with common search techniques, starts with an initial set of random solutions called population (individuals) which satisfy the constraints of the problem. Chromosome is called each individual in the population representing a solution to the problem at hand. Each chromosome comprises a number of structures known as genes. The chromosomes are then regressed via iterations which are commonly known as generations. During each iterative procedure, i.e., generation, the chromosomes are estimated by utilizing some measures of fitness. This means that, in every generation, the fitness of every individual in the population is calculated. Then the more fit individuals are selected from the current population, and each individual's genome is changed to form the population of the next generation. This new population is then used in the next iteration of the algorithm. The next generation is created according to the fitness values by forming new chromosomes. These chromosomes arise by merging two chromosomes from the current generation by using a crossover operator or by changing a chromosome via utilizing a mutation operator. The complete set of chromosomes is called genotype, and the resulting organism is called phenotype. Generally, the GA after numerous generations converges to the best chromosome, which represents the ideal solution to the problem. A typical GA includes a genetic representation of the solution domain and an efficient fitness function to evaluate the solution domain.

The proposed GA according to the requirements of the present study has the following basic components: (a) the representation mechanism which is a method to transform phenotypes into genotypes, (b) the decoding mechanism which is a method to map phenotypes to solutions, (c) the evaluation mechanism which is a method to compute the cost-function for each genotype, (d) the mechanism which generates the initial population of the genotypes, (e) the mechanism which generates new genotypes by applying operators on the entire population, (f) the control parameters, and (g) the termination condition. The block diagram of the present GA is illustrated in Figure 1 while its main steps are explained with more detail in the following subsections.

3.1. The Representation Mechanism. A GA can only find possible solutions to a problem when the solutions are transformed into a representation which the GA may handle. Thus, an appropriate representation mechanism is required

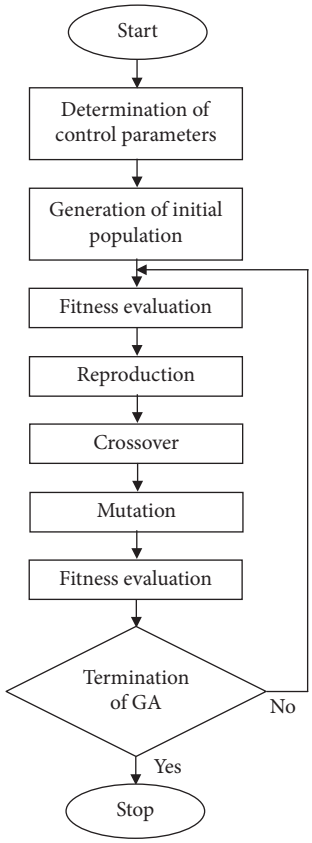

Figure 1: The block diagram of the proposed GA.

to transform possible solutions within the context of the original problem, called phenotypes, into individuals within the context of the GA, called genotypes. This encoding may be realized via a string of binary code, real-valued numbers, integers, or a tree structure. Nevertheless, for mechanical engineering problems the most efficient representation is a string of real-valued numbers. Thus, in the present study a real-valued GA has been adopted in which genotypes are represented by floating-point vectors. Since ALBP solutions are represented by strings of integers [1], the utilized representation mechanism should allow mapping from the genotypic state-level (the real-valued vectors) to the phenotypic level (the actual ALB solutions). This is realized by a simplified, however, efficient topological ordering scheme which is based on the relative priorities imposed by the components of a genotype. Assuming the n task of the ALBP with precedence relations given by a DAG $G = (V, E)$, the utilized representation mechanism aims to generate a topological sort of G from a specific n-dimensional floating-point vector ψ (genotype). Each vector's component ψ_i ($i = 1, 2, \ldots, n$) represents the relative priority of task i ($i \in V$). The topological sort is therefore a ranking of all the tasks in line with their priorities and precedence constraints. During the procedure, the tasks with no predecessors are identified and put in set V'. Then, the task in V' which has the highest gene's value in ψ is removed from V' and placed in the next available position of a new string (initially empty) called partial schedule (PS). The process is continued until the completion of PS is achieved.

3.2. The Decoding Mechanism. After encoding a specific genotype into a phenotype, the decoding mechanism is required to assign the tasks in the generated task-sequence into the stations. The proposed technique [49] seems to be more effective in contrast with other traditional schemes [1] and therefore preferred in the proposed GA. The utilized scheme consists of the following steps:

Step 1. Set $\widetilde{c}$ equal to the theoretical minimum fuzzy cycle time; i.e., $\widetilde{c}_{\text{th}} = \widetilde{t}_{\text{sum}}/m$.

Step 2. Assign as many tasks as possible into the first $m - 1$ workstations. Assign all the remaining tasks to the last workstation m.

Step 3. Calculate the fuzzy work load $\widetilde{\text{W}}_z$ for each workstation z ($z = 1, \ldots, m$) and the potential fuzzy workload $\widetilde{\text{PW}}_z$ ($z = 1, \ldots, m - 1$), where $\widetilde{\text{PW}}_z$ is the sum of $\widetilde{t}\text{S}_z$ and the processing time of the first task assigned to $(z + 1)$-th station ($z = 1, \ldots, m - 1$).

Step 4. Set $\widetilde{c}_{\text{W}} = \max\{\widetilde{\text{W}}_1, \widetilde{\text{W}}_2, \ldots, \widetilde{\text{W}}_{\text{m}}\}$ and $\widetilde{c} = \max\{\widetilde{\text{PW}}_1, \widetilde{\text{PW}}_2, \ldots, \widetilde{\text{PW}}_{\text{m}-1}\}$.

Step 5. If $\widetilde{c}_{\text{W}} > \widetilde{c}$, then go to Step 2; else return $\widetilde{c}_{\text{W}}$.

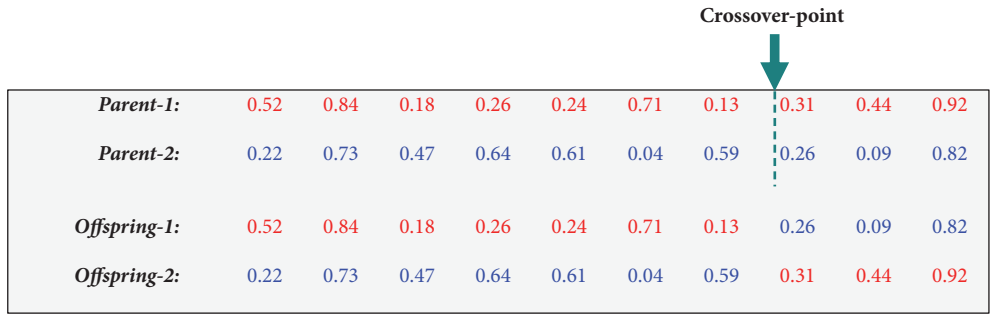

Figure 2: Example of one-point crossover: choose at random a cut-point and then exchange the genetic material between the parents.

Figure 3: Example of mutation operator: choose at random a gene and then replace it with another floating number randomly selected within U(0,1).

3.3. The Evaluation Mechanism. The evaluation mechanism corresponds to the computation of the objective function $\tilde{c}$ for each phenotype of the current population. The objective of SALBP-2 is to minimize the fuzzy cycle time $\tilde{c}$. The objective function has to be transformed to the fitness function f, which is evaluated for all the chromosomes of the population. The value of the fitness function for one chromosome expresses its ability to survive and be reproduced in the next generation. The fitness function is the inverse of the objective function:

$$f = \frac{1}{\tilde{c}} \tag{5}$$

Equation (5) aims to maximize the fitness function and consequently forcing $\tilde{c}$ to a minimum value. For the evaluation of the solution candidates, (2) is applied to compare the fuzzy numbers.

3.4. The Initial Population. In order to initialize the process, the solutions in the first generation have to be defined. Commonly, this is done randomly since the main desire is to spread the first individuals over the complete search space before converging to more promising regions. Nevertheless, when the area of the optimum solution may be estimated beforehand, then the algorithm could be initiated around this area to speed up the convergence.

3.5. The Genetic Operators. A genetic operator is used in GAs to maintain the genetic diversity. Genetic operators such as crossover, mutation, and selection are used in GAs to assure genetic variation for the process of evolution. Roulette wheel selection [50] is the best known selection operator and thus adopted here. The concept is to evaluate selection probability for each chromosome proportionally to the fitness value. Then a model roulette wheel is made which displays these probabilities. The selection process is based on spinning the specific wheel the number of times equal to the population size. Crossover is an operator which aims to produce new individuals by joining parts of several individuals of the previous generation. The selection of individuals is made randomly according to a predefined probability, i.e., one-point crossover rate [50]. Mutation is required to insert new genetic material into the population by slightly modifying the genotype representation. In this way, the early convergence to local minima is avoided. The modification is applied stochastically to discover potential better solutions based on the current best solutions. The mutation operator is applied by changing a random gene (i.e., a floating number) according to a small-predefined probability (mutation rate) [50]. Figures 2 and 3 demonstrate two application examples of these operators on random selected chromosomes. For the sake of simplicity, the presented chromosomes have a length of 10, although in our problem the length of the chromosomes is 57.

3.6. Control Parameters. The most important control parameters are the population size, the crossover ratio, the mutation rate, and the elitism.

Population size is one of the most important topics in evolutionary computation since small population size may lead the algorithm to poor solutions while a large population size may require a much more computational time to find a solution. The population size selection should be made according to the nature and the complexity of the current problem. In the present work, a variety of tests have been made considering the influence of the population size on the convergence of the algorithm. The algorithm has been run several times starting with different population sizes and the

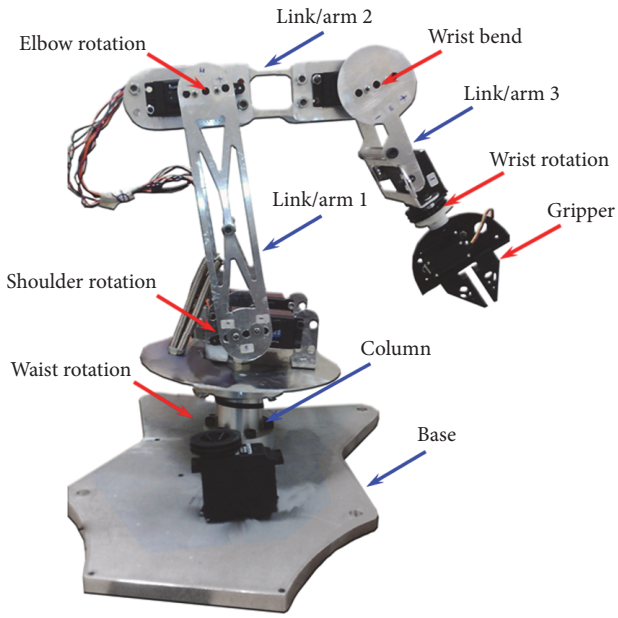

Figure 4: Robotic arm description.

convergence has been evaluated. Finally, the population size has been set to 100 for the SALBP-2 under investigation which involves 4 workstations and 57 tasks.

The crossover rate controls the frequency with which the crossover is applied. The higher crossover rate is, the more quickly new individuals are added to the population. Several convergence tests have proved the effectiveness of a crossover rate equal to 0.8 for the purpose of the present research.

The mutation rate defines the probability according to which the position of each individual in the intermediate population undergoes a random change. A GA with a too high mutation rate will inevitably become a random search. Thus, the mutation rate is typically chosen to be less than 0.4. The value of 0.1 has been chosen here after a considerable number of trials.

When creating new population via crossover and mutation, there is a chance that the best chromosome will be lost. Elitism [50] is a method according to which the best chromosome is copied to the new population. A comparison involving the best chromosome between current and previous generation is required. Elitism increases the performance of the GA since it prevents the loss of the best-found solution.

3.7. Termination Conditions. The termination condition should be theoretically satisfied and thus end the algorithm when the optimum solution has been found. However, for many optimization problems, the ideal solution is unknown and therefore there is always an uncertainty whether better solutions exist. In addition stochastic procedures may require a significant computational cost and take a long time to converge to the optimum solution. Commonly used termination conditions are therefore based on the maximum allowed number of iterations (generations) which however present limitations since it is difficult to determine beforehand the number of generations needed to find near-optimum solutions. Thus, in the proposed scheme, the termination of the GA is chosen to occur when the repetitions of the same solution have reached a predefined number. Consequently, the algorithm terminates when a specific chromosome has appeared for a sufficiently large number of times.

4. Description of Assembly under Investigation

The robotic arm, which is manufactured for the requirements of the present study, is a 6-degree-of-freedom manipulator. It is mainly constructed from a 3 mm aluminum sheet, has a length of about 600 mm, and has the ability to pick up a small object of 0.3 kg. In order to keep the design as simple as possible, the pivoting parts include six standard step motors. Additionally, the robotic arm under investigation incorporates a controller which governs the arm movements and operations. A simple, scalable control system has been adopted to allow control in a Cartesian coordinate system, which offers expandability for future research. The idea behind the specific design is to investigate the potential of developing a simple robotic arm capable of moving small objects. The skeleton of the robotic arm is constructed by using exclusively aluminum bars and sheets, whereas basic conventional machines are used during the manufacturing process.

Figure 4 depicts the manufactured robotic arm consisting of a waist, a shoulder, an elbow, a wrist, and a gripper which are connected to each other via metal links. These links are appropriately designed and machined so that they may offer stability, smooth motion, and, if required, effective support for specific motors.

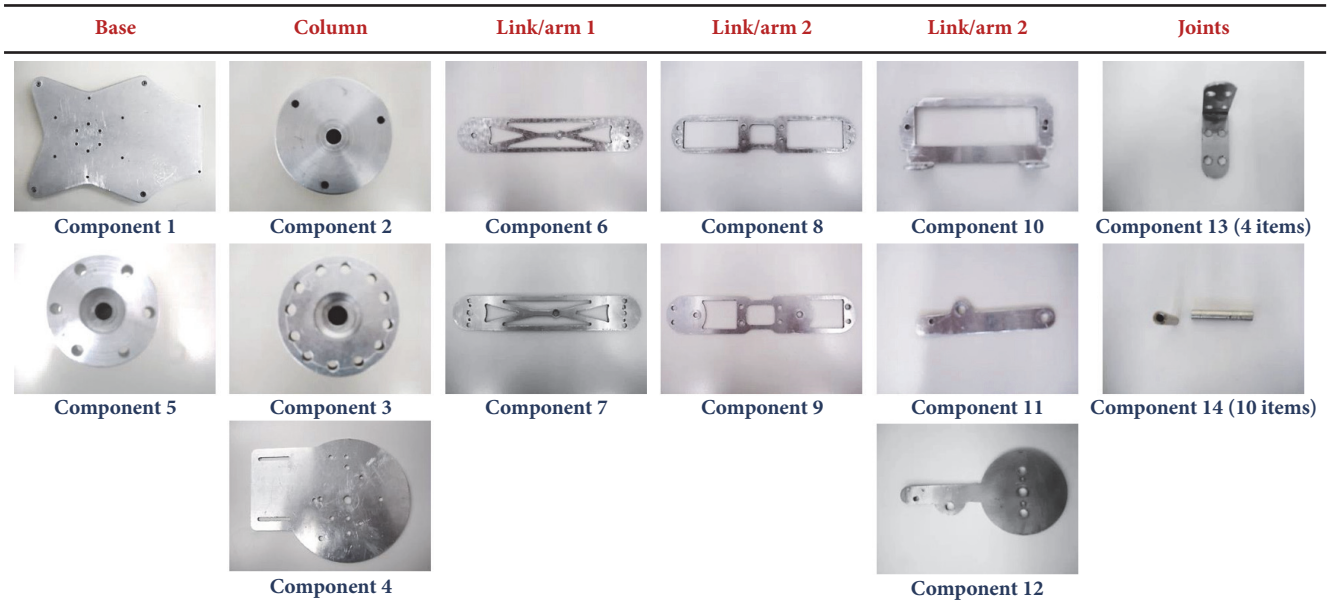

Figure 5: Numbered components of the robotic aluminum frame.

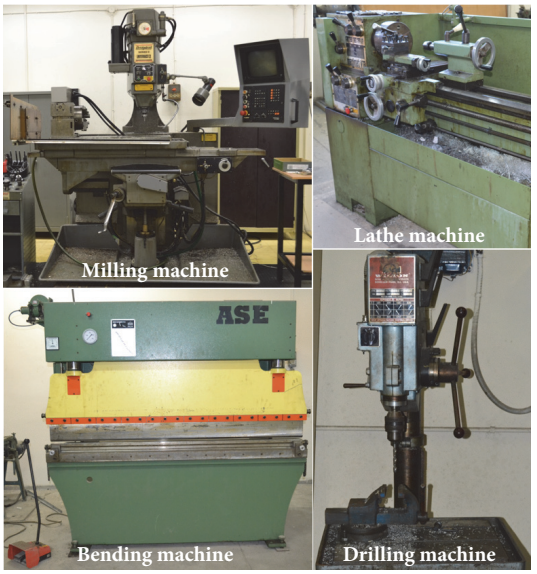

Figure 6: The four types of machines of the assembly line.

The mechanical design of the robotic arm includes a heavy bottom base of 20 mm thick aluminum. The aluminum base is designed in such way that it provides enough space for the more powerful motor which is responsible for the waist rotation. A column joined with a lighter upper base is manufactured to offer smooth shoulder rotation and appropriate motor support. The link/arm 1 connects the shoulder and elbow while the link/arm 2 connects the elbow with the wrist. The second link is formed in such a way to bracket both the elbow rotation and wrist bend motors. The wrist rotation motor is attached on link/arm 3 which connects the wrist bend with the wrist rotation mechanisms. The gripper is appropriately attached on the outer edge of this third link. All these robotic parts are coupled with appropriate cylindrical joints. The metal frame of the above described robotic arm is composed of several aluminum components which are illustrated and numbered in Figure 5.

The metal components of the robotic frame are machined using conventional processes in which appropriate pieces of raw material are progressively cut and/or formed into the desired final shape and size. The whole machining process takes place in a simple assembly line of four workstations. The assembly line under consideration includes four types of machining operations, i.e., milling, drilling, lathing, and bending. Conventional machines such as those depicted in Figure 6 are utilized for the purpose of the present study.

Table 1: Fuzzy execution times for each robot component.

No. of tasks	No. of components	Type of task	Total fuzzy time (s)
1	1	milling	(3096, 3105, 3111)
2	1	drilling	(73, 74, 76)
3	2	milling	(788, 792, 795)
4	2	drilling	(51, 53, 55)
5	3	milling	(822, 826, 831)
6	3	drilling	(40, 41, 42)
7	4	milling	(858, 863, 868)
8	4	drilling	(66, 67, 69)
9	5	milling	(518, 523, 527)
10	5	drilling	(44, 45, 46)
11	6	milling	(842, 849, 854)
12	6	drilling	(42, 43, 45)
13	7	milling	(1043, 1052, 1058)
14	7	drilling	(17, 18, 19)
15	8	milling	(780, 785, 789)
16	8	drilling	(57, 59, 61)
17	9	milling	(803, 806, 810)
18	9	drilling	(54, 55, 57)
19	10	milling	(540, 544, 549)
20	10	drilling	(24, 25, 26)
21	10	bending	(40, 41, 42)
22	11	milling	(390, 396, 401)
23	11	drilling	(25, 26, 27)
24	12	milling	(381, 385, 390)
25	12	drilling	(40, 41, 42)
26	13 (1 out of 4 items)	milling	(947, 951, 956)
27	13	drilling	(248, 252, 255)
28	13	bending	(39, 41, 42)
29-37	13 (3 items)		
38	14 (1 out of 10 items)	lathing	(1560, 1569, 1576)
39	14	drilling	(63, 65, 66)
40-57	14 (9 items)		

5. Computational Study

According to Figure 5, in order to construct the metal structure of the robotic arm, 14 different types of components should be manufactured using the aforementioned machines that do not work in parallel. To be more precise, a total of number of 26 parts should be machined since the robotic arm design requires 4 and 10 items of components 13 and 14, respectively. All experiments have taken place in the laboratory of Computer Numerical Control Machines (CNC Lab) in the Mechanical Engineering Department of the Technological Educational Institute (TEI) of Western Greece, using milling, lathe, bending, and drilling machines. A number of 10 students (representing 10 "workers" with different capabilities) have participated actively in the experiments. Table 1 summarizes the fuzzy execution times for the 57 total tasks associated with the robot components. The computational study is focused on finding the optimum sequence of tasks assigned to stations which may lead to the minimum total fuzzy time for executing all tasks.

Considering fuzziness for the processing times, fuzzy data are represented by triangular fuzzy numbers. TFN is one of the most commonly used in the literature shapes of fuzzy numbers representation [47] composed of three estimates (the lowest expected, the most likely, and the highest expected) of the unknown individual value. The reason of using triangular fuzzy shapes is because of their computational simplicity in comparison with other fuzzy shapes, considering the calculations in (1). TFNs differ from statistical distributions in the fact that they do not require historical data to establish their values. This is a major advantage of using TFNs as opposed to statistics.

In practice, this was achieved by assigning the 57 total tasks to 10 "workers" and writing down the resulting times.

For all tasks, the most likely values for the TFNs (i.e., the fuzzy element with the membership value of 1) are considered to be the middle written times at the last column of Table 1. These most likely values for each task were set equal to the average of the corresponding ten measured times by the ten "workers". The extreme TFN values in Table 1 were taken equal to the minimum and maximum times of the 10 execution times provided by the "workers", respectively. In a fuzzy set $\widetilde{A} = (\alpha_1, \alpha_2, \alpha_3)$, the minimum time represents the optimistic value α_1, the maximum time represents the pessimistic value α_3, and the middle time represents the most plausible value α_2. Although, in practice, the actual time is more possible to be longer and not shorter than α_2, we decided to set the most likely value in the middle of the two extreme values in order to keep "equal distances" between the optimistic and pessimistic value. Generally speaking, a shifted triangular fuzzy number for modeling the uncertainty would be more realistic; however, in our problem, the variations in times were rather small giving us the opportunity for the above admittance.

The precedence constraints are summarized in Table 2. For each row, the task in the first column precedes the task in the second column and the task in the second column precedes the task in the third column.

The minimum fuzzy cycle time is yielded considering the total fuzzy processing time for each of the 57 tasks (see Table 1) as well as the precedence relations given above. The resulting minimum fuzzy cycle time after running the proposed GA is (8150, 8211, 8259) s. Concerning the station load for each workstation, it is provided by the GA best solution, considering the aforementioned constraints, and involves the task sequence assigned to each workstation. In particular, Workstation 1 starts with task 53 and after finishing, it continues with task 24 and so on until it finishes with task 3. Similarly, Workstation 2 starts with task 22, then accomplishes task 38, and finishes with task 10. The robotic arm is manufactured when all tasks assigned to each workstation have been accomplished. For the problem addressed here, the resulting task sequence and the fuzzy station time for each workstation are presented in Table 3. The simulation test was implemented in Matlab and run on a Pentium IV 2.13 GHz core2 PC and the CPU time was 993 sec. Given the nature and the complexity of the present problem, a rather insignificant computational effort was required. However, it has to be mentioned that the selection of a larger population size would significantly increase the CPU time. Auspiciously, various numerical tests on the population size showed that the selection of a population size larger than 100 had a negligible effect on the convergence of the method.

Figure 7 depicts the triangular membership function for the fuzzy cycle time. It is clear that the least likely values are 8150 and 8259 while it is found that the most likely value is 8211.

To compare the fuzzy numbers, the greatest associate ordinary number (see (2)) is used. Thus, the value for the cycle time presented in the following has been calculated through (2), and Figures 8, 9, and 10 illustrate the evolution of the GA through the generations for the best, average, and worst individuals, respectively. It is clear from Figure 8 that the best cycle time (equal to 8207.75 s corresponding to (8150, 8211, 8259) s) is achieved in the 1459th generation.

Table 2: The precedence constraints.

No. of tasks		
1	2	
3	4	
5	6	
7	8	
9	10	
11	12	
13	14	
15	16	
17	18	
19	20	21
22	23	
24	25	
26	27	28
29	30	31
32	33	34
35	36	37
38	39	
40	41	
42	43	
44	45	
46	47	
48	49	
50	51	
52	53	
54	55	
56	57	

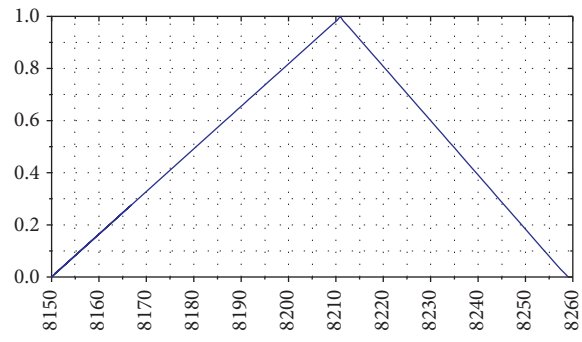

Figure 7: The fuzzy cycle time $\tilde{c}$.

6. Conclusions

Due to the fact that the nature of manufacturing systems is accompanied with uncertainty, the main idea for this paper is to treat the problem considering fuzziness in the operation times. Thus, the main focus of this work lies on the

Table 3: Results provided by the proposed GA.

Workstation z	**Task sequence** (S_z)	**Fuzzy station time** ($\widetilde{tS}_z$) (s)
1	52-53-24-40-35-17-5-6-29-30-3	(8159, 8207, 8253)
2	22-38-39-31-4-25-15-16-11-19-20-21-23-12-1-9-10	(8151, 8210, 8259)
3	18-42-43-48-49-56-57-32-33-34-50-51-2-36-37	(8140, 8202, 8251)
4	26-27-54-55-44-45-28-13-14-46-47-7-8-41	(8150, 8211, 8259)
Fuzzy cycle $\widetilde{c}$ (s)	(8150, 8211, 8259)	

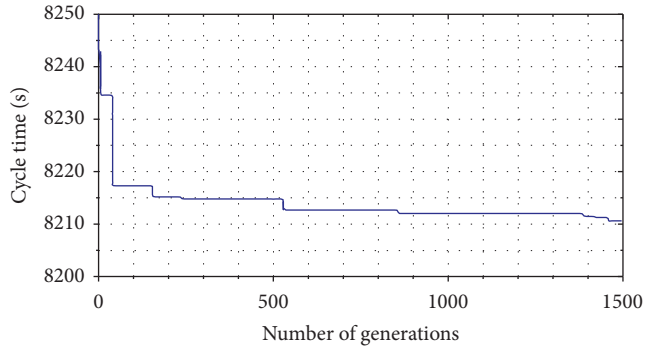

Figure 8: Best cycle time versus generations.

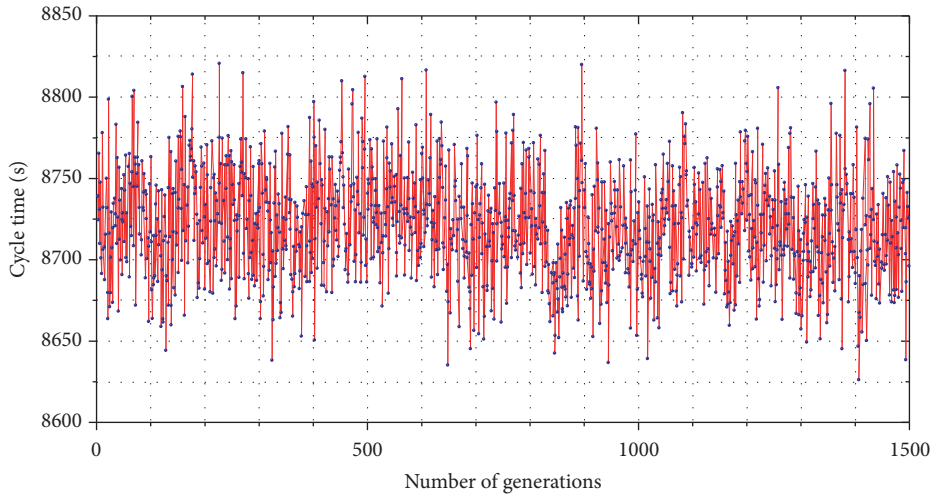

Figure 9: Average cycle time versus generations.

construction process considering variability and ambiguity associated with real situations. In this context, this paper studies the solution of the fuzzy ALBP problem type 2 for the real problem of constructing a robotic arm. The robot components are formed using a number of machine tools, which are handled by a specific number of "workers". The metal parts of the robotic arm are manufactured in four machining workstations. The construction process is enhanced in terms of time reduction using a GA that takes into account fuzziness in times and is subject to the constraints imposed by the precedence relations.

The proposed approach was tested in a real manufacturing environment, where real data was yielded for the simulation tests. The experimental results demonstrated that the approach is effective and efficient at determining the optimum fuzzy cycle time for the accomplishment of robotic arm construction without violating the precedence constraints. Considering future research, a U-shaped assembly line layout could be applied, where stations work at two segments of the line facing each other simultaneously.

Data Availability

All the data (numerical, experimental, figures, diagrams, tables, etc.) used to support the findings of our study are included within the article. Thus, data sharing regarding the aforementioned paper is totally allowed and any reader can access the data supporting the conclusions of the study.

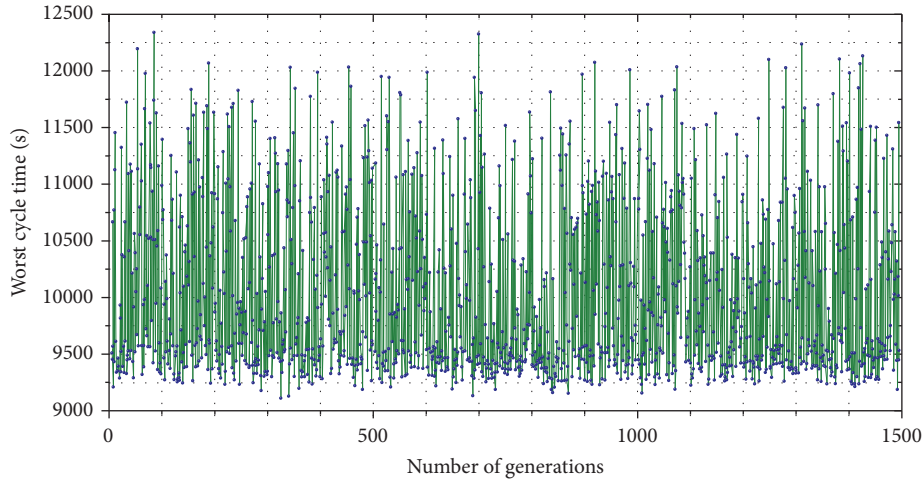

Figure 10: Worst cycle time versus generations.

Conflicts of Interest

The authors declare that they have no conflicts of interest.

Acknowledgments

This research has been cofinanced by the European Union (European Social Fund, ESF) and Greek national funds through the Operational Program "Education and Lifelong Learning" of the National Strategic Reference Framework (NSRF), Research Funding Program: ARCHIMEDES III. Investing in Knowledge Society through the European Social Fund.

References

[1] A. Scholl and C. Becker, "State-of-the-art exact and heuristic solution procedures for simple assembly line balancing," *European Journal of Operational Research*, vol. 168, no. 3, pp. 666–693, 2006.

[2] J. F. Gonçalves and J. R. De Almeida, "A hybrid genetic algorithm for assembly line balancing," *Journal of Heuristics*, vol. 8, no. 6, pp. 629–642, 2002.

[3] S. D. Lapierre, A. Ruiz, and P. Soriano, "Balancing assembly lines with tabu search," *European Journal of Operational Research*, vol. 168, no. 3, pp. 826–837, 2006.

[4] O. Kilincci and G. M. Bayhan, "A Petri net approach for simple assembly line balancing problems," *The International Journal of Advanced Manufacturing Technology*, vol. 30, no. 11-12, pp. 1165–1173, 2006.

[5] Z.-Q. Zhang, W.-M. Cheng, L.-S. Tang, and B. Zhong, "Ant algorithm with summation rules for assembly line balancing problem," in *Proceedings of the International Conference on Management Science and Engineering, (ICMSE'07)*, pp. 369–374, China, 2007.

[6] A. C. Nearchou, "Multi-objective balancing of assembly lines by population heuristics," *International Journal of Production Research*, vol. 46, no. 8, pp. 2275–2297, 2008.

[7] O. Kilincci and G. M. Bayhan, "A P-invariant-based algorithm for simple assembly line balancing problem of type-1," *The International Journal of Advanced Manufacturing Technology*, vol. 37, no. 3-4, pp. 400–409, 2008.

[8] D.-H. Yeh and H.-H. Kao, "A new bidirectional heuristic for the assembly line balancing problem," *Computers & Industrial Engineering*, vol. 57, no. 4, pp. 1155–1160, 2009.

[9] M. N. I. Sulaiman, Y. H. Choo, and K. E. Chong, "Ant colony optimization with look forward ant in solving assembly line balancing problem," in *Proceedings of Conference on Data Mining and Optimization (3rd DMO 2011)*, pp. 115–121, 2011.

[10] J. Dou, J. Li, and Q. Lv, "A hybrid particle swarm algorithm for assembly line balancing problem of type 1," in *Proceedings of the IEEE International Conference on Mechatronics and Automation, (ICMA 2011)*, pp. 1664–1669, China, 2011.

[11] D. Jianping, S. Chun, and L. Jun, "A Discrete Particle Swarm Optimization Algorithm for Assembly Line Balancing Problem of Type 1," in *Proceedings of the International Conference on Measuring Technology and Mechatronics Automation (ICMTMA)*, vol. 1, pp. 44–47, Shanghai, China, 2011.

[12] M. Fathi, A. Jahan, M. K. A. Ariffin, and N. Ismail, "A new heuristic method based on CPM in SALBP," *Journal of Industrial Engineering International*, vol. 7, no. 13, pp. 1–11, 2011.

[13] M. K. A. Ariffin, M. Fathi, and N. Ismail, "A new heuristic method to solve straight assembly line balancing problem," *Pertanika Journal of Science & Technology*, vol. 20, no. 2, pp. 355–369, 2012.

[14] J. Dou, J. Li, and C. Su, "A novel feasible task sequence-oriented discrete particle swarm algorithm for simple assembly line balancing problem of type 1," *The International Journal of Advanced Manufacturing Technology*, vol. 69, no. 9-12, pp. 2445–2457, 2013.

[15] Y. Atasagun and Y. Kara, "Bacterial Foraging Optimization Algorithm for assembly line balancing," *Neural Computing and Applications*, vol. 25, no. 1, pp. 237–250, 2014.

[16] R. Zhang, D. Chen, Y. Wang, Z. Yang, and X. Wang, "Study on line balancing problem based on improved genetic algorithms," in *Proceedings of the International Conference on Wireless Communications, Networking and Mobile Computing (WiCOM 2007*, pp. 2033–2036, 2007.

[17] L. Gu, S. Hennequin, A. Sava, and X. Xie, "Assembly Line Balancing Problems Solved by Estimation of Distribution," in *Proceedings of the IEEE International Conference on Automation*

Science and Engineering (IEEE CASE 2007), pp. 123–127, Scottsdale, AZ, USA, 2007.

[18] O. Kilincci, "A Petri net-based heuristic for simple assembly line balancing problem of type 2," *The International Journal of Advanced Manufacturing Technology*, vol. 46, no. 1-4, pp. 329–338, 2010.

[19] C. Blum, "Iterative beam search for simple assembly line balancing with a fixed number of work stations," *SORT. Statistics and Operations Research Transactions*, vol. 35, no. 2, pp. 145–164, 2011.

[20] Q. Tang, S. Lu, M. Li, and C. A. Floudas, "Novel cellular automata algorithm for assembly line balancing problem of type-2," in *Proceedings of the 6th International Conference on Pervasive Computing and Applications, (ICPCA 2011)*, pp. 422–428, South Africa, 2011.

[21] S. Avikal, P. K. Mishra, and R. Jain, "A model for assembly line balancing problems," in *Proceedings of the Students Conference on Engineering and Systems (SCES 2012)*, pp. 1–4, Allahabad, Uttar Pradesh, India, 2012.

[22] Q. Zheng, M. Li, Y. Li, and Q. Tang, "Station ant colony optimization for the type 2 assembly line balancing problem," *The International Journal of Advanced Manufacturing Technology*, vol. 66, no. 9-12, pp. 1859–1870, 2013.

[23] O. Battaïa and A. Dolgui, "A taxonomy of line balancing problems and their solutionapproaches," *International Journal of Production Economics*, vol. 142, no. 2, pp. 259–277, 2013.

[24] P. Sivasankaran and P. Shahabudeen, "Literature review of assembly line balancing problems," *The International Journal of Advanced Manufacturing Technology*, vol. 73, no. 9–12, pp. 1665–1694, 2014.

[25] A. Caggiano, "Fuzzy Logic," in *CIRP Encyclopedia of Production*, pp. 562–568, Springer, 2014.

[26] F. Y. Kalender, M. M. Yilmaz, and O. Türkbey, "A fuzzy approach to assembly line balancing problem," *Journal of the Faculty of Engineering and Architecture of Gazi University*, vol. 23, no. 1, pp. 129–138, 2008.

[27] U. Özcan and B. Toklu, "Multiple-criteria decision-making in two-sided assembly line balancing: a goal programming and a fuzzy goal programming models," *Computers & Operations Research*, vol. 36, no. 6, pp. 1955–1965, 2009.

[28] P. Tapkan, L. Ozbakir, and A. Baykasoglu, "Bees Algorithm for constrained fuzzy multi-objective two-sided assembly line balancing problem," *Optimization Letters*, vol. 6, no. 6, pp. 1039–1049, 2012.

[29] Ö. Mutlu and E. Özgörmüş, "A fuzzy assembly line balancing problem with physical workload constraints," *International Journal of Production Research*, vol. 50, no. 18, pp. 5281–5291, 2012.

[30] G. La Scalia, R. Micale, G. Aiello, and M. Enea, "Solving type-2 assembly line balancing problem with fuzzy binary linear programming," *Journal of Intelligent & Fuzzy Systems. Applications in Engineering and Technology*, vol. 25, no. 3, pp. 517–524, 2013.

[31] Y. Tsujimura, M. Gen, and E. Kubota, "Solving fuzzy assembly-line balancing problem with genetic algorithms," *Computers & Industrial Engineering*, vol. 29, no. 1-4, pp. 543–547, 1995.

[32] M. Gen, Y. Tsujimura, and Y. Li, "Fuzzy assembly line balancing using genetic algorithms," *Computers & Industrial Engineering*, vol. 31, no. 3-4, pp. 631–634, 1996.

[33] F. Khoshalhan and S. H. Zegordi, "Solving type one and type two fuzzy assembly line balancing problems using genetic algorithms," *Amirkabir (Journal of Science and Technology)*, vol. 14, no. 55 D, pp. 910–923, 2003.

[34] P. T. Zacharia and A. C. Nearchou, "Multi-objective fuzzy assembly line balancing using genetic algorithms," *Journal of Intelligent Manufacturing*, vol. 23, no. 3, pp. 615–627, 2012.

[35] H. Rajabalipour Cheshmehgaz, H. Haron, F. Kazemipour, and M. I. Desa, "Accumulated risk of body postures in assembly line balancing problem and modeling through a multi-criteria fuzzy-genetic algorithm," *Computers & Industrial Engineering*, vol. 63, no. 2, pp. 503–512, 2012.

[36] M. H. Alavidoost, M. Tarimoradi, and M. H. F. Zarandi, "Fuzzy adaptive genetic algorithm for multi-objective assembly line balancing problems," *Applied Soft Computing*, vol. 34, pp. 655–677, 2015.

[37] S. Khalili, H. Mohammadzade, and M. S. Fallahnezhad, "A new approach based on queuing theory for solving the assembly line balancing problem using fuzzy prioritization techniques," *Scientia Iranica*, vol. 23, no. 1, pp. 387–398, 2016.

[38] S. Avikal, P. K. Mishra, and R. Jain, "A fuzzy AHP and PROMETHEE method-based heuristic for disassembly line balancing problems," *International Journal of Production Research*, vol. 52, no. 5, pp. 1306–1317, 2014.

[39] P. Su, N. Wu, and Z. Yu, "A Petri net-based heuristic for mixed-model assembly line balancing problem of Type-E," *International Journal of Production Research*, vol. 52, no. 5, pp. 1542–1556, 2014.

[40] J. Pereira, "Empirical evaluation of lower bounding methods for the simple assembly line balancing problem," *International Journal of Production Research*, vol. 53, no. 11, pp. 3327–3340, 2015.

[41] K. Ağpak and S. Zolfaghari, "Mathematical models for parallel two-sided assembly line balancing problems and extensions," *International Journal of Production Research*, vol. 53, no. 4, pp. 1242–1254, 2015.

[42] I. Kucukkoc and D. Z. Zhang, "Balancing of parallel U-shaped assembly lines," *Computers & Operations Research*, vol. 64, pp. 233–244, 2015.

[43] A. Roshani and D. Giglio, "Simulated annealing algorithms for the multi-manned assembly line balancing problem: minimising cycle time," *International Journal of Production Research*, vol. 55, no. 10, pp. 2731–2751, 2017.

[44] L. A. Zadeh, "Fuzzy sets," *Information and Computation*, vol. 8, no. 3, pp. 338–353, 1965.

[45] J. H. Holland, *Adaption in Natural and Artificial Systems*, University of Michigan Press, Ann Arbor, MI, USA, 1975.

[46] D. E. Goldberg, *Genetic algorithms in search, optimization, and machine learning*, vol. 27, Addison-Wesley, Reading, Mass, 1989.

[47] D. J. Fonseca, C. L. Guest, M. Elam, and C. L. Karr, "A fuzzy logic approach to assembly line balancing," *Mathware & Soft Computing*, vol. 12, pp. 57–74, 2005.

[48] A. Kaufmann and M. M. Gupta, *Introduction to Fuzzy Arithmetic*, Van Nostrand Reinhold Company, 1985.

[49] Y. K. Kim, Y. J. Kim, and Y. Kim, "Genetic algorithms for assembly line balancing with various objectives," *Computers & Industrial Engineering*, vol. 30, no. 3, pp. 397–409, 1996.

[50] Z. Michalewicz, *Genetic Algorithms + Data Structures = Evolution Programs*, Springer, Heidelberg, Germany, 3rd edition, 1996.

Hindawi
Mathematical Problems in Engineering
Volume 2018, Article ID 4539054, 9 pages
https://doi.org/10.1155/2018/4539054

Research Article

Transient Thermal-Electric Simulation and Experiment of Heat Transfer in Welding Tip for Reflow Soldering Process

Jatuporn Thongsri

Computer Simulation in Engineering Research Group, College of Advanced Manufacturing Innovation, King Mongkut's Institute of Technology Ladkrabang, Bangkok, 10520, Thailand

Correspondence should be addressed to Jatuporn Thongsri; jatuporn.th@kmitl.ac.th

Received 7 October 2018; Accepted 3 December 2018; Published 20 December 2018

Guest Editor: Anders E. W. Jarfors

Welding tip is an appliance for making footprint to connect the arm and head gimbal assembly (HGA) together in reflow soldering process. The welding tip is made from 3 materials: copper alloy, stainless steel, and haynes 230. It works based on Joule heating effect. The haynes 230 head tip is the area used to create a footprint. In the past, failure in the reflow soldering process of a hard disk drive factory was found resulting in defective products; therefore, a solution to resolve this problem must be researched. This article reports a solution to the aforementioned problem by using transient thermal-electric simulation to investigate the heat transfer in the welding tip and a simple experiment to verify the simulation. By using ANSYS, the simulation results revealed the temperature of welding tip. The maximum temperature was 406°C on the head tip at t=0.7s and then it rapidly decreased. The reflow soldering process failure occurred when footprint was done after 0.7s causing the temperature to be too low for melting the solder so the arm and HGA were unable to connect to each other. We proposed simple solutions and ways to improve the efficacy of the reflow soldering process; e.g., footprints should be done at 0.7s, and the welding tip's material should be changed from haynes 230 to 556. After the factory implemented our results, the problem could truly be resolved. Not only do products have a higher quality but also miscellaneous expenses from defective products are saved.

1. Introduction

A hard disk drive (HDD) is computer data storage equipment. In 2015, over 469 million HDD units were exported worldwide with an overall value of 28,140 million USDs. Over 60% of HDDs traded in the global market are manufactured in Thailand. Therefore, Thailand may be deemed as the World's center of HDD manufacturing. The HDD consists of over 2,000 electronic parts, all of which must be manufactured in a clean room by advanced manufacturing technology. The arm and head gimbal assembly (HGA) are important parts of the HDD used for supporting read/write head's stability to record data on platter correctly. In the HDD manufacturing process, the HGA was connected to the arm using reflow soldering process by the welding automation machine (WAM). The reflow soldering process may be explained as follows: a target of connection between the arm and HGA is called the connected area, which exists both on the arm and on the HGA. The connected area of the arm will already have a small drop of specific lead. When the connected area of both the HGA and arm are aligned, the WAM's control system will press the welding tip down, leaving a footprint on the connected area at a temperature of approximately 400°C. The special type of lead will melt and connect the arm and HGA together. The reflow soldering process uses 2.5 s to complete in a cycle time. Figure 1 shows the connected area, HGA, and arm inside a completed HDD. In a conceptual design of the welding tip based on Joule heating effect, heat with high temperature will be generated at the head tip by applying suitable alternating current or voltage at tail tip. To control a cycle time and the maximum temperature generated at the head tip to make reflow soldering process precisely, the WAM has an automated system designed for supporting this purpose.

This research is collaboration with an HDD manufacturing factory. During the past, research and development of the reflow soldering process had been carried out using methods of trial and error for over a decade. This method

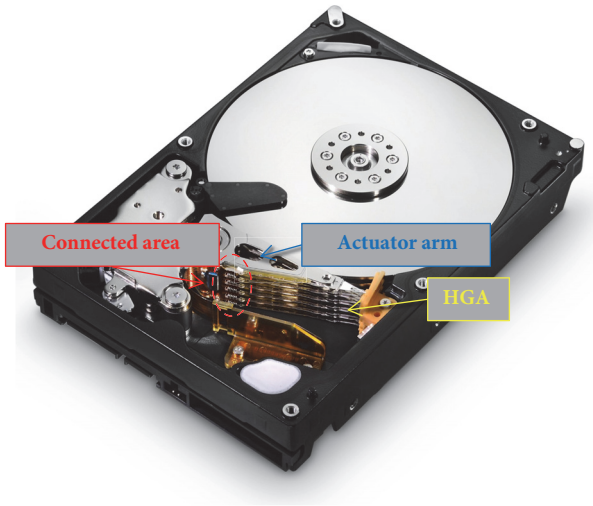

Figure 1: Connected area, HGA, and arm of HDD.

costed the factory excessive expenses in experimenting to find a suitable welding tip. Worse, the development of welding tip once used in the manufacturing process was not problem-free. Sometimes the lead did not melt, making it impossible to connect the HGA and arm resulting in defects which must be eliminated. This waste costed several million USD in loss per year. The factory anticipated that the problem rooted from unsuitable heat transfer in the welding tip; therefore, an urgent attempt to solve this problem must be undergone. The factory consulted the authors. The authors accepted and responded by using transient thermal-electric analysis, computer simulation, and suitable experiment to solve the problem. Moreover, the experiment for validation would be set up using instruments readily available in the factory so the factory's engineers might apply our methodology for own further research.

In searching articles related to thermal-electric analysis, we found that most researches focus on using thermal-electric analysis to study, design, build, or improve thermoelectric generators (TEGs) that have high efficacy in converting heat energy to electric energy, since it is environment-friendly [1–3]. Computer simulation using the ANSYS program is an important tool to pervasively develop this research branch, e.g., to design, simulate, and optimize the TEGs for higher efficacy [4–7]. The most similar research to ours is Bumrungwong's, which used thermal-electric simulation to enhance the hot bar's heat transfer efficiency for a hard disk drive factory [8]. All mentioned simulations in the research are steady-state; therefore, the results are not ample enough to use in certain researches that require the study in time-dependent conditions and thus require transient simulation [9, 10]. The difference of this research from others which is our challenge is that this research converts alternating current to heat in a short amount of time, which steady-state simulation is not enough to resolve the problem. Time greatly affects the experiment and simulation. Therefore the methodology used with steady-state conditions from others cannot be applied to our research, requiring us to seek for other suitable methodologies that simulate and investigate the heat transfer in the welding tip to solve the factory's problem.

This article reports our methodology including thermal-electric simulation and experiment setup to investigate the heat transfer in transient mode of welding tip using actual conditions collected at the factory. Also, the cause to why the lead would not melt along to the solution to the problem will also be found. Moreover, simulation results will be analyzed to find ways to improve the efficacy in the footprint process.

2. Theoretical Background

The welding tip functions by the Joule heating effect, also known as resistive heating and Ohmic heating, or the effect of transferring electricity to the conductor, generating heat. The basic equation used to study Joule heating effect is the same used to study the thermoelectric effect, as presented in (1) and (2). Equation (1) derived from heat flow equation, while (2) derived from the continuity of charge equation [6, 11]:

$$\rho C\left(\frac{\partial T}{\partial t}\right) + \nabla \bullet ([\Pi] \bullet \boldsymbol{J}) - \nabla \bullet ([\lambda] \bullet \nabla T) = \dot{q} \tag{1}$$

$$\nabla \bullet \left([\varepsilon] \bullet \nabla \frac{\partial \varphi}{\partial t}\right) + \nabla \bullet ([\sigma] \bullet [\alpha] \bullet \nabla T) + \nabla \bullet ([\sigma] \bullet \nabla \varphi) = 0. \tag{2}$$

Equations (1)-(2) are used as the fundamental information for selecting suitable materials to be invented and assembled to welding tip. Materials used to make the welding tip should be alloy with low resistivity and low specific heat but high thermal conduction. Materials found to be suitable for making the welding tip are copper alloy and haynes 230. A model of the welding tip will be explained in Section 4.1.

The finite element method for thermal-electric simulation in ANSYS, in the case that material properties relied on the temperature and time (transient), is nonlinear equation [6, 12]:

$$\begin{bmatrix} C^{TT} & 0 \\ 0 & C^{\varphi\varphi} \end{bmatrix} \begin{Bmatrix} \dot{T}_e \\ \dot{\varphi}_e \end{Bmatrix} + \begin{bmatrix} K^{TT} & 0 \\ K^{\varphi T} & K^{\varphi\varphi} \end{bmatrix} \begin{Bmatrix} T_e \\ \varphi_e \end{Bmatrix} = \begin{Bmatrix} Q \\ I \end{Bmatrix} \tag{3}$$

Transient thermal-electric simulation to investigate the heat transfer can be achieved by solving (1)-(3). In this research, the welding tip is complicated model and has many boundary conditions. Since we require high solution accuracy, we are not able to solve all equations manually, hence requiring the thermal-electric simulation in ANSYS software. ANSYS is a popular engineering simulation program widely used to solve various problems in the industry to help simulate and solve the equation successfully.

When the welding tip is stimulated by alternating current, heat will be generated and then released to air called convection. The equation that covers convection heat transfer is defined by Newton's law of cooling:

$$\frac{q}{A} = h(t)\left(T_s - T_f\right). \tag{4}$$

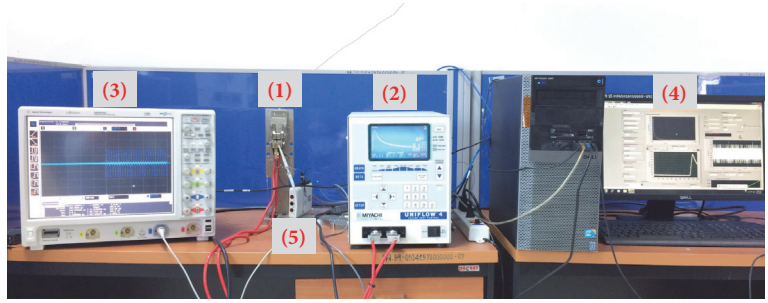

Figure 2: Instruments setup in the experiment.

$h(t)$ in (4) is the value that depends on time, which can be determined by the experiment. It is necessary for determining $h(t)$ to set in the boundary conditions. A high value of $h(t)$ indicates that an object rapidly loses heat to the surrounding air before cooling down.

3. Experiment

In this section, we explain the experimental setting, which is a novel experiment. No researches have set the experiment to measure the temperature of welding tip like this before. All boundary conditions are set to be similar to practical use in the reflow soldering process of the factory as possible. The data collected from this experiment is necessary for setting the boundary conditions in ANSYS to be explained later in Section 4.3. Some results will be used for validation. Figure 2 presents instruments used in the experiment consisting of (1) the welding tip, (2) Uniflow#4, (3) digital oscilloscope, (4) computer with LabVIEW program, and (5) data acquisition (DAQ) box. The welding tip was installed on a stand. Model and details of the welding tip will be mentioned in Section 4.1. Uniflow#4 applied alternating current to the welding tip. We can control a characteristic of alternating current by adjusting voltage and applied time by Uniflow#4. A digital oscilloscope was employed to measure the real applied voltage and frequency at the tail tip. We found that the results recorded from the oscilloscope can be plotted into a sine curve in terms of $V(t) = 1.66 \sin [2\pi(50)t]$. The total time of applied alternating current was 0.7s. During 0.615-0.7s the maximum voltage declined 17% per period from the previous point. The computer with LabVIEW program was connected to the DAQ box. The DAQ box was connected to the thermocouple with $\pm 0.01^{\circ}$C accuracy to measure temperature at the measured point. The LabVIEW program was written to control precision of time, which was every 5 ms per point. In fact, ANSYS thermal-electric simulation for this boundary condition can be used in the case that problems found are steady-state only. Still, we were able to do transient calculations since we wrote special commands in ANSYS Parametric Design Language (APDL) to constrain each element to be calculated in transient mode. This is a special technique which the author thinks is beneficial towards readers who would like to research in this field. That command may be written as "ANYTYE, TRANS".

In measuring the temperature, we chose the measured point to be slightly away from the head tip, similar to the actual setting at the factory, since the head tip was used in making the footprint onto the connected area in the welding process, thus making it impossible to measure the temperature at the point. For convenience purposes, the factory assumed that the temperature at the measured point and head tip is equal. Afterwards, the temperature from the measured point was used as reference for an automation system to control the footprint process. Since the welding process took a cycle time of 2.5 s, the computer would record the temperature versus time for all 500 measured points. We expected that this is detailed enough to validate all results from the simulation.

4. Simulation

4.1. Welding Tip. Figure 3 shows a simplified solid model of welding tip. This type of welding tip is used for manufacturing 3.5-inch hard disk drive. A small picture presents the actual welding tip near the measured point. Below, there are two signal wires: first wire was connected to the thermocouple and the DAQ box to measure the temperature versus time. Another wire was connected to the Uniflow#4 and the WAM for feedback control system. Above, signal wires were connected to the digital oscilloscope for measuring the applied voltage from Uniflow#4. The welding tip consists of 3 materials: copper alloy, stainless steel, and haynes 230. The copper alloy is divided into 2 bars separated from one another where alternating current applied through both sides. Haynes 230 was between the two bars of copper alloy. It was designed based on the Joule heating principle to generate high temperature at the head tip once applied with alternating current. Haynes 230 is a key material following the conceptual design since its property is excellent in high temperature and has long-term thermal stability and outstanding resistance to oxidizing environment. Lastly, nut and bolt were made of stainless steel, which fixed the copper alloy and haynes 230 together.

4.2. Mesh Model. Figure 4 shows the mesh model, all of which is hexahedral mesh with 29,138 elements and 110,572 nodes. The head tip has the smallest element with 0.1 mm in sizing. The copper alloy bars have the largest element with 1 mm in

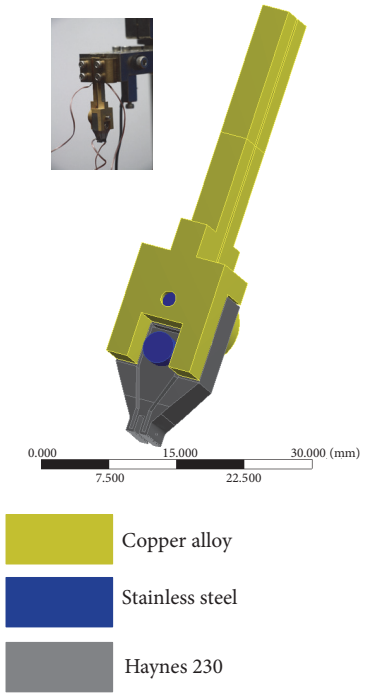

Figure 3: A simplified solid model of welding tip.

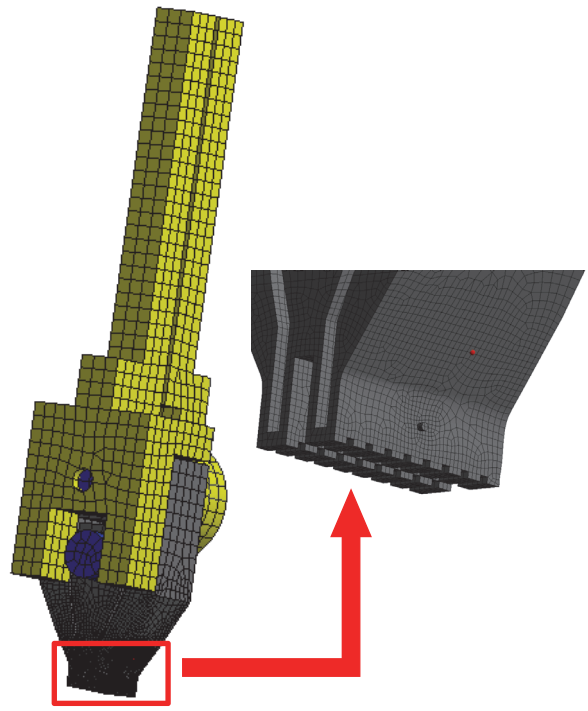

Figure 4: Mesh model of welding tip.

sizing. This mesh type provides the most accurate solution using the least amount of computational time.

4.3. Boundary Conditions. Figure 5 shows the boundary conditions setting in the transient thermal-electric simulation of ANSYS. One side of the tail tip of copper alloy was set using $V(0) = 0$ and $T(0) = 30^{\circ}\text{C}$ which was at room temperature. The other tail tip was $V(t) = 1.66 \sin [2\pi(50)t]$ and changed according to the data measured from the digital oscilloscope as mentioned in Section 3.

The *h(t)* value is vital in determining boundary conditions, which depend on both time and temperature. The more intense the heat and shorter the time, the higher the *h(t)* value. From studies, no *h(t)* values fit with the welding tip shape and operating conditions in our research. This is the challenge and difficulty in our work. We must seek the value by calculating along with experimenting. In order to find a suitable *h(t)* value in our work, we experimented to observe the heat transfer behavior at several welding tips used at the factory along with studying additional and related documents with thermal-electric devices and materials [8, 13]. We realize that when copper alloy and stainless steel receive electric currents, the temperature does not rise to be too intense and change slowly when compared to haynes 230, where temperature rises quickly. Thus, for simulation convenience we set the properties of copper alloy and stainless steel, e.g., specific heat, thermal conduction, resistivity to be constant values, and not altering to the time and temperature. If the material properties that we set are not too different from the actual values and ANSYS program calculates and discovers an unreasonable value, the program's solver with an inner

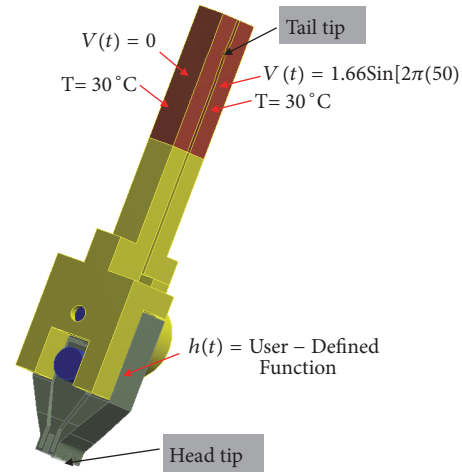

Figure 5: The boundary conditions setting in ANSYS.

function will compensate values to be more realistic [12]. As for haynes 230, material properties depend on the time and temperature. For the *h(t)* value calculation for haynes 230, we wrote a User-Defined Function (UDF) program to calculate the *h(t)* value at an amount great enough to accurately check occurring heat transfer. In this procedure, we used 500 values to compile with the amount of time steps in the analysis setting. Heat flux *q/A* from (4) can be found using the function probe in ANSYS at the measured point. As for T_s and T_f, they were gained from actual experiment using a thermocouple accordingly. This UDF will

Table 1: Material properties of copper alloy.

Properties (Unit)/ Temperature (°C)	Specific heat (J/kg-°C)	Thermal conductivity (W/m- °C)	Isotropic resistivity (Ω-m)	Convection film coefficient (W/m^2-K)
25	385	401	1.69E-08	35
100	385	398	2.28E-08	35
Density			8,300 kg/m^3	

Table 2: Material properties of stainless steel.

Properties (Unit)/ Temperature (°C)	Specific heat (J/kg-°C)	Thermal conductivity (W/m- °C)	Isotropic resistivity (Ω-m)	Convection film coefficient (W/m^2-K)
25	480	15.1	7.70E-07	35
Density			7,750 kg/m^3	

Table 3: Material properties of haynes 230.

Properties (Unit)/ Temperature (°C)	Specific heat (J/kg-°C)	Thermal conductivity (W/m- °C)	Isotropic resistivity (Ω-m)	Convection film coefficient (W/m^2-K)
25	397	8.9	1.250E-06	1.8E12
100	419	10.4	1.258E-06	8.8E11
200	435	12.4	1.265E-06	4.5E11
300	448	14.4	1.273E-06	3.0E11
400	465	16.4	1.284E-06	1.8E11
Density			8,970 kg/m^3	

be inputted into ANSYS to simulate occurring heat transfer. The more detailed and numerous *h(t)* is, the more accurate the simulation results. Tables 1–3 show some of the necessary material properties of copper alloy, stainless steel, and haynes 230, as to determine boundary conditions. All values were provided by the vendors, except for the *h(t)* of haynes 230, which the researchers calculated. We cannot present all 500 *h(t)* values of haynes 230 into this article, since it will make the document too long. Naturally, the true properties of the *h(t)* value depend on the airflow, temperature, and welding tip shape during convection. Thus, the material properties in Tables 1–3 are an average value for primary simulation only. The interesting point from this research is that the *h(t)* in Table 3 is an important value we calculated from transient state experimenting for every 5ms per point which is extremely high as it depends on the time and temperature while convection occurred. But the *h(t)* value of objects in general research is low due to being calculated from a steady-state condition at a low temperature. When the *h(t)* is high, the welding tip emits heat quickly. If *h(t)* in a steady state is used, the simulation will be wrong. We also learned that if the welding tip shape and size are changed, the *h(t)* value also varies accordingly. Therefore, to check the heat transfer occurring at the welding tip, coupling both simulation and experiment is necessary for accurate results.

In analysis setting, the calculation was divided into 500 steps, 5 ms per step. Each step has 20 iterations per step; therefore, the computer must calculate all 10,000 iterations covering 2.5 s of cycle time for footprint process. This calculation was deemed as highly detailed. From all these settings, we believed that the simulation provided credible and accurate results.

5. Results and Discussion

By using the transient thermal-electric simulation in ANSYS to investigate the heat transfer and determine the temperature in the welding tip, Figure 6 reveals the temperature comparison results from the simulation and experiment at the measured point. We found that they were very well consistent. The maximum discrepancy was 2.89% at t=0.795s, in which T_{exp} = 390.4°C and T_{sim} = 379.1°C. This might be due to the fact that we used 5 ms per time step in calculation. At t = 0.7 to 1.5s, the welding tip released heat rapidly. If we used 1 ms for time step and the material properties in Tables 1–3 that depend on the time and temperature are more detailed**,** it was assured that the discrepancy would no longer be presented but that action requires more computational time. Moreover, we also observed that the temperature at the nut, bolt, and tail tip was around 30-40°C throughout for both simulation and experimental results. All these make us confident that our simulation and experimental results are deemed accurate and reliable.

To simulate the transient thermal-electric heat transfer, Figure 7 shows the temperature distribution during 0–2.5s. Notice the start at t=0s until near t =0.7s. The welding tip quickly heated up from the tail to the head. At t= 0.7s, the head tip's maximum temperature was 406°C before gradually cooling down. The behavior of changing in temperature versus time is consistent with the experimental results reported

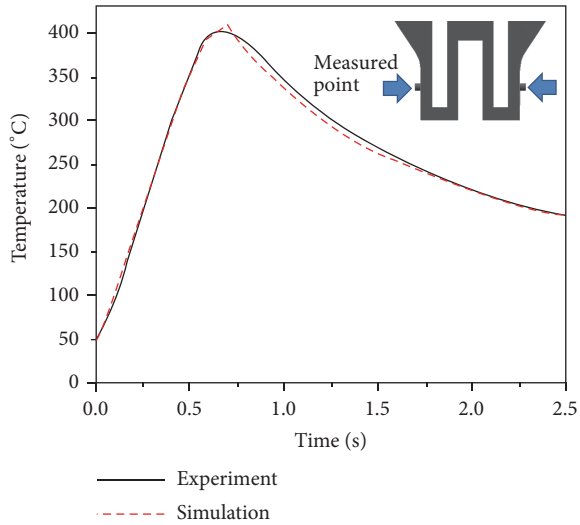

Figure 6: Temperature comparison results from the simulation and experiment at the measured point.

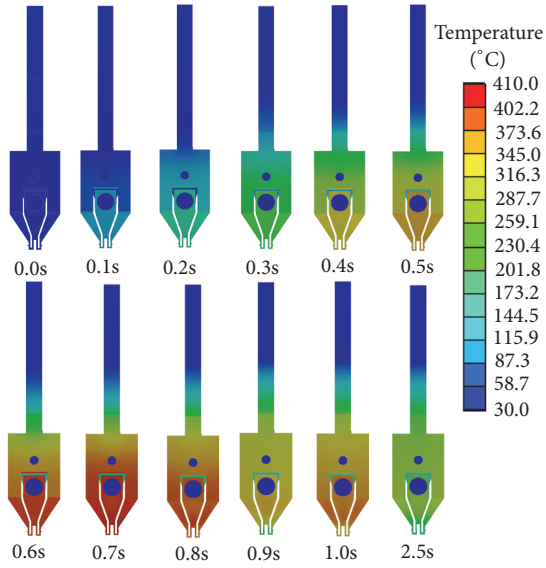

Figure 7: Temperature distribution on welding tip surface during 0–2.5s.

in Figure 6. Haynes 230 has higher temperature than other materials, especially at the head tip. Therefore, the welding tip could be designed to have the highest temperature at the head tip as precise as the conceptual design. Figure 8 shows the highest temperature at the head tip specifically for 0.5-1.0s. From 0.7s to 1.0s, the maximum temperature promptly lessened 100°C within a short amount of time. This figure also indicated that, in using the welding tip, footprints should be done at 0.7s for the highest efficacy in heat generating.

Because in real reflow soldering process, the factory measured the temperature at the measured point rather than the inconvenient head tip that was used in making the footprint. The temperature collected from the measured point was sent to a feedback control system of the WAM as temperature reference. The WAM has functioned continuously, which assumed that the temperatures at head tip and at measured point were equal for convenience purposes. Due to this, we also calculated the temperature at head tip and measured point. Compared results are shown in Figure 9. It was found that the temperatures were similar to each other only during the first 0-0.7s. After 0.7s onwards, after the highest temperature, when the time was increased, the temperature even showed greater differences. At t=2.5s, temperature differed at about 10%. All this may be used to explain the reason why sometimes while making footprints, the lead melts and sometimes it did not. This is due to the fact that the lead is a special type that has a melting point about 400°C. Thus, when the lead did not melt it is because the machine was too slow to make the footprint and the temperature at the head tip below 400°C already. For example, if the footprint was done at t=0.75s, the temperature at the head tip was 390°C and measured point was 401°C. To solve this problem, the engineers should design a controlled footprint processing system that makes footprint at precisely 0.7s. At this time, the temperatures of head tip and measured point were 406°C. This way the lead will melt resulting in no product defects.

To enhance the efficacy of the welding tip, haynes 214, 242, and 556 were chosen to simulate the heat transfer and temperature. The reason why these 3 were selected is due to their tensile strength which is equal to or greater than haynes 230 of the original welding tip. All haynes' properties were given by the vendors. Figure 10 reports the temperature at head tip for all types of haynes. We found that the temperatures of all types were similar to each other in the first 0.7s of cycle time. At t= 0.7s, haynes 556's maximum temperature was slightly higher than others by 5°C. Afterwards, haynes 556 is the slowest type to release heat. This may be applicable in controlling Uniflow#4. When the first footprint is completed, the engineers will design Uniflow#4 to apply less voltage. Due to the lesser amount of time, the temperature will rise to its highest faster than haynes 230. This can be considered as energy conservation. Moreover, haynes 556 is also durable towards reshaping and can absorb more impact force; therefore, it is suitable to develop to be more effective welding tip.

In actual manufacturing, the welding tip was installed into the WAM inside the clean room with cool air supplied as reported in the works of Thongsri et al. [14–16] Within the machine, there was a laminar flow generated by fan filter units to ventilate the air in and out the WAM with temperature lower than 24.5°C. This environment could slightly affect the welding tip lose heat faster rate. Hence, if the further research included thermal-electric simulation and computational fluid dynamics within the laminar flow of a machine is conducted, research results will be even more accurate and beneficial.

The results of this research were submitted to the HDD factory. The changes in footprint process following our recommendation reduced the factory's costs in 2 ways; 1st is development in the laboratory. A newly designed welding tip: in the past procedures were the trial and error method which the factory must order large quantities of

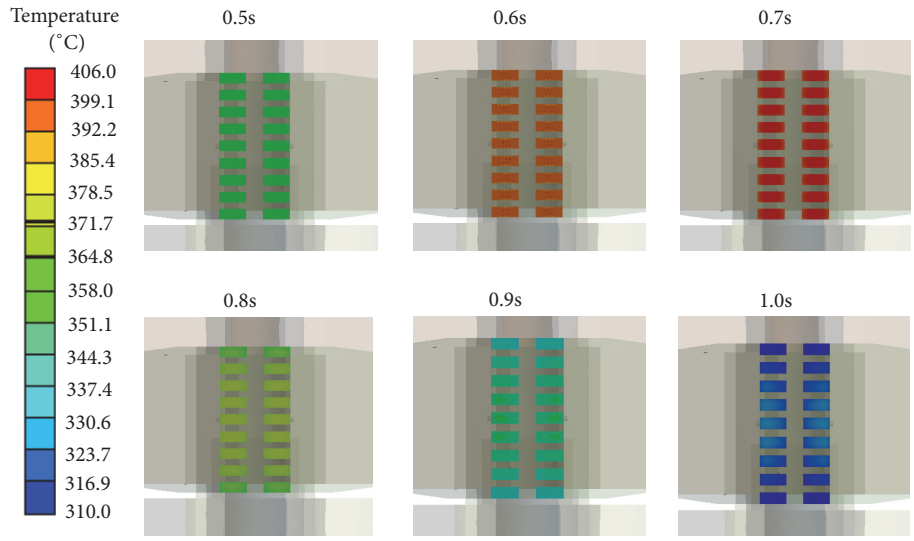

Figure 8: The highest temperature at head tip during 0.5–1.0s.

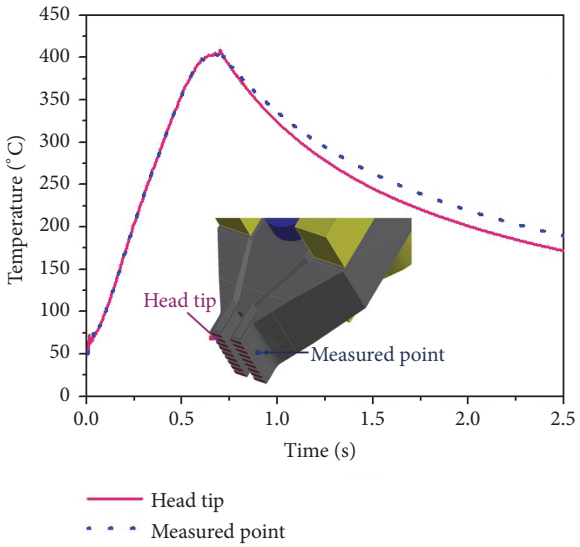

Figure 9: Temperature comparison results from the head tip and the measured point.

welding tip prototypes to experiment and find the best operating condition. Once the tips have deteriorated, they will be disposed of immediately. After applying research results, factory engineers can design highly efficient welding tips as demanded. This reduces the ordered welding tip prototypes for trial by 50%. Moreover, after experimenting the welding tips can still be used. As for the 2nd way in actual usage, the welding tip had greater efficiency, durability, and an extended usage life, reduced the quantity of defective products of 15,000 pieces per year, enhanced product quality, and saved more than 0.15 million USD annually.

6. Conclusion

This article is an author's experience in solving the problem found at the HDD manufacturing process. Welding tips are used as the equipment in making footprint to connect the arm and HGA together by using a specific lead as solder in the reflow soldering process. Applying alternating current to the welding tip, heat with high temperature is generated at the head of welding tip based on Joule heating principle.

In making footprints, the head tip is pressed onto the lead to melt in order to connect the arm and HGA parts together. Previously, reflow soldering process error was in certain products when the lead did not melt. This resulted in unconnected arms and HGAs, causing losses towards the factory. A solution must be found urgently. We used transient thermal-electric simulation in the ANSYS program to simulate heat transfer that happens within 2.5s of cycle time by using the actual boundary conditions collected from the factory. The simulation results were confirmed by the novel experiment that we set up using simple instruments readily available at the factory. The simulation results showed the temperature in all areas of the welding tip. At the start of the process, the temperature increased rapidly with a maximum at t=0.7. The maximum temperature was 406°C at the head tip, and then it slowly declined. At t=2.5s, the temperature of the head tip decreased to 170°C. Welding process failure might be caused by making footprints after 0.7s. After this time, the temperature of the head tip would drop to lower than 400°C, which could not melt the lead and thus failing to connect the arm and HGA together. In order to solve this problem, we recommended the factory's engineers that footprints should be precisely done at t=0.7s.

From the simulation, we also found that when the welding tip material was changed from the traditional model using haynes 230 to haynes 556, the maximum temperature at head tip increased 5°C higher along with a slower heat-release rate. Other than this, haynes 556 also has yield tensile strength

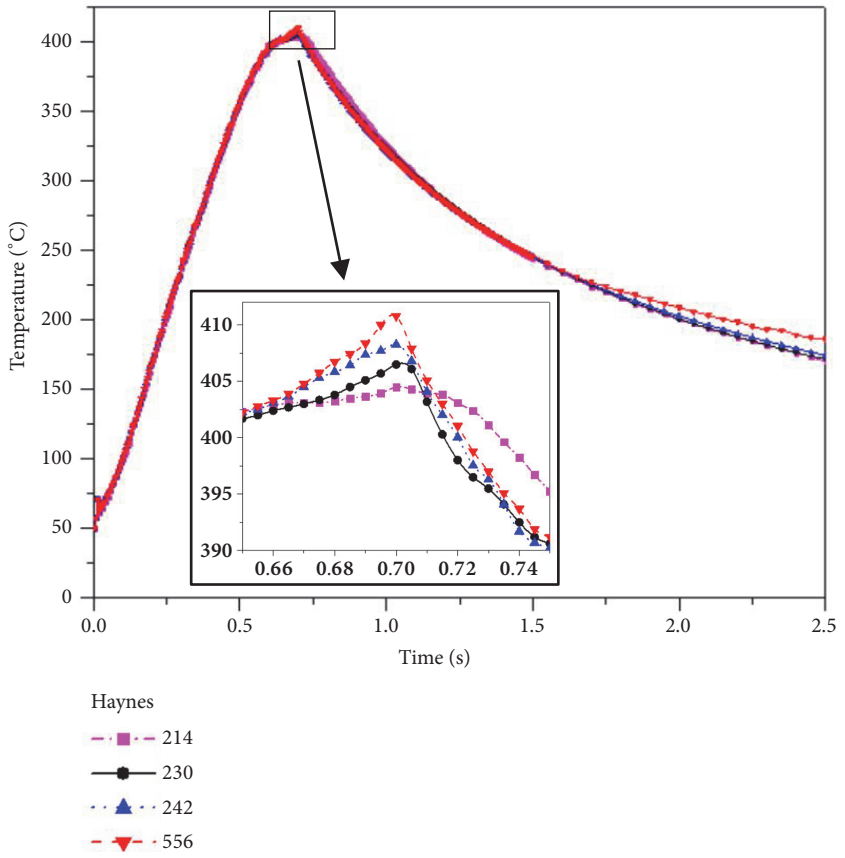

Figure 10: Simulated temperatures at the head tip for haynes 214, 230, 242, and 556.

that is greater than haynes 230 as well, making it suitable to develop into highly-efficient welding tips in the future. The results of this research, once applied to the factory, helped the factory save costs more than 0.15 million USD annually.

Nomenclature and Abbreviations

T: Absolute temperature (K)
T_f: Air temperature (K)
A: Area of surface according to the heat flux (m^2)
h: Convection film coefficient (W/m^2-K)
ρ: Density (kg/m^3)
$[C^{\varphi\varphi}]$: Dielectric damping matrix
$[\varepsilon]$: Dielectric permittivity matrix (F/m)
$[\sigma]$: Electric conductivity matrix (S/m)
$\boldsymbol{J}$: Electric current density (A/m^2)
$\{I\}$: Electric power load vector
φ: Electric scalar potential (V)
$[K^{\varphi\varphi}]$: Electric stiffness matrix
HDD: Hard disk drive
HGA: Head gimbal assemble
q: Heat generation (W)
$\dot{q}$: Heat generation rate per unit volume (W/m^3)
$[\Pi]$: Peltier coefficient matrix (V)
$[\alpha]$: Seebeck coefficient matrix (V/K)
$[K^{\varphi T}]$: Seebeck stiffness matrix
C: Specific heat capacity (J/kg-K)
T_s: Surface temperature (K)
$[\lambda]$: Thermal conductivity matrix (W/m-K)
$[C^{TT}]$: Thermal damping matrix
$[K^{TT}]$: Thermal stiffness matrix
t: Time (s)
$\{Q\}$: Vector of combined heat generation (W/m^3)
$\{\varphi_e\}$: Vector of nodal electric potential
$\{\dot{\varphi}_e\}$: Velocity vector of nodal electric potential
$\{T_e\}$: Vector of nodal temperature
$\{\dot{T}_e\}$: Velocity vector of nodal temperature
$V(t)$: Voltage applied by Uniflow#4 (V)
WAM: Welding automation machine.

Data Availability

The data used to support the findings of this study are available from the corresponding author upon request.

Conflicts of Interest

The author declares that there are no conflicts of interest for this article.

Acknowledgments

This research was supported by College of Advanced Manufacturing Innovation, King Mongkut's Institute of Technology Ladkrabang.

References

[1] D. Champier, "Thermoelectric generators: A review of applications," *Energy Conversion and Management*, vol. 140, pp. 167–181, 2017.

[2] W. He, G. Zhang, X. Zhang, J. Ji, G. Li, and X. Zhao, "Recent development and application of thermoelectric generator and cooler," *Applied Energy*, vol. 143, pp. 1–25, 2015.

[3] D. Zhao and G. Tan, "A review of thermoelectric cooling: materials, modeling and applications," *Applied Thermal Engineering*, vol. 66, no. 1-2, pp. 15–24, 2014.

[4] A. S. Korotkov, V. V. Loboda, S. B. Makarov, and A. Feldhoff, "Modeling thermoelectric generators using the ANSYS software platform: Methodology, practical applications, and prospects," *Russian Microelectronics*, vol. 46, no. 2, pp. 131–138, 2017.

[5] M. N. Zulkifli, I. Ilias, A. Abas, and W. M. W. Muhamad, "Finite element analysis of thermoelectric generator with aluminum plate for waste heat recovery application," *International Journal on Advanced Science, Engineering and Information Technology*, vol. 7, no. 4, pp. 1328–1333, 2017.

[6] E. E. Antonova and D. C. Looman, "Finite elements for thermoelectric device analysis in ANSYS," in *Proceedings of the 24th International Conference on Thermoelectrics (ICT '05)*, pp. 19–23, IEEE, Piscataway, NJ, USA, June 2005.

[7] Y. Shi, X. Chen, Y. Deng et al., "Design and performance of compact thermoelectric generators based on the extended three-dimensional thermal contact interface," *Energy Conversion and Management*, vol. 106, pp. 110–117, 2015.

[8] J. Bumrungwong, "The Study of the hot bar for reflow process in interconnecting of head stack assembly," *International Journal of Applied Computer Technology and Information System*, vol. 4, no. 2, pp. 10–13, 2015.

[9] W. Li, M. C. Paul, A. Montecucco et al., "Multiphysics simulations of thermoelectric generator modules with cold and hot blocks and effects of some factors," *Case Studies in Thermal Engineering*, vol. 10, pp. 63–72, 2017.

[10] W. Li, M. C. Paul, A. Montecucco et al., "Multiphysics Simulations of a Thermoelectric Generator," *Energy Procedia*, vol. 75, pp. 633–638, 2015.

[11] L. D. Landau, E. M. Lifshitz, and L. P. Pitaevskii, *Electrodynamics of Continuous Media*, Butterworth-Heinemann, Oxford, UK, 2nd edition, 1984.

[12] Ansys, *Inc Nonlinear and transient thermal analysis, Ansys Mechanical Heat Transfer*, 2016.

[13] S. K. Thangaraju and K. M. Munisamy, "Electrical and Joule heating relationship investigating using finite element method," in *IOP Conference Series: Materials Science and Engineering*, vol. 88, 2015.

[14] J. Thongsri, "A successful CFD-based solution to a water condensation problem in a hard disk drive factory," *IEEE Access*, vol. 5, pp. 10795–10804, 2017.

[15] J. Thongsri, "A Problem of Particulate Contamination in an Automated Assembly Machine Successfully Solved by CFD and Simple Experiments," *Mathematical Problems in Engineering*, vol. 2017, Article ID 6859852, p. 9, 2017.

[16] J. Thongsri and M. Pimsarn, "Optimum airflow to reduce particle contamination inside welding automation machine of hard disk drive production line," *International Journal of Precision Engineering and Manufacturing*, vol. 16, no. 3, pp. 509–515, 2015.

Hindawi
Mathematical Problems in Engineering
Volume 2018, Article ID 2039153, 18 pages
https://doi.org/10.1155/2018/2039153

Research Article

Tolerance Analysis of Over-Constrained Assembly Considering Gravity Influence: Constraints of Multiple Planar Hole-Pin-Hole Pairs

Xia Liu,[1] **Luling An**,[1] **Zhiguo Wang**,[1] **Changbai Tan**,[2] **and Xiaoping Wang**[1]

[1]*Nanjing University of Aeronautics and Astronautics, Jiangsu Key Laboratory of Precision and Micro-Manufacturing Technology, Nanjing 210016, China*
[2]*College of Engineering, University of Michigan, Ann Arbor 48105, USA*

Correspondence should be addressed to Luling An; anllme@nuaa.edu.cn

Received 5 July 2018; Revised 19 October 2018; Accepted 31 October 2018; Published 14 November 2018

Guest Editor: Sutasn Thipprakmas

Over-constrained assembly of rigid parts is widely adopted in aircraft assembly to yield higher stiffness and accuracy of assembly. Unfortunately, the quantitative tolerance analysis of over-constrained assembly is challenging, subject to the coupling effect of geometrical and physical factors. Especially, gravity will affect the geometrical gaps in mechanical joints between different parts, and thus influence the deviations of assembled product. In the existing studies, the influence of gravity is not considered in the tolerance analysis of over-constrained assembly. This paper proposes a novel tolerance analysis method for over-constrained assembly of rigid parts, considering the gravity influence. This method is applied to a typical over-constrained assembly with constraints of multiple planar hole-pin-hole pairs. This type of constraints is non-linear, which makes the tolerance analysis more challenging. Firstly, the deviation propagation analysis of an over-constrained assembly is conducted. The feasibility of assembly is predicted, and for a feasible assembly, the assembly deviations are determined with the principle of minimum potential energy. Then, the statistical tolerance analysis is performed. The probabilities of assembly feasibility and quality feasibility are computed, and the distribution of assembly deviations is estimated. Two case studies are presented to show the applicability of the proposed method.

1. Introduction

Mechanical parts are always manufactured with more or less geometrical deviations. Tolerance analysis aims to predict the influence of these manufacturing deviations on the quality level of a mechanical system at the design stage. The gaps in mechanical joints between different parts, coupled with the manufacturing deviations, impact the functionality of an assembly system. The manufacturing deviations are assumed to be independent random variables defined by their tolerance zones and the probability distributions with respect to manufacturing process, while the gaps are characteristic of epistemic uncertainty which makes the tolerance analysis complex [1]. The gaps are seldom considered in iso-constrained assembly, but in over-constrained assembly they allow the parts to be assembled without deformation and interference, and cannot be ignored. Over-constrained assembly of rigid parts is widely used in products, such as aircrafts and automobiles, because this kind of assembly can increase stiffness and accuracy of mechanical structure [2]. However, the feasibility of assembly is weakened due to the introduction of redundant constraints into the assembly, and the deviations of assembled products are difficult to predict because of the uncertain gaps. This is one of the key challenges in assembly tolerance analysis.

Some studies have been conducted on tolerance analysis of over-constrained assembly. Compared to worst case method, statistical tolerance analysis is regarded to be better to understand the behavior of a mechanical system, and the over-constraints have to be considered for accuracy in the tolerance analysis of over-constrained assembly [3]. Dantan and Qureshi [4] introduced the quantifier notion, including existential quantifier "there exists" and universal quantifier "for all", to describe the condition corresponding

to a functional requirement. The mathematical formulation of tolerance analysis was computed with quantified constraint satisfaction problem solvers and Monte Carlo simulation (MCS). With the mathematical formulation based on quantifier notion, Qureshi et al. [5] acquired the probability of the functional operation of an assembly based on MCS and optimization technique, which is used to find the worst case for gap configuration. This approach was generalized and applicable to both explicit and implicit response function, as well as both linear and non-linear constraints. For explicit function and linear constraints, MCS is time consuming and computationally expensive. Ballu et al. [3] solved probability of failure by using first order reliability method (FORM) and second-order reliability method (SORM) to determine the feasible extreme gap configuration. Beaucaire et al. [6, 7] proposed the mathematical formulation from the structural reliability domain considering several contact point situations, and computed the defect probability by FORM. For non-linear constraints, Dumas et al. [8] investigated different linearization strategies and discussed the impact of these strategies on the predicted probability of failure. In addition, Dumas et al. [1] formulated the tolerance analysis problem by using the Lagrange dual form of optimization, where a simulation-based selective search algorithm, i.e., a genetic algorithm, was developed and then the probability of failure was estimated by FORM. The above studies [1, 3–8] focused on computing the probability that the assembled product can fulfill its intended functional requirement.

Another problem related to statistical tolerance analysis is the distributions of assembly deviations of functional points, where these deviations characterize the fulfillment of functional requirement of assembled product. In over-constrained assembly, the presence of gaps in mechanical joints makes the deviations of assembled product difficult to predict, because a large variety of possible gap configurations exist during the assembly process. Franciosa et al. [9] determined the best-fit assembly configuration by using optimization algorithm, where the optimization objective is to minimize the sum of the squares of the distances between object plane/axis and target plane/axis respectively. However, this optimization objective is not suitable for most of practical assemblies in production. Li et al. [10] defined two planar hole-pin pairs as 3-2-1 location mode, and expressed the ranges of location deviations by the intersection of inequations which is approximated to an elliptic. However, this study did not develop an approach to get the certain location deviations.

Furthermore, tolerance analysis of over-constrained assembly is subject to many nongeometrical factors involved in an assembly process, such as thermal flux, contact force, gravity, etc. Pierre et al. [11] integrated thermomechanical strains into variational tolerance analysis. Gouyou et al. [2] discussed the part deformation subject to contact forces which allow the parts to be assembled when the interference happens. However, although the influence of gravity on the assembly deviations of rigid parts has been well recognized [12], there is still limited research in tolerance analysis of over-constrained assembly integrating the influence of gravity. Specifically, in aircraft assembly, planar hole-pin-hole joints are widely used to join different parts and locate parts on the fixtures. Because many parts and fixtures in aircraft assembly are large and heavy, the gravity will significantly impact the configuration of gaps in hole-pin-hole joints, and thus the assembly accuracy. In view of the strict dimensional accuracy requirement in aircraft manufacturing, a reliable prediction of assembly deviations by considering the gravity influence is especially important to realize effective dimensional management in aircraft assembly.

This paper proposes a method for tolerance analysis of over-constrained assembly incorporating the influence of gravity on assembly deviations. This method will be applied to a typical over-constrained assembly with constraints of multiple planar hole-pin-hole pairs. First of all, the deviation propagation throughout an over-constrained assembly is analyzed. Here, the feasibility of assembly is predicted; for a feasible assembly, the assembly deviations are determined considering the gravity influence. Then, the statistical tolerance analysis is performed by using MCS, and its output results include the probabilities of assembly feasibility and quality feasibility, as well as the distributions of assembly deviations. Especially, in the deviation propagation analysis, the judgment of assembly feasibility is formulated as a search problem. And for a feasible assembly, with the principle of minimum potential energy, the calculation of assembly deviations is modeled as an optimization problem. These search and optimization problems are inefficient and difficult to solve, because of the non-linear studied constraints of planar hole-pin-hole pairs. These problems are solved by using the search algorithms including sequential search and binary search, and the optimization algorithms including particle swarm optimization (PSO) and linear programming (LP).

The paper is organized as follows. Section 2 gives problem definition and mathematical representation. Sections 3 and 4 present deviation propagation analysis and statistical tolerance analysis of over-constrained assembly, respectively. Section 5 shows case studies. Section 6 draws conclusions.

2. Problem Definition and Mathematical Representation

2.1. Problem Description and Assumption. Tolerance analysis consists in predicting the functionality of an assembly system based on the consideration of the manufacturing deviations of parts. For over-constrained assembly of rigid parts, tolerance analysis consists of two key problems to be studied, including assembly feasibility prediction and assembly deviation calculation. In over-constrained assembly of rigid parts, the feasibility of assembly is weak because of redundant constraints, even with the gaps in mechanical joints between different parts. Furthermore, due to the uncertainty of gaps, the assembly deviations are difficult to predict, especially coupled with non-linear constraints and non-geometrical factors.

With considering the influence of gravity, the proposed method of tolerance analysis of over-constrained assembly is illustrated by a typical assembly with constraints of multiple

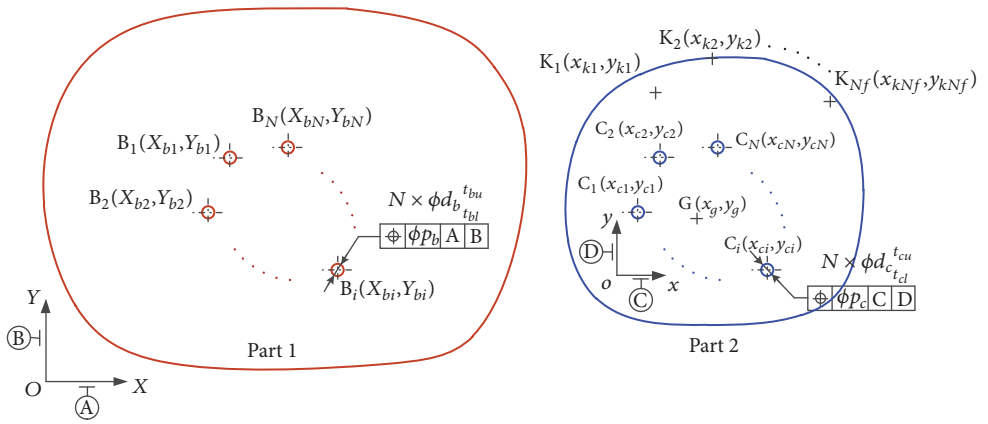

FIGURE 1: Two parts to be assembled with constraints of multiple planar hole-pin-hole pairs.

planar hole-pin-hole pairs. This type of constraints possesses the feature of non-linearity. As shown in Figure 1, each of the two parts, denoted as Part 1 and Part 2, has two or more pairs of mating holes on the mating plane. Part 1 is assumed to be fixed, and Part 2 will be assembled onto Part 1 with the planar hole-pin-hole joints. The centers of the mating holes of Part 1 are denoted as B_1 ~B_N. Similarly, these centers of Part 2 are denoted as C_1 ~C_N. N is the number of hole-pin-hole joints. Furthermore, the quality requirement concerns the deviations of Part 2 with respect to (w.r.t.) Part 1. The functional points are on Part 2, denoted as K_1 ~K_{Nf}. N_f is the number of functional points. The deviations of the functional points are used to represent the assembly deviations. In addition, G denotes the center of gravity of Part 2.

Notably, for simplifying the analysis and highlighting the research focus, some assumptions are made as follows:

(a) The assembly tolerance analysis is performed only considering the degrees of freedom (DOFs) on plane, such that the mating planes are assumed to be perfect.

(b) The parts are treated as rigid bodies, and deformation and interference are not allowed.

(c) The direction of gravitational field is on the mating planes.

(d) The position of gravity center of Part 2 is not affected by its manufacturing deviations.

(e) The hole-pin-hole pairs adopt clearance fit.

(f) For the manufacturing deviations of hole-pin-hole pairs, dimensional deviations of diameters of holes and pins, and position deviations of centers of holes are considered, but the shape deviations are ignored.

2.2. Mathematical Representation

2.2.1. Definition of Coordinate Systems. In order to express the deviations as well as their relationships, four types of coordinate systems (CSs) are defined, including global coordinate system (GCS), part coordinate system (PCS), gravitational field coordinate system (GFCS), and functional point coordinate system (FPCS).

GCS is considered to be error free and unchangeable during the entire assembly process. PCS is associated with a part. Similarly to GCS, GFCS and FPCS are also unchanged. GFCS is constructed according to the direction of gravitational field, and the Y_g-axis is in the opposite direction to gravitational field. Each FPCS is used to represent the deviations of a functional point. The origin of a FPCS is in the nominal position of a functional point w.r.t. GCS, and the axes correspond to the direction required to be measured. Moreover, the spatial relationships among different CSs can be described by homogeneous transformation matrix (HTM) [13].

As shown in Figure 2, Part 2 without any deviation is in the nominal position w.r.t Part 1. *XOY* is the GCS, which is assumed to coincide with the PCS of Part 1. *xoy* is the PCS of Part 2 denoted as PCS_2. $X_gO_gY_g$ is the GFCS, whose origin is in the nominal position of G w.r.t. GCS, and Y_g-axis has the angle θ from Y-axis of GCS. $X_{fj}O_{fj}Y_{fj}$, $j = 1, 2, \ldots, N_f$, are the FPCSs. Furthermore, the HTMs of nominal PCS_2, GFCS and $FPCS_i$ w.r.t. GCS are $\mathbf{T}_2^G$, $\mathbf{T}_g^G$, and $\mathbf{T}_{fj}^G$, $j = 1, 2, \ldots, N_f$, respectively.

2.2.2. Tolerance Representation. The dimensional and geometric tolerances indicate the deviation of an actual feature from its nominal one. The features are allowed to rotate and translate within their tolerance zone [10], and these rotations and translations can be described by the small displacement torsor (SDT) model [14]. In SDT model, tolerance zones and feature deviations are defined as vectorial representation [15], i.e., $\boldsymbol{\tau} = [\boldsymbol{\omega} \ \boldsymbol{\varepsilon}]^{\mathrm{T}}$. $\boldsymbol{\omega} = [\alpha \ \beta \ \gamma]^{\mathrm{T}}$ denotes the rotation vector, which has three components α, β, and γ around x, y, and z axes, respectively. Similarly, $\boldsymbol{\varepsilon} = [u \ v \ w]^{\mathrm{T}}$ denotes the translation vector, which has three components u, v, and w along x, y and z axes, respectively. In this paper, it is assumed that $\alpha = \beta = 0$, $w = 0$, thus $\boldsymbol{\tau} = [\gamma \ u \ v]^{\mathrm{T}}$.

The assembly deviations are caused by deviation sources which are propagated and accumulated through the assembly process. This data stream of deviations can be analyzed by deviation propagation model [16–18]. For example, the deviation of feature i is $\boldsymbol{\tau}_i = [\gamma_i \ u_i \ v_i]^{\mathrm{T}}$. An arbitrary point on feature i is A, and its coordinates are denoted as $\mathbf{a}$ =

$[x_a \;\; y_a]^{\mathrm{T}}$. The deviation of point A can be calculated with HTM [19, 20] as

$$[\Delta\mathbf{a} \;\; 1]^{\mathrm{T}} = \mathbf{T}_i [\mathbf{a} \;\; 1]^{\mathrm{T}} - [\mathbf{a} \;\; 1]^{\mathrm{T}} \tag{1}$$

where the HTM $\mathbf{T}_i$ is

$$\mathbf{T}_i = \begin{bmatrix} \mathbf{R}_i & \boldsymbol{\varepsilon}_i \\ \mathbf{0} & 1 \end{bmatrix} = \begin{bmatrix} \cos\gamma_i & -\sin\gamma_i & u_i \\ \sin\gamma_i & \cos\gamma_i & v_i \\ 0 & 0 & 1 \end{bmatrix}. \tag{2}$$

3. Deviation Propagation Analysis

Deviation propagation analysis studies the introduction, propagation and accumulation of data stream of deviations through an assembly process. For an over-constrained assembly with constraints of multiple planar hole-pin-hole pairs, the deviation propagation analysis is performed with considering the influence of gravity, which contains assembly feasibility judgment and assembly deviation determination.

3.1. Assembly Feasibility Judgment. An assembly with over constraints is usually disturbed by the infeasibility of assembly, even though normal joint gaps are reserved. Dantan and Qureshi [4] introduced the existential quantifier "there exists" to correctly formulate this problem concerning assembly with gaps, i.e., if there exits at least one gap configuration such that the assembly is feasible, then assembly feasibility of the mechanical structure is ensured. The mathematical expression is

$$\exists \mathbf{g} \in [0, \mathbf{g}_{\max}(\mathbf{M})] : f_{ai}(\mathbf{M}, \mathbf{g}) \le 0, \quad i = 1, 2, \cdots, N \tag{3}$$

where $\mathbf{M}$ denotes the manufacturing deviations of parts, $\mathbf{g}$ denotes the gaps and $\mathbf{g}_{\max}$ is the allowable gap widths, f_{ai}, $i = 1, 2, \ldots, N$, are the functions of assembly requirement, and N is the number of the functions. All of these functions have to be non-positive to ensure the feasibility of assembly.

According to the above formulation, the judgment of assembly feasibility can be transformed to a search problem. Moreover, this search problem is inefficient to be solved due to the non-linear studied constraints of multiple planar hole-pin-hole pairs. Firstly, the search problem is modeled. Then in order to improve the efficiency, a solving method is given by reducing dimensionality of search object and narrowing down search space.

3.1.1. Formulation of Assembly Requirement. In over-constrained assembly, the gaps in mechanical joints are correlated with each other and their worst configuration depends on the manufacturing deviations of parts [3]. For the constraints of multiple planar hole-pin-hole pairs, the correlation of gaps, coupled with the relationships between gap configurations and part manufacturing deviations, is complicated. In an assembly process, the deviation of PCS_2 w.r.t GCS is denoted as $\boldsymbol{\tau}_2 = [\gamma_2 \;\; u_2 \;\; v_2]^{\mathrm{T}}$, and one $\boldsymbol{\tau}_2$ corresponds to a configuration of gaps.

As shown in Figure 1, the coordinates of $\mathrm{B}_i, i = 1, 2, \ldots, N$, w.r.t. GCS are $\mathbf{B}_i^G = [X_{bi} \;\; Y_{bi}]^{\mathrm{T}}$. The coordinates of C_i, $i = 1, 2, \ldots, N$, w.r.t. PCS_2 are denoted as $\mathbf{C}_i^2 = [x_{ci} \;\; y_{ci}]^{\mathrm{T}}$. Then when Part 2 is in the nominal position w.r.t. GCS, they w.r.t. GCS are $\mathbf{C}_i^G = [X_{ci} \;\; Y_{ci}]^{\mathrm{T}}$ as

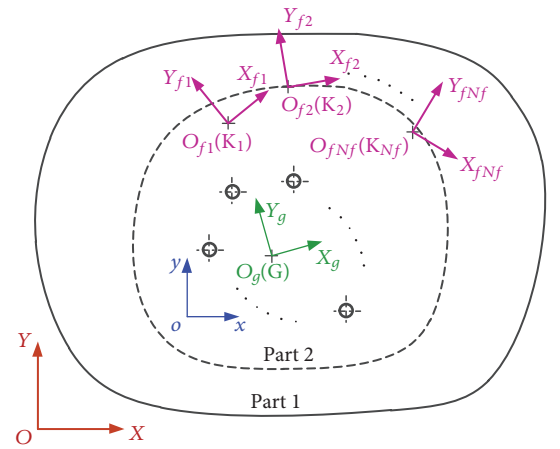

Figure 2: Definition of coordinate systems.

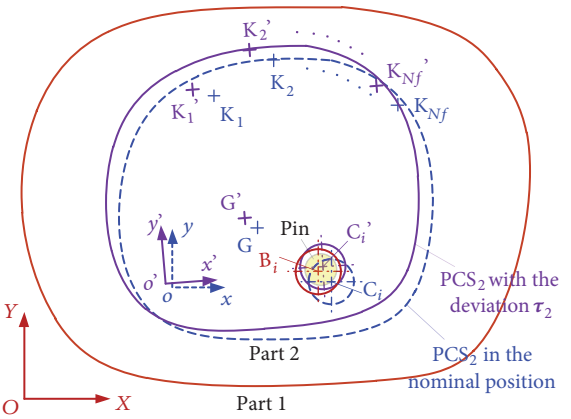

Figure 3: Assembly of two parts under a constraint of planar hole-pin-hole pair.

$$\left[\mathbf{C}_i^G \;\; 1\right]^{\mathrm{T}} = \mathbf{T}_2^G \left[\mathbf{C}_i^2 \;\; 1\right]^{\mathrm{T}}, \quad i = 1, 2, \cdots, N \tag{4}$$

With the deviation $\boldsymbol{\tau}_2$, the coordinates of C_i', $i = 1, 2, \ldots, N$, w.r.t. GCS are changed into $\mathbf{C}_i^{G\prime} = [X_{ci}' \;\; Y_{ci}']^{\mathrm{T}}$ as

$$\left[\mathbf{C}_i^{G\prime} \;\; 1\right]^{\mathrm{T}} = \mathbf{T}_2 \left[\mathbf{C}_i^G \;\; 1\right]^{\mathrm{T}}, \quad i = 1, 2, \cdots, N \tag{5}$$

where $\mathbf{T}_2$ is the HTM of $\boldsymbol{\tau}_2$.

The functions of assembly requirement concern the planar hole-pin-hole joints. As shown in Figure 3, by taking the ith constraint of planar hole-pin-hole pair as an example, the function of assembly requirement is

$$f_{ai} = \left|\overrightarrow{\mathrm{B}_i\mathrm{C}_i'}\right| - s_i \tag{6}$$

where $s_i = (1/2)(d_{bi} + d_{ci} - 2d_{pi})$ and d_{bi}, d_{ci}, and d_{pi} denote the diameters of the two mating holes and the pin respectively.

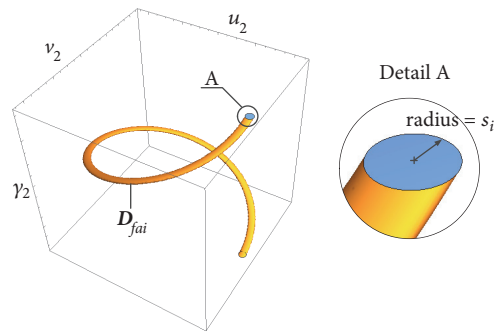

FIGURE 4: Feasible solution space under constraint of a planar hole-pin-hole pair.

It is definite that $s_i \geq 0$, due to clearance fit of hole-pin-hole pairs. According to the assembly requirement as seen in (3), the judgment of assembly feasibility is to judge whether f_{ai} is non-positive, i.e., to judge whether $|\overrightarrow{B_iC_i'}|$, is not larger than s_i, or whether $|\overrightarrow{B_iC_i'}|^2$ is not larger than ${s_i}^2$. Therefore, from the view of judging assembly feasibility, (6) can be translated to (7) as

$$\hat{f}_{ai} = \left|\overrightarrow{B_iC_i'}\right|^2 - {s_i}^2 \tag{7}$$

where $\hat{f}_{ai}$ is decorated with a topscript "^", in order to distinguish from the original assembly requirement function f_{ai}.

By referring to (5), (7) can be further arranged as

$$\begin{aligned}\hat{f}_{ai} = {} & \left(u_2 + X_{ci}\cos\gamma_2 - Y_{ci}\sin\gamma_2 - X_{bi}\right)^2 \\ & + \left(v_2 + X_{ci}\sin\gamma_2 + Y_{ci}\cos\gamma_2 - Y_{bi}\right)^2 - {s_i}^2\end{aligned} \tag{8}$$

For coordinates and diameters above mentioned, the nominal values are decorated with a superscript "0," whereas they represent the actual ones with manufacturing deviations of parts. In (8), coupled with the correspondence between $\boldsymbol{\tau}_2$ and configuration of gaps, the part manufacturing deviations and gap configuration are both incorporated.

According to (3) and (8), the assembly requirement under the constraints of N planar hole-pin-hole pairs is formulated as: if there exits at least one real vector $\boldsymbol{\tau}_2$ satisfying all the inequalities $\hat{f}_{ai} \leq 0, i = 1, 2, \ldots, N$, then assembly feasibility of the mechanical structure is ensured. The mathematical expression is

$$\begin{aligned}&\exists \boldsymbol{\tau}_2 \in \mathbf{R}_{3\times1} \cap \gamma_2 \in (-\pi, \pi] : \hat{f}_{ai} \\ &\quad = \left(u_2 + X_{ci}\cos\gamma_2 - Y_{ci}\sin\gamma_2 - X_{bi}\right)^2 \\ &\qquad + \left(v_2 + X_{ci}\sin\gamma_2 + Y_{ci}\cos\gamma_2 - Y_{bi}\right)^2 - {s_i}^2 \leq 0, \\ &\qquad\qquad i = 1, 2, \cdots, N\end{aligned} \tag{9}$$

where $\mathbf{R}_{3\times1}$ denotes three-dimensional real vector space.

3.1.2. Solving Method of Search Problem. The judgment of assembly feasibility depends on solving the search problem modeled by (9). As a common search algorithm, sequential search algorithm is used. The search object is $\boldsymbol{\tau}_2 = [\gamma_2 \ u_2 \ v_2]^{\mathrm{T}}$ with three dimensions. The search space is difficult to narrow, due to the non-linearity of the functions $\hat{f}_{ai}$, $i = 1, 2, \ldots, N$. Therefore, the solving of this search problem is inefficient because of the multi-dimensional search object and the large search space. To improve the efficiency, the dimensionality of search object is reduced into one, and the search space is reasonably narrowed.

The feasible solution space of the search object $\boldsymbol{\tau}_2$ can be shown in a Cartesian coordinate system $o_2 - u_2v_2\gamma_2$. Referring to Figure 4, the feasible solution space for an inequality $\hat{f}_{ai} \leq 0$ is denoted as $\mathbf{D}_{fai}$. When γ_2 is constant, $\mathbf{D}_{fai}$ is a certain circle, and its radius always equals to s_i. Besides, the locus of center of this circle with γ_2 is a right-hand circular helix. Then the feasible solution space under constraints of N planar hole-pin-hole pairs, denoted as $\mathbf{D}_{fa\_in}$, can be expressed as the intersection of the spaces $\mathbf{D}_{fai}, i = 1, 2, \ldots, N$. Figure 5 shows an example of non-empty $\mathbf{D}_{fa\_in}$ when N=2.

When γ_2 is constant, $\mathbf{D}_{fa\_in}$ represents the intersection of N circles with the known centers and radii. The situation of this intersection denoted as $S_{fa\_in}(\gamma_2)$ can be judged with a geometry algorithm [21] especially when N>2. It is assumed that when the intersection is empty, $S_{fa\_in}(\gamma_2) < 0$; when the intersection is only a point, $S_{fa\_in}(\gamma_2) = 0$; otherwise, $S_{fa\_in}(\gamma_2) > 0$. Then (9) can be redefined as follows: if there exits at least one real γ_2 such that the intersection of N circles is non-empty, then assembly feasibility of the mechanical structure is ensured. The mathematical expression is

$$\exists \gamma_2 \in \mathbf{D}_{se\_\gamma2} : S_{fa\_in}(\gamma_2) \geq 0 \tag{10}$$

where $\mathbf{D}_{se\_\gamma2} = \{\gamma_2 \mid \gamma_2 \in [\gamma_{2se\_\min}, \gamma_{2se\_\max}]\}$ denotes the search space of γ_2, which is determined as follows:

(a) The ranges of γ_2 under constraints of each two planar hole-pin-hole pairs are successively calculated. For example, as shown in Figure 5, the range of γ_2 is denoted as $\gamma_2 \in [\gamma_{2\_12\_\min}, \gamma_{2\_12\_\max}]$. According to geometric characteristic of $\mathbf{D}_{fa1}$ and $\mathbf{D}_{fa2}$, $\gamma_{2\_12\_\min}$, and $\gamma_{2\_12\_\min}$ correspond to the situations when the two circles $\hat{f}_{a1}(\gamma_{2\_12\_\min,\max}, u_2, v_2) \leq 0$ and $\hat{f}_{a2}(\gamma_{2\_12\_\min,\max}, u_2, v_2) \leq 0$ are externally tangent as

$$\begin{aligned}&\left[-a_2\sin\gamma_{2\_12\_\min,\max} + a_1\cos\gamma_{2\_12\_\min,\max} + a_3\right]^2 \\ &\quad + \left[a_1\sin\gamma_{2\_12\_\min,\max} + a_2\cos\gamma_{2\_12\_\min,\max} + a_4\right]^2 \\ &\quad - {a_5}^2 = 0\end{aligned} \tag{11}$$

where $a_1 = X_{c2} - X_{c1}$, $a_2 = Y_{c2} - Y_{c1}$, $a_3 = X_{b1} - X_{b2}$, $a_4 = Y_{b1} - Y_{b2}$, and $a_5 = s_1 + s_2$.

If (11) has no real solutions, this range of γ_2 is empty.

(b) The intersection of these ranges of γ_2 in (a) is calculated as $\mathbf{D}_{se\_\gamma2}$.

As shown in Figure 6, if $\mathbf{D}_{se\_\gamma2}$ is empty, it is sure that the assembly is infeasible; but if $\mathbf{D}_{se\_\gamma2}$ is non-empty, the feasibility of assembly is still not ensured and the search algorithm has to be performed, unless N=2.

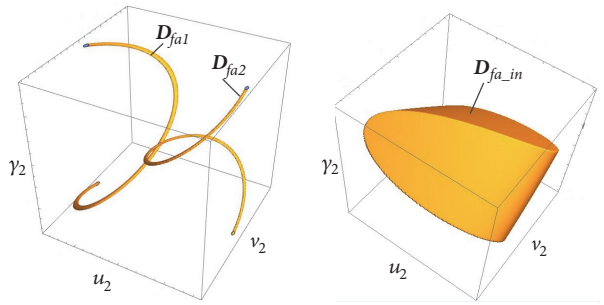

(a) Two feasible solution spaces $\mathbf{D}_{fa1}$ and $\mathbf{D}_{fa2}$

(b) Intersection of the spaces $\mathbf{D}_{fa1}$ and $\mathbf{D}_{fa2}$

Figure 5: Feasible solution space under constraints of two planar hole-pin-hole pairs.

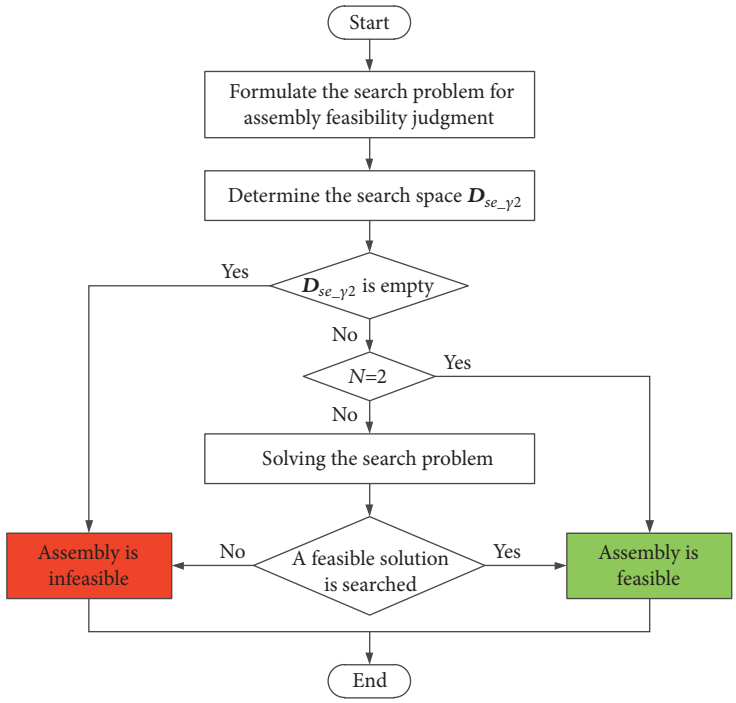

Figure 6: Flow chart of solving search problem.

3.2. Assembly Deviation Determination. Assembly deviations are difficult to quantify in over-constrained mechanical structure due to uncertainty of gaps, when the assembly is feasible. Here, the influence of gravity is considered. According to the principle of minimum potential energy, the gravitational potential energy of Part 2 tends to be minimum. In other words, the center of gravity of Part 2 drops along the direction of gravitational field as large as possible, within the constraints of satisfying assembly requirement. Therefore this section involves an optimization problem. Furthermore, the non-linear studied constraints make the optimization difficult to solve. Firstly the optimization problem is modeled. Then similarly to Section 3.1, a solving method is given by reducing dimensionality of optimization object and narrowing search space, to improve both accuracy and efficiency. Finally, the assembly deviations of functional points are calculated, and the quality feasibility is judged.

3.2.1. Optimization Problem Modeling. As shown in Figure 1, the coordinates of G w.r.t. PCS_2 are denoted as $\mathbf{G}^2 = [x_g \;\; y_g]^{\mathrm{T}}$, and it is assumed that $\mathbf{G}^2 = {}^0\mathbf{G}^2$. When Part 2 is in the nominal position and has the deviation $\boldsymbol{\tau}_2$ w.r.t. GCS, the coordinates of G w.r.t. GCS are denoted as $\mathbf{G}^G = [X_g \;\; Y_g]^{\mathrm{T}}$ and $\mathbf{G}^{G'} = [X_g' \;\; Y_g']^{\mathrm{T}}$ respectively, which can be calculated similarly to (4)-(5), as

$$\left[\mathbf{G}^G \;\; 1\right]^{\mathrm{T}} = \mathbf{T}_2^G \left[\mathbf{G}^2 \;\; 1\right]^{\mathrm{T}} \tag{12}$$

$$\left[\mathbf{G}^{G'} \;\; 1\right]^{\mathrm{T}} = \mathbf{T}_2 \left[\mathbf{G}^G \;\; 1\right]^{\mathrm{T}} \tag{13}$$

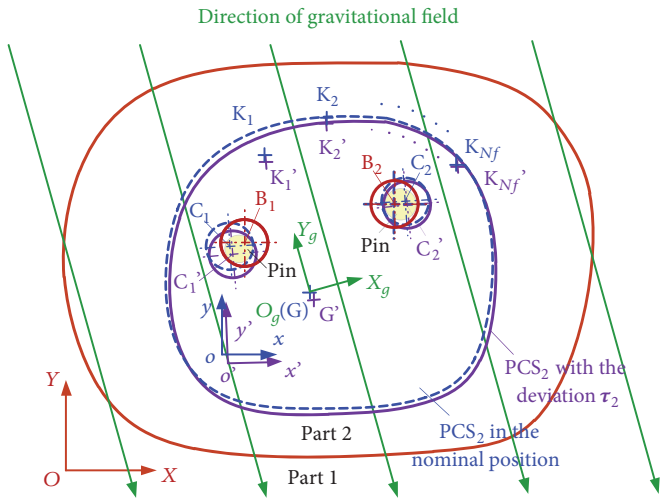

FIGURE 7: Assembly under constraints of two planar hole-pin-hole pairs with considering gravity influence.

Then with the deviation $\boldsymbol{\tau}_2$, the coordinates of G w.r.t. GFCS are $\mathbf{G}^{g\prime} = \left[X_g^{g\prime} \quad Y_g^{g\prime}\right]^{\mathrm{T}}$ as

$$\left[\mathbf{G}^{g\prime} \quad 1\right]^{\mathrm{T}} = \left(\mathbf{T}_g^G\right)^{-1}\left[\mathbf{G}^{G\prime} \quad 1\right]^{\mathrm{T}} \tag{14}$$

Here, Y_g-axis of GFCS has the angle θ from Y-axis of GCS. Then (14) can be arranged as

$$\begin{aligned} X_g^{g\prime} &= \left(X_g \cos\gamma_2 - Y_g \sin\gamma_2 + u_2 - X_g\right)\cos\theta \\ &\quad + \left(X_g \sin\gamma_2 + Y_g \cos\gamma_2 + v_2 - Y_g\right)\sin\theta \\ Y_g^{g\prime} &= -\left(X_g \cos\gamma_2 - Y_g \sin\gamma_2 + u_2 - X_g\right)\sin\theta \\ &\quad + \left(X_g \sin\gamma_2 + Y_g \cos\gamma_2 + v_2 - Y_g\right)\cos\theta \end{aligned} \tag{15}$$

where $Y_g^{g\prime}$ is the coordinate of G against the direction of gravitational field.

When the influence of gravity is considered, $Y_g^{g\prime}$ is minimum within the constraints of satisfying assembly requirement, according to the principle of minimum potential energy. The optimization model is constructed as

$$\begin{aligned} \min \quad & F_{fd}\left(\boldsymbol{\tau}_2\right) = Y_g^{g\prime}\left(\boldsymbol{\tau}_2\right) \\ \text{s.t.} \quad & \boldsymbol{\tau}_2 \in \mathbf{D}_{fa\_in} \end{aligned} \tag{16}$$

where $\boldsymbol{\tau}_2$ is the optimization object, $F_{fd}(\boldsymbol{\tau}_2)$ is the objective function, and $\boldsymbol{\tau}_2 \in \mathbf{D}_{fa\_in}$ is the constraint condition.

Without considering the influence of gravity and other physical factors, the deviation $\boldsymbol{\tau}_2$ is randomly distributed within the feasible solution space $\mathbf{D}_{fa\_in}$. When the influence of gravity on the assembly deviations is taken into account (the influence of other physical factors is not considered), the value of $\boldsymbol{\tau}_2$ corresponds to the optimal solution of (16). Figure 7 shows an example of the assembly under constraints of two planar hole-pin-hole pairs. With considering the gravity influence, the center of gravity G on Part 2 moves along the direction of gravitational field to the farthest position allowed by the assembly constraints.

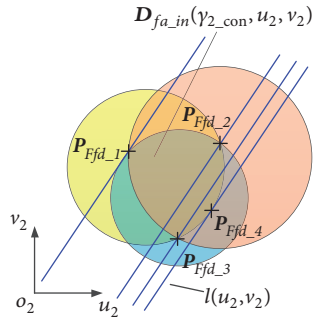

FIGURE 8: Constraint condition and objective function with constant γ_2.

3.2.2. Optimization Problem Solving. The assembly deviations correspond to the optimal solution of (16). As a selective search algorithm, PSO algorithm is used to solve the optimization problem. This optimization solving is difficult due to the non-linear constraint $\boldsymbol{\tau}_2 \in \mathbf{D}_{fa\_in}$. Here, the dimensionality of search object is reduced, and the search space is calculated, to improve the accuracy and efficiency of solving.

As seen in (16), when γ_2 equals a real constant γ_{2_con}, the constraint $\boldsymbol{\tau}_2 \in \mathbf{D}_{fa\_in}(\gamma_{2\_con}, u_2, v_2)$ represents the intersection of N known circles by referring to Section 3.1, and the objective function $F_{fd}(\gamma_{2\_con}, u_2, v_2)$ is regarded as a line. The slope of this line is unchangeable, which is only related to the direction of gravitational field. The line equation denoted as $l(u_2,v_2)$ is

$$l\left(u_2, v_2\right) = au_2 + bv_2 + c \tag{17}$$

where $a = -\sin\theta$, $b = \cos\theta$, $c = (-X_g \sin\theta + Y_g \cos\theta)(\cos\gamma_{2\_con} - 1) + (Y_g \sin\theta + X_g \cos\theta)\sin\gamma_{2\_con}$.

Therefore, the optimization modeled by (16) can be treated a LP problem when $\gamma_2 = \gamma_{2\_con}$. Figure 8 gives a graphical schematic of constraint condition and objective function when N=3. Here, the minimum value of $F_{fd}(\gamma_{2\_con}, u_2, v_2)$

is denoted as $F_{fd\_\min}(\gamma_{2\_con}, u_2, v_2)$. The coordinates of the point corresponding to $F_{fd\_\min}(\gamma_{2\_con}, u_2, v_2)$ are denoted as $\mathbf{P}_{Ffd\_\min} = \begin{bmatrix} u_{2\_Ffd\_\min} & v_{2\_Ffd\_\min} \end{bmatrix}^{\mathrm{T}}$. Obviously, this point belongs to intersection points of the arcs which comprise boundary of the domain $\mathbf{D}_{fa\_in}(\gamma_{2\_con}, u_2, v_2)$, or tangency points of the line $l(u_2, v_2)$ and these arcs. Furthermore, it is certain that $\mathbf{P}_{Ffd\_\min}$ depends on γ_{2_con}, i.e., $u_{2\_Ffd\_\min} = u_2(\gamma_{2\_con})$, $v_{2\_Ffd\_\min} = v_2(\gamma_{2\_con})$. Hence, (16) can be remodeled with a nested LP as

$$\begin{aligned} \min \quad & F_{fd\_\min}\left(\gamma_2, u_2\left(\gamma_2\right), v_2\left(\gamma_2\right)\right) \\ \text{s.t.} \quad & \gamma_2 \in \mathbf{D}_{fa\_in\_\gamma 2} \end{aligned} \tag{18}$$

where the search space $\mathbf{D}_{fa\_in\_\gamma 2} = \{\gamma_2 \mid \gamma_2 \in [\gamma_{2\min}, \gamma_{2\max}]\}$ is the range of γ_2 in $\mathbf{D}_{fa\_in}$, which is calculated as follows: As seen in Section 3.1, a feasible solution of (10), denoted as γ_{2_a}, has been found to ensure the assembly feasibility of the mechanical structure. It is obvious that $\gamma_{2\_a} \in [\gamma_{2\min}, \gamma_{2\max}]$. Moreover, for the search space of (10) denoted as $\mathbf{D}_{se\_\gamma 2} = \{\gamma_2 \mid \gamma_2 \in [\gamma_{2se\_\min}, \gamma_{2se\_\max}]\}$, it is definite that $\mathbf{D}_{se\_\gamma 2} \supseteq \mathbf{D}_{fa\_in\_\gamma 2}$, and then $\gamma_{2se\_\min} \le \gamma_{2\min} \le \gamma_{2\_a}$ and $\gamma_{2\_a} \le \gamma_{2\max} \le \gamma_{2se\_\max}$. $\gamma_{2\min}$ and $\gamma_{2\max}$ can be approximately calculated by binary search algorithm. Especially, when N=2, $\gamma_{2\min} = \gamma_{2se\_\min}$ and $\gamma_{2\max} = \gamma_{2se\_\max}$, thus the binary search algorithm is omitted.

3.2.3. Assembly Deviation Calculation and Quality Feasibility Judgment. By the solving method in Section 3.2.2, the optimal solutions of the optimization model (18), as well as the global best particle $\boldsymbol{\tau}_{2\_g}$, are determined. Then the coordinates of functional point K_j w.r.t. FPCS_j, $j = 1, 2, \ldots, N_f$, are calculated as

$$\begin{aligned} \left[\mathbf{K}_{j\_g}^{fj\ \prime} \quad 1\right]^{\mathrm{T}} &= \left(\mathbf{T}_{fj}^{G}\right)^{-1} \mathbf{T}_{2\_g} \left[\mathbf{K}_{j}^{G} \quad 1\right]^{\mathrm{T}}, \\ & j = 1, 2, \cdots, N_f \end{aligned} \tag{19}$$

where $\mathbf{T}_{2\_g} = \mathbf{T}_2(\boldsymbol{\tau}_{2\_g})$ and $\mathbf{K}_{j\_g}^{fj\ \prime} = \left[X_{fj\_g}^{fj\ \prime} \quad Y_{fj\_g}^{fj\ \prime}\right]^{\mathrm{T}}$, $j = 1, 2, \ldots, N_f$, represent the assembly deviations.

The quality requirement is denoted as $\mathbf{QR} = [\mathbf{QR}_1 \quad \mathbf{QR}_2 \quad \cdots \quad \mathbf{QR}_{Nf}]$, where $\mathbf{QR}_j = \left[\mathbf{QR}_j^{Xfj} \quad \mathbf{QR}_j^{Yfj}\right]^{\mathrm{T}}$ and $\mathbf{QR}_j^{Xfj} = \{X_{QRj} \mid X_{QRj} \in [X_{QRj\_\min}, X_{QRj\_\max}]\}$, $\mathbf{QR}_j^{Yfj} = \{Y_{QRj} \mid Y_{QRj} \in [Y_{QRj\_\min}, Y_{QRj\_\max}]\}$, $j = 1, 2, \ldots, N_f$. An assembly is regarded to be qualified when all the assembly deviations of functional points meet the quality requirement, i.e., $X_{fj\_g}^{fj\ \prime} \in \mathbf{QR}_j^{Xfj}$ and $Y_{fj\_g}^{fj\ \prime} \in \mathbf{QR}_j^{Yfj}$, $j = 1, 2, \ldots, N_f$.

4. Statistical Tolerance Analysis

Because as deviation sources, manufacturing deviations of parts are generally random deviations within their tolerance zones and statistical analysis is necessary rather than a single case analysis. As one of the most common methods for statistical analysis, the MCS is often computationally expensive and time-consuming, but quite comprehensive and easy to use even for implicit and non-linear problems. The MCS with deviation propagation analysis in Section 3 is used to perform statistical tolerance analysis. The flowchart of the statistical analysis is shown in Figure 9.

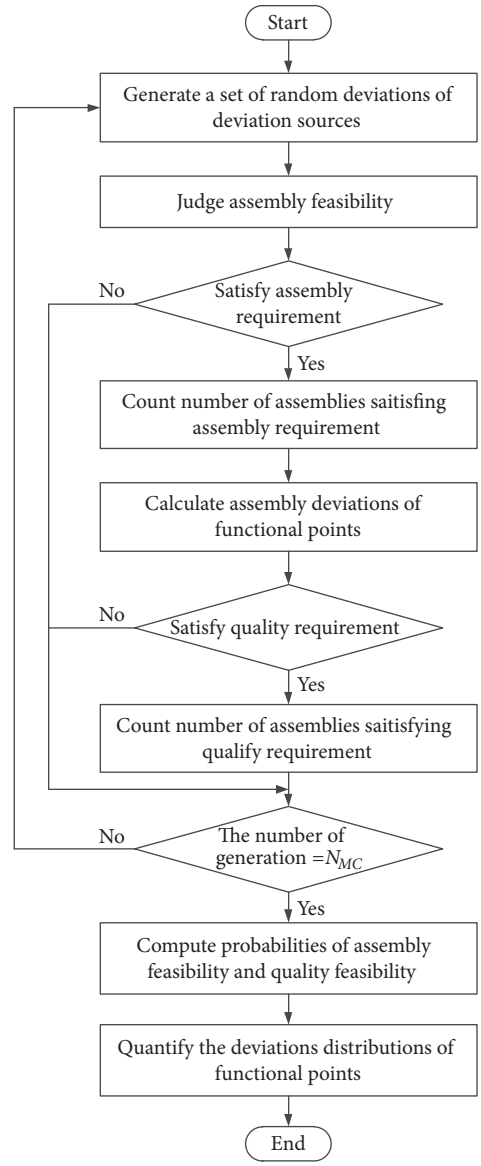

Figure 9: Flow chart of statistical tolerance analysis.

Iteratively, a set of random deviations of the sources are generated within their tolerance zones; then the assembly feasibility is judged; for the feasible assembly, the assembly deviations of functional points are calculated and the quality feasibility is judged. The process of random generation, judgment and calculation is iterated until the samples are enough. As to random generation of deviations within their tolerance zones, it is assumed that the deviations are independent of one another and present normal distributions, and the deviations and their tolerances have a relationship as $T = 6\sigma$.

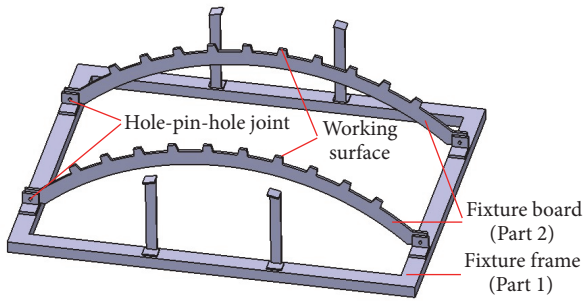

Figure 10: An assembly fixture with boards.

After all the iterations, the probabilities of assembly feasibility and quality feasibility are estimated as [8]

$$P_{a,q} = \frac{1}{N_{MC}} \sum_{i=1}^{N_{MC}} I_{a,q}(\mathbf{M}) \tag{20}$$

where N_{MC} is the maximum number of iterations of the MCS and $I_{a,q}(\mathbf{M})$ is an indicator function. The functions for assembly requirement and quality requirement are

$$I_a(\mathbf{M}) = \begin{cases} 1, & \text{if the assembly is feasible} \\ 0, & \text{if the assembly is infeasible} \end{cases} \tag{21}$$

$$I_q(\mathbf{M}) = \begin{cases} 1, & \text{if the quality requirement is fulfilled} \\ 0, & \text{if the quality requirement is unfulfilled} \end{cases} \tag{22}$$

Furthermore, for feasible assemblies, the deviations distributions of functional points can be quantified, where the frequency distributions and the statistical characteristics are computed, seen in Section 5.

For the statistical tolerance analysis, the input is deviation sources, and the output contains probabilities of assembly feasibility and quality feasibility, as well as deviations distributions of functional points for feasible assemblies.

5. Case Studies

The proposed method is applied to two cases. Firstly stability and accuracy of the optimization seen in Section 3.2 are verified. Then the output results of statistical tolerance analysis for the gap configuration influenced by gravity are compared with the output results for random configuration and worst configuration of gaps.

The computational works are implemented by MATLAB. For sequential and binary search algorithms seen in Section 3, the precision is set as 10^{-7} for γ_2. In the statistical tolerance analysis with MC simulation seen in Section 4, the number of iterations in an experiment is set as N_{MC}=10000.

5.1. Case Description

Case 1. This case is from a fixture with boards as shown in Figure 10, which is widely used for locating aircraft panels in the panel assembly process. The small working surfaces on a fixture board are applied to constraining the normal displacement of the panels. Each fixture board is mounted on fixture frame with two planar hole-pin-hole joints. This case is the assembly of a fixture board and a fixture frame, denoted as Part 1 and Part 2. Each small working surface of Part 2 is abstracted as a functional point.

Figure 11 shows the definition of CSs. For simplicity, the axes of GCS, GFCS, and nominal PCS_2 are assumed to be all parallel to each other. As to FPCSs, three of the functional points are selected for discussion. The Y_{fj}-axis (j=1,2,3) of a FPCS is along the nominal normal direction of the corresponding working surface. The dimensions and tolerances are shown in Figure 12. The fit tolerances of hole-pin-hole pairs are both H7/g7/H7. The coordinates of related points w.r.t. GCS/PCS_2 are as $\mathbf{B}_1^G = [195 \ 246.126]^T$, $\mathbf{B}_2^G = [2805 \ 246.126]^T$, $\mathbf{o}^G = [1500 \ 200]^T$, and $\mathbf{C}_1^2 = [-1305 \ 46.126]^T$, $\mathbf{C}_2^2 = [1305 \ 46.126]^T$, $\mathbf{G}^2 = [0 \ 524.435]^T$, $\mathbf{O}_k^2 = [0 \ -1200]^T$. Besides, the quality requirement is $\mathbf{QR} = [\mathbf{QR}_1 \ \mathbf{QR}_2 \ \mathbf{QR}_3]$, where $\mathbf{QR}_j = \mathbf{QR}_j^{Yfj} = \{Y_{QRj} \mid Y_{QRj} \in [-0.07, 0.07]\}$, j=1,2,3.

Case 2. This case is the assembly of two aircraft fuselage sections from a type of military aircraft. The front section and the rear section, denoted as Part 1 and Part 2, are assembled with the constraints of eighteen hole-pin-hole pairs on planar bulkheads. The quality requirement concerns the displacement deviations of Part 2 w.r.t Part 1.

Figure 13 shows the CSs, dimensions and tolerances. In order to simplify the computation, it is assumed that GCS, GFCS, FPCS and nominal PCS_2 are all coincided with each other. Besides, the fit tolerances of hole-pin-hole pairs are all D8/d7/D8. The quality requirement is $\mathbf{QR} = \left[\mathbf{QR}^{Xf} \ \mathbf{QR}^{Yf}\right]^T$, $\mathbf{QR}^{Xf} = \{X_{QR} \mid X_{QR} \in [-0.1, 0.1]\}$, and $\mathbf{QR}^{Yf} = \{Y_{QR} \mid Y_{QR} \in [-0.1, 0.1]\}$.

5.2. Stability and Accuracy of Optimization (PSO).

As seen in Section 3, PSO is used to determine assembly deviations, which further impacts the output results of statistical tolerance analysis. In this PSO algorithm, the swarm size is 10, and the number of iterations is 20. PSO is a heuristic optimization algorithm, with simple parameters and fast convergence, but it is easily trapped into local optimum. Therefore, it is necessary to verify stability and accuracy of this optimization algorithm.

Firstly, the experiment of statistical tolerance analysis is performed and repeated 10 times, and the 10 sets of output results are observed and compared. In order to eliminate the disturbance of different generated deviation sources, the same N_{MC} sets of deviation sources are required for all experiments.

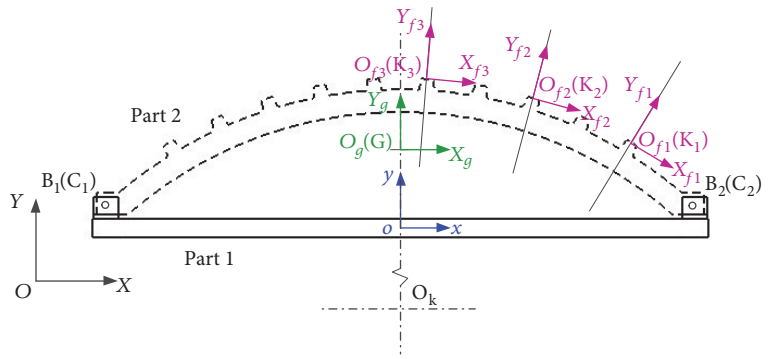

Figure 11: CSs of a fixture frame and a fixture board.

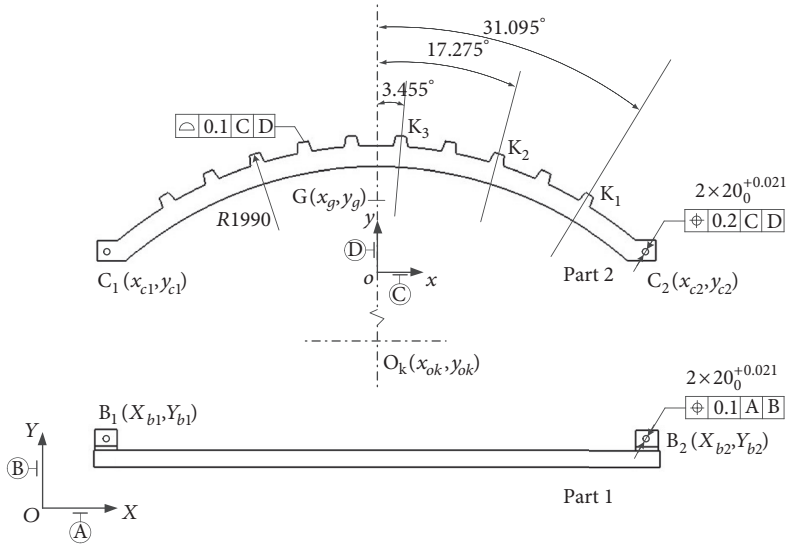

Figure 12: Dimensions and tolerances of a fixture frame and a fixture board.

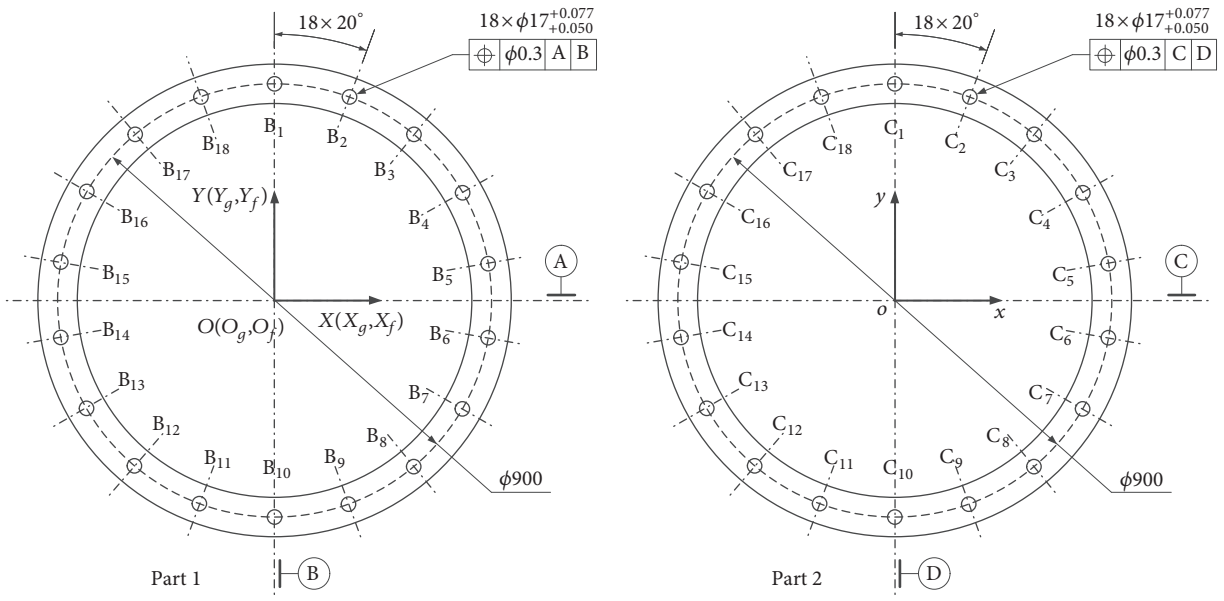

Figure 13: CSs, Dimensions and tolerances of two fuselage sections.

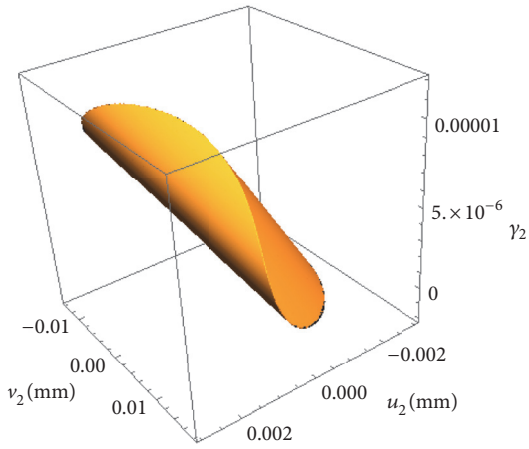

Figure 14: A feasible solution space for Case 1.

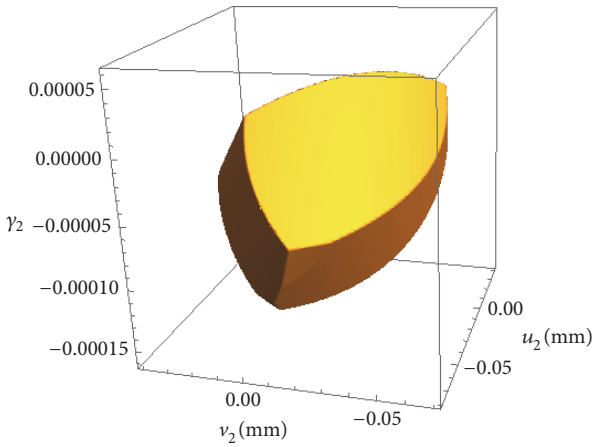

Figure 15: A feasible solution space for Case 2.

Three iterative sub-processes are separated from the experiment process. The iterative sub-process of deviation sources generation is denoted as Sub-process 1, and N_{MC} sets of generated deviation sources are stored in a matrix $\mathbf{H}_M$. Then with these deviation sources, the iterative sub-process of assembly feasibility judgment is denoted as Sub-process 2, and N_a ($N_a \leq N_{MC}$) sets of deviation sources, which can make sure the feasibility of assembly, are selected and stored in a matrix $\mathbf{H}_a$. Finally, with the deviation sources from $\mathbf{H}_a$, the iterative sub-process of assembly deviation calculation and quality feasibility judgment is denoted as Sub-process 3. After the three sub-processes, the output results can be calculated.

Therefore, the 10 experiments are designed as: Sub-processes 1 and 2 are implemented in advance, and then Sub-process 3 is repeated 10 times. The 10 sets of output results with 4 figures after the decimal point are all the same, as shown in Table 1 for Case 1 and Table 2 for Case 2, where deviations of functional points (denoted as DFP) are classified into the deviations satisfying quality requirement (denoted as DFP_QR) and that not satisfying quality requirement (denoted as DFP_NQR).

For further verification, with a set of deviation sources arbitrarily selected from $\mathbf{H}_a$, the PSO procedure is performed and repeated 10 times, and the 10 sets of optimization results are compared. Tables 3 and 4 show the selected deviation sources for Cases 1 and 2, respectively. The corresponding feasible solution space $\mathbf{D}_{fa\_in}$ is shown in Figure 14 for Case 1 and Figure 15 for Case 2. In the 10 PSO procedures, the global best particles γ_2 and the corresponding Y_g-coordinates are shown in Figure 16 for Case 1 and Figure 17 for Case 2. It is observed that the 10 optimization procedures for each case are all convergent, and the 10 sets of optimization results, including global best particles and objective function values, are all the same when these values are rounded to 6 decimal places.

Therefore, Tables 1 and 2 and Figures 16 and 17 indicate this PSO algorithm is quite robust and accurate, and thus the output results of tolerance analysis by using the proposed method are reliable.

5.3. Comparison with Random Configuration and Worst Configuration of Gaps. The proposed method considers the influence of gravity on the gap configuration when determining the assembly deviations. In order to exhibit the significance of incorporating the influence of gravity to tolerance analysis, two comparison experiments with common gap configurations are given. The first comparison experiment is denoted as EX1, where the deviation $\boldsymbol{\tau}_2$ is randomly generated within the feasible solution space based on normal distribution. The second comparison experiment, denoted as EX2, uses the worst configuration of gaps, which makes the assembly deviations largest. Besides, the experiment considering the gravity influence is denoted as EX0.

In EX 2, the determination of the worst configuration of gaps is an optimization problem. The modeling and solving of this optimization are both similar to (16)-(19). For example, worst gap configuration corresponds to the largest assembly deviation of the jth functional point along Y_{fj}-axis. The optimization is modeled as seen in (23), and solved by PSO with a nested LP.

$$\begin{aligned} \max \quad & F_{fd\_wor}(\boldsymbol{\tau}_2) \\ & = \left| Y_{fj}^{fj\prime}(\boldsymbol{\tau}_2) - \frac{Y_{QRj\_\min} + Y_{QRj\_\max}}{2} \right| \\ \text{s.t.} \quad & \boldsymbol{\tau}_2 \in \mathbf{D}_{fa\_in} \end{aligned} \tag{23}$$

In EX2 of Case 1, it is assumed that the worst configuration of gaps corresponds to the largest assembly deviations of K_2 along Y_{f2}-axis. In EX2 of Case 2, the worst configuration of gaps is assumed to concern the largest assembly deviations along Y-axis, to make a straight comparison between the output results of EX2 and EX0.

The output results of EX0, EX1 and EX2 are compared. In order to avoid the distractions of different generated deviation sources, the three experiments, denoted as a group of experiments, are designed as follows: Sub-processes 1 and

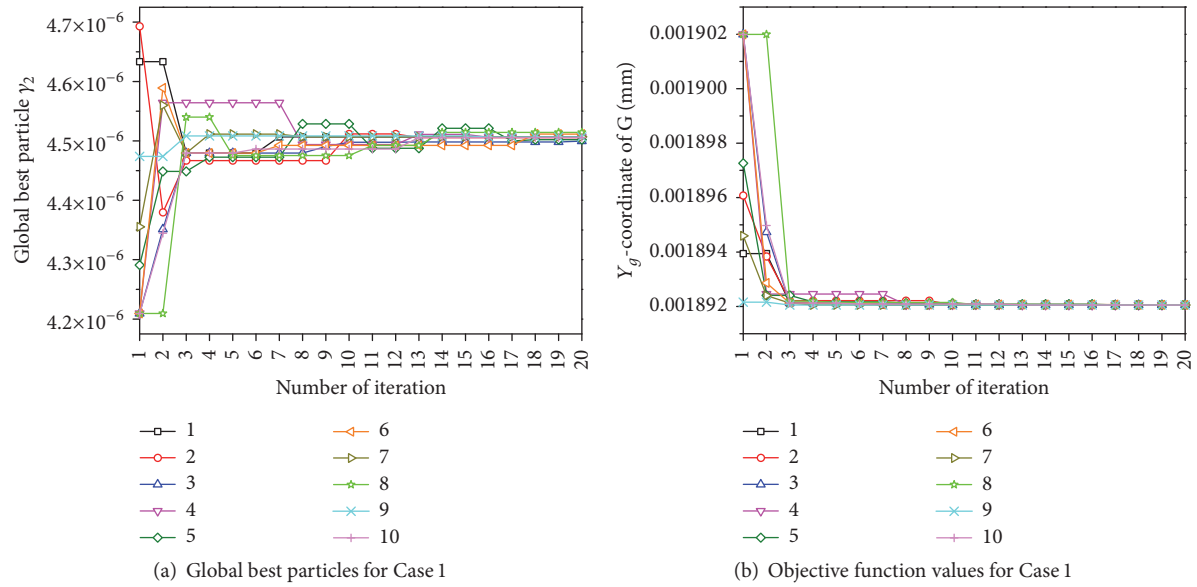

(a) Global best particles for Case 1

(b) Objective function values for Case 1

Figure 16: Global best particles and objective function values of PSO procedures for Case 1.

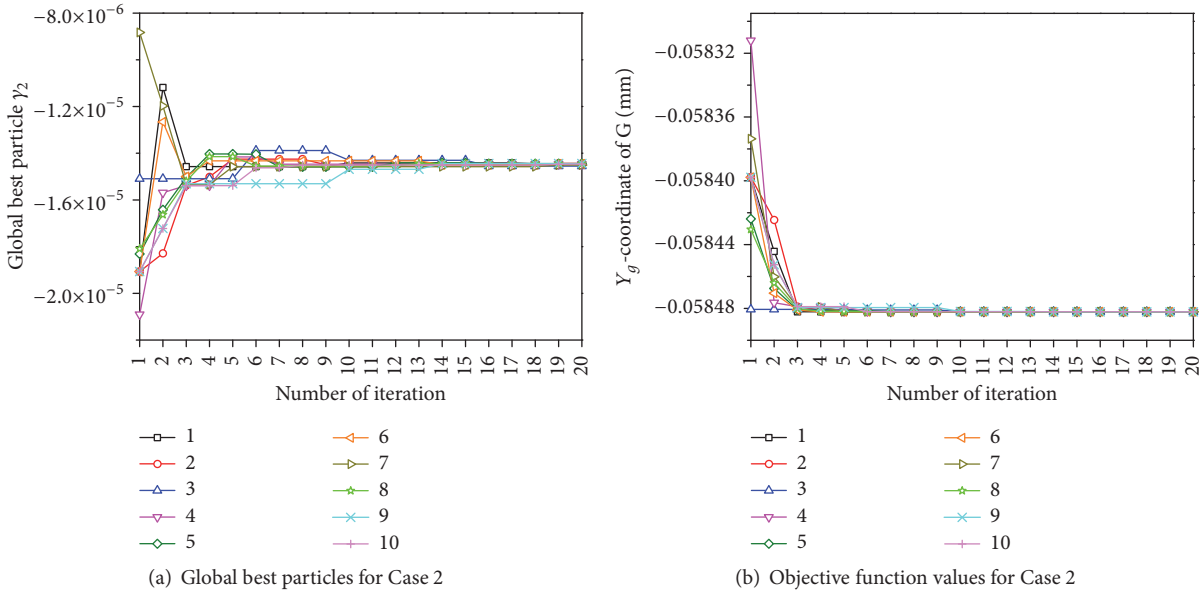

(a) Global best particles for Case 2

(b) Objective function values for Case 2

Figure 17: Global best particles and objective function values of PSO procedure for Case 2.

2 are implemented in advance, and then Sub-process 3 for EX0, EX1, and EX2 is performed, respectively. To enhance the reliability of the predicted output results, a group of experiments are repeated 10 times, and the 10 groups of output results are averaged, which are shown in Table 5 for Case 1 and Table 6 for Case 2. Furthermore, by taking the output results of a group of experiments as examples, the distributions of assembly deviations are shown in Figure 18 for Case 1 and Figure 19 for Case 2, and the distributions of the corresponding $\boldsymbol{\tau}_2$ are shown in Figure 20 for Case 1 and Figure 21 for Case 2.

From Tables 5 and 6 and Figures 18–21, the following is observed:

(1) As to EX0, except for the output results along X-axis of Case 2, the mean of DFP is unequal to 0. The DFP_NQR and the corresponding $\boldsymbol{\tau}_2$ are unsymmetrically distributed. This may be because of the following: (a) part 2 (PCS_2) drops along one constant direction to the boundary of feasible solution space $\mathbf{D}_{fa\_in}$, where the constant direction is related to Y_g-axis; (b) Y_{fj}-axis, $j = 1, 2, \ldots, N_f$, is not perpendicular to Y_g-axis.

(2) As to EX1, P_q is the highest. The DFP_NQR and the corresponding $\boldsymbol{\tau}_2$ are symmetrically distributed. This may be due to the normal distribution of $\boldsymbol{\tau}_2$ within $\mathbf{D}_{fa\_in}$. The deviation $\boldsymbol{\tau}_2$ in the center of $\mathbf{D}_{fa\_in}$ has much more probabilities to be selected than the one around the boundary

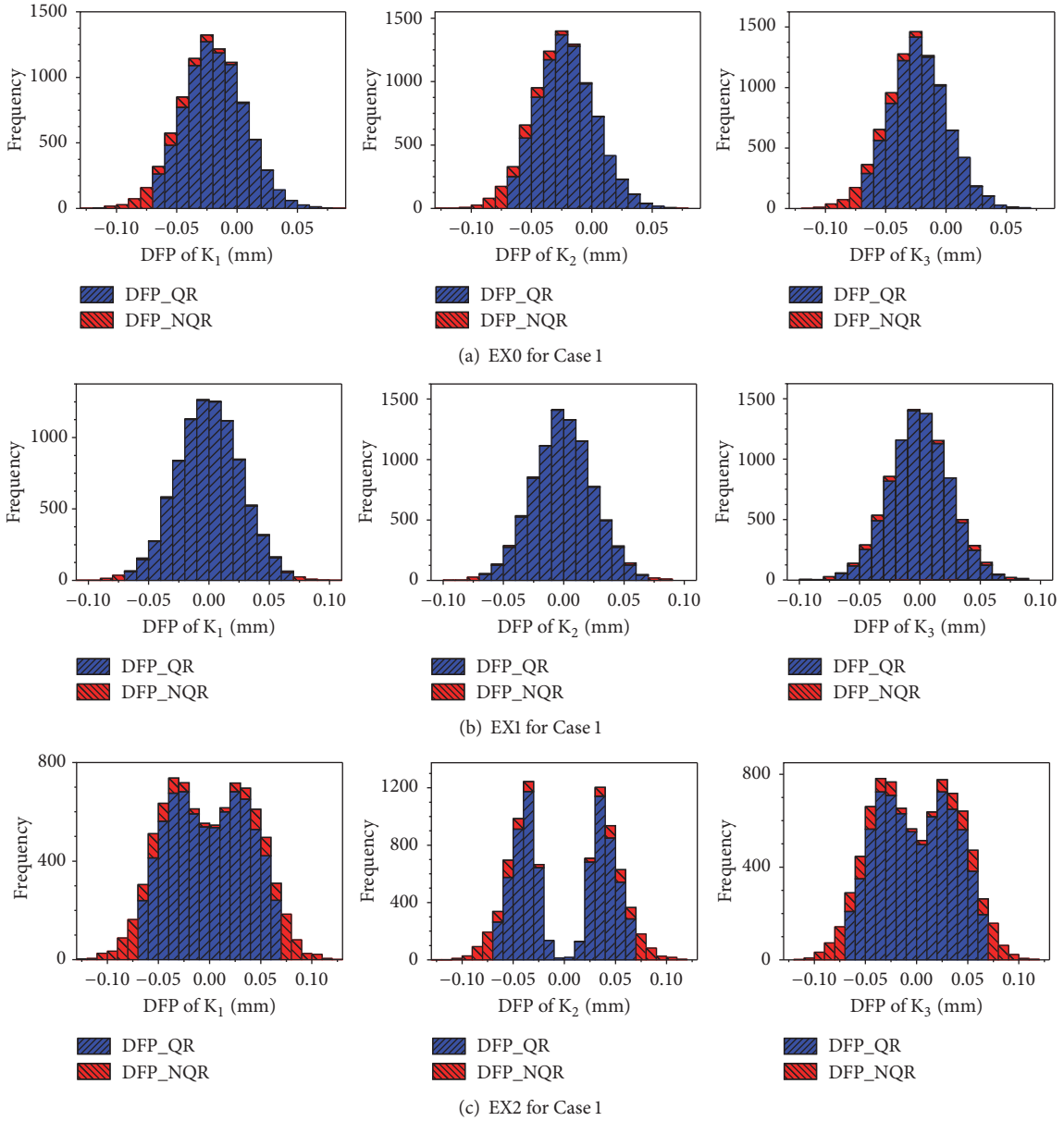

Figure 18: Distributions of assembly deviations for Case 1.

Table 1: Output results of experiments for Case 1.

Output result		K_1	K_2	K_3
Probability of quality feasibility (P_q)			80.22%	
DFP	Mean(mm)	-0.0208	-0.0235	-0.0243
	Standard deviation(mm)	0.0267	0.0255	0.0250
DFP_QR	Mean(mm)	-0.0177	-0.0204	-0.0213
	Standard deviation(mm)	0.0242	0.0231	0.0227

of $\mathbf{D}_{fa\_in}$. The former one is more likely to correspond to the smaller DFP than the latter one.

(3) As to EX2, the P_q is the lowest. For the DFP corresponding to $Y_{fj}^{fj'}(\boldsymbol{\tau}_2)$ in (23), the standard deviation is markedly lager than that of EX0 and EX1. These DFP are bimodal distributed, and the DFP_NQR are symmetrically distributed. Furthermore, the point cloud of $\boldsymbol{\tau}_2$ has two areas of high-density points, and $\boldsymbol{\tau}_2$ corresponding to the DFP_NQR are also symmetrically distributed. This may be because the optimization function in (23) has the form "max $|\cdot|$". Part 2 may fall along two opposite directions to the

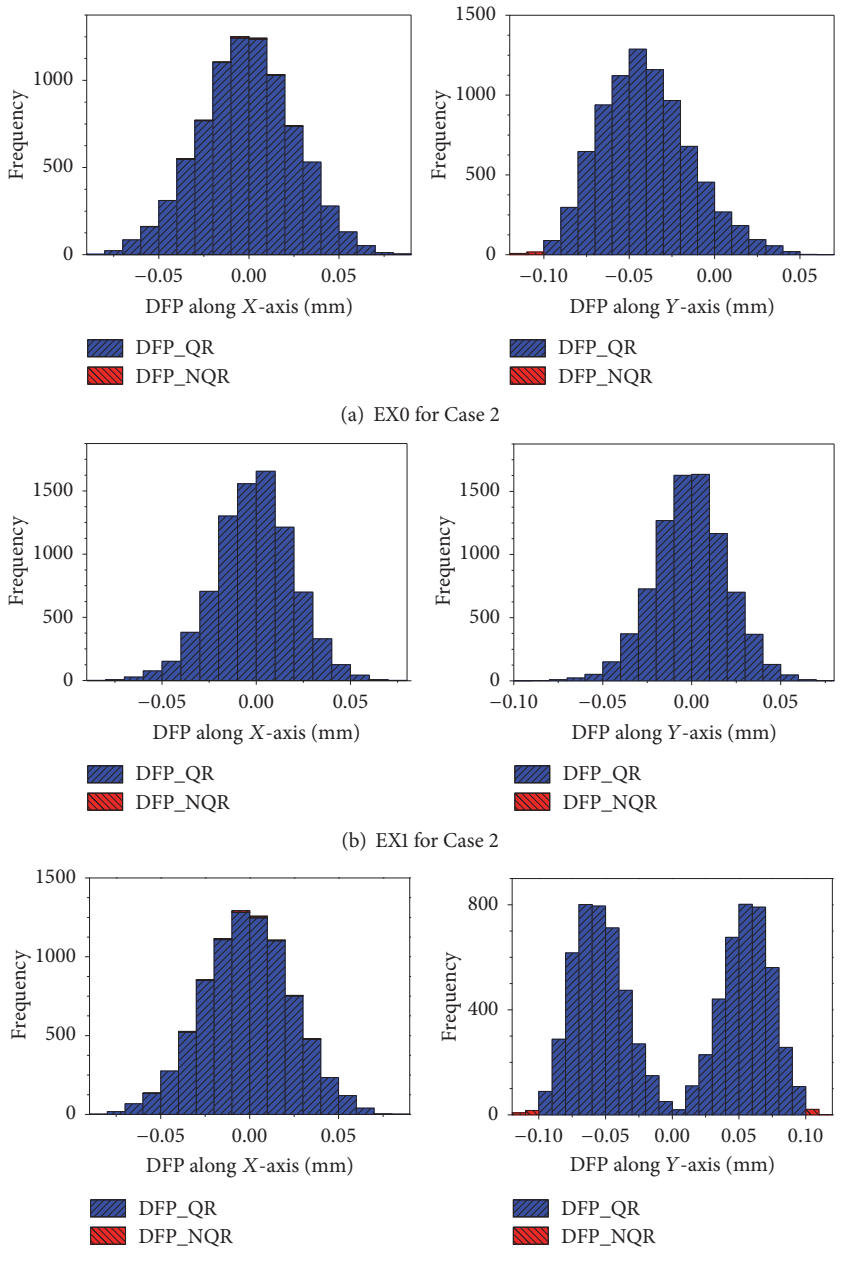

Figure 19: Distributions of assembly deviations for Case 2.

Table 2: Output results of experiments for Case 2.

Output result		X	Y
Probability of quality feasibility (P_q)		82.62%	
DFP	Mean(mm)	-0.0010	-0.0402
	Standard deviation(mm)	0.0261	0.0263
DFP_QR	Mean(mm)	-0.0010	-0.0400
	Standard deviation(mm)	0.0262	0.0261

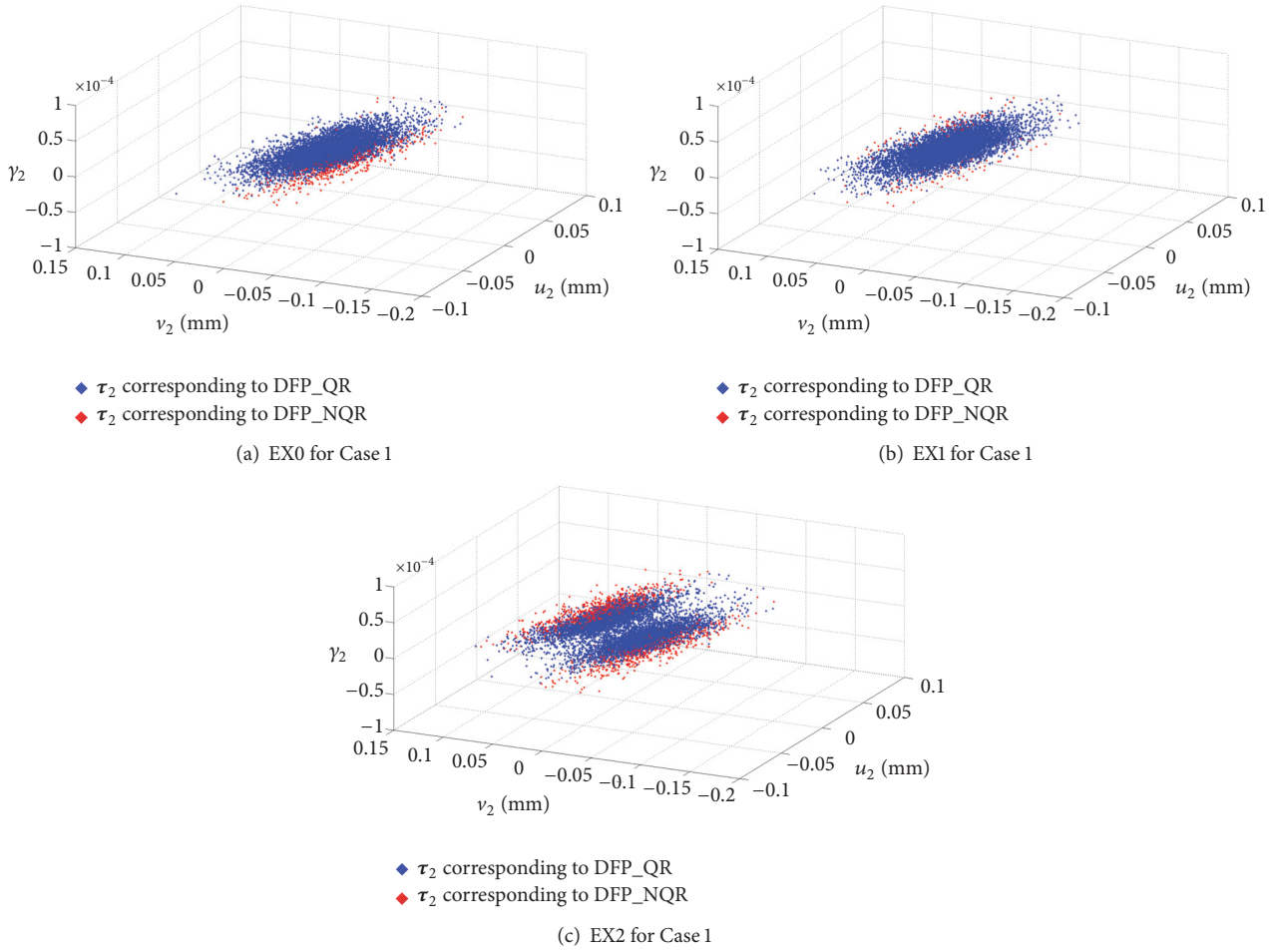

(a) EX0 for Case 1

(b) EX1 for Case 1

(c) EX2 for Case 1

Figure 20: Distributions of $\boldsymbol{\tau}_2$ for Case 1.

Table 3: A set of deviation sources for Case 1.

Deviation source	Coordinates of B_i w.r.t. GCS		Coordinates of C_i w.r.t. PCS_2		s_i
(mm)	X	Y	x	y	
Hole B_1-pin-Hole C_1	194.9787	246.1397	-1305.0518	46.1361	0.0324
Hole B_2-pin-Hole C_2	2804.9946	246.1302	1305.0297	46.1142	0.0351

boundary of $\mathbf{D}_{fa\_in}$, where the opposite directions are related to X_{fj}-axis or Y_{fj}-axis, $j = 1, 2, \ldots, N_f$.

Certainly the output results of EX0 are significantly different from that of EX1 and EX2. For the feasible assembly of over-constrained mechanical structure, gravity has a remarkable impact on gap configuration and then assembly deviations. The gravity influence in tolerance analysis of over-constrained assembly cannot be ignored.

6. Conclusions

This paper presents a tolerance analysis method for over-constrained assembly considering the influence of gravity. The proposed method contains deviation propagation analysis and statistical tolerance analysis. The probabilities of assembly feasibility and quality feasibility can be computed, and the deviations distributions for feasible assemblies can be quantified.

The detailed tolerance analysis process is illustrated for a typical over-constrained mechanical structure with constraints of multiple planar hole-pin-hole pairs. This type of constraints has non-linearity, which increases complexity of assembly tolerance analysis. In the deviation propagation analysis, the judgment of assembly feasibility and the calculation of assembly deviations are formulated as a search problem and an optimization problem, respectively. Due to the non-linear constraints, it is inefficient and difficult to solve these problems. In order to improve accuracy and efficiency, according to characteristic of this type of constraints, the search and optimization problems are solved by reducing object dimensionality and narrowing search space, where the search algorithms, such as sequential search and binary

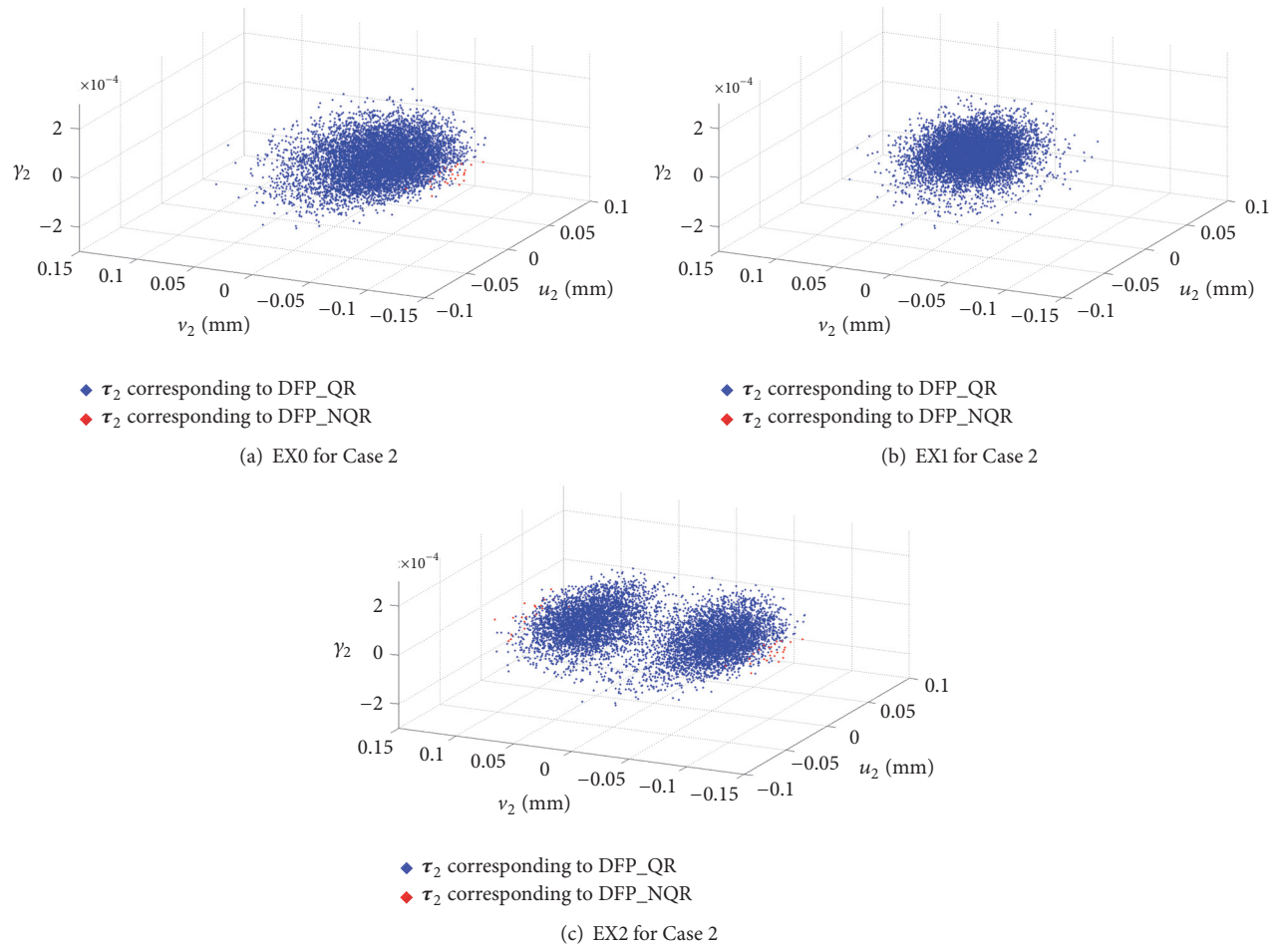

(a) EX0 for Case 2

(b) EX1 for Case 2

(c) EX2 for Case 2

Figure 21: Distributions of $\boldsymbol{\tau}_2$ for Case 2.

Table 4: A set of deviation sources for Case 2.

Deviation source (mm)	Coordinates of B_i w.r.t. GCS		Coordinates of C_i w.r.t. PCS_2		s_i
	X	Y	x	y	
Hole B_1-pin-Hole C_1	450.0372	-0.0106	449.9975	-0.0411	0.1358
Hole B_2-pin-Hole C_2	422.7972	153.8436	422.8378	153.9293	0.1250
Hole B_3-pin-Hole C_3	344.7235	289.2612	344.7289	289.2649	0.1273
Hole B_4-pin-Hole C_4	225.0135	389.7606	225.0130	389.7105	0.1300
Hole B_5-pin-Hole C_5	78.1725	443.1735	78.1648	443.1337	0.1236
Hole B_6-pin-Hole C_6	-78.0688	443.2002	-78.1283	443.1470	0.1217
Hole B_7-pin-Hole C_7	-225.0053	389.6915	-224.9820	389.6781	0.1264
Hole B_8-pin-Hole C_8	-344.7693	289.2210	-344.6785	289.2782	0.1218
Hole B_9-pin-Hole C_9	-422.8215	153.9050	-422.8642	153.9120	0.1149
Hole B_{10}-pin-Hole C_{10}	-450.0165	0.0108	-450.0530	0.0023	0.1264
Hole B_{11}-pin-Hole C_{11}	-422.8637	-153.9604	-422.8953	-153.9496	0.1298
Hole B_{12}-pin-Hole C_{12}	-344.7204	-289.2573	-344.6876	-289.2419	0.1211
Hole B_{13}-pin-Hole C_{13}	-224.9730	-389.7477	-224.9676	-389.7089	0.1179
Hole B_{14}-pin-Hole C_{14}	-78.1358	-443.1664	-78.1309	-443.1260	0.1352
Hole B_{15}-pin-Hole C_{15}	78.1410	-443.1581	78.1550	-443.2297	0.1315
Hole B_{16}-pin-Hole C_{16}	224.9878	-389.6686	224.9854	-389.7149	0.1369
Hole B_{17}-pin-Hole C_{17}	344.7059	-289.2523	344.6852	-289.1532	0.1266
Hole B_{18}-pin-Hole C_{18}	422.7669	-153.9629	422.8744	-153.8547	0.1373

Table 5: Output results of EX0, EX1, and EX2 for Case 1.

Output result			EX0	EX1	EX2
Probability of assembly feasibility (P_a)				87.01%	
Probability of quality feasibility (P_q)			80.24%	85.26%	73.55%
DFP	Mean(mm)	K_1	-0.021	0.000	0.000
		K_2	-0.023	0.000	0.000
		K_3	-0.024	0.000	0.000
	Standard deviation(mm)	K_1	0.026	0.026	0.042
		K_2	0.026	0.025	0.047
		K_3	0.025	0.025	0.041
DFP_QR	Mean(mm)	K_1	-0.018	0.000	0.000
		K_2	-0.020	0.000	0.000
		K_3	-0.021	0.000	0.000
	Standard deviation(mm)	K_1	0.024	0.025	0.036
		K_2	0.023	0.024	0.042
		K_3	0.023	0.024	0.035

Table 6: Output results of EX0, EX1, and EX2 for Case 2.

Output result			EX0	EX1	EX2
probability of assembly feasibility (P_a)				82.88%	
probability of quality feasibility (P_q)			82.61%	82.87%	82.38%
DFP	Mean(mm)	X	0.000	0.000	0.000
		Y	-0.040	0.000	0.000
	Standard deviation(mm)	X	0.026	0.021	0.025
		Y	0.026	0.021	0.058
DFP_QR	Mean(mm)	X	0.000	0.000	0.000
		Y	-0.040	0.000	0.000
	Standard deviation(mm)	X	0.026	0.021	0.025
		Y	0.026	0.021	0.058

search, as well as the optimization algorithms, such as PSO and LP, are used.

The results of the case studies show the following: (a) the PSO algorithm for the assembly deviation determination is demonstrated to be quite robust and accurate, thus the output results of the tolerance analysis are reliable and accurate enough; (b) for predicting the assembly deviations of the over-constrained mechanical structure, the influence of gravity is remarkable and cannot be ignored.

Our main contribution lies in developing a reliable and accurate method for assembly tolerance analysis with overconstraints of multiple planar hole-pin-hole pairs, considering the influence of gravity. Besides gravity, it can be used to incorporate the influence of other conservative forces into tolerance analysis of over-constrained assembly as well.

In the proposed method, Monte Carlo simulation (MCS) is used for the statistical tolerance analysis, due to its general applicability for implicit and non-linear problem. The accurate and reliable application of the MCS lightly depends on the number of iterations. The accuracy of prediction can be improved by increasing the number of iterations at the cost of computational time. To relieve the required computational effort, the first-order reliability method (FORM) method combining with a reasonable linearization strategy for the non-linear constraints will enable a reasonably accurate prediction of defect probabilities at a lower computational effort. However, it should be noted that the loss of accuracy of prediction on defect probability would be unavoidable.

Furthermore, the proposed method is applied to the two-dimensional tolerance analysis of over-constrained assemblies, but the analytical framework of the proposed method may be extended to three dimension applications, i.e., for over-constrained mechanical structure, the assembly feasibility judgment and the assembly deviation determination considering the influence of gravity can be modeled as a search problem and an optimization problem, respectively. For the three-dimensional case, the DOFs in space instead of the ones on plane are required to be considered, and the analysis of assembly requirement is more challenging. Then, the search and optimization problems for judging assembly feasibility and determining assembly deviations are more difficult to be modeled and solved. The authors are already working on the extension of the method employed in this paper to the three-dimensional tolerance analysis of over-constrained assembly. Besides, in future work, part deformation for eliminating the interference between different parts will also be integrated into the assembly tolerance analysis.

Data Availability

The data used to support the findings of this study are available from the corresponding author upon request.

Conflicts of Interest

The authors declare that there are no conflicts of interest regarding the publication of this paper.

Acknowledgments

The work described in this paper is supported by the National Natural Science Foundation of China (under Grant nos. 51275236, 51075206, and 51575266) as well as Jiangsu Key Laboratory of Precision and Micro-Manufacturing Technology (ZAA1400105).

References

[1] A. Dumas, N. Gayton, J.-Y. Dantan, and B. Sudret, "A new system formulation for the tolerance analysis of overconstrained mechanisms," *Probabilistic Engineering Mechanics*, vol. 40, pp. 66–74, 2015.

[2] D. Gouyou, Y. Ledoux, D. Teissandier, and V. Delos, "Tolerance analysis of overconstrained and flexible assemblies by polytopes and finite element computations: application to a flange," *Research in Engineering Design*, vol. 29, no. 1, pp. 55–66, 2018.

[3] A. Ballu, J.-Y. Plantec, and L. Mathieu, "Geometrical reliability of overconstrained mechanisms with gaps," *CIRP Annals - Manufacturing Technology*, vol. 57, no. 1, pp. 159–162, 2008.

[4] J.-Y. Dantan and A.-J. Qureshi, "Worst-case and statistical tolerance analysis based on quantified constraint satisfaction problems and Monte Carlo simulation," *Computer-Aided Design*, vol. 41, no. 1, pp. 1–12, 2009.

[5] A. J. Qureshi, J.-Y. Dantan, V. Sabri, P. Beaucaire, and N. Gayton, "A statistical tolerance analysis approach for overconstrained mechanism based on optimization and Monte Carlo simulation," *Computer-Aided Design*, vol. 44, no. 2, pp. 132–142, 2012.

[6] P. Beaucaire, N. Gayton, E. Duc, M. Lemaire, and J.-Y. Dantan, "Statistical tolerance analysis of a hyperstatic mechanism, using system reliability methods," *Computers & Industrial Engineering*, vol. 63, no. 4, pp. 1118–1127, 2012.

[7] P. Beaucaire, N. Gayton, E. Duc, and J.-Y. Dantan, "Statistical tolerance analysis of over-constrained mechanisms with gaps using system reliability methods," *Computer-Aided Design*, vol. 45, no. 12, pp. 1547–1555, 2013.

[8] A. Dumas, J.-Y. Dantan, and N. Gayton, "Impact of a behavior model linearization strategy on the tolerance analysis of overconstrained mechanisms," *Computer-Aided Design*, vol. 62, pp. 152–163, 2015.

[9] P. Franciosa, S. Gerbino, and S. Patalano, "Variational modeling and assembly constraints in tolerance analysis of rigid part assemblies: Planar and cylindrical features," *The International Journal of Advanced Manufacturing Technology*, vol. 49, no. 1-4, pp. 239–251, 2010.

[10] H. Li, H. Zhu, P. Li, and F. He, "Tolerance analysis of mechanical assemblies based on small displacement torsor and deviation propagation theories," *The International Journal of Advanced Manufacturing Technology*, vol. 72, no. 1-4, pp. 89–99, 2014.

[11] L. Pierre, D. Teissandier, and J. P. Nadeau, "Variational tolerancing analysis taking thermomechanical strains into account: Application to a high pressure turbine," *Mechanism and Machine Theory*, vol. 74, pp. 82–101, 2014.

[12] A. Corrado, W. Polini, and G. Moroni, "Manufacturing signature and operating conditions in a variational model for tolerance analysis of rigid assemblies," *Research in Engineering Design*, vol. 28, no. 4, pp. 529–544, 2017.

[13] N. Cai and L. Qiao, "Rigid-compliant hybrid variation modeling of sheet metal assembly with 3D generic free surface," *Journal of Manufacturing Systems*, vol. 41, pp. 45–64, 2016.

[14] S. Jin, H. Chen, Z. Li, and X. Lai, "A small displacement torsor model for 3D tolerance analysis of conical structures," *Proceedings of the Institution of Mechanical Engineers, Part C: Journal of Mechanical Engineering Science*, vol. 229, no. 14, pp. 2514–2523, 2015.

[15] C. Mickaël and A. Bernard, "3D ISO manufacturing specifications with vectorial representation of tolerance zones," *The International Journal of Advanced Manufacturing Technology*, vol. 60, no. 5-8, pp. 577–588, 2012.

[16] R. Mantripragada and D. E. Whitney, "Modeling and controlling variation propagation in mechanical assemblies using state transition models," *IEEE Transactions on Robotics and Automation*, vol. 15, no. 1, pp. 124–140, 1999.

[17] J. Liu, J. Jin, and J. Shi, "State space modeling for 3-D variation propagation in rigid-body multistage assembly processes," *IEEE Transactions on Automation Science and Engineering*, vol. 7, no. 2, pp. 274–290, 2010.

[18] H. Li, H. Zhu, X. Zhou, P. Li, and Z. Yu, "A new computer-aided tolerance analysis and optimization framework for assembling processes using DP-SDT theory," *The International Journal of Advanced Manufacturing Technology*, vol. 86, no. 5-8, pp. 1299–1310, 2016.

[19] D. E. Whitney, O. L. Gilbert, and M. Jastrzebski, "Representation of geometric variations using matrix transforms for statistical tolerance analysis in assemblies," *Research in Engineering Design*, vol. 6, no. 4, pp. 191–210, 1994.

[20] A. Desrochers and A. Rivière, "A matrix approach to the representation of tolerance zones and clearances," *The International Journal of Advanced Manufacturing Technology*, vol. 13, no. 9, pp. 630–636, 1997.

[21] F. Librino, M. Levorato, and M. Zorzi, "An algorithmic solution for computing circle intersection areas and its applications to wireless communications," *Wireless Communications and Mobile Computing*, vol. 14, no. 18, pp. 1672–1690, 2014.